

**Geometric Parameterisation in
Finite Element Models of
Femoroacetabular Impingement**

Robert John Cooper

Submitted in accordance with the requirements for the degree of
Doctor of Philosophy

The University of Leeds
School of Mechanical Engineering

October 2017

The candidate confirms that the work submitted is his own, except where work which has formed part of jointly-authored publications has been included. The contribution of the candidate and the other authors to this work has been explicitly indicated below. The candidate confirms that appropriate credit has been given within the thesis where reference has been made to the work of others.

Chapters 3 and 4 of this thesis contain material published in a jointly authored paper:

Cooper RJ, Mengoni M, Groves D, Williams S, Bankes MJK, Robinson P, Jones AC. (2017). Three-dimensional assessment of impingement risk in geometrically parameterised hips compared with clinical measures. *International Journal for Numerical Methods in Biomedical Engineering*. e2867.

The candidate developed the computational methods and analysed the results in this paper. Co-authors contributed valuable discussion of the paper and provided access to patient CT scans used.

This copy has been supplied on the understanding that it is copyright material and that no quotation from the thesis may be published without proper acknowledgement.

© 2017 The University of Leeds and Robert John Cooper

The right of Robert John Cooper to be identified as Author of this work has been asserted by him in accordance with the Copyright, Designs and Patents Act 1988.

Acknowledgements

I would like to thank everyone who helped me to complete this project. Thanks in particular to my primary supervisor Dr Alison Jones for her helpful guidance throughout the project. Particular thanks also to: my co-supervisors; Dr Marlène Mengoni for countless invaluable suggestions, and Dr Sophie Williams for additional reading of my work and feedback, and to the other co-authors on my paper; Dr Dawn Groves, Mr Marcus Bankes, and Dr Phil Robinson for all their valuable contributions. I am thankful that I have been fortunate enough to have been supported throughout my PhD by an EPSRC studentship, and I am tremendously grateful to have been lucky enough to meet many fantastic people in Leeds and elsewhere.

Abstract

Abnormal bony morphology is a factor implicated in hip joint soft tissue damage and an increased lifetime risk of osteoarthritis. One geometric feature causing impingement and thus resulting in such damage is a bony lump on the femoral neck, known as a cam deformity. A three-dimensional geometric parameterisation system was developed to capture key variations in the femur and acetabulum of subjects with clinically diagnosed cam deformity. Novel quantitative measures of the size and position of cams were taken and used to assess differences in morphological deformities between males and females. The precision of the measures was sufficient to identify differences between subjects that could not be seen using two-dimensional imaging; cams were found to be more superiorly located in males than in females. As well as providing a means to distinguish between subjects more clearly, the geometric hip parameterisation facilitated flexible and rapid automated generation of a range of hip geometries including cams. These were used to develop finite element models. Patient-specific parametric finite element models of hips under impingement conditions were verified with comparison to their patient-specific segmentation-based equivalents. The parameterisation system was then used to generate further models to investigate the effects of bone morphology on tissue strains. This demonstrated that a combination of cam location and extent affect impingement severity, highlighting the importance of reporting the full three-dimensional geometry used for parametric models.

Contents

Declaration	i
Acknowledgements	ii
Abstract	iii
Contents	iv
List of Tables	xii
List of Abbreviations	xiii
List of Figures	xiv
1 Introduction	1
1.1 Introduction	1
1.2 Software and imaging resources	2
1.3 Thesis overview	3
2 Literature Review	5
2.1 Introduction	5
2.2 Hip joint morphology	5

2.3	Femoroacetabular impingement	8
2.4	Hip joint measurements	11
2.4.1	Femoral shape	12
2.4.2	Acetabular coverage	13
2.5	Radiographic signs and diagnosis of hip abnormality	15
2.5.1	Assessment of cam impingement using alpha angles	16
2.5.2	Diagnosis and treatment of hip impingement	17
2.5.3	Differences between females and males	18
2.6	Finite element modelling background	18
2.7	Methods of modelling hip geometry	19
2.7.1	Parameterised and segmentation-based geometry	19
2.7.2	Mathematically describing hip shape	20
2.8	Computational models of the natural hip	23
2.8.1	Approaches and applications	23
2.8.2	Loading and boundary conditions	26
2.8.3	Material properties	28
2.8.3.1	Cartilage	28
2.8.3.2	Bone	30
2.8.3.3	Labrum	31
2.8.4	Contact interactions	32
2.8.5	Variation in hip morphology	32
2.8.6	Validation and verification	34
2.9	Parametric and segmentation-based models	37

2.9.1	Parameterised and segmentation-based models of FAI	37
2.9.2	Consequences of simplified geometry	39
2.10	Challenges in hip impingement contact modelling	43
2.11	Conclusions	45
3	Development of Parameterisation Methods	47
3.1	Introduction	47
3.2	Approach to geometric parameterisation	49
3.3	Bone segmentation	50
3.4	Geometric parameterisation of the proximal femur	52
3.4.1	Femoral parameterisation 1: head-neck and cam separately	52
3.4.1.1	Initial parameter extraction	52
3.4.1.2	Parametric surface generation	56
3.4.2	Femoral parameterisation 2: ellipse-based parameterisation	57
3.4.2.1	Ellipse parameter extraction	57
3.4.2.2	Parametric surface generation	60
3.5	Optimisation and evaluation of femoral parameterisations	61
3.5.1	Fitting error calculations	61
3.5.2	Optimisation	61
3.5.2.1	Parameterisation 1 optimisation	62
3.5.2.2	Parameterisation 2 optimisation	62
3.6	Femoral parameterisation results and discussion	62
3.7	Geometric parameterisation of the acetabulum	67
3.7.1	Development of acetabular parameterisation	68

3.7.1.1	Initial method	68
3.7.1.2	Improving the method	69
3.7.2	Final acetabular parameterisation method	70
3.8	Discussion	71
3.8.1	Femoral surfaces	72
3.8.2	Acetabular surfaces	73
3.8.3	Conclusion	73
4	Parameterisation Study	75
4.1	Introduction	75
4.1.1	Overview of study methodology	76
4.2	Cam severity measurements	77
4.2.1	Comparison to control femurs	78
4.2.2	Sensitivity to neck-axis	79
4.3	Acetabular angle measurements	80
4.4	Mesh optimisation and fitting error calculations	82
4.5	Two-dimensional measurements	83
4.6	Statistics	84
4.7	Results	85
4.7.1	Severity measurement results	85
4.7.1.1	Comparison of females and males	85
4.7.1.2	Comparison of controls and cam patients	86
4.7.1.3	Sensitivity to femoral neck axis	87
4.7.2	Mesh optimisation and fitting error results	88

4.7.3	Comparison of 3D and 2D measurements	90
4.7.3.1	Inter-user variation in 2D measurements	91
4.8	Discussion	91
4.8.1	Study significance	92
4.8.1.1	Difference in male and female cams	92
4.8.1.2	Assessment of alpha angle in different radiographic views	93
4.8.1.3	Two and three-dimensional acetabular measures	93
4.8.1.4	Inter-user variation	94
4.8.2	Study limitations and challenges	94
4.8.2.1	Assumption of anatomical orientation	94
4.8.2.2	User variation in parametric and severity measures	95
4.8.2.3	Image and mesh resolution	95
4.8.2.4	Sensitivity of severity measures to parametric method	96
4.8.3	Conclusions	96
5	Development of Finite Element Modelling Methodology	98
5.1	Introduction	98
5.2	Preliminary investigations for calibration of modelling settings	100
5.2.1	Background	101
5.2.2	Preliminary model sensitivity tests	102
5.2.3	Findings of preliminary investigations	105
5.2.3.1	Balancing mesh refinement and cartilage thickness with contact convergence	106
5.2.3.2	Applying femoral rotations	107

5.2.3.3	Nonlinearities	107
5.2.4	Conclusion of preliminary investigations	109
5.3	Development of soft tissue representation	109
5.3.1	Initial generation in ScanIP	111
5.3.2	Using ScanIP +NURBS	112
5.3.3	Producing soft tissue geometry within Abaqus	113
5.3.3.1	Cartilage generation using mesh offsetting	113
5.3.3.2	Manual generation of acetabular soft tissue	115
5.3.3.3	Spherical acetabulum geometry	118
5.4	Models to investigate boundary conditions and geometry	120
5.4.1	Methods	120
5.4.2	Process automation using Python	124
5.4.3	Findings of boundary condition and geometry tests	125
5.4.3.1	Translation control boundary conditions	125
5.4.3.2	Force control boundary conditions	126
5.4.3.3	Simplified acetabular geometry	127
5.4.3.4	Pinned boundary conditions	128
5.4.3.5	Model run times	129
5.5	Discussion	129
5.5.1	Geometry considerations	130
5.5.2	Boundary condition considerations	132
5.5.3	Material properties	132
5.5.4	Conclusions	133

6	Finite Element Model Study	135
6.1	Introduction	135
6.1.1	Study methodology	136
6.2	Material property sensitivity	137
6.2.1	Results and discussion	140
6.3	Segmented vs parametric femoral geometry	146
6.3.1	Methods	146
6.3.1.1	Outputs of interest	147
6.3.1.2	Mesh convergence	148
6.3.2	Results	149
6.4	Parametric study of morphology changes	155
6.4.1	Methods	155
6.4.1.1	Parametric cam morphology tests	155
6.4.1.2	Parametric acetabular morphology tests	156
6.4.2	Results	158
6.5	Discussion	159
6.5.1	Damage regions and mechanisms	160
6.5.2	Segmented vs parametric models	161
6.5.3	Parametric tests	162
6.5.4	Study limitations and challenges	163
6.5.4.1	Geometric simplifications	164
6.5.4.2	Boundary conditions	164
6.5.4.3	Material properties	165

6.5.5	Conclusions	165
7	Overall Discussion and Conclusions	167
7.1	Summary	167
7.2	Key achievements and findings	168
7.3	Overall discussion	170
7.3.1	Femoral shape analysis	170
7.3.2	Cam severity measurements	171
7.3.3	Acetabular shape analysis	172
7.3.4	Parametric and segmentation-based FE models	173
7.3.5	Software constraints	174
7.3.6	Model outputs to assess soft tissue damage	175
7.4	Conclusion	177
	Bibliography	178
	Appendix A: Publications	190
	Appendix B: Tabulated raw data for parameterisation study	191

List of Tables

2.1	Key FE modelling studies of the hip	25
2.2	Anderson et al.'s study on geometric simplification in hip models	40
3.1	Initial fitting error results	63
4.1	Range of femoral severity measurements	85
4.2	Convergence of fitting error	88
4.3	Fitting error results for parametric surfaces	89
5.1	Overclosure relationships to meshing and cartilage thickness	107
5.2	Impingement boundary conditions	123
5.3	Decision process for boundary conditions	125
A1	Femoral severity measurements	191
A2	Alpha angle measurements	192
A3	CE angle measurements	192
A4	AV angle measurements	193
A5	Strain and rotation centre for patient-specific models	193

List of Abbreviations

2D	Two-Dimensional
3D	Three-Dimensional
AP	Anterior-Posterior
AV	Acetabular Version (angle)
BCs	Boundary Conditions
CCD	Centrum Collum Diaphyseal (angle)
CE	Centre Edge (angle)
CT	Computed Tomography
DICOM	Digital Imaging and Communications in Medicine
DoF	Degrees of Freedom
E	Young's modulus
FAI	Femoracetabular Impingement
FEA	Finite Element Analysis
GB	Gigabytes
GFLOPS	Floating Point Operations Per Second $\times 10^9$
HR	Head Radius
MR	Magnetic Resonance
NURBS	Non-Uniform Rational Basis Splines
OA	Osteoarthritis
PC	Personal Computer
PCA	Principal Component Analysis
STL	Stereolithography
RAM	Random Access Memory
ν	Poisson's ratio

List of Figures

2.1	Natural human hip	6
2.2	Anatomical Planes	7
2.3	Axial schematic showing features of the hip	8
2.4	Femoracetabular impingement morphology.	8
2.5	Femoracetabular impingement damage mechanisms.	9
2.6	Alpha angle	12
2.7	CCD angle	13
2.8	Centre Edge angle	14
2.9	AV angle	14
3.1	Femoral bone segmentation in ScanIP	50
3.2	Acetabular bone segmentation in ScanIP	51
3.3	Axes set up	52
3.4	Initial parameterised proximal femur	53
3.5	Extracting original neck and cam parameters	55
3.6	Spherical cap angle	57
3.7	Segmented and parametric femurs showing ellipse parameters	59
3.8	Scatter plots of poorly fitted vertices	65

3.9	Excess undulation on parametric femurs	66
3.10	Segmented and parametric femoral surfaces	67
3.11	Initial acetabular loft in MATLAB	68
3.12	Selection of nodes on acetabulum for spline fitting	69
3.13	Segmented and parametric acetabular surfaces	71
4.1	Impingement severity parameters defined on an ellipse	78
4.2	Rotations to align femurs to their neck axis	79
4.3	Acetabular AV angles calculated from parametric nodes	80
4.4	Acetabular AV angles as a function of their position on the superior- inferior axis.	81
4.5	Acetabular CE angles calculated from parametric nodes	82
4.6	Examples of 2D measurements on radiographs	84
4.7	Comparison of cam position in females and males	86
4.8	Comparison of cam-rad in cam patients and controls	87
4.9	Strong correlations between cam-rad values at different neck angles	88
4.10	Applying the femoral parameterisation to a sphere	89
4.11	Correlations between cam size measurements	90
4.12	Correlations between 2D and 3D acetabular angles	91
5.1	Overclosure diagram	102
5.2	Preliminary model set up	103
5.3	Preliminary model contact	106
5.4	Hourglassing in labrum elements	108
5.5	Patient and cadaveric CT scans	110

5.6	Suboptimal soft tissue geometry in ScanIP	112
5.7	Meshing a NURBS surface	113
5.8	Position of femoral cartilage.	114
5.9	Generation of femoral cartilage.	115
5.10	Generation of acetabular cartilage in specific regions	116
5.11	Manually generated acetabular soft tissue.	118
5.12	Simplified spherical acetabular geometry	119
5.13	Additional ellipse to avoid femur slipping into cavity	121
5.14	Meshed hip models for testing boundary conditions	122
5.15	Translation control boundary conditions	126
5.16	Force control boundary conditions	128
5.17	Pinned boundary conditions	129
6.1	Axes defined on acetabular soft tissues	139
6.2	Deformed and undeformed cartilage-labrum junction, and deformed mesh	141
6.3	Strain shown on a deformed cartilage-labrum junction	142
6.4	Location of peak strain as impingement progresses	143
6.5	Material property sensitivity graph	144
6.6	Strain in parametric models with varying material properties	145
6.7	Meshed segmented and parameterised femurs	147
6.8	Graphs demonstrating mesh convergence	149
6.9	Graphs of max. displacement and strain (low mesh density)	151
6.10	Graphs of max. displacement and strain (high mesh density)	152
6.11	Poor agreement between models	153

6.12	Local fitting causing differences between models	154
6.13	Parametric femoral variations	156
6.14	Parametric acetabular variations	157
6.15	Parametric changes to femur	158
6.16	Parametric changes to acetabulum	159
6.17	Mechanisms of elevated tensile strains in cartilage in the cam models . . .	161

Chapter 1

Introduction

1.1 Introduction

Abnormal geometry of the hip joint is associated with femoroacetabular impingement (FAI), which can result in pain and intra-articular damage. Repeated contact between the femoral bone and acetabular rim (typically resulting from flexion and internal rotation) can cause labral pathology and progressive delamination of cartilage, and has been linked to the development and progression of osteoarthritis (Ganz et al., 2003; Beck et al., 2005; Jaberri and Parvizi, 2007; Okano and Yamaguchi, 2013). The damage mechanisms of impingement are not fully understood and it is unclear why some abnormally shaped hips result in pain and damage while others do not (Khanna et al., 2014). Finite element (FE) models provide a method of studying contact occurring in natural joints, and in particular can be used to help identify the effects of varying morphological properties on tissue strains (Chegini et al., 2009; Li et al., 2013).

This thesis is concerned with the geometric parameterisation of the bones forming the hip joint, and assessment of the potential severity of impingement resulting from abnormal bone morphologies through the use of parametric FE models. The focus is on cam type FAI, in which excess bone on the femoral neck abuts against the acetabular rim. A significant new contribution of this work is a novel method of parametrically representing the geometry of femurs with cam deformity, allowing new measures of the size of cams on the femoral neck to be defined, and providing a computational tool to parametrically investigate tissue strains occurring under different morphologies.

The general aims of this research were to:

1. Develop a geometric parameterisation method to generate subject-specific parametric surfaces to represent morphology of proximal femurs with cams and lunate articular acetabular surfaces.
2. Apply the parameterisation method to a clinical data set in order to define measurements to assess impingement risk and hence investigate morphological differences between male and female hips diagnosed with cam type impingement.
3. Develop methodology to simulate impingement movements in finite element models using parametric and segmented bone surfaces.
4. Compare models using geometrically parameterised surfaces against models using their segmented equivalent.
5. Use parametric models to investigate the effects of geometric variation on soft tissue strains in the hip joint during impingement.

1.2 Software and imaging resources

The main software packages used in this project are now introduced. First, for FE modelling, the commercial software Abaqus CAE 6.14-1 (Dassault Systèmes, Vélizy-Villacoublay, France) was used. In all areas of model development, the Python 2.7.3 scripting interface (Python Software Foundation, Wilmington, DE, USA) was used as much as possible to automate processes.

The numerical computing environment, MATLAB R2014b (The MathWorks Inc, Natick, MA, USA) was used for developing computational tools for geometric parameterisation and for generating statistics and graphs.

The commercial image processing and mesh generation software package Simpleware ScanIP 7.0 (Synopsys, Mountain View, CA, United States) was used for image segmentation. The image processing software, ImageJ 1.49m (National Institute of Health, MD, USA) was used for angle measurements. The image processing application for Mac dedicated to DICOM images, OsiriX lite 32 bit 6.0.1 (Pixmeo, Geneva, Switzerland), was also used for this purpose on medical images.

The clinical images used in this work are now described. A database of pre-operative pelvic Computed Tomography (CT) images (Sensation 16 CT scanner, Siemens, Berlin and Munich, Germany, voxel size: $0.7422 \times 0.7422 \times 1$ mm) of patients who underwent surgery for cam type impingement was available for use in this project ($n = 82$) (Guy's Hospital, London). The field of view in these scans was limited to the pelvic region with only some of the distal femoral region visible. All patients included in these databases

were able to give written, informed consent, were aged 18 years or over (and skeletally mature at the time of scanning), and had a clinical diagnosis of cam FAI with pre-operative CT scans readily available. Patients had been excluded from the study database if they had undergone surgery in the affected hip prior to the CT scan being taken, or in the opinion of the associated clinical investigator (Marcus Bankes), had an existing condition that would compromise their participation in the study (e.g. osteoarthritis). Additionally, a set of control scans was available from patients who had undergone CT scans in the same clinic due to hip pain, but were not diagnosed with cam impingement ($n = 24$). Ethical approval (reference MEEC 11-044) was granted by the Faculty of Engineering research ethics committee at the University of Leeds. In addition to the clinical scans, micro-CT scans (voxel size: $0.082 \times 0.082 \times 0.082$ mm) of cadaveric hip specimens conducted at the University were available ($n = 12$, from 6 subjects). Ethical approval for these (reference MEEC 13-002) was granted by the Faculty of Engineering research ethics committee at the University of Leeds.

1.3 Thesis overview

Chapter 2 is a literature review providing background material on the hip joint and FAI, and on FE modelling, as well as discussion of the most pertinent literature related to FE modelling of the natural hip joint using both parametric and segmentation-based techniques. The focus is particularly on FAI and on the development of models used to investigate the effects of morphological variation.

Chapter 3 discusses the development of geometric parameterisation systems to represent the bony geometry of hips with cam deformities. Chapter 4 describes a study applying the chosen parameterisation system to a set of patients to assess key shape differences and compare these outputs with two-dimensional measured results.

Chapter 5 discusses the development of methodology to generate FE models. Whilst bone tissue is clearly defined in the clinical CT images of FAI patients used in this project, cartilage and labral tissue are not, so soft tissue geometry could not be reproduced from these CT scans. Development of methods to represent soft tissue geometry for inclusion in models is also discussed in Chapter 5.

Chapter 6 contains studies using the developed FE methodology: investigating material properties, verifying patient-specific parametric FE models with comparison to their segmentation-based equivalents, and using parametric models to investigate the effects of bone morphology on tissue strains.

In Chapter 7 this work is reviewed, with overall conclusions drawn from the results that have been presented, and some suggestions for future work are proposed.

Finally, Appendix A details the publications associated with this thesis, and Appendix B contains tabulated raw data.

Chapter 2

Literature Review

2.1 Introduction

There are several radiographical signs associated with femoroacetabular impingement and other hip abnormalities, but there is also evidence that some of these signs can present in asymptomatic populations, meaning diagnosis is not straightforward (Harris et al., 2014), and understanding normal anatomy is crucial for diagnosing hip pathologies. In this chapter, Section 2.2 gives an overview of normal hip joint morphology and Section 2.3 discusses femoroacetabular impingement in more detail. Particular attention is afforded to measurements of the hip joint and the diagnosis of hip disorders in Sections 2.4 and 2.5. Section 2.7 covers potential methods of representing hip geometry in computational models, in particular by using segmentation-based or parameterisation approaches. Background on finite element modelling is then given in Section 2.6, and remaining sections provide discussion of the available literature on modelling the natural hip joint (Section 2.8), concerned with the comparison of parametric and segmentation-based models particular (Section 2.9). The challenges with modelling are highlighted in Section 2.10, and conclusions are given in Section 2.11.

2.2 Hip joint morphology

The hip joint is the ball-and-socket synovial joint between the head of the femur and the acetabulum, the cup-like cavity of the pelvis that occurs at the union of three pelvic bones: the ilium, pubis, and ischium. Thus the hips connect the legs to the pelvis and hence to

the axial skeleton of the trunk. The hips support the weight of the body in both static and dynamic postures. The morphology of the natural human hip joint is shown in Figure 2.1.

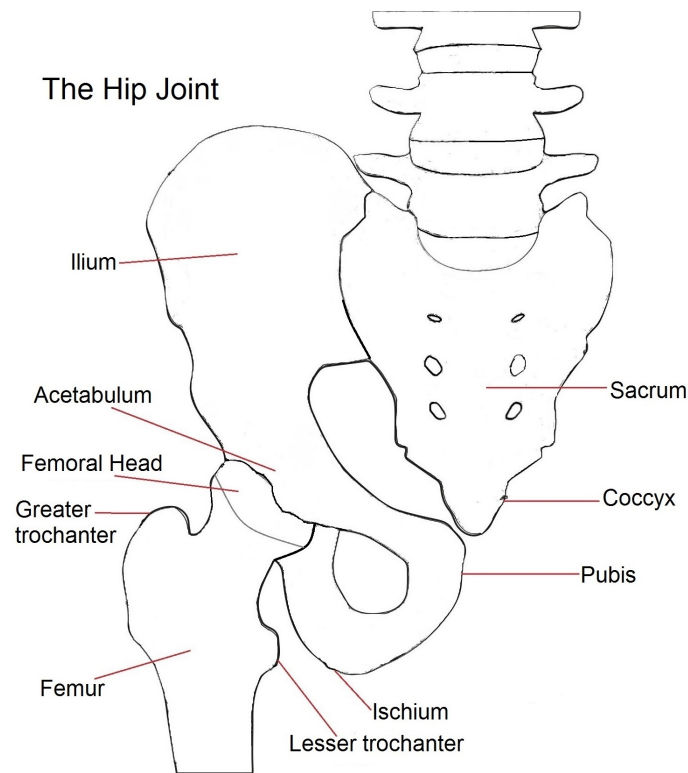


Figure 2.1: Schematic of the natural human hip joint (adapted from (Blausen, 2015)).

The femur is the long bone in the thigh, between the knee and pelvis, and is the longest and strongest bone in the human body. In addition to the femoral head at the end of the neck, there are two protrusions close to the top of the femur: the greater trochanter and lesser trochanter. Articular cartilage covers the head of the femur up to the head-neck junction. It is thicker at the peak of the head than at the circumference and completely covers the surface, except at the fovea capitis femoris, where the ligamentum teres attaches it to a notch in the acetabulum.

Located inferior to the acetabular notch is a circular non-articular perforated depression, the acetabular fossa, which acts as a foramen to allow nerves and vessels to enter the joint. Articular cartilage covers the lunatic surface of the rest of the acetabulum, where it articulates with the femur. The layers of cartilage between the acetabulum and femur are lubricated by synovial fluid, resulting in a coefficient of friction less than that of ice on ice (< 0.1) (Cowin and Doty, 2007).

The acetabular labrum is a fibrocartilaginous rim with a tissue structure similar to the meniscus in the knee, and it provides a further ring of cartilage around the acetabulum. The labrum attaches to the lunatic surface of the articular cartilage and deepens the ac-

etabular socket, reducing the likelihood of the femur slipping out of place. It joins with the transverse acetabular ligament, bridging the acetabular notch and forming a complete circle (Grant et al., 2012).

The hip joint is strengthened by other ligaments attaching it to the pelvis; the iliofemoral, ischiofemoral, and pubofemoral ligaments. The stability of the hip joint is also enhanced by its encasement in a capsule that contains the synovial fluid, and by the muscles that surround the hip and allow movement. The joint allows for an extensive range of movements, made possible by a combination of: flexion and extension (sagittal plane), adduction and abduction (coronal plane), and internal-external rotation (transverse or axial plane) (Figure 2.2).

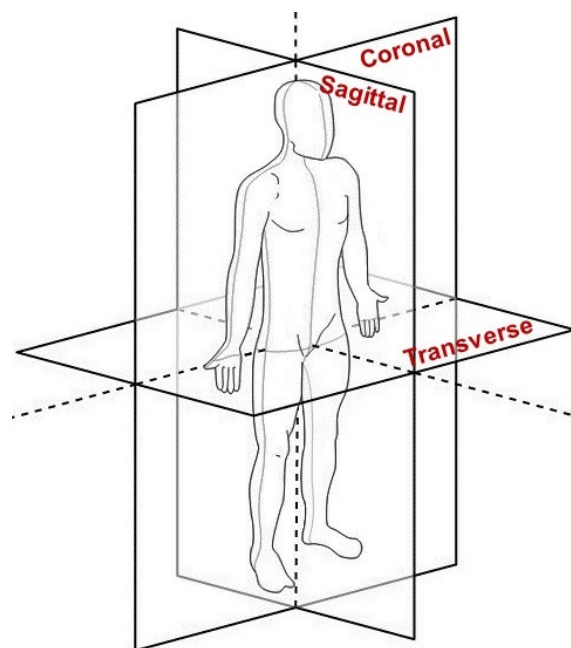


Figure 2.2: Anatomical planes on a human.

The complex morphology of the hip joint can be described in a more approximate way by relatively simple geometric shapes. The femoral head can be thought of as slightly more than half a sphere. The femoral neck attaches the head to the shaft and is essentially cylindrical, but concave to ensure anterior superior head-neck clearance without impingement (Figure 2.3). The position of the head may be such that its centre lies along an imagined continuation of the geometric neck axis, or may be slightly displaced inferior and posterior to the neck (Banerjee and Mclean, 2011). The acetabulum is cup shaped, and the cross-section of the labrum is triangular, with the base attached to the acetabulum and the top forming the free edge of the labrum, which is turned in against the femoral head (Ferguson et al., 2000) (Figure 2.3).

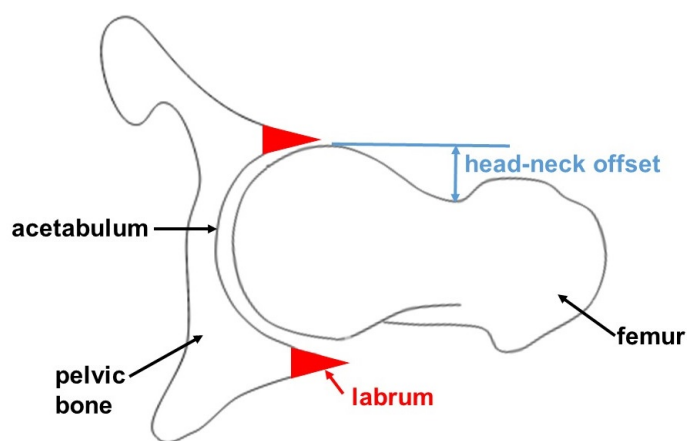


Figure 2.3: Schematic of the hip joint shown in an axial view. The labrum and definition of head-neck offset are indicated.

2.3 Femoroacetabular impingement

The primary hip abnormality of interest in this work is femoroacetabular impingement (FAI), defined as abnormal contact between the acetabular rim and the femur, caused by abnormal shape of the proximal femur and/or abnormal shape of the acetabulum (Tannast et al., 2007; Banerjee and Mclean, 2011). FAI symptoms can be bilateral or unilateral (Bredella et al., 2013), and the condition can cause pain and reduced joint function. Because it can lead to cartilage damage it has been suggested as a potential mechanism for development of osteoarthritis (OA) (Ganz et al., 2003). It is important that diagnosis and treatment of FAI occurs as early as possible to prevent development of OA and thus delay the need for total hip replacement surgery (Jaberi and Parvizi, 2007). Various abnormal morphologies have been reported as potential causes of FAI, and these can be grouped into two main types: cam impingement and pincer impingement (Figure 2.4).

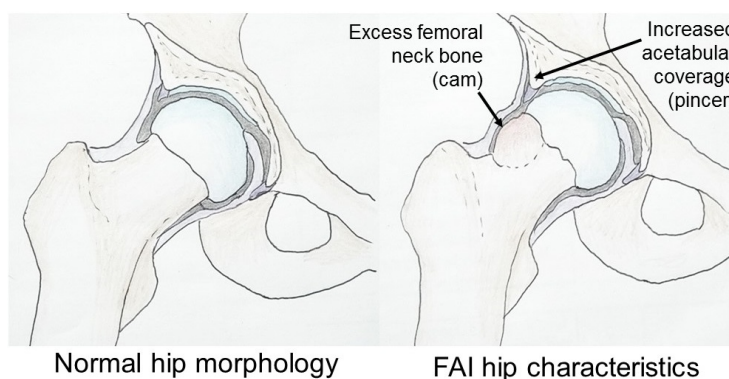


Figure 2.4: Femoroacetabular impingement morphology (adapted from (AAOS, 2015)).

In a normal hip, no impingement should occur during a normal range of flexion (Figure

2.5a). A cam bump can cause shear force from the outside in, along the acetabular cartilage surface, resulting in damage especially to the anterosuperior cartilage (Figure 2.5b). Excess acetabular bone found in pincer impingement results in the labrum undergoing compressive damage by the femur, which is levered backwards causing contrecoup damage to the femoral cartilage where it abuts against the posteroinferior acetabulum (Figure 2.5c).

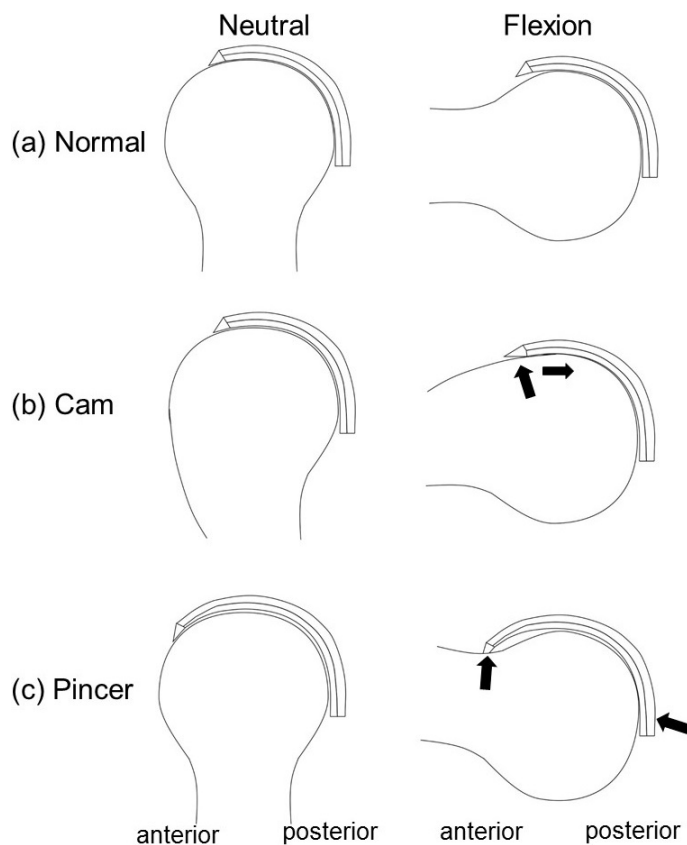


Figure 2.5: Schematic of femoral heads and acetabulums viewed in the sagittal plane with anterior on the left. Anticipated regions of damage due to impingement are indicated by arrows.

Cam impingement is most common in young active men (Tannast et al., 2007), and is caused by excess bone on the anterior femoral neck, resulting in asphericity of the femoral head which consequently abuts against the acetabular rim. The osseous cam bump lacks cartilage cover and is normally located on the anterosuperior quadrant of the femur. A further recognised variation is the pistol grip deformity, in which excess bone on the superior side of the femoral head-neck junction causes the femur, when viewed in the coronal plane, to resemble the grip of a flintlock pistol. The size of cams is highly variable, from small focal points of excess bone on the neck, to large deformities covering much of the femoral head and neck on one side, and they generally result in reduced femoral head-neck offset (Banerjee and Mclean, 2011) (Figure 2.3). Repeated contact between

the femoral neck and acetabular rim (resulting from flexion and internal rotation) can result in joint damage as the cam causes a displacement force on the underside of labrum, acting normal to the cam, so that the labrum rotates. Damage occurs to the chondrolabral junction as the labrum is translated away from the joint while the cartilage is pushed in the opposite direction. Labral pathology, with a tear developing in the chondrolabral junction, can occur in conjunction with cartilage degeneration as a result of elevated compressive and shear forces in the joint. Progressive delamination, in which cartilage separates from the underlying subchondral bone creating an unstable cartilage flap, and cleavage of cartilage may occur, with repetitive microtrauma particularly resulting in outside-in cartilage abrasion (Ganz et al., 2003; Tannast et al., 2007; Banerjee and Mclean, 2011; Bredella et al., 2013; Roels et al., 2014; Kuhns et al., 2015).

Pincer impingement is more common in middle-aged active women (Tannast et al., 2007), and involves an acetabular deformity such as an overly deep or retroverted socket. Acetabular retroversion is an abnormal alignment of the acetabulum; rather than facing in the usual anterolateral direction, it inclines more posterolaterally so that there is less posterior cover (Reynolds et al., 1999). Spinal deformities causing pelvic rotation may lead to functional retroversion of the acetabulum and also result in pincer impingement. Pincer impingement is less aggressive than cam, and primarily results in labral degeneration and avulsion (Beck et al., 2005). Ossification of the acetabular rim and cartilage damage can also occur. Additionally, contrecoup damage to the femoral head cartilage can develop due to its abutment against the posteroinferior acetabulum (Tannast et al., 2007; Banerjee and Mclean, 2011; Bredella et al., 2013).

In both cam and pincer FAI, abnormal joint contact can also result in labral tears, which are classified into two types. The first involve detachment of labrum from the articular cartilage surface, and these are thought to be caused by shear forces within joint. The second are intrasubstance tears, thought to result from compression forces on labrum, and these types are irreparable because of the lack of intrasubstance blood supply. The location of labral tears can give an indication of their cause; tears most commonly associated with FAI are anterolateral, but posterior tears can also be caused by contrecoup damage from FAI (Grant et al., 2012; Botser and Safran, 2013).

There is difficulty in categorising FAI because of the high level of variation found in morphologies that can cause impingement. Developmental disorders such as Perthes disease and slipped upper femoral epiphysis have been suggested as aetiological factors for cam impingement (Tibor and Leunig, 2012; Siebenrock and Schwab, 2013; Murgier et al., 2014). Deformities may also be exacerbated as impingement damage progresses and osteophytes develop as a result. Femoral anteversion is another indicator of FAI, with re-

duced femoral anteversion linked to cam impingement and increased femoral anteversion linked to pincer impingement (Botser and Safran, 2013). Other deformities that can be found in FAI cases include os acetabuli (secondary ossified regions of the acetabulum), coxa profunda (overly deep acetabulum seen as the fossa being medial to the ilioischial line), and protrusio acetabuli (medialisation of the medial wall of the acetabulum past the ilioischial line) (Pfirrmann et al., 2006). Hips with FAI have also been seen to have significantly higher prevalence of herniation pits (small cystic lesions seen as radiolucencies surrounded by a sclerotic margin), but the cause of these is not understood and they may be benign and incidental (Tannast et al., 2007; Botser and Safran, 2013). Finally, impingement is also influenced by the position of the pelvis and therefore by lumbar spine morphology (Bouma et al., 2015).

It is unclear whether cam and pincer morphologies are more likely to occur together or in isolation. Beck et al. (2005) stated that patients most commonly display both cam and pincer abnormalities, based on 149 hips where just 26 had isolated cam and 16 had isolated pincer. In this study however cam and pincer were defined based on pistol-grip deformity and coxa profunda respectively. Pistol grip deformity is only one manifestation of cam morphology, and some authors suggest that coxa profunda should not be considered an abnormal radiographic finding, and that it is unnecessary and insufficient for diagnosing impingement (Anderson et al., 2012; Nepple et al., 2013). Another study, Allen et al. (2009), found out of 201 hips with a cam deformity, 84 also had a pincer deformity. However Cobb et al. (2010) disputed the notion that the two types usually occur together; following CT investigations of normal, cam and pincer hips (20 of each), they concluded that cam and pincer hips are distinct conditions. Cam hips were found to have slightly shallower acetabula than normal, whilst pincers had deeper acetabula than normal. This group later compared 37 cam hips with normal hips and found no correlation between acetabular morphology and severity of cams (Masjedi et al., 2013a).

2.4 Hip joint measurements

Geometric measurements of femoral shape and acetabular coverage can be used to describe hip morphology. This can aid clinical assessment of abnormalities, but diagnosis is dependent on clinical opinion and available imaging modalities.

2.4.1 Femoral shape

The alpha angle is the angle between the line passing through the femoral neck midpoint and the femoral head centre, and the line from the femoral head centre to the anterior point where the femoral head diverges from spherical (Figure 2.6). A reported normal alpha angle range is $40^\circ < \alpha < 50^\circ$ (Chegini et al., 2009), with higher angles potentially indicating cam FAI (Nötzli et al., 2002; Pfirrmann et al., 2006; Tannast et al., 2007; Chegini et al., 2009). However it will be seen later (Section 2.5.1) that knowledge of the full three-dimensional (3D) structure and position of a cam may be of greater significance than alpha angle measurements (Harris et al., 2014).

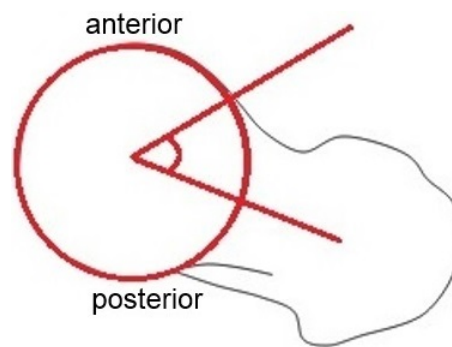


Figure 2.6: The alpha angle can be measured in various 2D views. In this schematic of the hip it is shown measured in the transverse plane.

The anterior head-neck offset is the difference between the anterior radius of the femoral head and the anterior radius of the femoral neck (Figure 2.3). This is the distance between the widest diameter of the femoral head and the most prominent part of the femoral neck. A normal head-neck offset has been reported as around 9 mm, with values less than 8 or 7 mm considered abnormal (Banerjee and Mclean, 2011; Ergen et al., 2014). However values of less than 10 mm have also been suggested as indicator of cam FAI (Tannast et al., 2007).

The position of the femoral head in relation to the femoral shaft can be described with the centrum collum diaphyseal (CCD) angle; the angle between longitudinal axes of the femoral neck and shaft (Figure 2.7). It is usually around 125° with lower values potentially indicating cam FAI (Tannast et al., 2007).

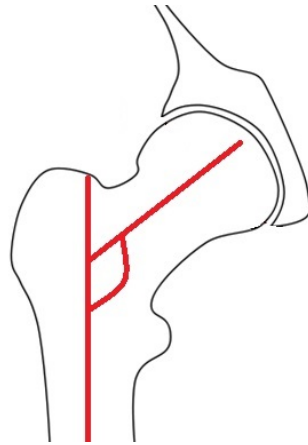


Figure 2.7: Schematic of the hip showing the centrum collum diaphyseal (CCD) angle in the coronal plane.

2.4.2 Acetabular coverage

The coverage of the acetabulum can be described by the centre edge (CE) angle. On an anteroposterior radiograph, the CE angle is the angle between the vertical line through femoral head centre and the line passing through the femoral head centre and the top edge of acetabulum (Figure 2.8). Normal CE angle ranges have been reported as $20^\circ < CE < 30^\circ$ (Chegini et al., 2009) and $25^\circ < CE < 39^\circ$ (Tannast et al., 2007). Higher CE angles can indicate acetabular over-coverage and hence pincer type FAI (Chegini et al., 2009). CE angles of less than 20° are an indication of hip dysplasia, characterised by an abnormally shallow acetabular socket. Like FAI, dysplasia has been linked with early onset OA (Okano and Yamaguchi, 2013). Dysplasia can vary in severity, both in the degree of undercoverage of the socket and the overall incongruence of the joint. The smaller weight-bearing surface in dysplastic hips results in increased contact stresses that lead to labral or articular cartilage damage (Harris-Hayes and Royer, 2011). Damage to the chondral labrum junction may progress to OA, but not all patients with dysplasia develop OA, and symptomless dysplasia is not treated (Wenger, 2013). Dysplasia may cause other hip deformities; a study of 112 patient radiographs found significant correlation between femoral head deformity (measured by roundness index) and severity of dysplasia (Okano and Yamaguchi, 2013). There may also be a compensating increase in labral length when there is a lack of bony acetabular coverage (Garabekyan et al., 2016).

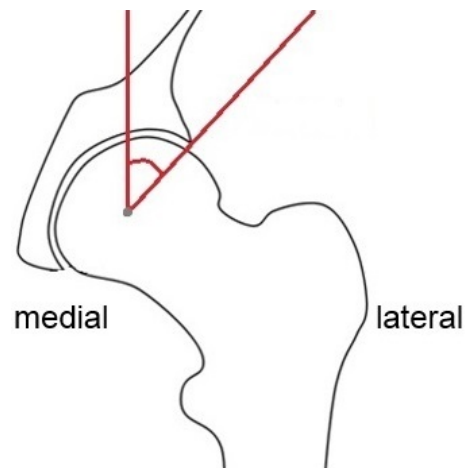


Figure 2.8: Schematic of the hip in the coronal plane showing the Centre Edge (CE) angle.

When acetabular retroversion is present, total acetabular coverage may be normal (around 75%), but there is more anterior cover than usual. This can be seen in anteroposterior radiographs by the cross-over sign, indicating the anterior wall being more lateral than the posterior wall, but the sign can be unreliable because the inclination of the pelvis will change the appearance of X-ray scans (Tannast et al., 2007; Ergen et al., 2014). Dandachli et al. (2009) found the cross-over sign is sensitive but not specific, meaning it is good at detecting retroversion in retroverted patients, but also has a high false positive rate. The acetabular version (AV) angle is the angle between the line joining the anterior and posterior edges of the acetabulum and the line perpendicular to the line joining the posterior edges of the acetabula on both sides (Figure 2.9). A normal AV angle may be around 20° , whilst acetabular retroversion can be defined as an AV angle less than 15° (Ergen et al., 2014).

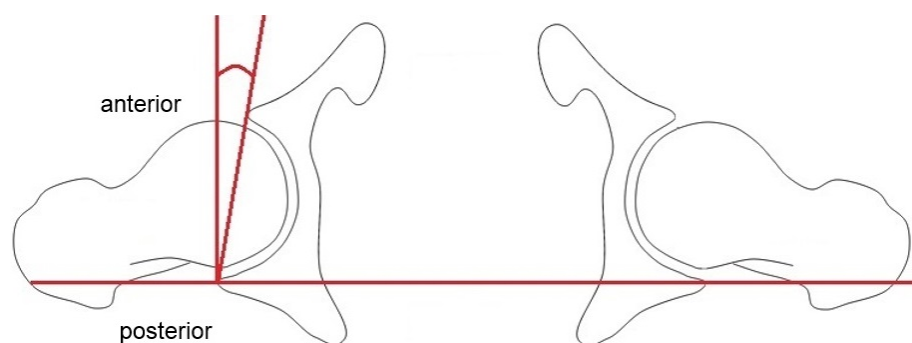


Figure 2.9: Schematic of the hips in the transverse plane showing the acetabular version (AV) angle.

2.5 Radiographic signs and diagnosis of hip abnormality

There is poor correlation between hip pain and radiographic findings of FAI; many studies have found asymptomatic individuals with abnormal morphology (Ranawat et al., 2011; Laborie et al., 2011; Khanna et al., 2014; Lepage-Saucier et al., 2014). Such findings demonstrate that the relationship between abnormal morphology and impingement leading to OA development remains unclear. As a particular example, Ergen et al. (2014) assessed CT scans of 131 hips from 68 patients with negative impingement tests, and concluded that many measurements used for assessing FAI can exceed ranges considered normal in asymptomatic hips. The study found a mean AV angle of $21.52 \pm 4.98^\circ$ with a range of $12^\circ - 39^\circ$. Higher values were observed in females than males. In 10.2% (13 hips), the AV angle was less than 15° . In 11.7% (15 hips), there was an acetabular crossover sign. The mean CE angle was $37.28 \pm 6.12^\circ$ with a range of $25^\circ - 56^\circ$. In 25.8% (33 hips), the CE angle was greater than 40° . The mean head-neck offset was 9.01 ± 1.77 mm with a range of 5 – 13 mm. In 26.8% (37 hips), the offset was less than 8 mm. This study also found a prevalence of increased radial alpha angle ($> 55^\circ$) of 20%. The use of alpha angles to assess cam impingement severity is a particular case where the relationship between abnormal morphology and FAI is unclear (Section 2.5.1).

It remains unclear why some hips with abnormal geometry do not develop OA, but there are other factors that play a role in impingement severity, including patient activity level and vulnerability of the labrum and articular cartilage to injury. Patient pain levels are often self-assessed (Omoumi et al., 2014), and it is possible that some patients downplay or exaggerate their hip pain. Furthermore, difficulties in using 2D radiographic parameters for diagnosing 3D hip abnormalities may be exacerbated by the varying levels of agreement amongst experts analysing radiographs (Kenyon et al., 2014).

Not all patients presenting with morphologies such as decreased head-neck offset are considered to have FAI, since their range of motion is not restricted and they do not suffer from pain. Individual characteristics such as vulnerability of the labrum may be the reason for this (Bredella et al., 2013). It is also possible that some patients are asymptomatic due to comparatively lower levels of physical activity, especially intensity of activities involving a high degree of movement in the hip; sports requiring hip flexion along with varying torque and axial loading can exacerbate FAI. Equally important is that the absence of obvious radiographic signs does not guarantee there is no pathology present; hypermobility, seen in activities like dancing and martial arts, can also result in impingement (Bredella et al., 2013).

The issue is further complicated by the fact that some patients initially without pain may eventually develop hip damage. In a 3-year follow up study, Reichenbach et al. (2011) found that some patients with radiographic signs of FAI but no pain later developed anterolateral labral tears. Hogervorst et al. (2012) introduced the term “cartilotype” to assess susceptibility of cartilage to degradation in response to mechanical stress (resulting from genetically determined factors and load history). Along with differences in patient activity, this concept may in part explain why there are a significant number of patients with FAI or dysplasia who do not develop progressive OA.

2.5.1 Assessment of cam impingement using alpha angles

The alpha angle (Figure 2.6) as a measurement to quantify the size of cams was first described by Nötzli et al. (2002), and alpha angles above 50° or 55° have previously been suggested as indicators of cam impingement (Pfirrmann et al., 2006; Tannast et al., 2007; Chegini et al., 2009). Some authors are reasonably commendatory of alpha angles; one systematic review (deSa et al., 2014) concluded that the use of surgery to reduce the alpha angle in cam hips to less than 55° improves patients' range of motion, and it hence provides a simple and reproducible predictor of outcome for use intra-operatively and post-operatively. However, the review only found 14 studies eligible for inclusion, and among these there was variation both in surgical and alpha angle measuring techniques.

More recently the use of the alpha angle clinically has become controversial, due to several studies finding significant overlap in values between asymptomatic and symptomatic patients. Omoumi et al. (2014) found a high prevalence of CT signs of FAI morphotypes in individuals with asymptomatic, non-osteoarthritic hips, and found equivalence of these measurements between two age groups (below 40 and above 60). In particular, the study found an alpha angle above 55° in 23 out of 38 patients in the younger group, and 24 out of 39 in the older group.

A study by Harris et al. (2014) on 15 patients with 15 control individuals, found alpha angles were significantly greater in the patient group for all the radiographic views tested, and hence the authors suggested that, with sufficient viewpoints obtained through the use of 3D imaging, alpha angles may be successfully used to diagnose cam impingement. The ideal view for measuring alpha angles remains unknown, but this study found significant correlation between spherical deviation and alpha angles for all views measured, except for anteroposterior, which is not well suited for diagnosing cam deformities. The best views were the 45° Dunn view (patient supine with flexion) with 40° degree external rotation, cross-table lateral, and 60° radial CT views. These results support an earlier

study on radiographs (Meyer et al., 2006), which similarly concluded that the Dunn view in 45° or 90° flexion and cross-table projection in internal rotation are best for viewing femoral head asphericity, and found that anteroposterior and externally rotated cross-table views are more likely to miss asphericity.

Although 3D CT scans provide better images than X-rays alone and are more reproducible, they are expensive and result in higher radiation dosages to patients. Harris et al. (2014) however suggested 3D imaging is favourable because radiographic alpha angles alone may not accurately represent the size of a cam deformity. They report observing femurs becoming aspherical nearer the top of the head but without a large bump, resulting in a high alpha angle but relatively minor impingement. Conversely, some femurs were seen with a prominent bump further down the neck, resulting in a lower alpha angle but higher deviation from spherical and potentially more severe impingement. This evidence suggests that looking at the position, as well as size and shape, of cams would be beneficial for future studies that investigate the effects of geometry in relation to impingement damage.

2.5.2 Diagnosis and treatment of hip impingement

The subtlety of radiographic findings makes the diagnosis of hip disorders challenging. Moreover, FAI is a dynamic concept and morphology alone cannot fully explain the range of symptoms or predict whether OA will develop. Patients will first come to clinicians with pain; intermittent pain as opposed to the constant pain from OA can suggest a mechanical cause. Imaging is important to exclude other diagnoses such as avascular necrosis and stress fractures. Patients with FAI may have particular difficulty with chair rising and sitting, often prefer to slouch, and find confined spaces such as aeroplanes and cars uncomfortable. Impingement limits the physiologic hip range of motion (Tannast et al., 2007), so clinical examinations to assess the pain of patients in response to rotation and adduction during full flexion or extension are useful but still not sufficient for diagnosis. The gold standard for diagnosis remains patient reports of pain rather than imaging findings alone (Tannast et al., 2007), and this itself presents a difficulty, as different patients are likely to have different opinions on what constitutes a pain level worth seeking medical help for. Symptom management may be used in less severe cases, but prognosis of the hip joint is best if impingement is eliminated as early as possible (Tannast et al., 2007), so surgery may be recommended when symptoms first occur, with the goal of allowing a sufficient impingement-free range of motion (Bredella et al., 2013).

Open and arthroscopic surgeries to correct abnormal hips not yet presenting severe OA are

now fairly common and can allow patients to resume normal activities whilst minimising their predisposition to OA, but there is still insufficient long term controlled data to conclusively demonstrate that OA is prevented (Tannast et al., 2007; Banerjee and Mclean, 2011; Byrd and Jones, 2011; Bredella et al., 2013). Given the poor correlation between hip pain and radiographic findings it remains unclear exactly how surgical interventions result in pain relief. Similarly there is currently little long term data available on the natural history of FAI, in particular regarding the long term outcomes of patients who undergo surgery compared with those who do not (Botser and Safran, 2013).

2.5.3 Differences between females and males

There are some differences in FAI characteristics between males and females; cams are thought to be generally larger in males, and smaller and more diffuse in females; Yanke et al. (2015) reported that the volume and span of cams was greater in males, based on CT scans of 138 femurs. Similarly, Laborie et al. (2014) reported finding higher mean alpha angles for men than women in a study of 2038 healthy young adults. This does not necessarily imply that impingement is generally more severe in males since increased range of motion in females (resulting from muscle mass and ligament laxity differences) could mean that bony impingement occurs in the presence of smaller anatomical abnormalities in females (Halim et al., 2015). There may also be aetiological differences between sexes; for example differences in acetabular shape could affect the development of abnormalities and osteophyte formation on the femur. Movement differences could result in different stresses resulting in altered bone growth. This may relate to elevated subchondral bone stiffness, which has been reported in the context of cam FAI (Ng et al., 2016b), and could potentially lead to abnormalities through slipped growth plates, which can develop during adolescence (Siebenrock and Schwab, 2013; Murgier et al., 2014).

2.6 Finite element modelling background

The finite element method is a numerical method widely used for solving problems in engineering (Fagan, 1992; Wriggers, 2008; Khennane, 2013). To divide a complex problem into small elements, a system of points called nodes are used to make up a grid known as a mesh on a structure. Nodes can be assigned at different densities throughout the structure depending on the level of stress they are predicted to undergo, but often a uniform mesh is used. Each node is attached to every adjacent node by a mesh element. Governing equations for each individual element are assembled to describe the behaviour of the system

as a whole. The system of equations is generally expressed as

$$[k]\{U\} = [F]$$

where $[k]$ is the stiffness matrix, $\{U\}$ is the vector of unknown nodal displacements and $[F]$ is the vector of applied nodal forces. Before this equation can be inverted and solved for $\{U\}$, boundary conditions must be applied, constraining some of the nodes. Iterative techniques such as Newton's method are then used for solving the problem. Inverting large matrices is computationally inefficient and in practice each iteration will use techniques such as Gauss-Jordan elimination. After solving for the unknown nodal displacements, elemental stresses and strains can be derived. There are numerous software packages available, both commercial and open source, that assist in the development and processing of FE models. These have been developed over many years by large teams of engineers and programmers and are consequently capable of solving highly complex models. A particular example of a commercial finite element software is *Abaqus*, which was used for developing the models in this work.

2.7 Methods of modelling hip geometry

2.7.1 Parameterised and segmentation-based geometry

When developing 3D computer models of the hip, bone geometry can be incorporated using two main methods: either by using parameterised geometry or by utilising scans of patients, or cadaveric specimens, to develop segmentation-based models (Anderson et al., 2005; Chegini et al., 2009).

The geometry in parameterised models is created from relatively simple, mathematically defined shapes. Key dimensions of each component shape can be varied so that the final model geometry is a result of the component dimensions, and these dimension values are therefore the parameters referred to. Whilst it is not possible to capture every detail of the natural hip within a parameterisation system, using this approach in models allows for the isolation of the effects of particular geometric aspects without the influence of other confounding or complicating factors (Chegini et al., 2009; Anderson et al., 2010; Gu et al., 2011). Parameterised models are less computationally expensive than segmentation-based models in terms of development and analysis time, and their simplified geometry means they are easier to mesh. Depending on the desired level of geometric complexity however, extracting subject-specific parameters may require the use of 3D scans and image segmentation as used in the development of segmentation-based models. It has

previously been demonstrated that parameterised models can be used to investigate the relative influence of morphological parameters on joint contact mechanics (Chegini et al., 2009; Liechti et al., 2015). Such investigations are more efficient than using multiple segmentation-based models, but it is challenging to identify the set of parameters which, for a given application, should be precisely defined in order to produce meaningful, distinct model results. Some evidence suggests models with simplified geometries produce results in poor agreement with segmentation-based patient-specific models (Anderson et al., 2010; Gu et al., 2011) (Section 2.9).

Unlike parameterised models, the geometry for segmentation-based models is taken directly from scans obtained through medical imaging techniques such as CT or MRI. Tissue outlines can be segmented from these images to generate complex subject-specific geometry matching the hip morphology of particular individual patients. These models therefore better reflect real hips, with the extent dependent upon the imaging medium and resolution available (Anderson et al., 2005; Harris et al., 2012; Jorge et al., 2014). In segmentation-based, patient-specific FE models, high contact pressures have been observed in areas corresponding with clinical damage (Jorge et al., 2014). Whilst such models can produce valuable results, they are also time consuming to generate and analyse, and always require 3D imaging of the subject. Furthermore, although segmentation-based patient-specific models are favoured in the available literature on natural hip FE studies (Stops et al., 2012; Ng et al., 2016a), the geometries used in these studies are not perfect. For example, CT data can require geometry correction and manual intervention in order to create realistic articular surfaces and avoid convergence problems in models. Furthermore, comparisons may be complicated since not all segmentation-based models use the same techniques to obtain images, and a range of software may be used in the process of developing model geometry.

2.7.2 Mathematically describing hip shape

Many research groups have attempted to systematically describe hip shape mathematically. This can be for the purpose of developing parametric models or to better understand natural and impingement related morphologies. For example, Gu et al. (2008) concluded that acetabular cartilage surface can be better approximated as a rotational ellipsoidal shape than a spherical shape after using surface-fitting algorithms to analyse 25 specimens. Cereatti et al. (2010) focused on the proximal femur and found that the hip joint can be well modelled as spherical by comparing movements of four cadaveric joints with a spherical metal hinge in a given range of movement (flexion/extension from 20° to 70°;

abduction/adduction from 0° to 45° ; and internal/external rotation from 0° to 30°). These results suggest that estimating the proximal region of the femur as spherical could be an appropriate assumption in modelling applications.

Chegini et al. (2009) created parameterised models of the hip by modelling articulating joint surfaces as spherical surface portions with a common 25 mm radius. Femoral cartilage was 2 mm at thickest point, gradually reducing to 0 mm toward lateral edge of the femoral head, whilst acetabular cartilage had a constant thickness of 2 mm. FAI (cam and pincer) and dysplasia were simulated in the model by varying the value of CE angle and alpha angle parameters. The precise geometric alterations used to achieve this were not explicitly described, but intervals of 10° were used for the angles, resulting in a total of 25 models with alpha angles from 40° (normal) to 80° (cam); and CE angles from 0° (dysplastic) to 40° (pincer). This study successfully demonstrated that the complex morphology of the natural hip can be captured by various methods of parameterisation; discussion of the results can be found in Section 2.8.6 and in Section 2.9. These models were also later used to evaluate FAI based on penetration depth of the femur and acetabulum, finding strong correlation between the penetration depths and previously reported stress values (Arbabi et al., 2010).

Some researchers seeking to quantify morphologic variation in hip joints have made use of statistical shape modelling techniques such as principal component analysis to estimate average shapes from samples of a number of specimens. Within bioengineering generally, these techniques have potential uses for rapidly generating meshes for finite element models with complex geometries. However the modes describing variance in statistical models are not restricted to having clear physical meanings, such as femoral head radius, which can be adjusted to test the effects of specific morphological changes related to abnormalities. This makes them less suited to parametric study than models using parametric geometry introduced in Section 2.7.1.

Recently it appears that statistical models could provide information of clinical interest. Harris et al. (2013) used statistical shape modelling to investigate 3D variation between femurs with and without cams (30 patients and 41 controls), finding the greatest differences between the mean shapes of each group on the anterolateral head-neck junction, corresponding with the visible cams and areas of joint damage expected from previous studies. Noticeable variation in shape was also found among all the femurs in both groups, with large variation particularly in greater trochanter height and shape and femoral offset. The large geometric variation could explain the high variability of contact stresses between hips found in this group's earlier study (Harris et al., 2012) (Section 2.8.5). Another example is Bah et al. (2015), who achieved automatic generation of 1000 femurs using

statistical shape and intensity models developed from a training set of 109 patients. Measurements on these models highlighted morphological differences between sexes such as increased neck length and femoral head offset in males. This provides further evidence that the full 3D anatomy is important for consideration, in this case in terms of stratification of prosthesis choice. A larger training set including more unusual femoral shapes could aid this approach to further represent femoral shape variability and bone density. Furthermore, shape modelling of acetabula as well as femurs could help clarify whether these techniques could have greater clinical significance than radiographic measurements.

Another good example of the power of a parametric approach is Väänänen et al. (2015), who used two-dimensional radiographic dual-energy X-ray absorptiometry (DXA) hip bone images together with statistical appearance models to estimate 3D bone shape and density from 2D images. This work allowed patient specific FE models to be produced from DXA images to predict femoral strains and fracture load (Grassi et al., 2016), with models built from DXA images only slightly inferior to CT built models at predicting experimentally derived results. However, a method employing 2D rather than 3D images would be less viable for assessing contact mechanics in an impingement scenario, where the problem is inherently three-dimensional.

Although the alpha angle remains the most widely used parameter to quantify differences in femoral morphology, there is now a shift towards conducting clinical research investigating FAI in 3D. Masjedi et al. (2013b) sought to develop a mathematical description of the proximal femur for use in planning corrective surgery for cam hips, focusing on the head-neck junction. The femoral neck was found to be well described by a one sheeted hyperboloid, based on CT data of 46 normal proximal femurs, with an average root mean-squared fitting error of 1.0 ± 0.13 mm. The authors also provided a sinusoidal wave to show how the distance of the head centre to the head-neck articular margin varies around the circle of the head. This work demonstrates the possibilities for mathematically parameterising complex morphology like the femoral head-neck junction, but this was in a non-cam scenario. Bouma et al. (2015) focused on the interaction of femoral and acetabular sides of the hip and defined the “omega surface” on a set of example cases to define the region of impingement-free motion. This was based on alpha and CE angles, acetabular and femoral version, and neck-shaft angle. The surface was found to be smaller in FAI morphotypes than in a normal hip and was determined in different positions, with the impingement-free zone decreasing with increased flexion. However the surface was determined on a fairly small sample of just five different hip morphotypes, and the measurements require segmentation of patient geometry from CT scans, limiting their clinical application.

2.8 Computational models of the natural hip

2.8.1 Approaches and applications

There are many different motivations for developing FE models of the hip, and many different approaches to doing so. For example, models of the hip have been used to investigate cartilage contact stresses since elevated stresses may indicate increased risk of OA (Bachtar et al., 2006; Anderson et al., 2008). Modelling has also been used to assess changes in stresses following resection surgery to alleviate cam impingement (Alonso-Rasgado et al., 2012), including the assessment of resulting bone fracture risks (Rothenfluh et al., 2012). Other models are developed in order to further understanding of disease development; Roels et al. (2014) for example investigated mechanical factors that might cause cam FAI using a model of the proximal femur including an open growth plate.

Geometry for 3D hip models may be segmented from images or created with a parameterisation system (Section 2.7.1), but some earlier FE models of the natural hip used 2D geometry. Although they are inherently more simple than 3D models, 2D models have been used to obtain information on the relative importance of changes to certain parameters in hip models: Wei et al. (2005) found an increase in cartilage shear stresses occurred as a result of increasing subchondral bone stiffness, suggesting that increasing subchondral bone stiffness reduces stress dissipation capacity. Later work found that cartilage thinning increases shear stresses even more than stiffening of the subchondral bone, therefore suggesting that cartilage thinning can have a major influence on cartilage damage development (Wang et al., 2007). Though the simplified 2D geometry limits the strength of their conclusions, these exploratory studies demonstrate the potential to draw results of clinical interest from relatively basic models.

Increasingly high powered computers now allow for far more complex 3D models, some incorporating biphasic properties of cartilage, where solid and fluid phases of the tissue are considered (Li et al., 2013). In a review of FE and multi-body dynamics simulations of the natural hip, Stops et al. (2012) suggested that producing a highly realistic 3D hip model, incorporating micro-structural features remained an unrealistic goal with the technology at the time. This conclusion was given based on difficulties in segmenting cartilaginous tissues from bone using CT or MRI images, as well as the potential for very large meshes resulting from attempting to take into account anisotropy due to location specific collagen orientations. It remains challenging to produce highly realistic models due to these issues, but the identification of parameters that could be used to simplify

hip models without losing output relevance, along with further advances in computational power, may make highly realistic models a more realistic proposition in the future. It is important to remember however that no model can provide perfect predictions of responses to loading such as contact mechanics. All model inputs may be subject to error and uncertainty, and no matter how well model geometry captures native joint anatomy, material properties and loading conditions may not be entirely realistic. Even the most complex of constitutive equations used to describe material behaviour only provide approximations of the response of a material to external stimuli (Section 2.8.3).

Of particular interest in this work is the potential for FE models to help identify hip morphologies most at risk of OA development and provide elucidation as to why some morphologies are lower risk. Identifying a link between mechanical behaviour in the joint captured by models, and the onset of OA, could advance understanding of why disease progression is more severe in certain patients with abnormal joint morphology. In this regard, some of the most pertinent studies related to this work are summarised in Table 2.1.

Table 2.1: Key FE modelling studies of the hip, focused on the relationship between hip geometry and soft tissue contact.

Ref	Model	Loading and boundary conditions	Material properties	Key findings
Bachtar et al, 2006	CT image-based model of an elderly cadaveric hip.	Bergmann loading data applied to femoral head with upper part of pelvis fixed.	Cartilage: E=25 MPa, $\nu=0.3$; Bone: cortical E=17 GPa, $\nu=0.3$, trabecular E=70 MPa, $\nu=0.2$; Labrum: omitted	Peak stress in hip joint of 5.5 MPa, at heel strike of walking load.
Russell et al, 2006	CT image-based models: 6 dysplastic, 5 asymptomatic.	Loading and displacement applied to femoral head centre, data based on a single patient gait cycle scaled to each patient bodyweight.	Cartilage: E=12 MPa, $\nu=0.42$; Bone: cortical E=2 GPa, $\nu=0.3$, trabecular E=120 MPa, $\nu=0.3$; Labrum: omitted	Dysplastic hips (9.88 MPa) had higher peak contact pressures than healthy hips (1.75 MPa).
Chegini et al, 2009	Spherical ball-and-cup model with 25 variations to alpha angle and CE angle parameters.	Bergmann data for walking and standing to sitting using 836N bodyweight. Acetabulum fully fixed, femur motion by rotation about the femoral head centre with unconstrained translations.	Cartilage: E=12 MPa, $\nu=0.45$; Bone: rigid; Labrum: E=20 MPa, $\nu=0.4$	Stresses minimised by $20^\circ < CE < 30^\circ$ and $\alpha < 50^\circ$. Lowest peak contact pressure 2.35 MPa during walking, highest peak contact pressure 16.51 MPa during stand-to-sit with CE = 40° and $\alpha > 70^\circ$
Anderson et al, 2010	5 models with simplified hip geometries based on a previous image-based study.	Bergmann data for walking and stair climbing. Nodes along superior iliac crest and pubis joint of pelvic bone fully constrained, nodes at distal femur allowed to translate in plane perpendicular to direction of the equivalent joint reaction force.	Cartilage: hyperelastic G=13.6 MPa, K=1359 MPa, $\nu = 0.495$; Bone: E=17GPa, $\nu=0.29$; Labrum: omitted	Peak contact pressures of 10.8 - 12.7 MPa for subject-specific case, reduced when simplifications made and increased when rigid bones used.
Gu et al, 2011	CT image-based models: 2 hips, with 2 variations: cartilage replaced by an ellipsoid shape and by a spherical shape.	Bergmann data to simulate one-legged stance phase of a walking, external load of 5/6 bodyweight applied vertically to constrained pelvis nodes. Nodes in sacro-iliac joint and the pubic symphysis fixed in lateral directions, distal region of the femur fully constrained.	Cartilage: E=10.4 MPa, $\nu=0.2$; Bone: cortical E=17GPa, $\nu=0.3$, trabecular E=0.8GPa, $\nu=0.2$; Labrum: omitted	In the female hip, peak acetabular stresses were 14.79 MPa, rising to 17.01 MPa for the ellipsoid surface and 19.03 MPa for the spherical surface.
Ng et al, 2012	CT image-based models: 2 cams and 2 controls	Subject-specific intersegmental hip forces calculated using inverse dynamics on recorded squat motions. Forces applied through femoral head centre for two quasi-static loading scenarios: stance and maximum force endured during the impinged squat.	Cartilage: E = 12 MPa; $\nu = 0.45$ Bone: linear elastic orthotropic material; Labrum: omitted	Peak maximum shear stresses found at the anterosuperior region of the underlying bone during squatting. Peak shear stresses at the anterosuperior acetabulum were higher in patients (15.2 ± 1.8 MPa) than in controls (4.5 ± 0.1 MPa).
Harris et al, 2012	CT image-based subject-specific models of 10 healthy hips	Bergmann data for 7 activities. Rigid node sets created at the sacroiliac and pubis symphysis joints, motion applied superiorly to the distal femur to load the femur/acetabulum contact interface with femur allowed to translate in the medial-lateral and AP directions, but resisted by four springs placed at the distal femur.	Cartilage: hyperelastic G=13.6 MPa, K=1359 MPa, $\nu = 0.495$; Bone: E=17GPa, $\nu=0.29$; Labrum: omitted	More variability found among subjects for a given activity than among activities for a single subject; peak stress ranges of 7.52 ± 2.11 MPa for walking heel-strike and 8.66 ± 3.01 MPa for downstairs heel-strike.

Ref	Model	Loading and boundary conditions	Material properties	Key findings
Li et al, 2013	Model of a natural hip with biphasic cartilage layers	Nodes at sacroiliac and pubis symphysis joints constrained, static load based on average data for one leg stance from Bergmann applied to distal femur, ramped over 0.6s and then held constant for 3000s, whilst femur rotations constrained.	Cartilage: biphasic; Bone: E=17GPa, v=0.3; Labrum: omitted	Peak contact stresses in the range 2.7 - 4.1 MPa. Predictions for the period soon after loading were sensitive to hip size, clearance, thickness and cartilage aggregate modulus.
Jorge et al, 2014	MRI image-based models: 1 cam and 1 control	Bergmann walking force with 800N BW to femoral head centre, flexural and internal rotations applied, outer surfaces of tissues in contact with acetabulum fixed	Cartilage E=12 MPa, v=0.4; Bone: rigid; Labrum: E=20 MPa, v=0.4	Maximum contact pressures in non-cam hip were 6.6 MPa (flexural) and 6.04 MPa (internal rotation), corresponding results in cam hip were 9.65 MPa (flexural) and 11.68 MPa (internal rotation).
Liechti et al, 2015	Spherical ball-and-cup model with 6 variations to acetabular shape	Bergmann data over the full loading cycles during walking and standing to sitting. Acetabular bone-cartilage interface fully constrained while the femur free to move in all six degrees of freedom.	Cartilage: E=12 MPa, v=0.45; Bone: rigid; Labrum: E=20 MPa, v=0.4	During walking, highest contact pressure in the acetabulum shifted laterally in the dysplastic hip and medially in pincer hips, when compared with the normal hip model.
Hua et al, 2015	2 image-based models, and same 2 with acetabulum replaced by parametric geometry.	Bergmann data for 7 activities applied to femur. Region of nodes (with radius of approximately 4mm) was constrained to the load point at the centre of the head, making this region effectively rigid.	Cartilage: E=12 MPa, v=0.45; Bone: cortical E=17GPa, v=0.3, trabecular E=0.8GPa, v=0.2; Labrum: omitted	Differences in predicted results between the parameterised and segmentation-based models were found to be within 11% across 7 activities simulated, and parametric models were able to replicate features of the contact pressure/area fluctuations over the loading cycle that differed between the 2 subjects.
Ng et al, 2016	6 CT image-based models, 2 in each group: cam, asymptomatic cam, non-cam	Subject-specific muscle and hip contact forces estimated using a musculoskeletal modelling program (OpenSim). Quasistatic loading, using the highest resultant hip forces during terminal stance, forces applied at the femoral head.	Cartilage: hyperelastic Bone: isotropic, CT derived elasticity modulus Labrum: hyperelastic	Symptomatic cam group had high peak stresses (6.3 - 9.5 MPa) compared with asymptomatic (5.9 - 7.0 MPa) and control groups (3.8 - 4.0 MPa). Subjects with the lower femoral neck-shaft angles had higher peak stresses in their respective subgroups.
Hellwig et al, 2016	Spherical ball-and-cup models: 1 cam and 1 control	Bergmann data for normal walking and sitting down. Acetabular cartilaginous tissue on the bone-cartilage interface were fully constrained.	Cartilage: biphasic Bone: rigid; Labrum: biphasic	Cam impingement elevated stresses in the cartilaginous tissues with peak stress in posteromedial cartilage during stand-to-sit.
Liu et al, 2016	CT based model varied to adjustment alpha angle	Bergmann data for various movements, scaled to 60kg. Nodes at the sacroiliac and pubis symphysis joints fully constrained.	Cartilage: E=12 MPa, v=0.4; Bone: E=17GPa, v=0.29 Labrum: omitted	Greater alpha angles and larger hip flexion both resulted in increased peak contact pressures. Alpha angles > 80° substantially increase pressure under certain daily activities.

2.8.2 Loading and boundary conditions

Loading and boundary conditions govern the behaviour of FE models (Henak et al., 2013) and models of human hip joints attempt to replicate the fairly unconstrained environment of the human body using strict mathematical constraints. Examples of boundary conditions include initial joint orientation and areas where the model is restricted in movement. Some researchers choose to include more of the surrounding tissue in order to move the strict constraints away from the area of interest. Loading conditions can be created by specifying a direct force and by displacing components relative to one another, or by a combination of these methods. Establishing suitable loads to apply to computational models of joints can present a major challenge. For modelling *in vivo* situations, loading

conditions may be desired to emulate the hip forces found during real human gait cycles.

Work by Bergmann et al. (2001) has been valuable for many researchers developing computational models of the hip. This group measured hip contact forces *in vivo* with instrumented telemeterised hip implants and synchronous gait analyses in four patients during nine frequent daily activities. Hip contact forces were given using a femoral coordinate system and the individual results were used to calculate and provide loads occurring in a “typical” subject. The complete data were made available online. More recently, this group published work to establish realistic loads for testing hip implants (Bergmann et al., 2010).

It is important to highlight that the *in vivo* data supplied by Bergmann et al. (2001) was measured in elderly patients who had already undergone treatment for advanced hip OA, and whilst instrumented implants are the only direct measurements available of *in vivo* joint forces (Henak et al., 2013), they are not measurements of cartilage-on-cartilage contact. Furthermore, Bergmann et al. (2001) found large inter-patient variation in joint kinematics. These points mean that the average loading data they provide is unlikely to accurately represent the conditions present in imaged specimens used for developing patient-specific models, or present across all patient populations. In particular, younger patient groups and patients with abnormal hip morphologies could have significantly different force patterns from those measured by Bergmann et al. (2001). However, the data have been used to inform a substantial amount of subsequent research, and provided baseline loading conditions to apply to FE models of the hip joint (indeed, of the 14 key studies included in Table 2.1, 11 utilised data published by Bergmann and colleagues).

The boundary conditions used in models often depends on their geometrical complexity. For example, the acetabulum may be fixed in place whilst a load is applied to the femur; in whole pelvis models this may be achieved through restraining specific pelvis nodes (Gu et al., 2011), whereas in simpler models where most of the pelvis is omitted, the entire back of the acetabulum may be prevented from moving: Chegini et al. (2009) for example applied force vectors in the joint based on walking and standing-to-sitting loads from the data of Bergmann et al. (2001), with a bodyweight of 836 N, whilst the acetabulum was fully fixed and 3D motion data were simultaneously applied as rotation about the femoral head centre with unconstrained translations. Anderson et al. (2008) developed a segmentation-based hip model with more anatomical features included. In this case, nodes in specific anatomical positions were constrained. Nodes in the femur were constrained to move only in the direction of the load, while the nodes at the pubis, superior iliac and cement line were fully constrained to emulate the pelvis. This may not be entirely realistic as the acetabulum may not stay fully fixed with respect to the femur

in vivo when pelvic motions also occur.

2.8.3 Material properties

2.8.3.1 Cartilage

Cartilage is a complex composite material with chemical influence on its mechanical properties (for example glycosaminoglycans present in cartilage draw in water). It has been variously characterised as an elastic, viscoelastic or biphasic material but these are all approximations that enable the mechanical behaviour to be represented (Henak et al., 2013).

When articular cartilage is considered as a biphasic material, it has a solid matrix phase and an interstitial fluid phase (Fox et al., 2009; Mow et al., 1980). Water is the principal component of the fluid phase, contributing up to 80% of the wet weight of the tissue (Fox et al., 2009). The tensile modulus of cartilage is substantially higher than its aggregate modulus (Li et al., 2013) and this addition could be enough to capture a lot of the complexity of cartilage behaviour, and it could be important for capturing the mechanism of shear stress leading to cartilage delamination (Li et al., 2013; Henak et al., 2013; Henak et al., 2014a). Whilst many researchers disregard biphasic properties, others have tried to incorporate this complex behaviour into their studies. Li et al. (2013) developed an FE model of the natural hip incorporating biphasic properties in the cartilage in order to simulate joint response over a prolonged loading period of 3000 seconds. Sensitivity studies were undertaken to evaluate influence of various parameters on joint contact mechanic outputs. Cartilage thickness and clearance had the overall greatest effect on contact mechanics, whilst cartilage permeability initially had almost no effect, with it later becoming evident that fluid support ratio decreased with increasing permeability. This supports the notion that for simulating loads throughout the gait cycle, time-dependent properties may therefore be necessary, but there is evidence that suggests elasticity is an appropriate simplification for modelling the material behaviour of cartilage to predict short term contact stresses and instantaneous effects of loads (Ateshian et al., 2007; Stops et al., 2012; Henak et al., 2013; Li et al., 2013). Li et al's model had somewhat simplified geometry; in particular, the labrum was completely omitted, which may have exaggerated the effects of changing parameters since the labrum is less permeable than cartilage (Ferguson et al., 2000), and may support some of the applied load, or if moved, result in tensile forces in the cartilage.

When modelling cartilage as linearly elastic, it should be remembered that articular car-

tilage tends to stiffen with increased strain, so it is a simplification to describe it using a single Young's modulus. Rather, an experimentally derived modulus of the tissue will depend on the time at which the force measurement is taken during a stress-relaxation test (Fox et al., 2009). Where researchers use a linear elasticity assumption in representing cartilage, variation exists in the exact material property parameters chosen (values for Young's modulus (E) and Poisson's ratio (ν)).

Parameterised models may be developed and analysed with many variations in order to understand the effects altering each parameter, so researchers may generally want such models to remain as simple as possible to minimise analysis time. Chegini et al. (2009) modelled cartilage as an isotropic, linear elastic material, and set $E = 12$ MPa, and $\nu = 0.45$. Some segmentation-based FE models have used very similar material properties for cartilage, for example Jorge et al. (2014) used $E = 12$ MPa and $\nu = 0.4$; Russell et al. (2006) used $E = 12$ MPa and $\nu = 0.42$; and Gu et al. (2011) used $E = 10.4$ MPa and $\nu = 0.2$. It is not always clear from papers where chosen material properties originate from. It is reasonable to suspect that cartilage could have different properties in different locations, but Chegini et al. (2009) cite an FE model of the knee, whilst values used by Gu et al. (2011) can be traced back to a model of the shoulder, whose references can be followed further back to experimental work by Kempson et al. (1968). The similar values used by Jorge et al. (2014) however, are cited as being derived from experimental indentation studies on cartilage from knee joints (Shepherd and Seedhom, 1997).

The simplest form of linear elasticity is the isotropic case. Let G denote shear modulus, E denote Young's modulus and ν denote Poisson's ratio. Strain in the principal direction i is denoted ε_{ii} , and shear strain in the ij plane is denoted γ_{ij} . Similarly σ denotes principal and shear stresses. In the isotropic case of linear elasticity, the stress-strain relationship is given by

$$\begin{pmatrix} \varepsilon_{11} \\ \varepsilon_{22} \\ \varepsilon_{33} \\ \gamma_{12} \\ \gamma_{13} \\ \gamma_{23} \end{pmatrix} = \begin{bmatrix} 1/E & -\nu/E & -\nu/E & 0 & 0 & 0 \\ -\nu/E & 1/E & -\nu/E & 0 & 0 & 0 \\ -\nu/E & -\nu/E & 1/E & 0 & 0 & 0 \\ 0 & 0 & 0 & 1/G & 0 & 0 \\ 0 & 0 & 0 & 0 & 1/G & 0 \\ 0 & 0 & 0 & 0 & 0 & 1/G \end{bmatrix} \begin{pmatrix} \sigma_{11} \\ \sigma_{22} \\ \sigma_{33} \\ \sigma_{12} \\ \sigma_{13} \\ \sigma_{23} \end{pmatrix}$$

In anisotropy, the modulus is defined with directional dependence. Collagen fibrils in cartilage are believed to be orientated parallel to the articular surface in upper layers but perpendicular and anchored to the bone in lower layers (Fox et al., 2009; Chen et al., 2001). This may explain findings that the transverse elastic modulus is greater at the surface, reduced in middle layers and lowest at the base layer (boundary between subchon-

dral bone and cartilage), whilst the axial modulus is greatest at the base layer, reduced in middle layers and lowest at the articular surface (Chen et al., 2001; Osawa et al., 2014; Meng et al., 2017a). The structure of the labrum also has three layers of collagen fibril alignment, in the main layer the collagen fibrils are aligned circumferentially (Petersen et al., 2003; Grant et al., 2012). Collagen is important because it is the most abundant structural macromolecule in extracellular matrix (ECM), and it makes up about 60% of the dry weight of cartilage. Type II collagen represents 90% to 95% of the collagen in the ECM and forms fibrils and fibres intertwined with proteoglycan aggregates. Other collagen types are also present and help stabilise the type II collagen fibril network. The effects of considering depth dependent moduli were investigated by Osawa et al. (2014), who identified different stress distributions and elevated strains in surface layers in models for which inhomogeneous material properties were used.

2.8.3.2 Bone

As with cartilage, there is a wide variation in the material properties used to represent bone in FE models of the hip. The most fundamental difference between bone representation in models is whether bone sections are modelled as rigid (since bone is vastly stiffer than cartilage) (Chegini et al., 2009; Jorge et al., 2014), or bone is modelled as a deformable material like soft tissues (Russell et al., 2006; Anderson et al., 2010), and if the latter, whether areas of different composition are assigned distinct properties.

Parameterised models by Chegini et al. (2009) represented bone as rigid; they report that a pilot analysis using a simplified axisymmetric model of the acetabular socket and surrounding bone led them to conclude that the use of rigid rather than elastic bone material did not alter predicted cartilage stresses. Jorge et al. (2014) reached the same conclusion from previous 2D analyses, and hence also modelled bone as rigid. Others have used separate properties for deformable trabecular and cortical bone (Russell et al., 2006; Bachtar et al., 2006; Gu et al., 2011), but often different numerical values for their properties are used (Table 2.1). Again it is not always clear where these properties are derived from, although a value of $E = 17$ GPa for cortical bone can be traced back to strain gauge experimental work by Dalstra et al. (1995), used to validate FE models of pelvic bone.

Anderson et al. (2010) and Harris et al. (2012) modelled cortical bone as a homogeneous, isotropic material with elastic modulus $E = 17$ GPa and Poisson's ratio $\nu = 0.29$. Trabecular bone was omitted from these models because the group had previously found it had little effect on predicted cartilage contact pressures and substantially increased the solution time when compared with including only cortical bone shells to support the car-

tilage (Anderson et al., 2008). This group also investigated the effects of using rigid bone rather than deformable bone in a subject-specific case and found that representing the pelvis and proximal femur as rigid resulted in large changes to their model results, increasing peak and average pressures and decreasing the contact area, with the effect being most clear in the loading scenario simulating descending stairs (Anderson et al., 2008). This finding is in contrast with the findings of Chegini et al. (2009) and Jorge et al. (2014). However, both these studies concluded rigid bone is a suitable assumption based on the results of simplified analyses, whereas Anderson et al. (2008) found bone rigidity to result in differences in a more complex, subject-specific model based on CT data.

2.8.3.3 Labrum

The inclusion or exclusion of the acetabular labrum varies among FE models of the hip in the literature. A 2D plane strain, poroelastic model based on average measurements from MRI data sets of non-symptomatic hips suggested the labrum may be important for hip joint stability (Ferguson et al., 2000). Removal of the labrum from this model meant the centre of contact moved closer to the acetabular rim, as well as the loss of its structural resistance to lateral movement of the femoral head. Higher contact pressures were found without the labrum included (4.4 MPa) than with it present (3.7 MPa). However the 2D model in this study obviously did not accurately represent the complex geometry of the hip, and a more recent segmentation-based model found the labrum supported less than 3% of joint load in healthy subjects (Henak et al., 2011). For this reason Harris et al. (2012) omitted the labrum from their models.

Regardless of its role in healthy subjects, the labrum is certainly relevant when considering impingement (Beck et al., 2005; Tannast et al., 2007; Banerjee and Mclean, 2011), and therefore should be included in models used to investigate FAI. Chegini et al. (2009) therefore included the labrum in their parameterised models; it was modelled as a part extruding from the acetabular rim with a triangular cross-section and a height of 7 mm. The material properties of labral tissue were $E = 20$ MPa and $\nu = 0.4$, based on experimental findings from bovine labral tissue. Jorge et al. (2014) included the labrum in their segmentation-based cam hip model, modelling it as a linearly elastic, isotropic material tied to the acetabular cartilage, and using the same material property values as used by Chegini et al. (2009). The labrum was also included in parametric models developed by Liechti et al. (2015), who focussed on investigating pincer impingement, and found the locations of highest stress in the acetabulum to be affected by parametric variations made to labral geometry. In particular, when simulating a walking load, the highest contact pressure in the acetabulum shifted laterally in a simulated dysplastic hip and medially in

simulated pincer hips, when compared with their baseline normal hip model.

2.8.4 Contact interactions

As well as variation in material properties, the methods used for modelling the contact between surfaces in models is subject to variation between researchers. Abaqus 6.14 Documentation (2014) advises that the discontinuity between the contact states of sticking and slipping can result in convergence problems during simulations, so the default coefficient of friction used in Abaqus is 0, and friction should only be included in simulations when it has a significant influence on the model response. Friction in articular cartilage is low; an experimental study found the coefficient of friction for normal cartilage in femoral heads to be in the region of 0.119 (Lee et al., 2013). It is therefore unsurprising that cartilage-on-cartilage contact is modelled as frictionless by most researchers (Bachtar et al., 2006; Chegini et al., 2009; Anderson et al., 2010; Harris et al., 2012; Li et al., 2013; Jorge et al., 2014; Liechti et al., 2015). However, some researchers do assign a non-zero coefficient of friction for cartilage interactions: Gu et al. (2011) used a surface based finite sliding contact (in which the solver continually tracks which part of the master surface is in contact with each slave node) between femoral cartilage and acetabular cartilage with a friction coefficient of $\mu = 0.2$, and Ng et al. (2016b) used a friction coefficient of $\mu = 0.01$.

By default, contact pairs in Abaqus use a master-slave contact algorithm; nodes on the slave surface cannot penetrate the master surface, but the master surface can penetrate the slave surface between slave nodes. The slave surface should be the more finely meshed surface or the surface with the softer underlying material. In hip models, the femoral side is usually the master surface (Chegini et al., 2009; Gu et al., 2011; Jorge et al., 2014). In surface-to-surface contact discretisation, the shape of both the master and slave surfaces are considered, providing improved accuracy over the node-to-surface discretisation.

2.8.5 Variation in hip morphology

Different assumptions with regards to material properties and boundary and loading conditions make it challenging to confidently compare the results of different FE models of the hip. This is particularly evident with patient-specific results; reported estimates of typical contact area during the gait cycle can vary greatly, from around 300 mm² (average across cycle) (Anderson et al., 2008), to over 2000 mm² (at midstance) (Russell et al., 2006). It is important to recognise that even if material properties and loading options were standardised, model results may still vary substantially due to geometrical differ-

ences. These include the level of sphericity of the femoral head and acetabular cavity, the amount of clearance between them, and the precise shape of the subchondral bone surface, which may display radiographic signs associated with impingement even in asymptomatic hips (Ergen et al., 2014) (Section 2.5).

High cartilage contact stresses may indicate potential joint degeneration, but it can be difficult to ascertain normal magnitudes and distributions for these stresses in healthy hips using experimental techniques. Harris et al. (2012) constructed CT segmentation-based models of 10 healthy hips in order to determine acetabular contact stresses and areas occurring across loading scenarios representing seven activities. The distribution of contact stresses identified were highly non-uniform, with more variability found among subjects for a given activity than among activities for a single subject. These results suggest that contact patterns depend on hip geometry as much as on movements occurring during activity, and differences in bone and cartilage geometry result in significant variation in contact patterns and location of peak stresses, even among healthy individuals. Although the location of contact varied, the magnitude and area of contact stress were found to be consistent across activities measured. Peak stress ranged from 7.5 ± 2.1 MPa for heel-strike during walking to 8.7 ± 3.0 MPa for heel-strike during descending stairs, and the average contact area across all activities was 34% of the acetabular cartilage surface area. It is likely however that the loading scenarios applied to the models in this study did not represent the actual gait patterns of the individuals, so the contact estimates may not be entirely realistic.

It is interesting to notice that some segmentation-based modelling studies have reported peak pressures in normal hips with walking loads as low as 1.8 MPa (Russell et al., 2006), and peak stresses as high as 14.8 MPa (Gu et al., 2011), whilst others studies have produced results closer to the results seen by Harris et al. (2012). Bachtar et al. (2006) reported a maximum contact pressure of 5.5 MPa for the heel strike of typical gait cycle, and Anderson et al. (2008) reported a peak pressure of 10.8 MPa for a walking load, a result supported by experimental pressure films used for validation reaching their upper limit of 10 MPa. Some of the differences in stress levels found in the aforementioned studies could be due to differences in modelling choices as well as geometry (Table 2.1). Bachtar et al. (2006), Anderson et al. (2008), and Harris et al. (2012) used similar material properties and loading conditions. The much lower stress values reported by Russell et al. (2006) were from models that used loading conditions that were scaled to the body-weight of each patient, which may have been lower than bodyweights assumed by others. Additionally, higher peak stresses found by Gu et al. (2011) were in models that included external loads to represent bodyweight applied to the pelvis. With such high variation among healthy populations, it is clear that there are uncertainties inherent in comparing

results of modelling studies, including when seeking to identify the reliability of parameterised models in comparison to segmentation-based models, and when investigating differences between healthy and impinging hips.

The high level of variation between healthy hips also means it is difficult to establish average population values for geometric parameters that can describe hip shape. Such values may be useful to create parameterised models to study variation in general trends across different populations. For example, Gu et al. (2011) used a thickness of 1.2 mm for femoral and acetabular cartilages, and Russell et al. (2006) found an average thickness of 1.8 mm to be consistent with their CT observations, whilst in parameterised models Chegini et al. (2009) used a 25 mm radius for the femoral head with the femoral cartilage 2 mm at thickest point, gradually reducing to 0 mm toward lateral edge of the femoral head, and acetabular cartilage with a constant thickness of 2 mm. The thicknesses used by Anderson et al. (2008) in acetabular and femoral cartilage layers were 1.6 ± 0.4 and 1.5 ± 0.5 mm, respectively. Whilst the values used in these studies are not substantially different, it is clear there is no consistent average value for cartilage thickness that should be used in general parameterised models.

2.8.6 Validation and verification

It is possible for computational models to be developed with the unintentional inclusion of unnecessary or erroneous assumptions, so a process of verification (equations solved correctly), validation (correct equations used to model reality) and sensitivity (to changes in parameters) analysis is often required to demonstrate that developed models produce meaningful results (Anderson et al., 2007; Jones and Wilcox, 2008; Henninger et al., 2010). Validation of a model for a particular application does not mean it is also valid for obtaining results in a different scenario.

Verifying a model involves assessing its numerical accuracy; the degree to which its output provides accurate approximations of the solutions to the equations used by the model. Code used in commercial software is already well documented, but having considered the differences in modelling approaches and the variation in natural hip geometry, the use of different software should also be briefly mentioned. Whilst many researchers use Abaqus for FE analysis, FEBio, developed at the University of Utah and specifically designed for biomechanical applications, is also commonly used. Ideally the choice of software used by researchers should not significantly alter the results obtained, and a recent study found excellent agreement between Abaqus and FEBio, at least for biphasic contact problems (Meng et al., 2013).

Demonstrating mesh convergence is another important verification step. In order to check convergence, outputs from FE simulations should be compared with solutions obtained with a finer mesh for increased accuracy. If the more accurate solution is dramatically different from the original solution, then the solution has not converged, whilst if the solutions are approximately equal then convergence has been reached (Anderson et al., 2007). The complexity of the meshing approach may depend on the complexity of the model itself. Relatively simple parameterised models by Chegini et al. (2009) were meshed with 20 node quadratic brick elements; no further detail than this is reported. Anderson et al. (2005) reported more details on the meshing of their more complex segmentation-based model. Cortical bone was assigned quadratic 3-node shell elements with position-dependent shell thicknesses. Trabecular bone was then represented in the interiors of the cortical shell meshes with tetrahedral elements. Hexahedral element meshes were used for cartilage, and convergence tests were conducted on these by increasing the number of elements through the thickness of the cartilage, with the mesh considered converged when the change in average pressure between the meshes was less than 5%.

To validate models, comparisons with results from experimental work should be made. Such experimental tests themselves may not emulate exactly the *in vivo* situation, but a model's output matching *in vitro* experimental results can indicate its potential relevance to *in vivo* situations. It should be noted however that several different combinations of model parameters could lead to the same results, and consequently it may be possible to incorrectly "validate" a model by chance. This is also pertinent to sensitivity testing; it is possible for changes in parameters that initially appear unimportant to cause crucial differences in model output following the addition of further parameters.

Anderson et al.'s work prominently features validation of models. They first developed an FE model of the whole pelvis using subject-specific CT data from a cadaveric specimen (Anderson et al., 2005). This model was validated through comparison with experimental results using the same pelvis scanned to develop the model. A prosthetic femoral implant was used to apply loads to this pelvis in a manner replicable in the computational model, and cortical bone strains were measured using strain gauges. Strong correlation was found between experimental and computational results ($r^2 = 0.824$), and sensitivity studies revealed the model was most sensitive to changes in cortical bone elastic modulus and thickness. Though the model was not especially sensitive to changes in either cartilage thickness or modulus, it is interesting to notice that cartilage thickness had a greater influence on articular stresses than cartilage modulus, demonstrating again the importance of model geometry. The group later developed another subject-specific model of the hip using CT data of a cadaveric specimen, this time for predicting cartilage contact stresses (Anderson et al., 2008). Model results were compared with results from experimental

work which used pressure sensitive films to determine contact pressures and areas when applying loads to the cadaveric hip joint. The loads applied were based on data from Bergmann et al. (2001) to simulate walking as well as ascending and descending stairs. Experimental peak pressures, average pressures, and contact areas were 10.0 MPa (the maximum limit of film detection), 4.4 – 5.0 MPa and 321.9 – 425.1 mm², respectively. For the FE model, the corresponding values were 10.8 – 12.7 MPa, 5.1 – 6.2 MPa and 304.2 – 366.1 mm². The best agreement between the computational and experimental results was obtained in the stair climbing loading scenario. The model's sensitivity to various parameters was reported, with alterations to cartilage shear modulus, bulk modulus, and thickness resulting in peak pressure changes of $\pm 25\%$, but average pressure and contact area changes of just $\pm 10\%$.

Studies generating parameterised models used to isolate the effects of particular geometric parameters may be less concerned with explicit validation. Such models may assess trends in the relative differences in results when parameters are changed, but because of their inherent simplicity the actual numerical values they produce may be of less importance. Nevertheless studies utilising parametric modelling often seek to relate their findings to other research, and Chegini et al. (2009) reported that areas of high stress in their models corresponded with clinically observed regions of damage in the acetabular cartilage and labrum. In dysplastic joints (CE angle $< 20^\circ$), loads based on data from Bergmann et al. (2001) to simulate walking (high load activity) produced high acetabular rim stresses, whereas for impinging joints (pincer: CE angle $> 30^\circ$; cam: alpha angle $> 50^\circ$), standing-to-sitting loads (high range of motion activity) induced excessive distortion and shearing of the tissue-bone interface. Parameters minimising stresses were $20^\circ \leq CE \leq 30^\circ$ and $\alpha \leq 50^\circ$, resulting in 2.6 – 3.7 MPa peak contact pressures across this range for the standing-to-sitting and walking activities, compared to peaks of 9.9 MPa for dysplastic hips (walking load) and 16.5 MPa for pincer cam hips (standing-to-sitting load), and the lowest peak pressure of 1.8 MPa occurring in a pincer cam hip with the walking load. Interestingly, estimated contact pressures in the cam impingement models only began to seriously increase once alpha angles of 70° and above were used. This evidence supports the idea of increasing the alpha angle threshold value suggested by Sutter et al. (2012), whose study of MR images of 53 patients and 53 age and sex matched controls concluded that increasing the alpha angle threshold value from 55° to 60° would reduce false-positive results and maintain a reasonable sensitivity.

2.9 Parametric and segmentation-based models

It has been seen that the two main approaches to constructing 3D geometry for hip models are by segmentation from medical images and by developing a parameterisation system (Section 2.7.1). This section provides a discussion of differences between studies employing these two methods.

2.9.1 Parameterised and segmentation-based models of FAI

Two key studies that are well suited to the discussion of comparing parameterised and segmentation-based modelling methods are Chegini et al. (2009) and Jorge et al. (2014). The first used relatively simple parameterised geometry, whilst the latter constructed model geometry from geometrical data obtained from MRI scans. It is important when comparing models to consider differences in modelling approaches that could affect the likelihood of identifying agreement between model results. These two studies used similar material properties for cartilage and labrum tissues, and both modelled bone as rigid (Section 2.8.3). Both studies include only the femoral head (with enough femoral neck to define alpha angle) and the acetabular socket, omitting more of the femur and pelvis. Both used frictionless surface-to-surface interaction between cartilage articulating surfaces and loading conditions were informed by data from Bergmann et al. (2001); Chegini et al. used a 836 N bodyweight, and Jorge et al. used a walking load with 800 N bodyweight.

Chegini et al. (2009) evaluated contact pressures resulting from FE models with relatively simple geometry to represent hips with FAI and dysplasia (the geometry is described in Section 2.7.2). More detail on the study results was given in Section 2.8.6, but the variations in results from parameterised models in this study demonstrated that stresses occurring in the soft tissues of the hip joint depend on joint geometry as well as motion and load. The study successfully evaluated the influence of specific hip morphological variations despite lacking patient-specific geometry, and provides the best evidence for the value of developing parametric models by showing such models can capture differences between healthy, impinging, and dysplastic hips. The results would be more valuable if the models were able to use joint-dependent loading data to increase the accuracy of estimated stresses, but such data is not available from Bergmann et al.'s dataset.

Jorge et al. (2014) developed FE simulations of the hip joint of a specific patient with cam FAI undergoing physiological movements resulting in flexion and internal rotation of the femur. Analysis of a non-cam hip was conducted for comparison, but this comparison

would have been improved by finding a control subject better age and sex matched to the cam patient. Nevertheless contact areas found in the cam subject were in agreement with clinical observations of anteriorly located OA in cam hips, and the study concluded that movement is a determinant factor for occurrence of high contact pressures in cam hips. The maximum contact pressure found prior to movement was 5.2 MPa. During movement, the maximum contact pressures in the non-cam hip were 6.6 MPa (flexural) and 6.0 MPa (internal rotation), with corresponding results in the cam hip being 9.7 MPa (flexural) and 11.7 MPa (internal rotation).

The contact pressures seen by Jorge et al. (2014) in their FE model of a cam hip were similar to contact pressures found by Chegini et al. (2009) in cam hip models with idealised geometries. In particular Chegini et al. reported a value of 12.9 MPa for the peak contact pressure in the acetabular cartilage for the standing-to-sitting movement with a CE angle of 30° and an alpha angle of 80° , whilst Jorge et al. found maximum contact pressures in the cartilage at the end of simulated movements to be in the region of 12 – 13 MPa. Given their similar modelling strategies, it is perhaps not surprising that the two studies found similar contact results for cam hips. The results of both studies lie close to the experimentally derived range of normal hips of 1.7 – 10 MPa reported by Anderson et al. (2008). When considering the maximum contact pressure of 3.7 MPa for normal hips found by Chegini et al.'s models simulating standing-to-sitting movement, this is less comparable to the 6.6 MPa maximum contact pressure in Jorge et al.'s subject-specific non-cam hip model. This could be evidence for the simpler model underestimating contact pressures, a notion that is discussed further in Section 2.9.2.

Chegini et al.'s study investigated dysplastic hips as well as hips with FAI. A study by Russell et al. (2006) developed CT-based patient-specific models of six dysplastic and five asymptomatic hips and found dysplastic hips (9.88 MPa) had higher peak contact pressures than healthy hips (1.75 MPa). Although these values convincingly demonstrate the difference found between dysplastic and healthy hips, it should be noted that these figures were taken from the acetabulum for the control and from the femur for one of the dysplastic hips. In contrast to Chegini et al.'s bone rigidity simplification, Russell et al. modelled subchondral bone of the acetabular dome as 1 mm thick and deformable, and supported it by deformable cancellous bone with a fixed boundary at the medial pelvic wall. Like Chegini et al.'s study, the loading conditions in Russell et al.'s study were applied through a reference node at the femoral head centre, but Russell et al. did not use Bergmann et al.'s data, instead using gait cycle kinematics and kinetics from the weight-bearing stance phase of an individual patient. Unlike Chegini et al., Russell et al. made no mention of the acetabular labrum in their paper. Despite the differences between the studies however, the average peak pressure in the acetabulum from the six dysplastic hips

in Russell et al.'s study was 6.6 MPa, and this compares well with peak contact pressures of 6.1 MPa ($CE = 0^\circ$) and 9.9 MPa ($CE = 10^\circ$) found in Chegini et al.'s dysplastic models during the walking load.

Chegini et al.'s parameterised model results compare favourably to those from Jorge et al. and Russell et al.'s patient-specific models. Other studies also suggest aspects of hip joint geometry can also be reasonably well described using parameterised (or idealised) shapes; the acetabulum for example can be approximated by spherical (Gu et al., 2011) or elliptical surfaces (Cerveri et al., 2014) (Section 2.7.2). Cilingir et al. (2011) also recommended that axisymmetric FE models can be used for comparative parametric studies on contact mechanics studies because of their simple geometry and short computation time. However, further work is needed to elucidate the effects of using idealised geometry, and particularly to identify the information varying idealised parameters can sensibly be used to obtain.

2.9.2 Consequences of simplified geometry

There is evidence suggesting that models with simplified geometry could be inferior to segmentation-based models for predicting hip contact mechanics; differences in predicted results between segmentation-based models and models with idealised joint geometry may arise due to small irregularities in subject-specific geometry being lost (Henak et al., 2013).

Gu et al. (2011) developed two 3D FE models of healthy hips, based on CT images from volunteers (one male and one female). For each case, additional models were generated in which the natural cartilage shape (femoral and acetabular) was replaced by a rotational ellipsoid shape and by a spherical shape. The models simplified with spherical shapes exhibited increased contact stresses and uneven distribution of contact stress patterns. Similarly, the ellipsoidal models also led to increases in contact stresses, but their results were more consistent with the natural hip models, which was not unexpected because the ellipsoidal surface was a better fit to the natural shape than the spherical surface. As a specific example, peak acetabular stress in the female hip was 14.8 MPa, rising to 17.0 MPa for the ellipsoid replaced surface and 19.0 MPa for the spherical surface. These results demonstrate the potential for models using simplified geometries to overestimate peak contact stresses in the hip, which is in contrast to the findings of Anderson et al. (2010), who found simplified bone surfaces to underestimate peak contact pressures. Gu et al.'s conclusions would be more convincing with a larger dataset since just two hips does not capture the wide range of morphological variation across individuals. In particular,

no mention of the labrum was made in this study, and the effects of simplifying geometry in malformed hips was not addressed.

In contrast to Gu et al.'s conclusions, the earlier comparison of results from Chegini et al. (2009) to segmentation-based models did not highlight any obvious negative effects of idealised surface in impingement models (Section 2.9.1). Peak stresses reported by Chegini et al. (2009) were lower than those found by both Gu et al.'s simplified and natural models, but it is difficult to know whether this is due to the more simplified geometry in Chegini et al.'s model or due to other differences between the studies, such as Gu et al.'s use of deformable bone, inclusion of more of the pelvis and femur, and use of a non-zero coefficient of friction between cartilage surfaces. Furthermore, Gu et al. stated their contact stress predictions corresponded well to results from a study by Bachtar et al. (2006). However, Bachtar et al.'s models, developed using CT scans of an elderly cadaver, found a maximum contact stress of around 5.5 MPa during a load based on the heel strike of a typical gait cycle from data from Bergmann et al. (2001). This result is lower than Gu et al.'s stress findings even though Bachtar et al. used similar material properties.

Another key study to consider when discussing the consequences of geometric simplification is Anderson et al. (2010). In this study, a previously developed and validated subject-specific model (Anderson et al., 2008) (Section 2.8.6) was used to provide a baseline for developing five further FE models with varying degrees of simplification in order to analyse the affect of simplified femoral and acetabular geometries on contact pressures. These models and their findings are outlined in Table 2.2.

Table 2.2: Simplified FE models developed by Anderson et al. (2010) in their study on geometric simplification in hip models.

Model geometry	Contact compared to subject-specific model
1. Subject-specific bone with constant cartilage thickness	Slightly higher pressure and more localised Similar contact pattern
2. Subject-specific model with rigid bone	Higher pressure and more localised Similar contact pattern
3. Subject-specific bone model with varying cartilage thickness based on best-fit radius of joint space midline	Lower pressure and larger contact area Contact pattern more spread out
4. Best fit sphere bone model with constant cartilage thickness (1.28mm)	Much lower pressure and larger area Much more spread out contact pattern
5. Best fit conchoid bone model with constant cartilage thickness (1.28mm)	Much lower pressure and larger area Much more spread out pattern

Anderson et al. found that the conchoidal model had slightly lower fitting error (root mean squared distance that native nodes needed to move to conform to the best fit idealised surface) for the femoral head than the spherical model had, but the errors were essentially the same for the acetabulum. Mean and peak contact peak pressures increased in Mod-

els 1 and 2 but decreased for Models 3, 4 and 5 (Table 2.2). Correspondingly, contact area predictions decreased in Models 1 and 2 but increased in Models 3, 4 and 5. The spherical and conchoidal models with smoothed articulating cartilage (4 and 5) underestimated peak and average contact pressures by around 50%, and also overestimated contact area when compared with patient-specific geometries. Model 3, featuring subject-specific bone with smoothed cartilage, also underestimated pressures and predicted evenly distributed contact patterns. Model 1, with constant cartilage thickness and subject-specific bone, provided better predictions of contact than models with spherical or ellipsoidal joints, but still did not provide contact that was consistent with that found using subject-specific cartilage thickness. Model 2, with rigid bone, produced higher pressures than the models with deformable bone (Section 2.8.3.2). The results from this study led the authors to conclude that simplifications to model geometry can dramatically affect the predicted magnitude and distribution of cartilage contact pressures in the hip. Certainly in this case, spheres and conchoids appeared to lack sufficient geometrical detail to accurately predict the magnitude and spatial distribution of cartilage contact pressures. However, this study was based on a single cadaveric hip, so given the high level of morphological variation across individuals, it does not necessarily provide sufficient information to make conclusions on the effects of using simplified geometry in hip models in general. Another limitation of the study is that the labrum was omitted from the model because it was difficult to distinguish in CT data, and was removed as part of the experimental protocol. The labrum however is an important consideration in FAI, so again the effects of simplifying geometry in malformed hips in particular was not addressed.

Evidence found by modifying validated segmentation-based patient-specific models has shown that parameterised models using idealised bone geometry can underestimate contact pressures and overestimate contact areas (Anderson et al., 2010). In other cases simplified cartilage geometry has been shown to lead to overestimated contact stresses (Gu et al., 2011). There are several possible explanations for the different conclusions of these studies. Firstly, it could be due to the different hips used in the studies. Gu et al. used only two healthy volunteers, and Anderson et al. used a single cadaveric joint, but it is known that differences in joint geometry between subjects can lead to high variation in contact patterns (Harris et al., 2012) (Section 2.8.5). The difference could also have arisen from differences in modelling approaches. Anderson et al. did not include trabecular bone whereas Gu et al. did, but Anderson et al. found trabecular bone made little difference to results in their previous study, so this is unlikely to be important. Gu et al. used linearly elastic cartilage, whereas Anderson et al. used a hyperelastic model, but again this is probably not relevant since similar material property values were used and differences would occur only at high strains. Unlike Anderson et al., Gu et al. used

friction between the two layers of cartilage, but the coefficient was small (0.2). Anderson et al. stated the cortical bone thickness used, but Gu et al.'s paper does not mention it, and it would be useful to know how much of the pelvis was modelled as cortical (opposed to trabecular) bone since it has previously been reported that changes to cortical bone thickness can affect cortical bone strains and thus potentially cartilage stresses (Anderson et al., 2005).

Though it is challenging to reach a convincing conclusion when comparing Anderson et al. and Gu et al.'s findings, it is important to consider the confounding factors affecting the outcome of comparing subject-specific and simplified bone geometry. Anderson et al. stated that when bone geometry is approximated as spherical or conchoidal and the articular surface is smoothed, contact pressures are "grossly" underestimated and contact areas are overestimated. However, the simplified bone geometry provided a good surface fit to the native bone. Furthermore, smoothing the articular surface whilst maintaining the subject-specific bone surface also resulted in lower contact pressures. Therefore the increased cartilage conformity, and loss of varying clearance between the articular surfaces, could explain why the models with simplified bone geometry produce lower contact pressures, rather than the difference arising primarily due to the different bone geometry itself. Similarly, it is possible that Gu et al.'s models with simplified cartilage geometry produced higher contact stresses than the subject-specific cases because the simplified cartilage geometries had decreased conformity in comparison to the natural articular surfaces.

Considering again the models of Chegini et al. (2009), it is worth highlighting that Anderson et al. (2010) reported that modelling bone as rigid resulted in higher pressures, which may suggest an explanation for the agreement between results of Chegini's et al.'s parameterised FAI and dysplasia models and the patient-specific models in (Russell et al., 2006; Jorge et al., 2014). A combination of rigidity (increasing pressure) and simplified geometry (reducing pressure) might cancel one another out. This may be a tenuous suggestion since Chegini et al. found that using rigid instead of deformable bone had little effect on their model results, but this was only for simplified models. Furthermore, peak contact pressure found by Anderson et al. (2010) (using walking loads) of 10.8 MPa is much higher than Chegini et al.'s value of around 3 MPa for normal hips, whereas Anderson et al.'s values from spherical models are closer to Chegini et al.'s. It is tempting to conclude then that there is evidence for Chegini et al.'s simpler results being accurate for FAI and dysplastic hips, but not for normal hips, but this conclusion also falters because Anderson et al.'s patient-specific normal hip results are similar to the higher values that Chegini et al. and Jorge et al. found in FAI hips. Russell et al. (2006) on the other hand (without using Bergmann et al.'s loading data), found much lower results for normal hips (peak contact pressure just 1.8 MPa), whilst Harris et al.'s study suggests a peak stress

expectation of about 7.5 MPa in normal hips for common activities.

As well as reports of differences, similar trends between parameterised and segmented hip models have also been reported (Hua et al., 2015). In this study, segmentation-based models of two hips were developed, and two further models were produced with parametric geometry representing acetabular bone and cartilage used in place of the segmented geometry. This parametric geometry was produced using cuts to an initial cuboid shape representing the acetabular bone. Contact pressures and areas on the articular surface predicted from the parameterised and from the segmentation-based models were found to be within 11% of each other across the seven simulated activities, giving promise to the notion that the parameterised approach could produce results representative of real segmented hips. However, this study analysed just two hips, and only the acetabular geometry was parameterised, and this did not include the labrum. Further work is necessary to better understand the effects of replacing segmented geometry with parameterised equivalents to provide additional confidence in this approach.

Overall, whilst there are aspects of hip joint geometry that can be well described using parameterised shapes (Gu et al., 2011; Cerveri et al., 2014; Hua et al., 2015), and some authors have argued in favour of using spherical models (Yoshida et al., 2006), others (Henak et al., 2013) argue that peak contact stresses in range 2 – 5 MPa found in models like Yoshida et al.'s study are low compared to the *in vitro* range of 8 – 10 MPa found by Anderson et al. (2008) and earlier experimental studies from the 1980s and 90s. In contrast, Gu et al. (2011) found simplified geometries to increase hip contact stresses. This lack of clarity, and other confounding factors related to different approaches to modelling methodology, suggests further work should be done to elucidate the effects of idealised geometry, and in particular what information varying idealised parameters can be used to obtain.

2.10 Challenges in hip impingement contact modelling

The difficulty of solving complex contact problems is a limiting factor in the development of more sophisticated computational models of the hip, and software limitations dictate what can be modelled in a realistic time frame. Modelling contact between complex articulating surfaces can result in errors resulting from overclosure of surfaces, and achieving model convergence is not straightforward. Consequently, simplifications must be made to models, and the most obvious of these is to use idealised joint geometry. Although the effects of simplifying geometry have not yet been fully established (Section 2.9), param-

eterised models are still employed in the investigation of hip impingement. Hellwig et al. (2016) recently developed models with morphology based on the geometry developed by Chegini et al. (2009), with an anterior hump to represent the cam. This simplified geometry was optimised for convergence, excluding subject-specific effects, but used biphasic material properties for the cartilage and identified lower peak pore pressure in the control model (0.4 MPa, in the posterior cartilage) than in the cam model (3.8 MPa, in the anterosuperior cartilage). Another recent example is Liechti et al. (2015), who also used spherical ball-and-socket hip geometry, in this case to investigate pincer impingement (Section 2.8.3.3). Authors using spherical articular surfaces were able to generate cartilage with no subject-specific bumpiness, which can aid in achieving model convergence (Chegini et al., 2009; Liechti et al., 2015; Hellwig et al., 2016).

Frequently, studies featuring segmented patient-specific bone geometry are also subject to certain simplifications, including smoothing of cartilage surfaces in order to effectively simulate articulation. Ng et al. (2012) developed models with geometry segmented from subject-specific CT scans of two patients with cam FAI and two healthy control subjects, and applied subject-specific loading. Cartilage layers were formed using an offset method to extrude the surfaces of the acetabulum onto the femoral head, resulting in variable thickness cartilage layers, but these were adjusted to be modelled as smooth layers because the concavity of the acetabulum did not match the femoral head. The study identified elevated stresses on the anterosuperior bone surface, but the labrum was not included. Similarly, Liu et al. (2016) investigated contact pressures resulting from cam FAI by varying the geometry of a single CT scanned hip to adjust the alpha angle. However these models also used spherical cartilage and only reported the difference between their five cases in terms of a single alpha angle. Again, the labrum was omitted. The inclusion of the labrum would be beneficial for understanding how soft tissue deformation results in damage, rather than just reporting regions of increased contact pressure.

More recent CT image-based models have attempted to include more realistic detail in their models. Jorge et al. (2014) did include the labrum in their FE study of impingement by using segmentation from MRI data, although cartilaginous soft tissues were also smoothed and the femoral cartilage covered the whole head including the cam region, which is likely less realistic but beneficial for modelling contact without analysis errors. This study however modelled only a single patient and control (Section 2.9.1). Ng et al. (2016b) used a larger sample size, modelling six femurs (two cam, two asymptomatic cam and two controls), finding the highest peak stresses in symptomatic cam cases (Table 2.1). Ng and colleagues were able to include subject-specific loads derived from musculoskeletal modelling, and location-specific stiffness properties for the bone from CT scans. Furthermore, this study also featured cartilaginous soft tissues, segmented from

MRI scans. However even these complex models had other limitations, as cartilage layers were smoothed and modelled without biphasic properties, and tetrahedral elements were used for all tissues, which may be less suitable for contact modelling than hexahedral elements (Maas et al., 2016) (Section 5.3.2).

A further gap in the literature on FAI modelling relates to model outputs. In many cases researchers report stresses and contact pressures (Jorge et al., 2014; Liechti et al., 2015; Hellwig et al., 2016; Ng et al., 2016a; Liu et al., 2016). The reasons for this are multifactorial; primarily, elevated pressures and stresses may be indicative of increased risk of tissue damage and hence OA development. Historically, models of joint replacements where higher contact stresses could suggest an increase in material wear may also have influenced how the results of later models of the natural joint are reported. However these outputs are not necessarily the most useful for understanding impingement damage mechanisms, as strains and changes in position of soft tissues, especially the labrum, could be more pertinent. Note that whilst the definition of soft tissues encompasses various tissues in the body, such as muscles and ligaments, the term ‘soft tissue’ has been used in this thesis to refer to femoral and acetabular cartilage layers and the acetabular labrum, thus distinguishing them from bone tissue in the hip joint.

2.11 Conclusions

Whilst clinical observations suggest FAI can result in early development of OA (Ganz et al., 2003), there is still no clear way to distinguish between symptomatic and asymptomatic populations who may undergo similar mechanical loading resulting from hip deformities. In a recent systematic review of computational models of FAI, Ng et al. (2016a) suggested that the overall goal for the modelling research community should be to drive towards further development of subject-specific FE methodology incorporating the geometry and loading of individual patients in order to better replicate adverse loading conditions and help elucidate the damage mechanisms of pathological impingement. The challenges involved in developing and solving complex models of articular contact mean there are relatively few studies incorporating subject-specific geometry, and those that do exist have their own limitations, the most prominent being low numbers of participants (Table 2.1). Nonetheless, subject-specific FE modelling of the hip has developed substantially over the past few years and further advancements could lead to a greater understanding of the pathogenesis of OA and increased ability to optimise surgical techniques to correct abnormalities that predispose patients to early OA onset. More complex material models could be used to understand the progression of OA by analysing the carti-

lage response to repeated contact. The use of parametric geometry is a promising method to further understanding of the effects of individual morphological parameters on soft tissue damage. Whilst some studies have shown simplification of geometry can lead to poor estimates of hip contact stresses in comparison to segmented models (Anderson et al., 2010; Gu et al., 2011), similar trends between parameterised and segmented hip models have also been reported (Hua et al., 2015).

In order to establish geometric features that are most crucial for inclusion in models, it is important to progress understanding of why models with idealised geometry may poorly estimate *in vivo* and *in vitro* measured contact stresses. For example, the use of uniform rather than varying, patient-specific cartilage thicknesses may result in different contact stresses due simply to a change in the average thickness, or due to the loss of the undulation of cartilage thickness across the articular surface. Findings such as cartilage clearance and thickness affecting contact mechanics (Li et al., 2013), and higher levels of variability in contact mechanics among subjects for a given activity than among activities for a single subject (Harris et al., 2012), demonstrate that the required level of detail needed for FE hip models to achieve meaningful results remains unknown. FE modelling with parameterised geometry has the potential to increase understanding of mechanisms of soft tissue damage resulting from impingement. Analysing the strain response of the labrum to movements of the femur could aid understanding of the conditions that are most likely to result in pathological impingement.

Chapter 3

Development of Parameterisation Methods

3.1 Introduction

The aim of the work in this chapter was to develop a method of geometric parameterisation to capture three-dimensional geometry of bones in the hip within a small set of parameters, allowing the generation of subject-specific parametric surfaces to represent bone morphology. The parameterisation was required to capture shape characteristics of individuals in order to rate the relative severity of impinging hips. Geometric features pertinent to impingement include cam size in terms of discrepancy between head and neck, cam extent in terms of width around the neck, and cam position on the femur. On the acetabular side, important geometric features include location of the acetabular rim and the acetabular cavity depth. The goal for the parameterisation systems was to describe these features.

Parameterisation systems were developed and compared when applied to an initial subset of 10 patients from the cam patient database (Section 1.2). The chosen parameterisation systems were later applied to these patients and a further 10 patients in a study assessing impingement risk by defining severity measures based on the raw parameters describing the geometry; details of this are provided in Chapter 4. The sample size of 10 was chosen to provide a relatively small number in order to test different methods of geometric parameterisation rapidly, whilst still testing on different patients to ensure the systems could identify variations in shape. This sample was extended to 20 to provide a reasonable number for calculating statistics and to test whether the chosen parameterisation system could

distinguish between two groups (males and females). The sample size was not increased further in order to limit the time required for manually segmenting CT scans. The selection of the subsets of patients from the available database was performed by randomly selecting an equal number of males and females from the database, excluding any scans encountered with poorer resolution than the standard resolution that had been used for most of the scans in the database (Section 1.2).

The general approach to parameterisation is outlined in Section 3.2. The approach used required the segmentation of subject-specific bone surfaces, and this is explained in Section 3.3. Details of the development of the femoral parameterisation systems are described in Section 3.4. The aim of the femoral parameterisation was to capture geometry of proximal femurs with cam deformities. A successful system was required to replicate the bone geometry sufficiently to differentiate between patients, particularly in the head-neck junction where cams usually occur, whilst minimising the number of parameters used to describe the geometry. Additionally, the system was required to represent the femoral surfaces in sufficient detail for use in finite element models. An initial parameterisation system for the femoral surface was developed along with computational procedures to systematically extract parameter values from segmented femoral surfaces and generate parameterised specimen-specific surfaces. This initial parameterisation system for the femur used circle fitting to calculate parameters for the neck region, onto which cam geometry was added. This method is described in Section 3.4.1 and resulted in reasonable overall surface fittings errors, but was not able to emulate the cam region anatomy with sufficient accuracy. A further parameterisation system was subsequently developed to capture the geometry of entire neck region using ellipse fitting, which is described in Section 3.4.2 and resulted in parameterised surfaces better able to represent the segmented femurs. This was assessed using surface fitting errors between segmented and parametric femurs, following optimisation of the procedures. This is covered in Section 3.5, with the results discussed in Section 3.6.

Development of an acetabular parameterisation method, from initial tests, is described in Section 3.7. On the acetabular side, the parameterisation was required to capture the shape of lunate articular acetabular surface, differentiating between patients and in particular capturing the rim geometry, which, in combination with femoral geometry, may lead to impingement. The successful system used three-dimensional splines fitted to the segmented acetabular rim geometry. An overall discussion of the work in this chapter is provided in Section 3.8.

3.2 Approach to geometric parameterisation

The goal of geometric parameterisation was to generate a set of parameters which sufficiently describe the shape of the bone of interest (head and neck of femur, and lunate surface of acetabulum) in a particular individual. It is important that the chosen system is sensitive enough to distinguish between individuals, particularly in terms of cam shape. In this chapter, the parameterisation systems developed were applied to 10 hips (5 female and 5 male) from the cam patient database.

Three-dimensional geometric shapes can be constructed in Abaqus by revolving or extruding two-dimensional sketches consisting of lines and curves (such as arcs and splines), which are defined within Abaqus by the coordinates that they pass through. Coordinate values can depend on some previously defined parameters to create parameterised geometry. Once STereoLithography (STL) files of segmented masks are loaded into MATLAB, the vertices of the triangles describing the surface can be isolated as a list of 3D Cartesian coordinates. Parametric surfaces were semi-automatically generated in three main steps. First bone tissue was segmented and generated into surfaces meshed using ScanIP (Section 3.3). Then geometry parameters were systematically extracted from bone surface meshes using custom made code in MATLAB. The parameters are described in detail in sections 3.4 and 3.7, for the femoral head and acetabular cavity respectively. Parametric surfaces were then automatically generated from these parameters by using Python to generate the geometry within Abaqus.

In the femoral case, where parameter extraction was fully automatic, the entire process, excluding segmentation, could be automated. In order to make the process of comparing parametric and segmented surfaces more straight-forward, the centre of the femoral head (an arbitrary value based on its position in the original scan) was always first translated to coincide with the origin. Segmented femurs were first exported from ScanIP as Abaqus inp files, and MATLAB was used as a master script to import femurs into Abaqus and perform translations with a Python script, and then export the femurs as STL files into MATLAB again. MATLAB was then used to calculate parameters from STL files and pass these parameters to a Python script which runs Abaqus to generate the parametric geometry, output as an STL file which was read by MATLAB again to perform the fitting error calculation. The same general steps were followed in the acetabular case, but this required more manual intervention as parameter extraction was not fully automatic.

MATLAB was chosen as the main scripting language because its interface is well suited to working with large matrices, in particular lists of nodes describing surfaces. Python

is the scripting language of Abaqus and MATLAB is capable of automatically calling Python scripts to run in Abaqus.

3.3 Bone segmentation

Digital Imaging and Communications in Medicine (DICOM) data from the CT scans of all FAI patients (Section 1.2) used in this work were imported into ScanIP. Each CT slice shows the tissues inside the body with pixel greyscale values assigned according to material density. Bone tissue is clearly defined in these images and so 3D bone geometry was constructed using the segmentation tools and filters available in ScanIP.

Masks defining bone geometries were created using the “threshold” and “paint” tools to define the areas of interest in the image data and hence delineate the bone tissue. The threshold tool creates a mask based on greyscale values; the mask includes only those pixels whose greyscale value is in the specified range. The paint tool allows the mask to be edited by manually selecting pixels for inclusion or exclusion. The “close” (dilate followed by erode) and “cavity fill” (fill in internal holes in the mask) tools were also used to expedite the process of manually selecting the required pixels. A recursive Gaussian filter (1.0 pixel in all directions) was applied to the final masks in order to smooth the surface, removing segmentation artefacts and refining the surface contours. Femoral and acetabular bone masks are shown in Figures 3.1 and 3.2 respectively.

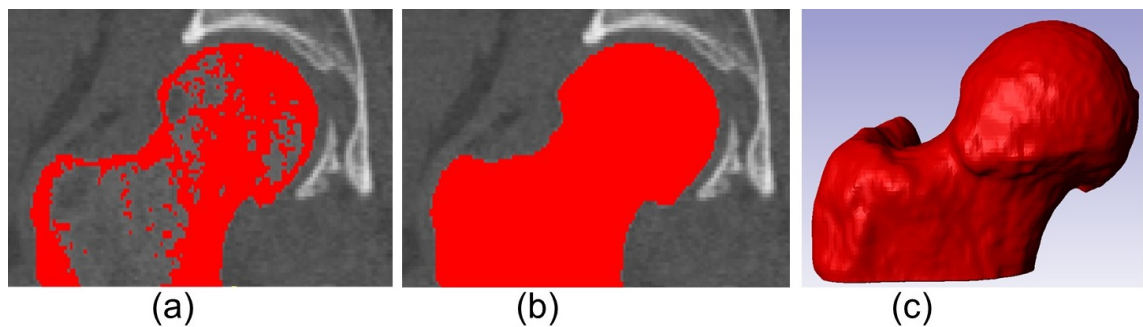


Figure 3.1: Femoral bone segmentation in ScanIP:

- (a) Mask from threshold (coronal plane).
- (b) Final filled and smoothed mask (coronal plane).
- (c) 3D rendering of the final mask in an AP view.

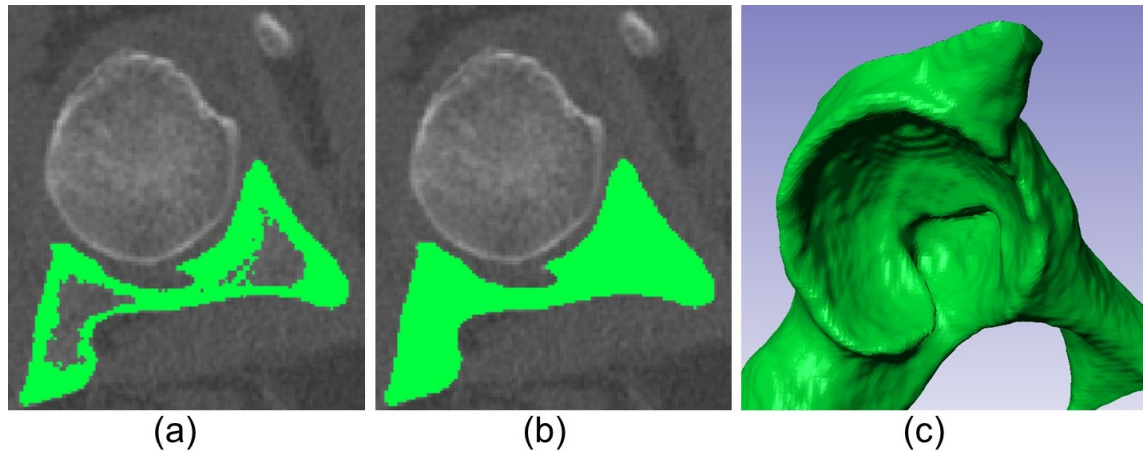


Figure 3.2: Acetabular bone segmentation in ScanIP:

(a) Mask from threshold (transverse plane).

(b) Final filled and smoothed mask (transverse plane).

(c) 3D model created from the final mask with view showing acetabular cavity.

Functions within ScanIP allow a 3D surface to be created from the final mask. These surfaces can be exported in various formats including as STL files. In STL format, the surface is described using a finite number of triangular faces, with a greater accuracy achieved by using a greater number of triangles. Triangulated surfaces are useful for comparing segmentation-based and parameterised surfaces because the coordinates of the triangle vertices on each surface can be compared.

The units used for distances in this section of work were mm, standardising the distances since CT scans can have different voxel sizes (although here all CT voxels were $0.7422 \times 0.7422 \times 1$ mm). It was assumed that the y -axis points anteriorly based on the likely position of a supine patient undergoing a CT scan, and this was later used for aligning femurs to the femoral neck axis (Figure 3.3). Mesh densities were such that nodes on each surface were spaced at distances of around 0.8 – 0.85 mm.

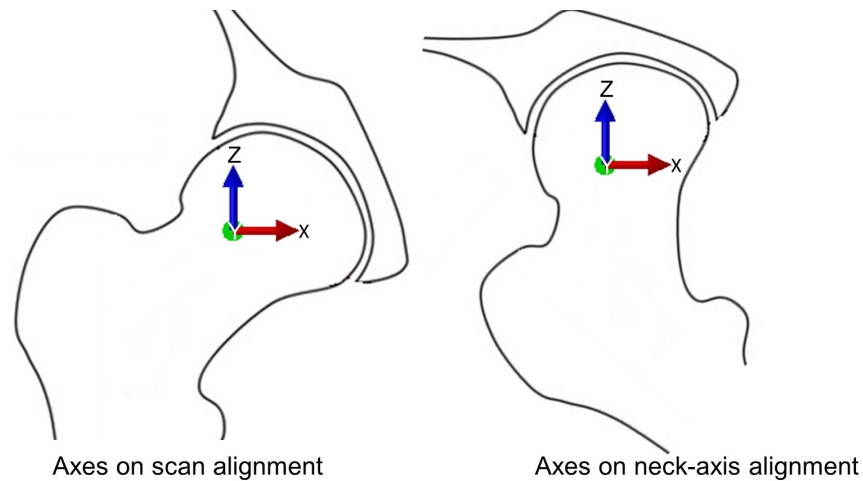


Figure 3.3: Schematic showing the axes set up.

3.4 Geometric parameterisation of the proximal femur

This section details the methods used to extract parameters from the segmented femur surfaces and thereby generate parametric femoral surfaces, initially using circle-fitting to parameterise the head-neck and cam separately, and subsequently using ellipse fitting to capture the geometry in a single set of parameters.

3.4.1 Femoral parameterisation 1: head-neck and cam separately

3.4.1.1 Initial parameter extraction

All segmented femurs were first rotated to align the neck axis with the vertical image axis (in line with the superior-inferior axis) using a rotation about the anterior-posterior axis. This rotation was based on the assumption that patients' hips were in a neutral position in the CT scans, and was chosen to be 40° for all femurs.

To maintain a small number of parameters in this system, the head and neck were represented with complete rotational symmetry in the longitudinal axis passing through the centre point of the head, defined as the origin. The parameters listed below were used to dictate the position and shape of the parameterised proximal femur, with the final three in particular dictating the shape and position of the cam. The parameters are shown in context in Figure 3.4.

- *Centre*: The centre point of the head.

- *Head radius (HR)*: The radius of the best fit sphere to the femoral head.
- *Neck radius mean (NR)*: The mean radius of the femoral neck excluding cam area.
- *Neck length mean (NL)*: Mean value of slice positions in the neck used to find mean radius.
- *Neck radius inferior (NRB)*: The radius of the femoral neck at the lowest slice.
- *Neck length inferior (NLB)*: The lowest slice in the neck.
- *Cam radius (CR)*: The mean radius of the femoral neck in the cam area.
- *Cam coverage angle (CA)*: Angle by which the cam extends around the neck.
- *Cam position angle (CP)*: Angle measured from anterior defining the position of the start of the cam.

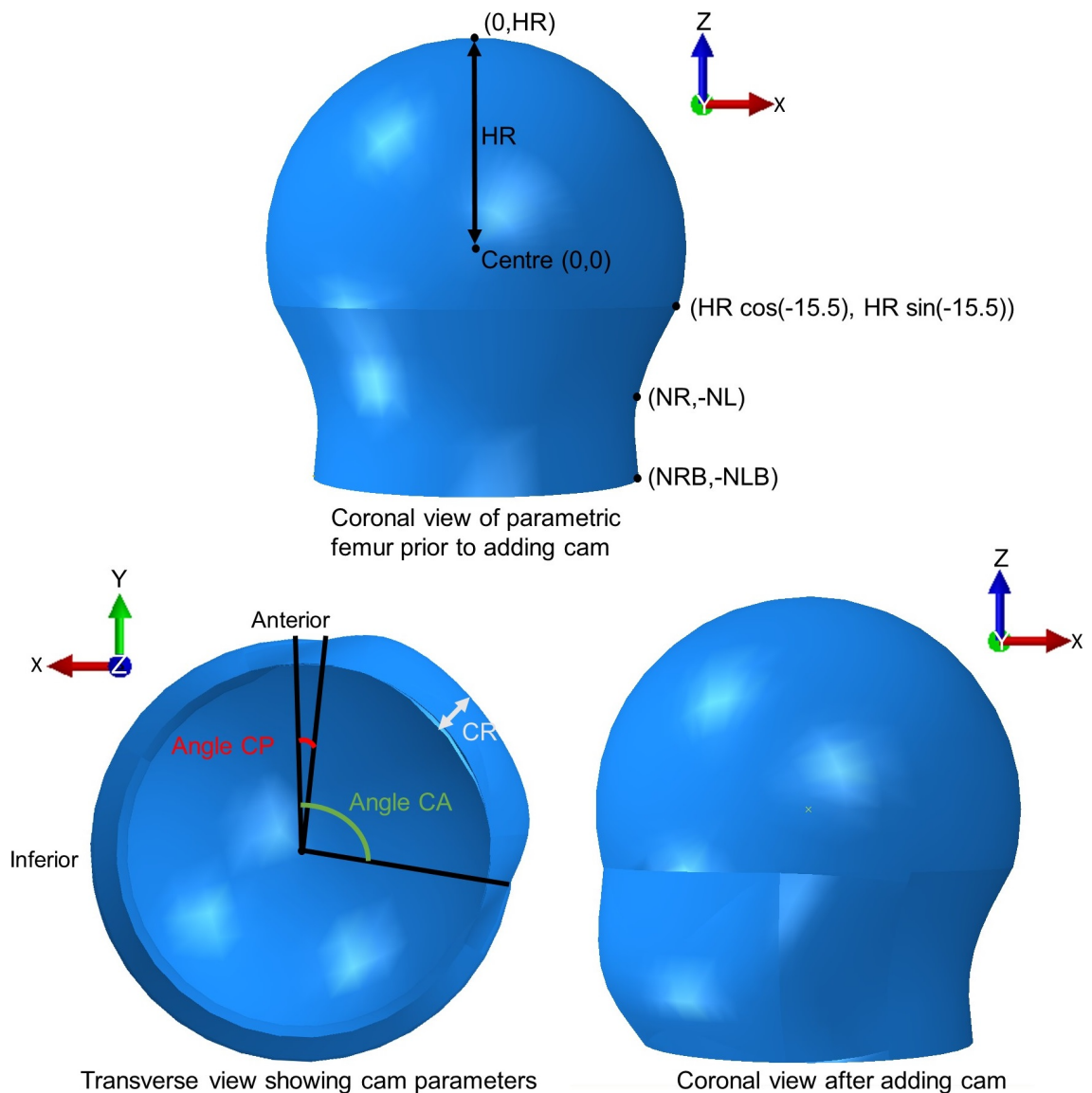


Figure 3.4: Example of the initial parameterisation of the proximal femur, with parameters labelled.

The parameters *HR* and *Centre* for the spherical portion were determined using a best fit

sphere for the femoral head, calculated from vertices describing masks of the top of the femoral head. These masks were generated in ScanIP by unpainting everything from the bone mask except the upper portion of the head, so that the neck and cam region did not affect the radius and centre of the fitted sphere.

In order to determine values for neck parameters, transverse slices through the neck were considered. Each slice consisted of the (x, y) coordinates in a given z -coordinate range of the STL vertices defining the segmented femoral surface. In practice, 5 slices were used in all cases, with slices having equal height between the z -values of -24 mm and -11 mm. This captured the neck region in all cases (Figure 3.5).

The process used for extracting the neck parameters used neck slices created by plotting the x and y values of vertices in a given range of z -values. A circle fitting function was used on these slices to obtain the best fitting centre point and radius by minimising the sum of squared distances from the points to the fitted circle (Figure 3.5).

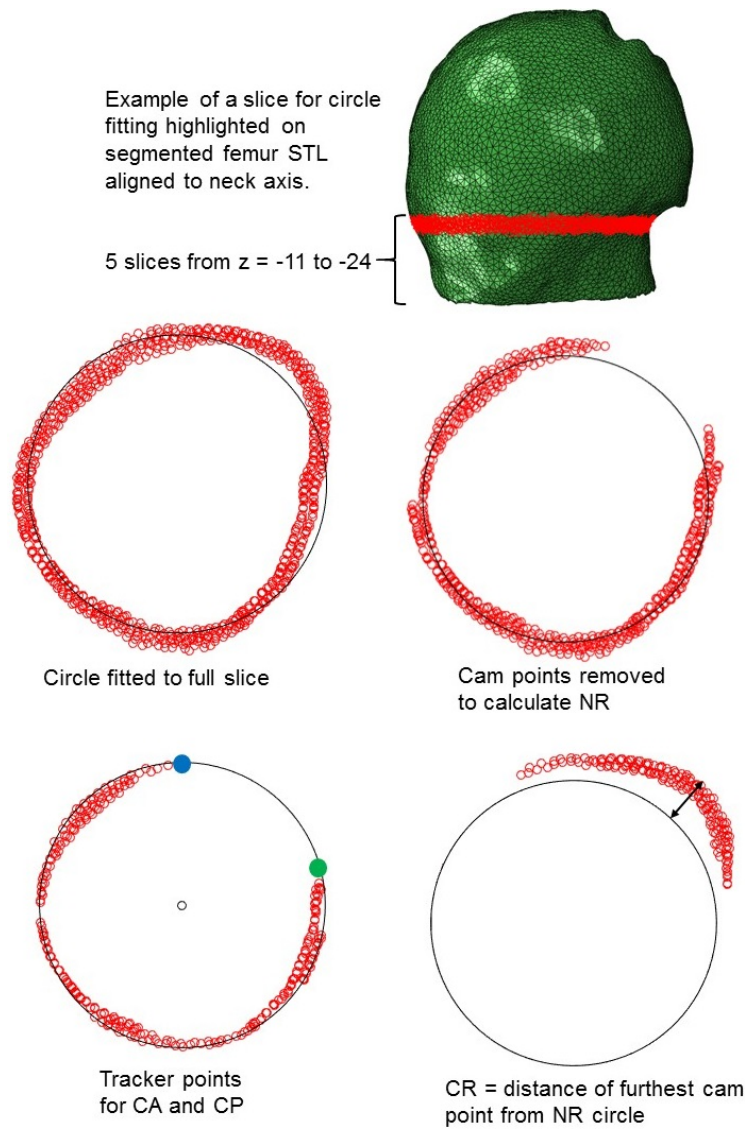


Figure 3.5: Extracting original neck and cam parameters from a segmented femoral head; STL vertices with best fit circles are shown in red. The tracker points used to calculate CP and CA are blue and green respectively.

An initial circle was fitted to all the vertices in each slice. The cam region was then isolated as the points outside this initial circle *and* within the upper half of the slice, assumed to be the anterior region. A non-cam circle was then defined as a new fitted circle for data in the slice excluding the cam region. For each slice, the parameters NR_{slice} (radius of non-cam circle), and CR_{slice} (distance of furthest point in cam region from non-cam circle centre) were defined, with the means of these giving the overall values of NR and CR respectively. The mean z -value of the slices used provided NL .

To calculate the cam angle parameters, tracker points on the non-cam circle were iteratively moved around the circle by adding or subtracting 1° to their position until they were sufficiently near a data point from the slice (that is, distance of tracker point to data point

< 2 mm). Cam angle parameters for each slice, CP_{slice} and CA_{slice} , were then calculated using the angle between vectors formula, $\theta = \arccos\left(\frac{u \cdot v}{\|u\| \times \|v\|}\right)$. The final parameters CP and CA were taken as the maximums of $CP_{slice} =$ and $CA_{slice} =$ respectively.

3.4.1.2 Parametric surface generation

The 3D parameterised femur object was created in Abaqus by initially rotating a 2D sketch consisting of a circular arc and a spline by 360° about the vertical axis and then adding an additional curved surface to the resulting 3D geometry to represent the cam.

The proximal head region was defined by the radius and centre of a circular segment, which was rotated to become a spherical cap (portion of a sphere cut off by a plane). In this parameterisation system, the head was assumed to be roughly $\frac{2}{3}$ of a spherical surface (Figure 3.6).

To find a spherical cap with surface area that is a known fraction of that of a full sphere, recall that the surface area of a sphere is $4\pi r^2$ and the surface area of a spherical cap is $2\pi r h$, where r is the radius of the sphere and h is the height of the spherical cap. Thus, calling the desired fraction x , and setting $x4\pi r^2 = 2\pi r h$, it can be seen that $h = 2rx$. Taking the centre of the sphere as the origin, the y value of the lowest point of the cap is $r - h$, so the point on the circular arc which was revolved to create the spherical cap is given by $r \sin \theta$, where θ depends only on x , since $\theta = \arcsin((r - h)/r) = \arcsin(1 - 2x)$. Notice that if the fraction $x > \frac{1}{2}$, the value of θ is negative, corresponding to a rotation down from the horizontal radius rather than up as is shown in Figure 3.6. In this parameterisation system, a fixed value of $\theta = -15.5^\circ$ was used, making the head roughly $\frac{2}{3}$ of a spherical surface.

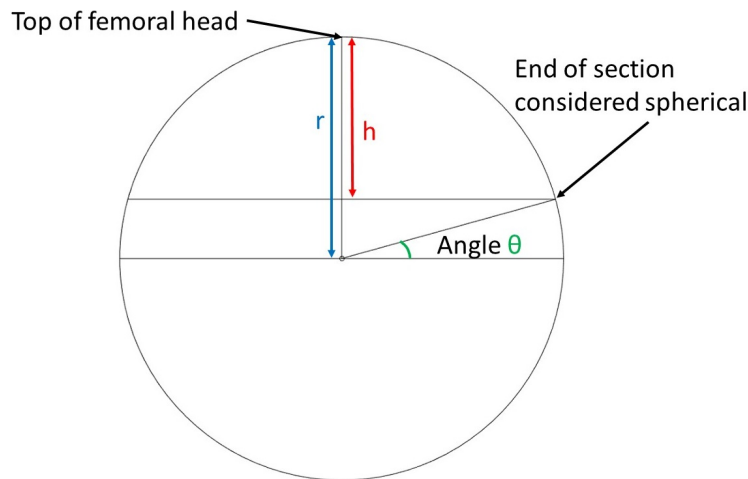


Figure 3.6: The angle θ as a rotation from the horizontal diameter of a circle, used for defining spherical cap sizes, where r is the radius of the sphere and h is the height of the spherical cap.

The femoral neck, excluding the cam region, was generated by a spline passing through three points whose (x, z) coordinate values are determined by the neck parameters (Figure 3.4). The first point is simply the lowest part of the circular section defining the head. The next point is the coordinate $(NR, -NL)$, so that the radius of the neck where $z = -NL$ (the mean z -value in the region neck slices were taken) was the mean of the radii of the fitted circles. Because the overall geometry was symmetrical, the centres of the fitted circles were not taken into account. The final point on the spline was at the coordinate $(NRB, -NLB)$. For the point at the lowest part of the neck spline, $-NLB$ was taken as the minimum z value from all the vertices in the segmented femur. The radius at this position was defined by NRB , taken as maximum radius found in all the slices to emulate the hyperboloid appearance of the neck. The parameters CR , CP and CA defined the geometry for an additional 3D surface added to the base femoral geometry to create the overall parameterised femur including the cam.

3.4.2 Femoral parameterisation 2: ellipse-based parameterisation

3.4.2.1 Ellipse parameter extraction

This parameterisation approach sought to capture the overall shape of the proximal femur, including the cam, within a single set of parameters, allowing the geometry to be constructed as one part without additional assembly. This was achieved by fitting ellipses (Gander et al., 1994) to (x, y) coordinates of vertices in 2D slices through the head-neck region.

First the head centre was located, by fitting a sphere to the nodes on the proximal side of the femoral head. The proximal region was defined here by generating a mask in ScanIP with the femoral neck removed so that only the femoral head was visible in the coronal plane. All segmented femurs were then rotated to align the neck axis with the vertical image axis (in line with the superior-inferior axis) using a rotation about the anterior-posterior axis, again chosen to be 40° for all femurs (Figure 3.7a). In this new orientation, nodes on the head surface were isolated as proximal nodes by taking only those with a z coordinate > 0 (recall that the femur was translated so that the initial estimate for its head centre coincided with the origin). At this stage, the head centre position and radius were recalculated by fitting a new sphere to these proximal nodes, giving the parameters *Centre* and *HR*. Surface nodes found in 2 mm thick intervals of the head-neck region perpendicular to the neck axis were then used to define slices of the proximal femur.

On the first attempt to use this new system to generate parametric femurs, 30 slices were plotted for each femur, and a manual visual check was made to find the slice where the greater trochanter first became visible (vertices appeared away from the main elliptical neck area). The slice prior to this was chosen as the final slice for lofting to create the parameterised surface. However, variations in trochanter size and position meant this method produced femurs of inconsistent size in terms of included neck length, which made comparing cam size difficult. Instead, the total number of slices, defined from the top of the head to the end of the modelled neck axis, was fixed to be equal to the head radius (rounded to the nearest mm) to ensure that the most distal slice was in a comparable position along the femoral neck for each femur. For example, for a head radius of 25 mm, 25 slices of 2 mm would be used, resulting in a height of 50 mm from the top of the head to the end of the neck. This was in contrast to the previous system, in which the slices were defined at z -values fixed across all the femurs.

Ellipses were fitted to the segmented bone surface in a selection of four of the defined slices (Figure 3.7b). The positions of the four slices were selected automatically to focus on the femoral neck region by taking a linearly spaced vector with four points between $z = \frac{x}{2}$ and $z = x$, where x was the total number of slices, and then rounding these points to integer values. Thus in addition to the parameters describing the top of the head, the parameters in this system were those defining the ellipses. Each parameter can therefore be thought of as a list, taking a different value at each slice where an ellipse fit is made, and the total number of ellipse parameters being the product of the number of ellipses lofted through, and 6, which is the number parameters describing each ellipse. These are listed below and shown in Figure 3.7.

- *Neck radius a (NRa)*: Ellipse radius a

- *Neck radius b (NRb)*: Ellipse radius b
- *Neck length position (NL)*: Vertical position of neck slice.
- *Neck angle (NA)*: Angle of the ellipse from horizontal
- *Ellipse centre x (NRx)*: x coordinate of ellipse centre
- *Ellipse centre y (NRy)*: y coordinate of ellipse centre

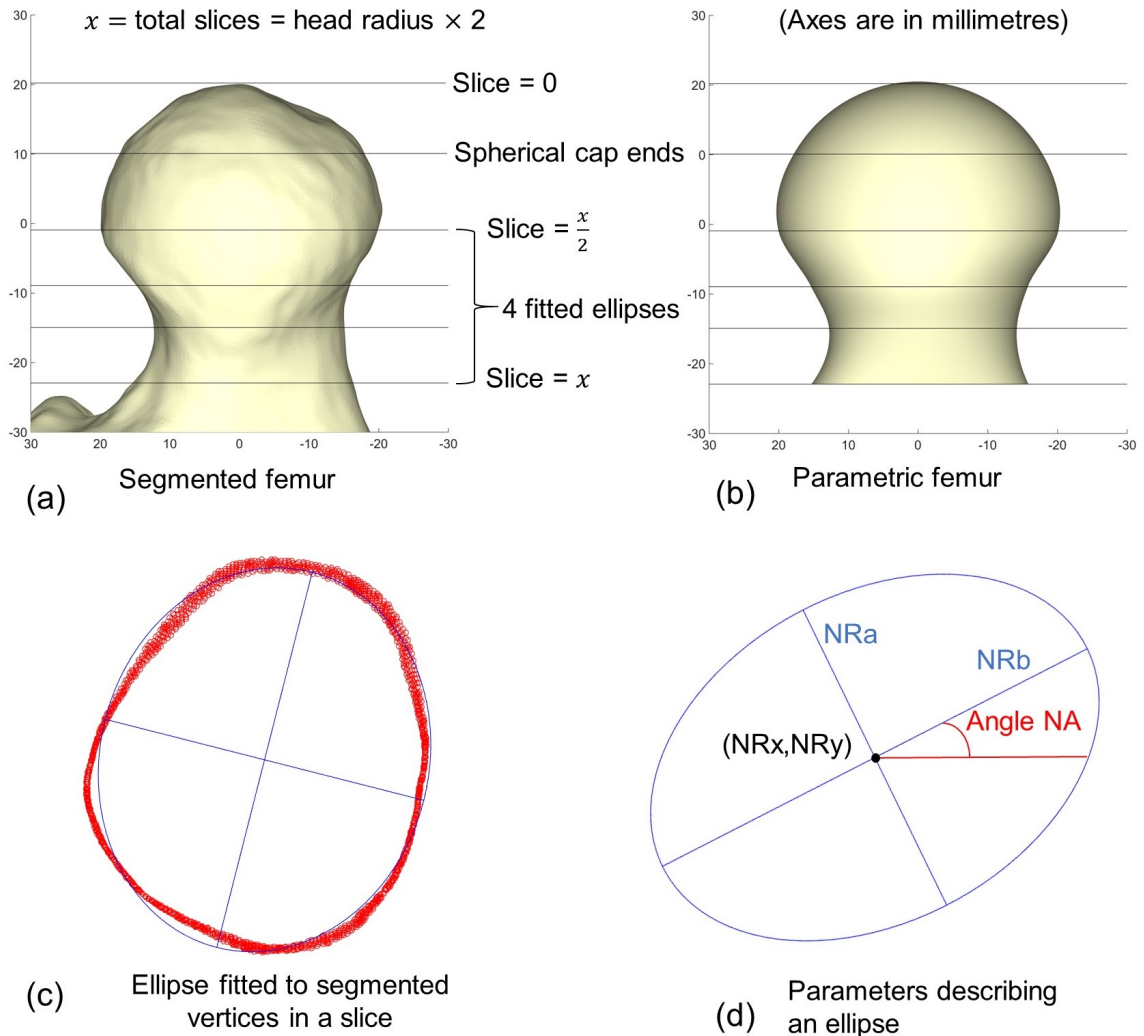


Figure 3.7: Segmented and parametric femurs showing ellipse parameters:

(a) & (b) Segmented and parametric femoral surfaces aligned to neck axis. Horizontal lines mark the top of the head (where slice counting begins), lowest part of the spherical cap region, and the positions of ellipses used for lofting. Ellipses were fitted to vertices on the triangulated surface falling within 2 mm slices centred on these lines.

(c) An example of a STL vertices (red circles) in a 2 mm slice through the femoral neck with a best fit ellipse (blue).

(d) The ellipse parameters displayed on an example ellipse.

The ellipse fit to vertices in each slice was generated using a least squares estimate of the coefficients that define a conic equation of the form $Ax^2 + Bxy + Cy^2 + Dx + Ey = 0$.

From this equation, the more useful parameters for describing the ellipse were extracted. When $B \neq 0$ the ellipse is tilted. Let x', y' be coordinates on the untilted equivalent of this ellipse. By considering the rotation matrix in the equation

$$\begin{pmatrix} x \\ y \end{pmatrix} = \begin{pmatrix} \cos \phi & \sin \phi \\ -\sin \phi & \cos \phi \end{pmatrix} \begin{pmatrix} x' \\ y' \end{pmatrix}$$

it can be seen that by substituting x with $cx' + sy'$ and y with $cy' - sx'$ (where $c = \cos \phi$ and $s = \sin \phi$), the untilted conic equation can be found. This can be written in the form $A'x'^2 + B'x'y' + Cy'^2 + D'x' + E'y' = 0$. Notice that the angle ϕ can itself be found because $B' = 0$, and by simplifying the substitution it can be seen that $\phi = \frac{1}{2} \arctan (B/(C - A))$.

Rewriting the new equation in the form

$$\frac{(x' - x'_c)^2}{a^2} + \frac{(y' - y'_c)^2}{b^2} = 1$$

allows the ellipse radii and the centre point of the untilted ellipse to be found. The centre of the originally tilted ellipse can then be found by rotating the point (x'_c, y'_c) back by ϕ using a rotation matrix.

3.4.2.2 Parametric surface generation

The parametric femurs in this system were again generated with a spherical cap to represent the top of the head using the parameters *Centre* and *HR*. The angle used to define the spherical cap representing the proximal head was changed from -15.5° used previously to 29.5° resulting in a cap with smaller surface area (Figure 3.6). This was done so that less of the head shape was assumed to be spherical, allowing for more variation. This spherical cap had approximately 25% of the surface area of a whole sphere.

Lofting was used to complete the surface, in which a 3D surface was generated by transforming from a starting section shape and orientation to an ending shape and orientation, with intermediate sections defining the shape of the surface as it passes through space. The lofting operation was performed from the circular end of the spherical cap through the four ellipses. The *NL* parameters describing the vertical position of each ellipse were taken as the mean z -value in the 2 mm slice of vertices to which the ellipse was fitted.

3.5 Optimisation and evaluation of femoral parameterisations

3.5.1 Fitting error calculations

Fitting errors between the segmented bone surfaces and the parametric bone surfaces were calculated in MATLAB from the triangulated surfaces as the root mean squared distance that nodes on the segmented surface in the region of interest had to move to conform to the nearest node on the parametric surface. That is,

$$F = \sqrt{\frac{\sum_{i=1}^N D_i^2}{N}}$$

where F is the fitting error, N is the total number of vertices on the segmented surface and each D_i is the Euclidean distance from vertex i on the segmented surface to the nearest vertex on the parameterised surface.

When compared to the overall size of the surface in question, these fitting errors provide a measurement of how well a parameterised model approximates the segmented geometry. Moreover, they can be used to compare the quality of different parameterisation methods.

In this chapter, fitting errors are discussed in terms of comparing the two parameterisation methods. Fitting errors are revisited in Section 4.4 in Chapter 4, as the density of the mesh representing the surfaces was increased to achieve lower fitting errors and compared to the lowest case possible. The approximate mesh density used was kept constant across femurs for valid comparison. As mentioned in Section 3.3 the mesh densities used in this chapter were such that nodes on each surface were spaced at distances of around 0.8–0.85 mm.

3.5.2 Optimisation

In order to optimise the surface fit and attempt to more accurately capture the neck and cam region, some additional steps were undertaken for each of the parameterisation methods.

3.5.2.1 Parameterisation 1 optimisation

Changes in the fitting error resulting from optimising the head centre position were recorded. The improved fitting error given in Table 3.1 is that found after optimising the centre parameters in the order x, y, z . To perform this optimisation, after the initial parameters were generated, each coordinate was iteratively varied by increasing or decreasing its value by 0.05 mm, until the fitting error no longer decreased (eventually the fitting error will increase). Similar tests were conducted to optimise other parameters in this way, but the greatest advantage was seen to result from adjusting the head centre position.

3.5.2.2 Parameterisation 2 optimisation

As well as generating parametric surfaces by lofting through ellipses fitted to four slices as described in Section 3.4.2, the same method was used to generate parametric surfaces by lofting through ellipses fitted to all 2 mm slices below the halfway point counting down the femoral head from the superior top region. The first column of fitting errors in Table 3.1 in the ellipse case are from surfaces generated by lofting through ellipses fitted to all slices below the halfway point down the head, and the second column of fitting errors is from surfaces generated by lofting through ellipses fitted to four slices in the same region (Figure 3.7).

3.6 Femoral parameterisation results and discussion

The fitting errors resulting from both parameterisation systems are tabulated in Table 3.1.

Table 3.1: Fitting error data for the ten cam femurs given in mm for the two parameterisation systems. Fitting errors after optimising and the change in centre position in the circle system are also given in mm. Fitting errors when the ellipse-based parameterisation system was used are given when lofting through all slices below the halfway slice, and 4 slices below the halfway slice were used. The total number of 2 mm slices used in this system is also reported.

Hip ID	Circle Parameterisation			Ellipse Parameterisation		
	Fitting Error Initial (mm)	Fitting Error Optimised (mm)	Centre Position Change x,y,z (mm)	Total number of slices	Fitting Error All slices loft (mm)	Fitting Error 4 slices loft (mm)
01R	1.2864	1.2267	0.6,-0.1,-0.5	22	0.6829	0.7044
02R	1.5508	1.3928	-0.4,1.1,-0.3	22	0.7216	0.8112
06R	1.1590	1.1219	-0.4,-0.4,0	23	0.8236	0.8362
07R	1.0797	1.0496	-0.4,0,-0.3	26	0.7591	0.7480
09R	1.2619	1.2270	-0.3,-0.3,-0.6	22	0.7362	0.7433
11R	1.4585	1.3573	-0.9,0,0.2	23	0.7423	0.7657
17L	1.5148	1.3980	0.9,0.6,-0.4	27	0.7956	0.8292
33L	1.5781	1.5193	-0.3,0,-0.9	23	0.7383	0.7577
34L	1.1908	1.1448	0.6,-0.2,0	28	0.7156	0.8906
51L	1.2660	1.2305	0,0.3,-0.6	24	0.8101	0.8246
Means	1.33	1.27			0.75	0.79

The results shown in Table 3.1 indicate that the fitting errors for Parameterisation 1 were in the region of 1.3 mm, whilst a femoral head radius is generally in the region of around 20 – 25 mm (the mean was 22.4 mm), and the mesh density of nodes on each surface was around 0.8 – 0.85 mm, so the errors appeared to be reasonably small considering the simplifications made in the parameterisation system. Parameterisation 1 was found to be capable of distinguishing different femur geometries from each other as the process resulted in different parameter values for the different femurs. For example, the range for cam radius above the head radius, CR , was 0.48 – 2.51 mm, so some of the detected difference was greater than the fitting error. The range for the extent of the detected cam, indicated by the difference between CP and CA , was $71^\circ - 148^\circ$. When optimising the fit by varying parameter values, the greatest advantage came from adjusting the head centre position. This was not surprising since varying the head centre parameters changed the position of all the vertices on the surface, whereas varying other parameters affected fewer vertices.

As well as distinguishing the femurs from each other, the parameterisation should represent the femoral surfaces in sufficient detail for use in finite element models. In particular, this meant capturing detail in the area typically causing impingement, specifically the shape of the cam region. However, visualising the poorest fitted vertices revealed that the Parameterisation 1 system was suboptimal for capturing geometry of the cam region, and it was observed that when optimising the surface fit by varying the head centre position, the overall fitting error was reduced at the expense of losing better fit in the cam region

(Figure 3.8). Note that there is a thickness effect visible in (Figure 3.8). In order to ensure that the part of the segmented surface used for the surface comparison matched the part of the femur included in Parameterisation 1 (the head and neck region only), a cropped mask was created in ScanIP by unpainting the bone below the proximal femur. When exported as an STL file, this mask had a finite thickness. In Parameterisation 2 (the ellipse-based system), this issue was avoided. To ensure that the part of the segmented surface used for surface comparison matched the part of the femur included in the ellipse-based parameterisation, the MATLAB script was adjusted. Only vertices on the segmented surface falling within the slice range used to create the parameterised geometry were used for the calculation, meaning that the cropped mask used in the previous system was no longer necessary.

Some observations noticed in the femurs, but not captured by the first parameterisation system, were that the cam tended to be wider proximally, and the centre points of neck slices often did not line up with the head centre position, meaning the head-neck offset was not accurately captured in the parametric surface. In a modelling situation, this could result in contact occurring in regions where no segmented bone existed. Therefore although the parameterisation could distinguish between cams, the simplified representation of neck cross sections as circles meant that the parametric surfaces produced by this parameterisation system were insufficient representations of cam geometry.

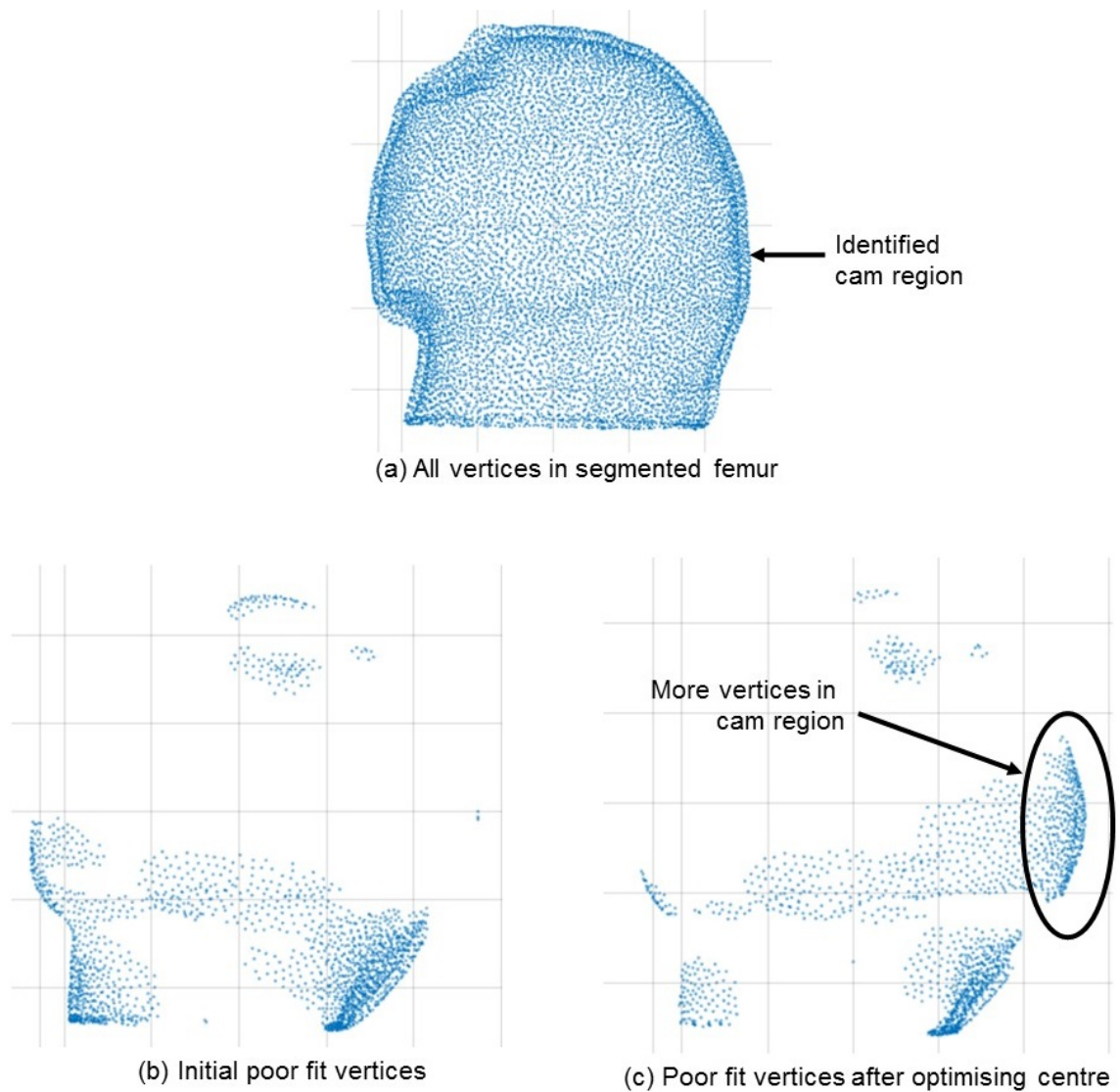


Figure 3.8: Scatter plots to visualise poorly fitted vertices in a segmented STL surface;
(a) All vertices.
(b) Vertices where the nearest parameterised vertex is further than 2 mm away.
(c) The same data after optimising the overall fit by moving the centre position shows more vertices in the cam region are now poorly fitted.

The fitting errors obtained using the ellipse-based parameterisation system are also provided in Table 3.1. It can be seen that lofting through four ellipses provides a fitting error close to that obtained when using slices throughout the neck. Using more than four slices resulted in an uneven surface because of the reduced distance between ellipses lofted through, and in addition increased the number of parameters required to describe the femur (Figure 3.9). Preliminary tests revealed that using less than four ellipses led to considerably poorer fits between the parametric and segmented surfaces (> 1 mm in all cases).

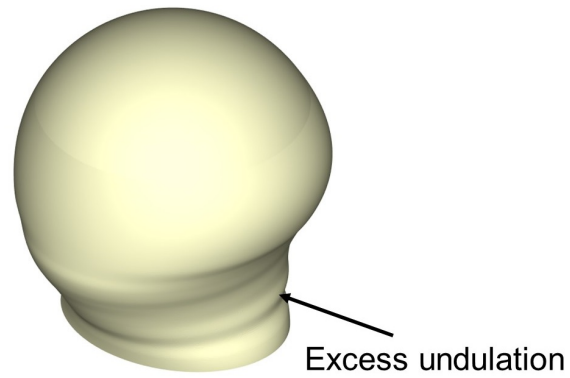


Figure 3.9: An example of a parametric femur produced by lofting through an ellipse fitted to every 2 mm slice of a segmented proximal femur. Excess undulation occurs on parametric femurs when lofting through many ellipses.

An example of a segmented femoral surface, together with the parametric versions from both systems, all plotted in MATLAB, are shown in Figure 3.10.

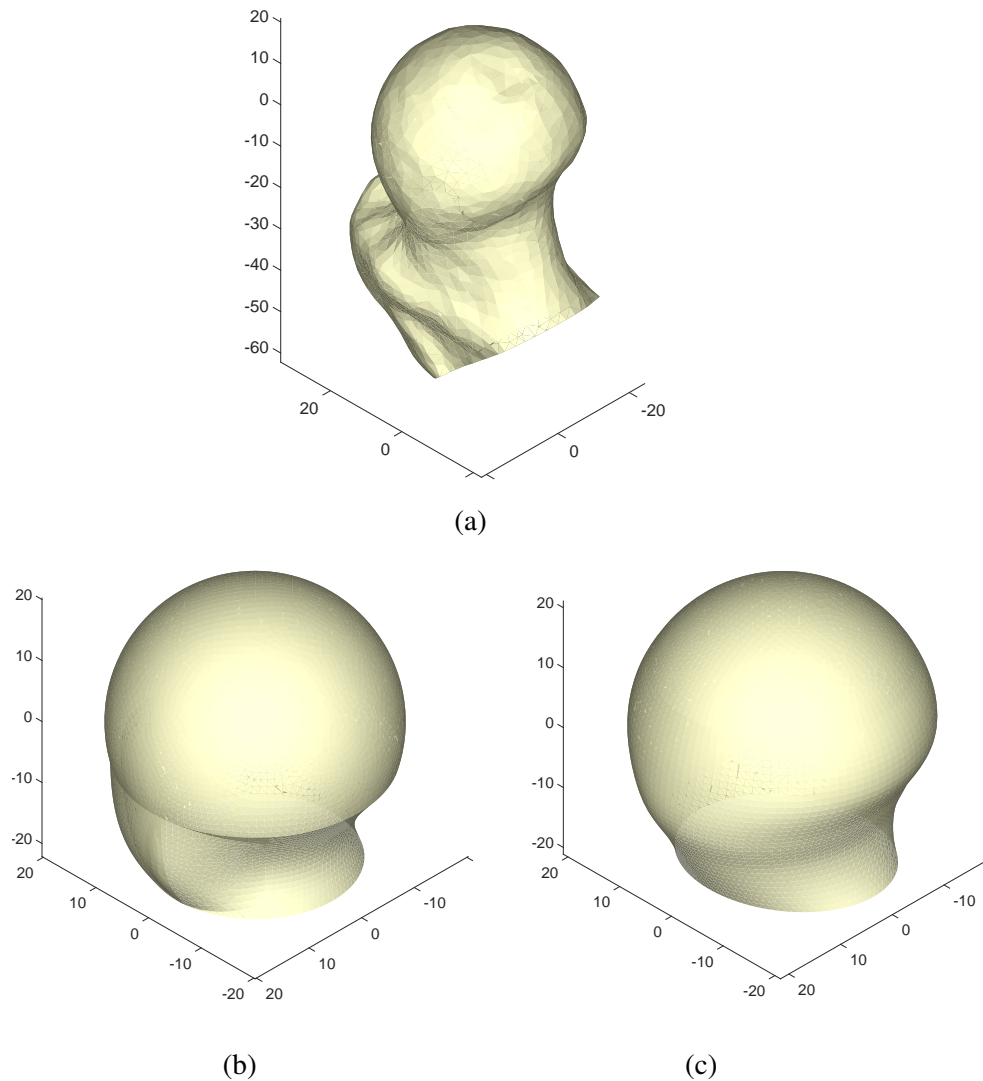


Figure 3.10: Femoral surfaces:

(a) Segmented from a CT scan, including some trochanter for context.

(b) Generated from the initial parameterisation system.

(c) Generated from the ellipse-based parameterisation system.

3.7 Geometric parameterisation of the acetabulum

This section describes the development of methods to produce parametric surfaces to capture the bone shape behind the articular surface of the acetabulum, particularly the acetabular bone rim geometry. Initial tests used lofting through 2D splines generated by selecting points in MATLAB. The final method used lofting through 3D splines generated from points selected directly in Abaqus, and optimised the number of points on each spline to achieve a better fit to segmented surfaces.

3.7.1 Development of acetabular parameterisation

3.7.1.1 Initial method

The process of generating parametric surfaces by lofting through shapes fitted to nodes on segmented surfaces was found to be successful in the ellipse-based femoral parameterisation. Therefore a similar approach was taken to parameterising the acetabular surface. Initially, parametric surfaces were generated by lofting through splines fitted to nodes in 2D coronal slices of the acetabulum. Five slices lying within the acetabulum were manually identified and nodes in these slices were manually selected within MATLAB to provide the coordinates to define the splines (Figure 3.11).

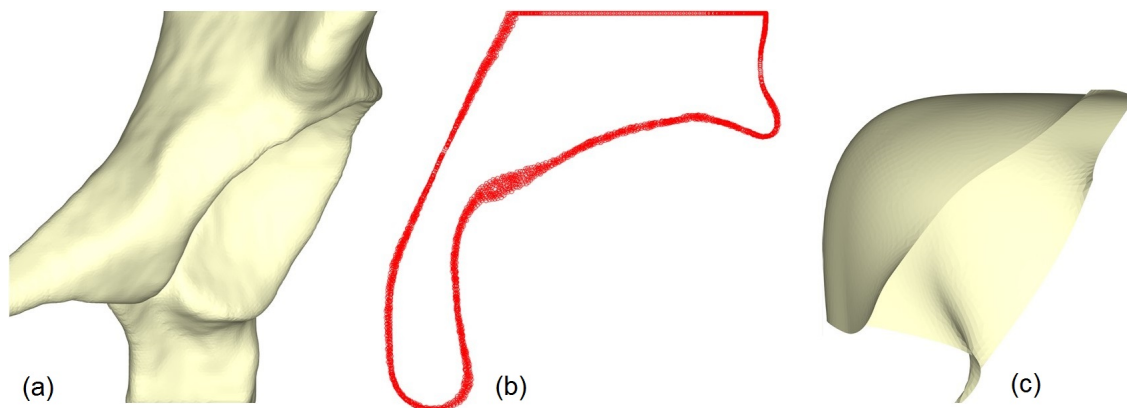


Figure 3.11: Views in MATLAB:

(a) Segmented pelvis;

(b) Nodes in a coronal slice of the pelvis;

(c) Parametric surface representing acetabular cavity after lofting through splines fitted to a selection of coronal slices.

Preliminary surfaces resulting from this method had relatively high fitting errors (> 2 mm). The splines were fitted to nodes in 2D slices in fixed coronal planes, meaning the full 3D shape was poorly captured. Furthermore, the shape of the fossa was not captured in the resulting 3D surface, so a fossa region was manually created within Abaqus using a cutting procedure with another 3D part. Because significant manual intervention was required and the surfaces produced were suboptimal, this method led to the development of an improved method, incorporating 3D splines to more closely match the surface.

3.7.1.2 Improving the method

In order to generate splines more closely matching the segmented surfaces, points were selected manually on the 3D segmented surfaces within Abaqus (Figure 3.12). Thus the selected points were not restricted to lie in a single coronal slice and the resulting splines were defined in three-dimensional space. 3D spline curves were generated as geometric parts within Abaqus passing through the selected points on the segmented acetabulum. These parts were merged and parametric acetabular surfaces were generated by lofting through the five spline curves.

This method was initially tested using 5 nodes per spline, but redistributing these nodes such that the splines had 5, 6, 3, 6, 5 nodes respectively meant it was possible to more accurately depict the shape of the articular surface (Figure 3.12). More specifically, splines fitted to the outer edges of the lunate surface had 5 nodes each and splines fitted to inner edges of lunate surface adjacent to fossa had 6 nodes each. The central spline represented the superior portion of the acetabular cavity and required fewer nodes, consisting of only 3. The additional nodes on the inner edges allowed the shape of the cavity to be represented without requiring an abrupt change in spline position between the inner edge splines and the central spline. This meant shape of the lunate surface could be more accurately represented following the lofting procedure.

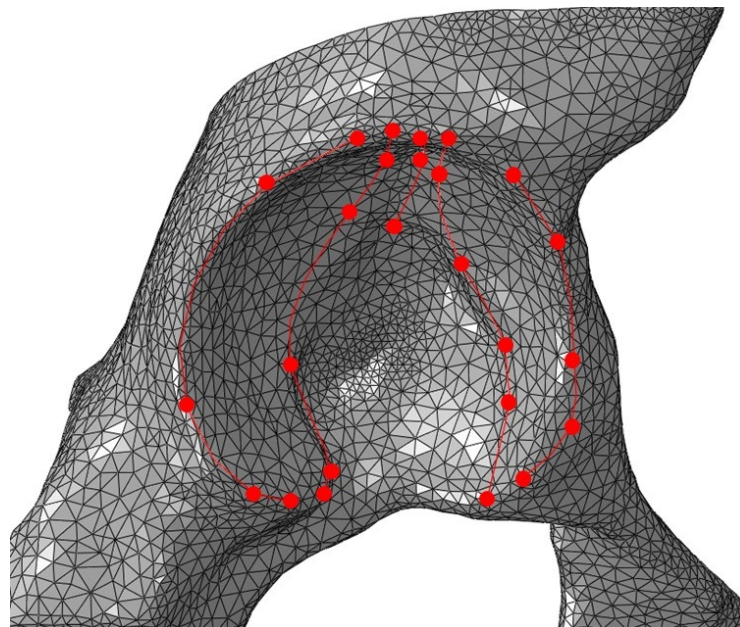


Figure 3.12: Selection of nodes (red) on a segmented acetabulum within Abaqus. Splines were fitted through the selected nodes. A loft through these splines produced a parametric surface representing the acetabular cavity.

Defining the inferior node on the central spline was initially problematic since its location

was required to coincide with the top of the fossa, but it was also required to be located sufficiently far down to avoid the generation of very thin sections at the outer edges of the fossa that could not be effectively meshed. Finding a balance between these often lead to a bump in the back of the surface so that central sections faced laterally instead of inferiorly, meaning the lofting transition was not smooth and the fitting error was poor. This issue was addressed by partitioning the inner edge splines to vary the length involved in the lofting operation, thus defining a further parameter (in addition to the 25 nodes). This parameter defined the position of the partition as a percentage down the inner edge splines to generate the partition. This parameter did not affect the severity measurements on the acetabulum which will be defined in Chapter 4, but was included to allow for optimisation of surface smoothness. This was desired when aiming to develop FE models with these surface, although as explained in Chapter 5, this aspect was not used in the final FE models in Chapter 6. It would also be possible to change the position of this partition on each side to represent the fossa more accurately at the expense of adding further parameters defining where each partition should be made.

A MATLAB script was developed to automatically isolate nodes within a specified distance of each of the manually selected nodes used to define the splines. This was used to test different combinations of nodes in order to optimise the fit between the parametric and segmented surfaces. However, denoting x as the number of nodes nearby a given selected node, and y as the number of nodes to select, there are $y!x^y$ possible combinations. The very large number of combinations to test meant that optimising the fit in this way was impractically time consuming.

3.7.2 Final acetabular parameterisation method

Parametric acetabular surfaces were generated by lofting through five 3D spline curves fitted to between three and six points on the segmented acetabulum (Figure 3.13a), manually selected within Abaqus to capture the lunate surface (Figure 3.13b). Each parametric lunate surface (Figure 3.13c) was generated from a total of 25 nodes selected from the segmented surface, on the outer edges of the acetabulum, the inner edges of the lunate surface, and the superior middle portion of the acetabular cavity.

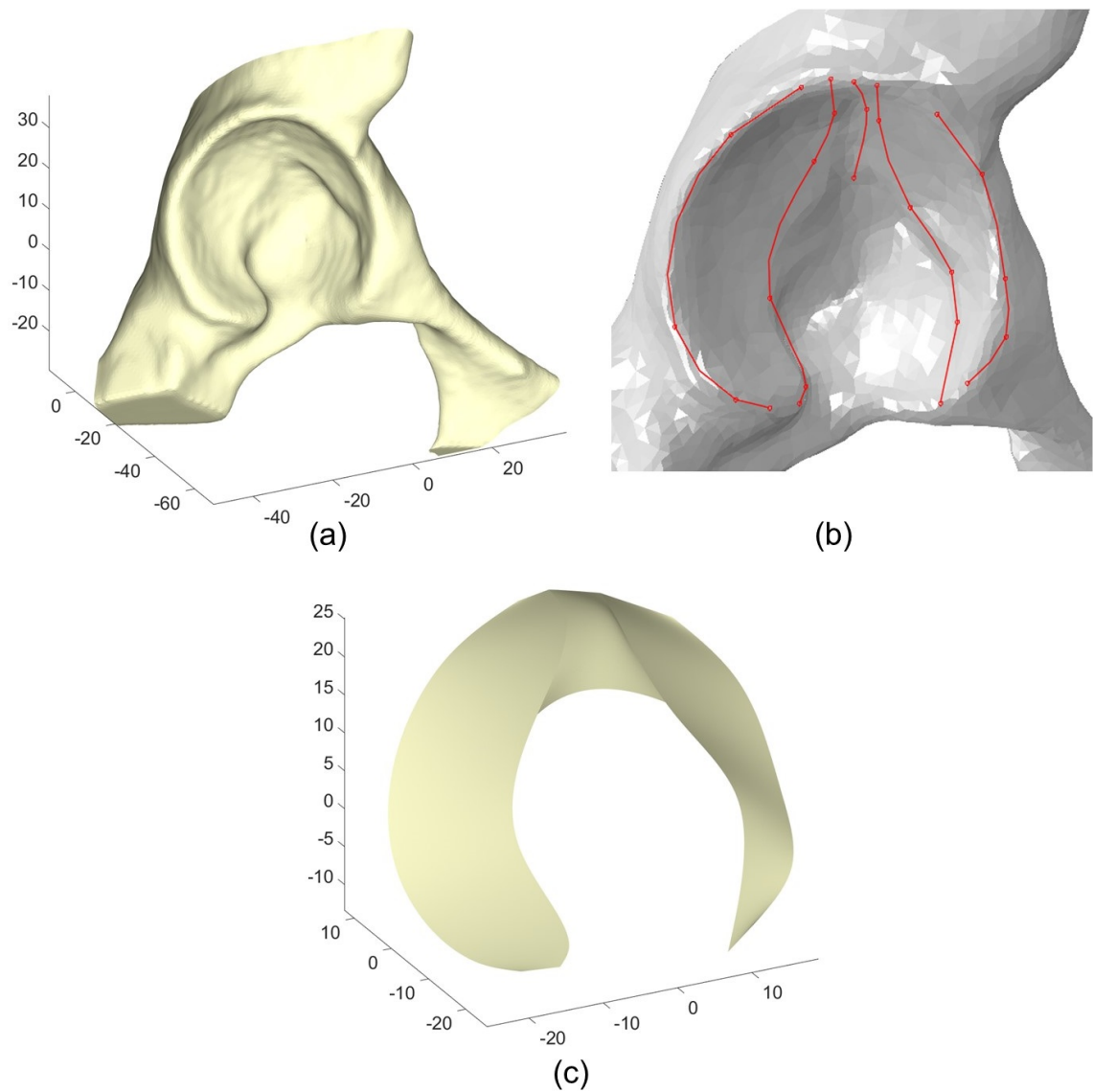


Figure 3.13:

(a) Pelvic surface segmented from CT scan (axes in mm).

(b) Splines fitted to selected nodes on the triangulated surface to capture the lunate surface geometry.

(c) Parametric acetabular surface generated by lofting through the splines (axes in mm).

3.8 Discussion

Although alpha angles remain the most widely used parameter to quantify differences in femoral morphology, there is a recent shift towards conducting clinical research investigating FAI in three-dimensions (Section 2.7.2). Harris et al. (2013) for example generated statistical shape models of hips with and without cams and found noticeable differences between the groups at the anterolateral head-neck junction. Modes describing variance

between statistical shape models do not have obvious physical meanings, making the generation of particular morphological changes related to abnormalities challenging. Another example is Bouma et al. (2015), who defined the “omega surface” as the region of impingement-free motion based on vectors derived from alpha angles and acetabular coverage angles. However this was tested on only five patients and still used alpha angles.

The aim of the work in this chapter was to develop a method of geometric parameterisation to capture three-dimensional geometry of the proximal femur and the acetabulum within a small set of parameters. This was achieved using lofting through shapes fitted to regions of the bones; ellipses through the femoral neck and splines on the acetabular rim.

3.8.1 Femoral surfaces

Fitting errors obtained using the ellipse-based method were appreciably lower than those obtained using the initial parameterisation method for every femur, and visually the ellipse-based parameterised surfaces better matched the segmented surfaces (Figure 3.10). This was particularly noticeable in the cam regions.

In the initial parameterisation system, the femoral neck was symmetrical except for the added cam region, meaning the centres of circles fitted to neck slices were ignored. Because of the extra information provided by the ellipse opposed to just a circle, there was no need to separately parameterise the cam, and the centre of the fitted ellipses varied through the neck, allowing a much more precise representation of the neck geometry. This was important since excess bone likely constituting cam deformities were often observed to be spread over large areas of the neck.

The anatomical meaning of the parameters used in the initial system are straightforward to interpret. With the ellipse-based system, the surface shape is better described at the expense of the ability to deduce the anatomical meaning of each parameter directly from its value. However it is still possible to consider the parameters in terms of their anatomical meaning since different ellipse angles, centres, and radii result in more bone in well defined regions. For example, different parameters would result from an anterior cam and a more superior, pistol-grip cam; even if the radii were the same, the rotations of the ellipses would be different. Chapter 4 provides details of how impingement severity ratings were derived from the ellipse parameters.

Overall the initial parameterisation method did not work well in comparison to ellipse-based parameterisation method (mean fitting errors of 1.33 mm and 0.79 mm respectively). The ellipse-based system was therefore chosen to be applied to more patients in

order to assess impingement risk based on 3D bone shape (Chapter 4) and used to create parameterised femoral surfaces for use in FE models (Chapters 5 and 6).

3.8.2 Acetabular surfaces

Initial methods to generate the acetabulum using 2D splines produced suboptimal surfaces, but once the methods using 3D splines were refined, the acetabular surface could be captured with relatively low fitting errors; details of these are provided in Chapter 4. The parameter values are simply the coordinates that each spline pass through, so their anatomical meaning can be interpreted as the positions of given boundaries on the acetabular cavity.

Although semi-automated, it should be noted that the subject-specific parameterised acetabular surface generation required more manual intervention than the femoral parameterisation method in the form of selection of nodes on the acetabulum to obtain an optimum fit, necessary because subject-specific irregularities in acetabular rim could not be readily estimated as standard shapes akin to ellipses on femoral neck slices. However, rapid automatic generation of acetabula with different shapes was possible by editing the coordinates of any given node.

The final acetabular surfaces were subsequently used in Chapter 4 to assess shape characteristics of the acetabulum in 20 patients. These surfaces were trialled in finite element model development covered in Chapter 5, but the final models generated in Chapter 6 used generic acetabular geometry to avoid convergence problems and allow rapid generation of acetabular soft tissues, which, as discussed in Section 5.3 was problematic on these surfaces.

3.8.3 Conclusion

The parameterisation system developed here allows morphological variation in hip bones to be described in terms of the defined parameters. The automatic method of generating parametric surfaces provides the ability to represent the large variation in hip morphology (Harris et al., 2012) across populations, allowing rapid surface generation with controllable, meaningful geometric parameterisation. Changes to individual parameters can be used to represent precisely defined, clinically relevant morphological differences. This made parametric surfaces suitable for use in finite element models to assess the effects of morphological changes on contact mechanics, providing potential to further investi-

gate impingement damage mechanisms; this is covered in Chapters 5 (which included development of soft tissue representations) and 6. First, in Chapter 4, a novel method of defining severity measures using the parameterisation systems developed here is presented.

Chapter 4

Parameterisation Study

4.1 Introduction

The risk of symptomatic impingement occurring in the hip joint is likely to depend on differences in natural soft tissue shape and quality, the activities performed by individuals, and, as focused on in this work, the position and shape of bone abnormalities (Khanna et al., 2014). Assessment of tissue abnormalities can be challenging, even in the case of radiographs for the analysis of bone, where the projected outline of the structures is relatively clear. Measurements from two-dimensional (2D) radiographs are commonly used in the diagnosis of FAI (Tannast et al., 2007; Banerjee and Mclean, 2011; Weinberg et al., 2016) (Section 2.5). In particular, recall that alpha angles were first described by Nötzli et al. (2002) to assess the size of cam deformities (excess bone on the femoral neck), whilst centre edge (CE) and anteversion (AV) angles are used to identify acetabular abnormalities such as pincer impingement (acetabular overcoverage) and dysplasia (undercoverage) (Ergen et al., 2014). However, such 2D measurements do not capture the full 3D geometry of the hip (Harris et al., 2014). The alpha angle is limited to providing a rough indication of the cam size in a single 2D view (Harris et al., 2014; Laborie et al., 2014), there is variation in alpha angle measuring techniques (deSa et al., 2014), and high alpha angles have been found in asymptomatic individuals (Omoumi et al., 2014). It is therefore not a reliable measurement to use to stratify the population by cam type.

The parameters described in Chapter 3 generate the geometry for parametric bone surfaces, but the anatomical interpretation of these parameters depends on their relationships to each other. In this chapter, new measurements were automatically derived from the geometrical parameters to indicate the risk of impingement based on 3D hip bone geometry.

In addition to the original 10 patients included in Chapter 3, a further 10 patients from the clinical dataset were included (Section 1.2), meaning a total of 20 patients were used in this part of the study. Clinical measurements of the same 20 hips were taken in 2D for comparison. An additional 18 control femurs were included to assess the the ability of the 3D measures to detect cam morphology.

The objectives of the work in this chapter were therefore to use the novel methods for generating parametric surfaces developed in Chapter 3 to develop and test 3D severity measures of cam deformity of the hip joint, and to further verify the parameterisation systems against 2D measurements of the patients' hips. A successful methodology was considered to be one precise enough to provide stratification of the population of subjects with cams, which was tested by analysing the difference between males and females. The specific aims of the work in this chapter were to:

1. Apply the parameterisation method across a larger clinical data set, allowing measurements assessing impingement risk to be obtained, and assess morphological differences between male and female hips diagnosed with cam type impingement.
2. Verify the ability of the femoral parameters to capture cam deformities by comparing with non-cam cases.
3. Verify the parameterisation system using shape fitting error assessment between segmented and parametric bone surfaces.
4. Compare 3D measures from the parameterisation system with clinical, 2D radiographic measures.

4.1.1 Overview of study methodology

Bone surfaces (the proximal femur including the cam deformity, and the lunate surface of the acetabulum) for each of the 20 hips (10 females and 10 males) were segmented from the patient CT scans using ScanIP as described in Section 3.3. Parametric versions of these bone surfaces were then generated using the methods detailed in Chapter 3. In order to assess potential for impingement based on morphology, on the femoral side, cam severity measurements were derived from the parameters describing the geometry (Section 4.2), and similarly on the acetabular side, angles were calculated from the spline data (Section 4.3). To verify the ability of parametric surfaces to represent segmented geometry, fitting errors were calculated between segmented and parametric triangulated surfaces at different mesh densities (Section 4.4). Two-dimensional clinical measurements of the same hips were taken from reconstructed radiographs, created by taking averages of CT slices in certain views, in order to provide further confidence in the 3D measurements and

understand the additional information they provide (Section 4.5).

4.2 Cam severity measurements

The femoral parameterisation process is based on fitting ellipses to slices of the femoral neck (Section 3.4.2). Measurements were defined to describe the size and position of the cam in order to isolate the region with potential to cause impingement. These were referred to as cam severity measurements. In this context, the term severity is used to highlight the possible potential for joint damage caused by differences in positions and sizes of cams. This is distinct from impingement severity as indicated by cartilage and labrum strains observed in finite element model results in later chapters, and also distinct from impingement severity as it may be assessed clinically in terms of patient pain.

Recall that 2 mm slices were defined from the top of the head to the end of the modelled neck axis (fixed to be equal to the head radius) for each femur, and on a selection of these slices, ellipses were fitted and the parametric surfaces generated through a lofting procedure (Figure 3.7). For each ellipse the following were defined (Figure 4.1):

- Cam-rad is the greatest planar distance between the head centre and the anterior half of the fitted ellipse, recorded as a percentage of the head radius. This indicates the level of offset between the head and neck in the cam region.
- Cam-angle describes the position of the point on the ellipse where cam-rad is defined (i.e. where the head-neck offset is lowest). A zero angle represents an anteriorly centred cam, and greater angles indicate a more superior position.
- Cam-width is the percentage of the neck circumference whose distance from the head centre is greater than 90% of the distance defined by cam-rad. Cam-width therefore indicates the extent to which the circumference of the neck is affected by the cam. The position along the neck where the ellipses were fitted is known from the geometrical parameters.

The average of these measurements on the ellipses fitted to the two central loft slices were recorded as the overall cam-rad, cam-angle and cam-width respectively.

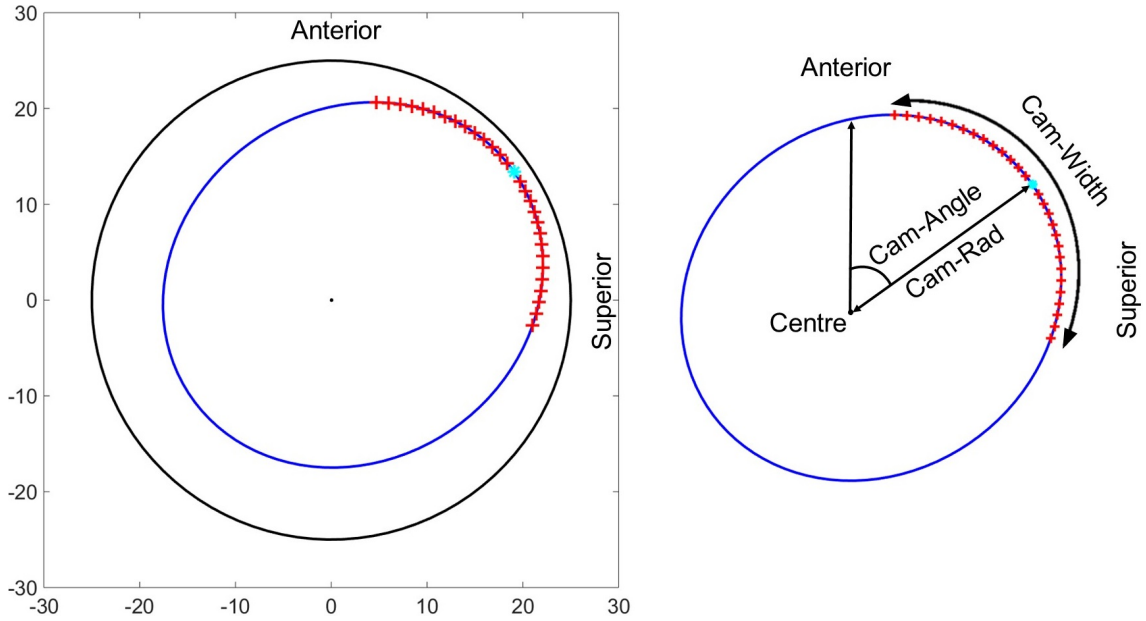


Figure 4.1: Cam impingement severity measures shown on a fitted ellipse (blue). The black circle represents the spherical portion of the femoral head. The cyan star is where the ellipse is nearest to the head; this defines cam-rad and its position defines the point where cam-angle is measured. Cam-width is represented by red crosses.

The cam severity measurements were automatically derived from the geometric parameters describing each femur using a MATLAB script. The severity measurements provide an overall indication of the cam shape, and the NL parameters (Section 3.4.2) indicate the position along the neck where these cam measurements were made. Cam-rad was always defined in the anterior half of each slice, since proximity between the posterior neck and head was not relevant to impingement caused by flexion. Whilst the NA parameter giving the tilt of the ellipse describes the geometry, it is not necessarily helpful for understanding the position of the cam since variation in the centre of the ellipse means there is no requirement for the major axis of the ellipse to coincide with cam-rad. Thus cam-angle provides the position of the cam with respect to the vertical line in the plane (assumed to point anteriorly). Notice also that there is not a bijection between the geometric parameters and resulting cam severity measurements; it is possible for example for the same cam-rad to occur for ellipses with different radii due to their centre position and rotation angle.

4.2.1 Comparison to control femurs

In order to assess the ability of the cam severity measurements to distinguish between patients diagnosed with cams and those without, the femoral parameterisation process

was also tested on an additional 18 control femurs (10 females and 8 males). Femoral bones from these patients were segmented and processed with the same methods used for the main patient group.

4.2.2 Sensitivity to neck-axis

Because severity measurements required the assumption that scans were taken with patients in standard anatomical position, this assumption was checked prior to aligning the neck axis of the segmented femurs to the vertical image axis. In cases where there was clear external rotation visible in the axial CT view, this was corrected by performing an initial rotation of 20° about the axial axis passing through the centre of the head. This value was chosen for consistency (that is, no rotation or a rotation of 20°) because although external rotation was visible, the abnormal morphology meant accurately aligning each femur was challenging. This was necessary in three of the cam patient femurs and one of the control femurs, where the rotations were likely due to the subjects moving from neutral position in the scanner. Following this the rotation of 40° was performed to align the femurs to their neck axis (Section 3.4.2) (Figure 4.2).

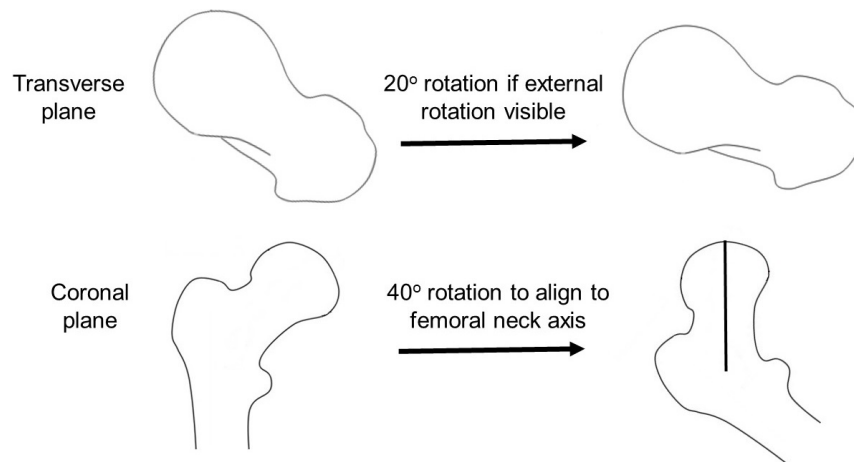


Figure 4.2: Rotations to align femurs to their neck axis.

The neck axis was assumed to be at 40° to the superior-inferior axis for all femurs since it was not possible to measure the femoral neck shaft angle given the field of view in the scans, and defining the neck axis for each femur presented a significant challenge because of the abnormal morphology resulting from the cam deformities. The value of 40° was therefore chosen to automate the process as it appeared in all cases to orientate the neck axis approximately vertically. In order to assess the sensitivity of the cam severity measurements to the value of 40° chosen to align the femurs to the neck axis, the cam-rad measurements were repeated with this angle increased by 25% to 50° .

4.3 Acetabular angle measurements

The acetabular parameterisation process is based on splines on the acetabular surface (Section 3.7.2). Recall that each parametric lunate surface was generated from splines fitted to nodes selected on the segmented surface (Figure 3.13). Two clinically relevant angles, anteversion (AV) angle and centre edge (CE) angle, were extracted from the three dimensional spline data representing the acetabula.

Five AV angles were calculated in the transverse plane as the acute angle between AP-axis and the line between the most anterior and posterior points on the acetabular rim (Figure 4.3). The most anterior and posterior points on the rim were captured by the nodes lying on the two outermost splines. AV angle measurements were taken at different positions along the superior-inferior axis corresponding to the five different nodes defining the outer splines. The AV angles varied according to the height on the superior-inferior axis at which they were measured (Figure 4.4). The mean AV angle from these five measurements was taken as the overall 3D measured AV angle, quantifying the amount by which the acetabulum as a whole was anteverted.

AV angle calculated from points in transverse plane of pelvis

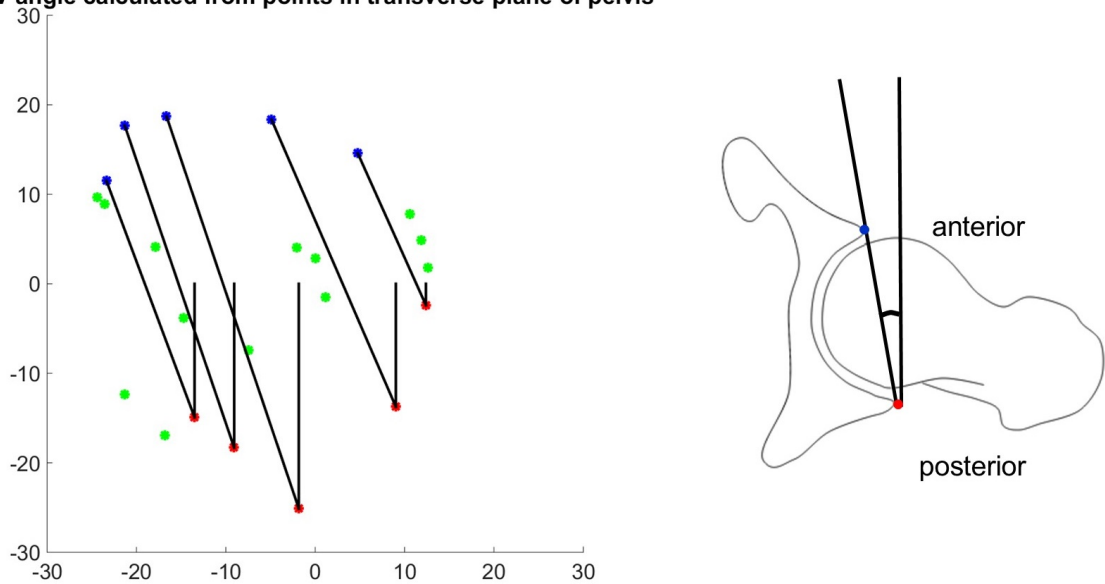


Figure 4.3: AV angle measurements in the transverse plane (axes are given in mm): the angle between the vertical anteroposterior line, and the line passing through the anterior and posterior edges of the acetabulum. Here these edges are corresponding points on the outer two splines (red and blue points). Green dots represent the points on the other splines.

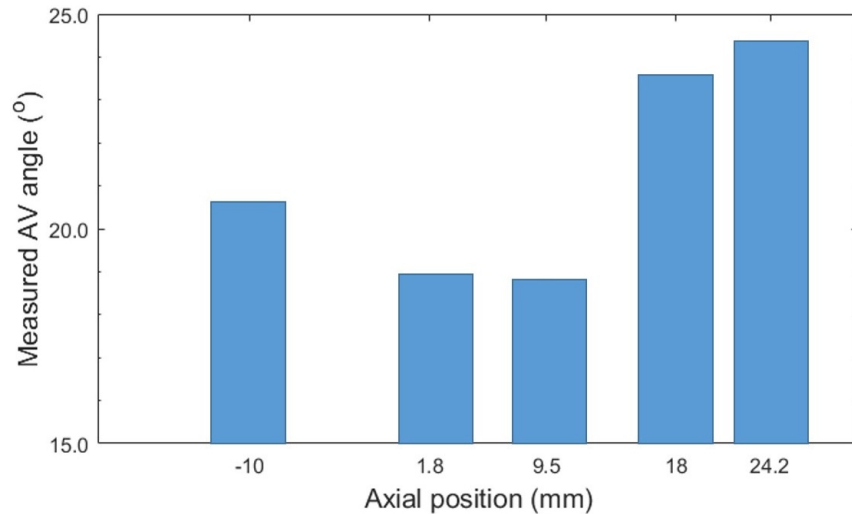


Figure 4.4: Example bar graph with acetabular AV angles plotted against the position they were measured at on the superior-inferior axis (taken as the mean of the superior-inferior positions of the two nodes used for the measurement), demonstrating that different angles were measured at different height positions. A value of zero on the superior-inferior (axial) line corresponds to the axial position of the femoral head centre, and greater values are more superior.

Five CE angles were calculated in the coronal plane as the angle between the vertical line passing through the femoral head centre, and the line joining the head centre and the edge of the acetabulum (Figure 4.5). The most superior node on each spline represented the top edge of the acetabulum. By taking the measurement for each spline, five measurements were obtained at different positions along the anterior-posterior axis. The maximum CE angle from these five measurements was taken as the overall 3D measured CE angle, quantifying the most severe overcoverage in the acetabulum.

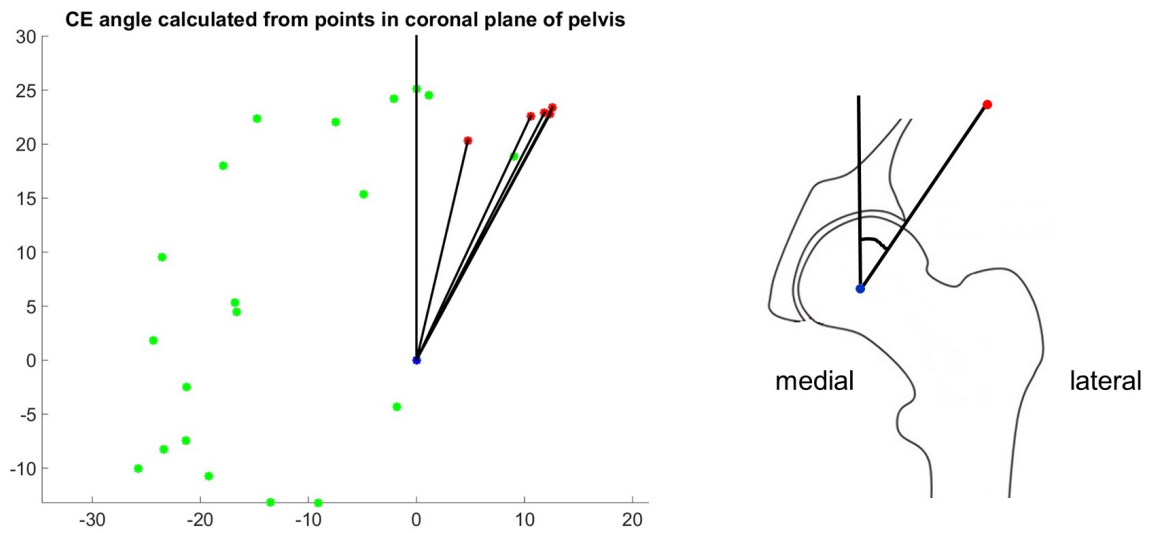


Figure 4.5: CE angle measurements in the coronal plane (axes are given in mm): the angle between the vertical line passing through the head centre, and the line passing through the head centre and the most superior point (red) on each spline. Green dots represent the other points on the splines.

4.4 Mesh optimisation and fitting error calculations

Fitting errors were calculated in MATLAB from the triangulated surfaces as the root mean squared distance that nodes on the segmented surface in the region of interest had to move to conform to the nearest node on the parametric surface (Section 3.5.2).

Fitting errors between triangulated surfaces are higher when coarse surface meshes are used because the distance from each node on a segmented surface to the nearest node on the equivalent parametric surface may be higher than the true distance between the surfaces at that point. Therefore the mesh densities of both the parametric and segmented surfaces were iteratively increased until the fitting errors converged so that the final fitting errors (and extracted parameters) were limited by the resolution of the original CT scans rather than the mesh density. Mesh densities were increased on the segmented surfaces using mesh settings in ScanIP, and on the parametric surfaces using the meshing options in Abaqus before exporting the STL data into MATLAB.

In order to obtain the baseline fitting error, i.e. the best fitting error that could be achieved using this method at the specified CT resolution, a sphere was created in the +CAD module of ScanIP and resampled to the CT scan voxel resolution of $0.7422 \times 0.7422 \times 1$ mm. The femoral parameterisation procedure was then applied to this triangulated sphere.

4.5 Two-dimensional measurements

For each of the 20 patients, three reconstructed radiographic views (axial, coronal and cross-table lateral) were generated by using ScanIP to rotate the CT slices where necessary and then ImageJ to average the slices of interest to create a simulation of a radiographic view. ScanIP was used for the rotations so that the non-cubic CT voxel size was accounted for, ensuring the images remained correctly scaled. This process used a fixed protocol and was not subject to inter-user variation.

An axial view was created by averaging the transverse CT slices that included the acetabula. The AV angle was measured in this view as the angle between the line perpendicular to the line joining the posterior edges of the acetabula on both sides (i.e. the anterior-posterior axis) and the line joining the anterior and posterior edges of the acetabulum (Figure 4.6a).

A coronal view was created by rotating transverse slices into the correct orientation and averaging the slices including the relevant femur. Both femurs were included in these images in order to verify that the vertical axis represented an inferior-superior axis. The CE angle was measured in this view as the angle between the vertical line through femoral head centre and the line passing through the femoral head centre and the top edge of acetabulum (Figure 4.6b).

A cross-table lateral view was created by rotating the femur 15° internally and by a 45° angle from the sagittal plane, and averaging CT slices with a view of the medial side of the femur. This was based on the assumed anatomical position of patient scans and the view was chosen to measure alpha angles because it is a standard radiograph and can be readily simulated by rotating CT slices to obtain an image similar in appearance to actual radiographs. Additionally, it has been reported that alpha angles measured in this view correlated well with 3D measured asphericity (Harris et al., 2014). The alpha angle was measured as the angle between the line passing through the femoral neck midpoint and the femoral head centre, and the line from the femoral head centre to the anterior point where the femoral head diverges from spherical (Figure 4.6c). Alpha angles were also measured on the original CT data with oblique axial reconstructions and measurement of the alpha angle at the mid-point image (Figure 4.6d) (Nötzli et al., 2002; Pfirrmann et al., 2006; Mast et al., 2011).

OsiriX was used to take 2D measurements of alpha angles, AV angles and CE angles from the reconstructed radiographs for each patient. This software was chosen as it is used clinically. Since the measuring of these angles was not an automated process, the

images were sent to a consultant radiologist (PR) to perform the measurements for the main results, providing greater credibility for publication. To investigate user variation in reading the angles from the reconstructed radiographs, where outer bone limits can be difficult to assess, the acetabular angle measurements were repeated by three users (RJC, MM, ACJ) and the alpha angle measurements were repeated by two users (RJC, MM).

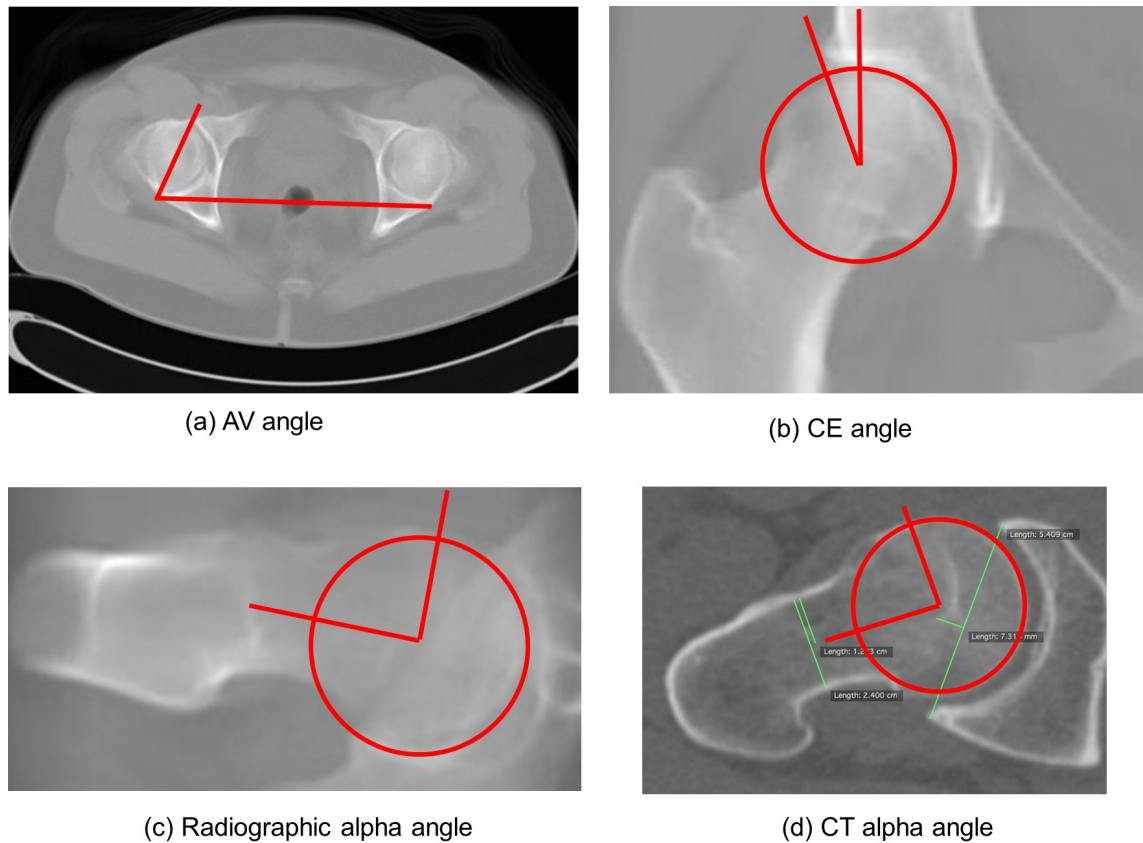


Figure 4.6: Examples of 2D measurements performed on radiographs in OsiriX:

- (a) AV angle on a reconstructed axial view radiograph.
- (b) CE angle on a reconstructed coronal view radiograph.
- (c) Alpha angle on a reconstructed cross-table lateral view radiograph.
- (d) Alpha angle on an oblique axial CT slice.

4.6 Statistics

Pearson's correlation coefficients (r) and linear regressions were calculated between the 3D severity measurements and the 2D measurements, and also between the two alpha angle measurements. Correlation between was also assessed between cam-rad measurements at different neck alignments to test whether the neck alignment assumption affected the relative severity of each cam. Independent samples t-tests were performed to test for differences in the potential impingement severity measurements between males and fe-

males (the data were first checked for normality). Independent samples t-tests were also used to test for differences in the femoral severity parameters between the patient and control femurs (the data were again first checked for normality). All statistics were calculated using the Statistics and Machine Learning Toolbox in MATLAB.

4.7 Results

The full raw data for this study are included in Appendix B (Tables A1, A2, A3 and A4).

4.7.1 Severity measurement results

4.7.1.1 Comparison of females and males

A wide range of values for the cam severity measurements was found (Table 4.1). In particular, a statistically significant difference ($P = 0.0011$) was identified showing that the average cam-angle was higher in male cam patients (mean 40.5°) than female cam patients (mean 16.5°) (Figure 4.7). The 95% confidence interval for the difference in means between these groups was ($11.1^\circ, 36.9^\circ$). None of the other cam severity measures and neither of the acetabular angles showed a significant difference between males and females. The identified difference in cam-angle between males and females was not present in the control femurs (t-test $P = 0.1$).

Table 4.1: Range of femoral severity measurements obtained from parameterised surfaces representing the 20 cam and 18 control femurs.

		Cam Patient Femurs			Control Femurs		
		Combined	Females	Males	Combined	Females	Males
Cam-rad (%)	Range	86.1- 100.4	86.1- 99.6	89.3-100.4	79.2- 93.9	85.1- 91.1	79.2- 93.9
	Mean \pm SD	93.9 \pm 4.4	92.7 \pm 4.8	95.0 \pm 4.0	89.3 \pm 3.4	89.1 \pm 2.3	89.5 \pm 4.6
Cam-angle ($^\circ$)	Range	4.0- 65.5	4.0- 34.7	21.2- 65.5	2.9- 50.8	2.9- 35.7	5.1- 50.8
	Mean \pm SD	28.5 \pm 18.2	16.5 \pm 11.5	40.5 \pm 15.7	19.8 \pm 12.5	15.3 \pm 10.1	25.3 \pm 13.6
Cam-width (%)	Range	28.0- 67.0	28.0- 67.0	30.5- 60.5	29.5- 100	35.5- 100	29.5- 70.5
	Mean \pm SD	47.1 \pm 13.4	44.7 \pm 14.1	49.5 \pm 13.0	56.4 \pm 20.9	61.7 \pm 24.9	49.7 \pm 13.2

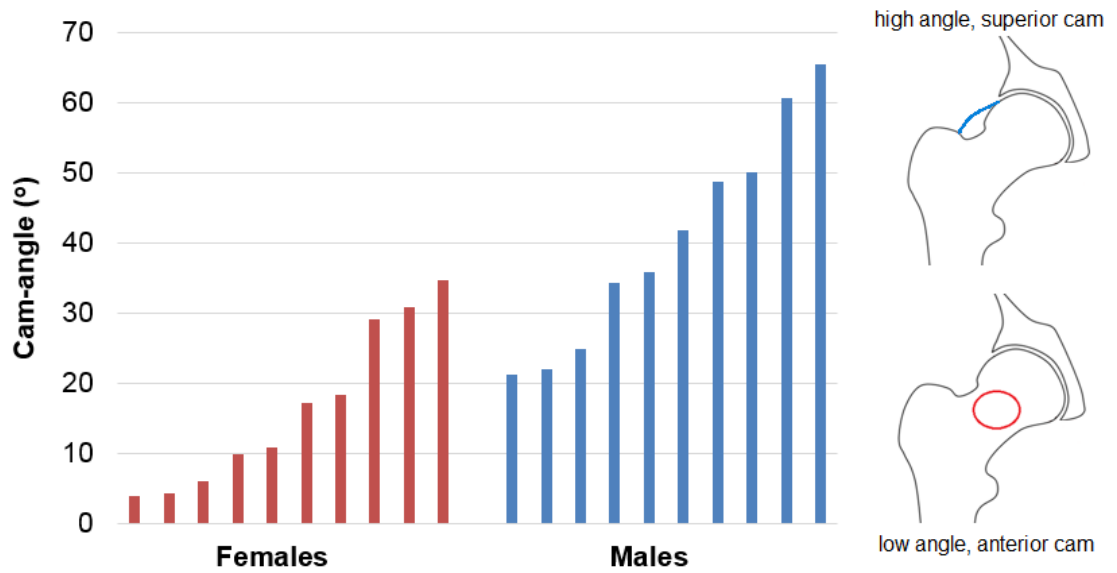


Figure 4.7: Comparison of cam position in females and males. Cams with a high cam angle are located more superiorly on the neck, shown in the femur diagrams.

4.7.1.2 Comparison of controls and cam patients

A statistically significant difference ($P = 0.0014$) was identified showing the average cam-rad was higher in the cam patient group than in the control group, and this was true for both the male and female groups as well as overall (Figure 4.8). The differences remained significant when outlying cases were removed. No significant difference was identified between the patient and control femurs for the other parameters.

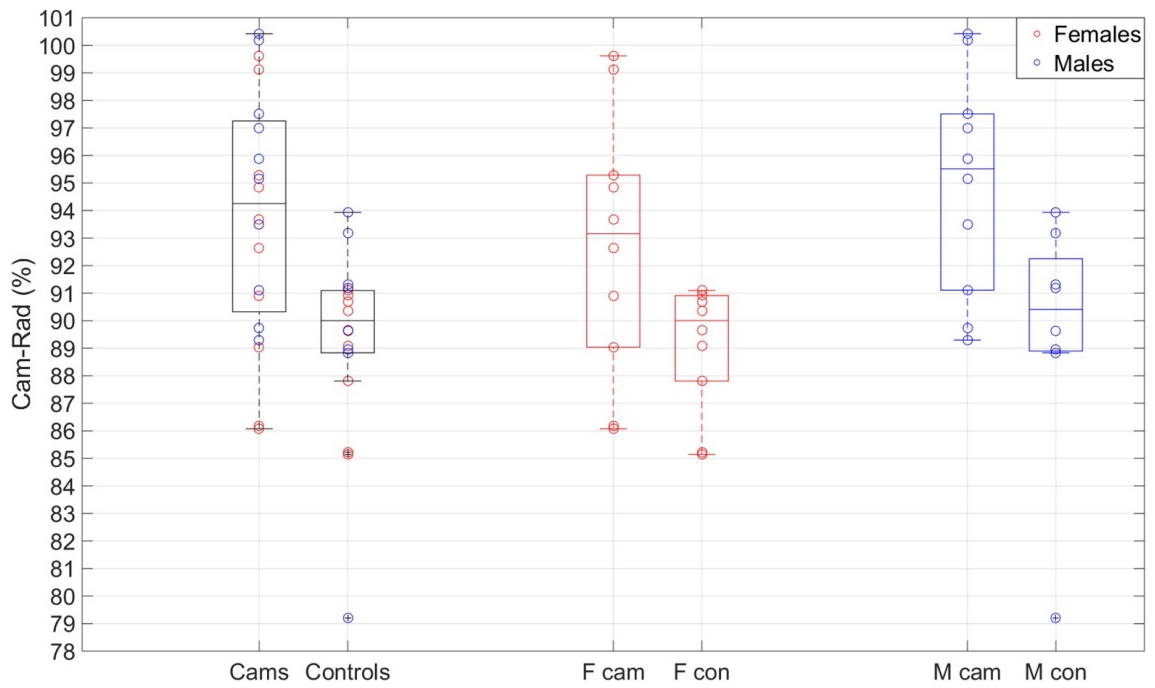


Figure 4.8: Box and dot plot showing all of the cam-rad measurements in the cam patient and control groups, in order to aid visualisation of the statistical significance of the differences between the control and cam groups, both overall and in female and male groups separately.

4.7.1.3 Sensitivity to femoral neck axis

Cam-rad measurements when the rotation applied to align femurs to their neck axis was adjusted were highly correlated with the original results (Figure 4.9). The mean absolute difference was 1.75%.

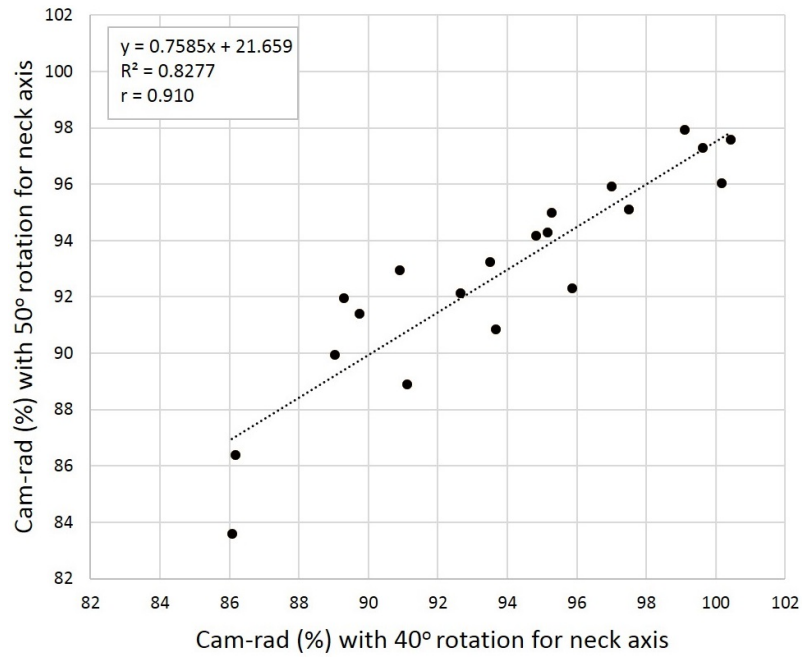


Figure 4.9: Strong correlation was found between cam-rad values measured at different neck angles.

4.7.2 Mesh optimisation and fitting error results

Fitting errors between the segmented and parametric surfaces converged when mesh densities were such that nodes on each surface were spaced at distances of around 0.25 – 0.3 mm. The iterative procedure used to determine this is shown for Hip 01R in Table 4.2. Note this is a higher mesh density than that used when reporting preliminary fitting errors used to compare parameterisation systems in Chapter 3.

Table 4.2: Example of fitting error convergence; results for Hip 01R. As well as fitting errors and their change over each iteration, software input parameters for generating the meshes on segmented and parametric surfaces (in ScanIP and Abaqus respectively) are shown, along with the mean distances between nodes on each of the resulting meshes.

Iteration number	Parameter used to generate surface mesh		Mean distance between nodes on meshed surface		Fitting error (mm)	Change in fitting error over iteration (mm)
	ScanIP mesh coarseness (segmented surface)	Abaqus mesh seed (parametric surface)	Segmented surface	Parametric surface		
0	-9	1	0.9194	0.9277	0.7025	
1	1	0.7	0.6548	0.6513	0.6497	-0.0528
2	10	0.6	0.574	0.5592	0.6296	-0.0201
3	25	0.5	0.4562	0.4654	0.6064	-0.0232
4	35	0.4	0.3843	0.3717	0.5964	-0.0100
5	45	0.3	0.2688	0.2791	0.5877	-0.0087

The fitting errors obtained using the final parameterisation systems for all hips are tabulated in Table 4.3.

Table 4.3: Converged fitting error results for femoral and acetabular parametric surfaces, with means and standard deviations indicated.

Hip ID	Sex	Slices	Fitting error Femur (mm)	Fitting error Acetabulum (mm)
01R	F	21	0.5877	0.7430
06R	F	22	0.5988	0.7884
11R	F	21	0.5687	0.8076
16R	F	22	0.6887	0.7129
18R	F	22	0.5590	0.6222
28L	F	20	0.4994	0.7593
33L	F	24	0.6022	0.7770
51L	F	22	0.6243	0.8921
75L	F	22	0.4214	1.2023
81L	F	21	0.6067	0.8446
02R	M	23	0.5322	1.1593
07R	M	25	0.5906	0.7462
09R	M	23	0.5788	0.8704
17L	M	25	0.5980	1.0407
22R	M	23	0.4420	0.5575
27R	M	25	0.5081	0.8302
34L	M	24	0.5040	0.9370
38L	M	24	0.6333	0.8734
53L	M	26	0.6692	0.8664
79L	M	25	0.6736	0.9897
		Mean ± Std Dev	0.57 ± 0.0704	0.85 ± 0.1556

The fitting error between the resampled sphere and the parametric sphere was 0.22 mm, representing the best fit that could be obtained with the femoral parameterisation procedure using the CT scan resolution and converged mesh density (Figure 4.10). Parametric bone surfaces were overall a good fit to the segmented surfaces, with an average error of 0.57 mm for femoral surfaces and 0.85 mm for the acetabular surfaces. The range found for the head radius measurement was 19.65 – 25.52 mm, so the error was much smaller than the magnitude of differences detected between subjects.

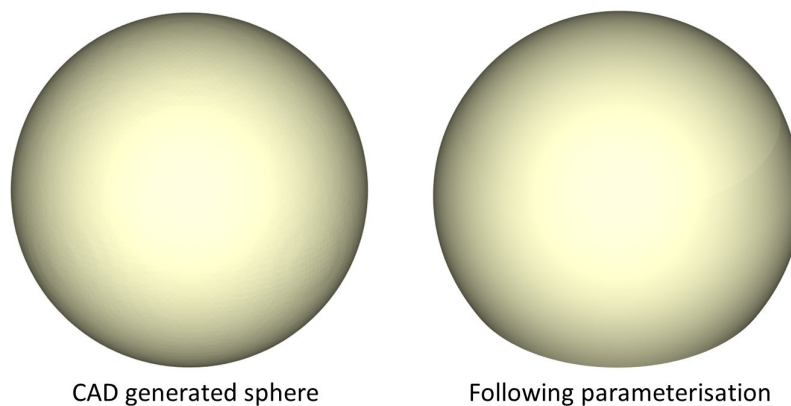


Figure 4.10: Applying the femoral parameterisation to a sphere of radius 25 mm.

4.7.3 Comparison of 3D and 2D measurements

The two alpha angle measurements on the cam patients were only moderately correlated with each other and both were only moderately correlated with the cam-rad measurements (Figure 4.11). In some cases, similar alpha angles did not translate into similar cam-rad measurements. For example, for Hips 06R and 11R had cross-table alpha angles of 73.3° and 74.8° respectively, but their cam-rad measures were markedly different, at 93.7% and 99.1% respectively.

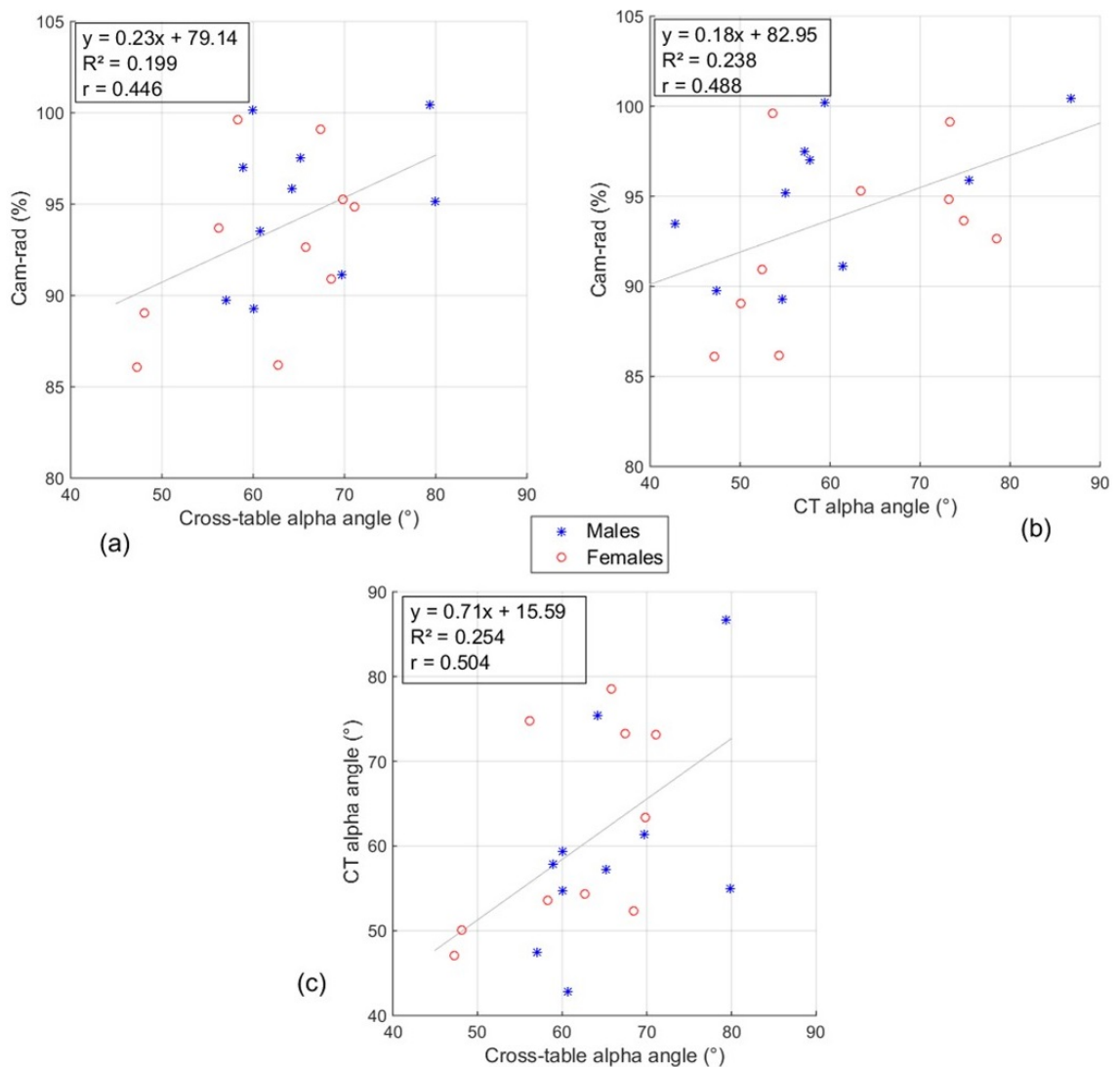


Figure 4.11: Moderate correlation was found between: (a) Cam-rad measurements and the cross-table measured alpha angles; (b) Cam-rad measurements and the CT measured alpha angles; (c) The two methods used to measure alpha angles.

The 2D measured CE and AV angles were well correlated with the 3D measured versions (Figure 4.12).

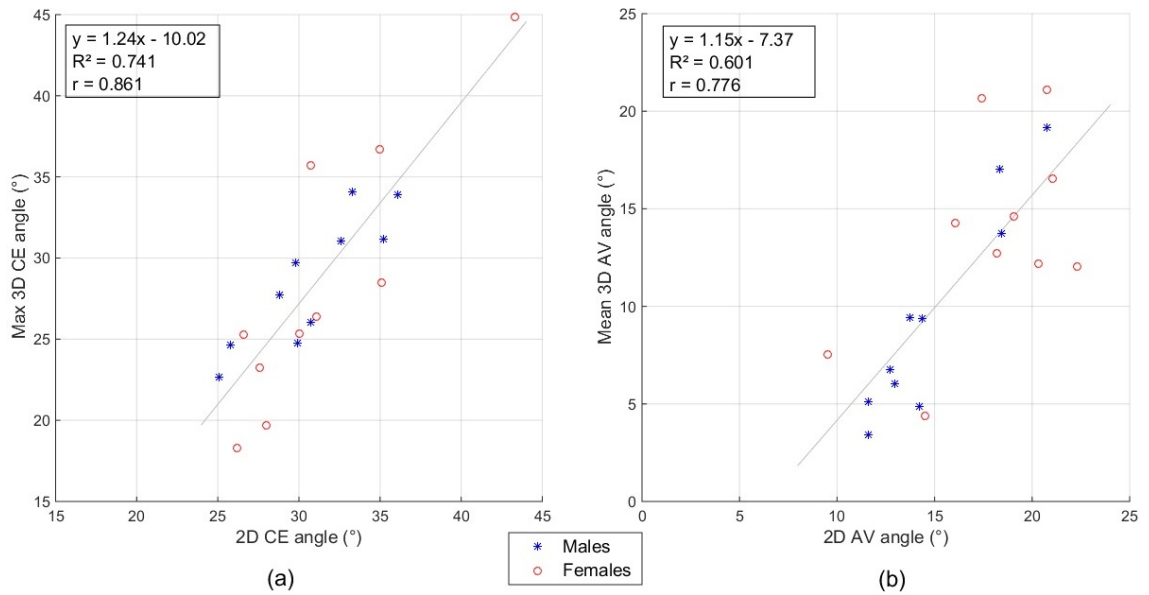


Figure 4.12: Strong correlation was found between: (a) the 2D CE angles and the maximum 3D CE angles; (b) the 2D AV angles and the mean 3D AV angles.

4.7.3.1 Inter-user variation in 2D measurements

All measurements taken by each user are tabulated in Appendix B.

When a further two users in addition to the radiologist measured the alpha angles on the reconstructed radiographs to investigate inter-user variability, the average over all of the femurs of the standard deviation across measurers was 5.59° .

When a further three users in addition to the radiologist measured the CE and AV angles to investigate inter-user variability, the average over all of the hips of the standard deviation across measurers was 1.97° and 1.90° respectively.

4.8 Discussion

The aims of the study in this chapter were to use the geometric parameterisation system developed in Chapter 3 to capture key hip shape variations in 3D, verify these against 2D measurements and to use them to assess for morphological differences in the patient group. The novel 3D measurements obtained from the semi-automatic parameterisation system provided additional information on the shape and position of cams not captured by 2D measurements. This allowed differences between the male and female groups to be identified. Male subjects were more likely to have a superiorly located cam (pistol

grip deformity), whereas cams in female subjects were more likely to be in an anterior position.

Performing the femoral parameterisation process on a sample of control femurs verified its ability to differentiate between femurs diagnosed with cams and those without. Although control femurs do not have cams, the cam-angle parameter still detects the region with smallest head neck offset. The lack of difference in cam-angle between males and females in the control group suggests that the more superior location in males of this region, may be a specific observation of morphological changes related to cam deformity, rather than being true in general. Since cam-width is a measure based on the value of cam-rad, a direct comparison between control and cam groups was less useful. Cam-width was generally higher in the control group simply because the cam-rad values were lower.

The average fitting errors between the parametric and segmented geometries were of a similar magnitude to others reported for articular surfaces of the hip approximated by sphere and conchoids (Anderson et al., 2010) and were smaller than differences between subjects. Good correlation was found between CE and AV angles and the 3D counterparts, providing additional confidence in the 3D representation of acetabular coverage. Comparisons between the 3D cam severity measures and the alpha angle measurements demonstrated the challenges in assessing cam geometry in a two dimensional view (Harris et al., 2014; Laborie et al., 2014) and support the notion that 3D measures are key to understanding morphological factors in impingement risk.

4.8.1 Study significance

4.8.1.1 Difference in male and female cams

Recently, Yanke et al. (2015) reported that cams in female patients present in roughly the same location as in males, but the volume and span of the cam was greater in males, based on analysis of point clouds derived from CT scans of 138 patients (Section 2.5.3). Cam positions have also previously been reported to be anterolateral to anterior in females, compared to lateral to anterior in males (Ito et al., 2001). Cam position was assessed in this study using the greatest radius of the cam with the femur aligned to the neck axis (the cam-angle parameter is defined based on cam-rad, defined by the region with the lowest head-neck offset). This allowed the detection of the more generally superior position of the cam in the male patient group and more anterior position in female patient group. This may have not been detected in earlier studies which reported large variation in span of the cams and used this to describe overall coverage. The difference detected here could be

due to differences in muscle mass and ligament laxity between sexes (Halim et al., 2015), potentially resulting in deformity development in different regions as a result of increased stresses in varying locations. Furthermore, differences in acetabular coverage could also lead to differences in femoral head deformities (Okano and Yamaguchi, 2013), as well as osteophyte formation in different locations when osteoarthritis due to impingement progresses (Siebenrock and Schwab, 2013).

4.8.1.2 Assessment of alpha angle in different radiographic views

The size of a cam (as measured here by cam-rad) cannot be easily predicted from a single radiographic alpha angle. It was seen that multiple subjects with very similar alpha angles had quite different 3D severity measures. Alpha angles are dependent upon the view in which they are measured, which is evident here in the differences between the CT and cross-table alpha angles (Figure 4.11), and has been reported by others (Meyer et al., 2006; Rakhra et al., 2009; Harris et al., 2014). Thus it is possible for the same alpha angle to be recorded for cams of different size and position. In addition to size of the cam in terms of head-neck offset, this study also provides a novel method of quantifying the variation in cam position and extent of neck coverage (captured by the cam-angle and cam-width measurements). Such information cannot be obtained from an alpha angle measurement. Whilst X-rays are taken as standard, not all clinics use CT scans, which expose patients to high levels of radiation, or MRI scans, which can be prone to distortion and are less optimal for viewing bone. However, the risk of impingement in different hip morphologies can be more accurately quantified when 3D imaging of the patient is available and this emphasises limitations of relying on radiographs alone. Radiographically, an AP view shows cams in a superior position more clearly, while the cross-table view is more effective for detecting cams in an anterior position. The differences seen between cam positioning in male subjects (more superior) and female subjects (more anterior) suggest that when only 2D imaging is available, the choice of primary radiographic view could be tailored to sex of the patient; cross-table radiographic views are even more important in females. However, AP view is still essential to identify abnormalities of acetabular morphology such as dysplasia and protrusio acetabuli.

4.8.1.3 Two and three-dimensional acetabular measures

It has been reported that AV angles are usually higher in females whilst CE angles are usually not different between males and females (Ergen et al., 2014). This corresponds with the general trends observed in this study. Further, strong correlation between the 2D

measured and maximum 3D measured CE angles (Figure 4.12a) suggests that the maximum 3D CE angle calculated from the parametric surfaces is a reliable assessment of the overall level of acetabular coverage. Consideration of all five CE angles could provide information on the level of acetabular coverage across different positions along the anterior-posterior axis, with a mean range across all patients for the five CE measurements of 15.8° . This information cannot be gleaned when only a radiographically measured CE angle is available. It may be possible to use differences in angles from the splines to indicate regions at higher risk of pincer impingement, although no pincer patients were available for this study. Similarly, strong correlation between the 2D measured and average 3D measured AV angles (Figure 4.12b) suggests that the mean 3D AV angles from the parametric surfaces provide a valid indication of the overall level of anteversion of the hip, and consideration of all five AV angles could provide information on the level of anterior acetabular coverage along different axial regions along the superior-inferior axis. The mean range across all patients for the five AV measurements was 7.5° . Again, this variation is information not captured when only a single 2D AV angle is recorded from an axial CT slice.

4.8.1.4 Inter-user variation

The low standard deviations between users when additional measures were taken of acetabular angles suggest that user variation would have minimal effect on the detected correlations. The higher inter-user variation seen in alpha angles measurements was not surprising even though fewer users repeated the measures, because alpha angles were much more challenging to measure and more subjective. The femoral head seen in radiographs is not actually circular and so placement of a circle on the femoral head is subjective and based on user judgement. This is also true clinically and was part of the rationale for using the radiologists' results. Furthermore, alpha angles are in any case greatly affected by viewpoint (Harris et al., 2014; Laborie et al., 2014).

4.8.2 Study limitations and challenges

4.8.2.1 Assumption of anatomical orientation

The parameterisation system depends on segmentation of bone from 3D images and on the assumption that hips are orientated neutrally in anatomical planes. In three cam femurs and one control femur this was seen in the axial view to be untrue, and an additional

rotation was used to align them approximately into a neutral rotation. Without this correction, the fitting errors for these cases were noticeably larger (> 1 mm). Further, the neck axis was assumed to be at 40° to the superior-inferior axis for all femurs since it was not possible to measure the femoral neck shaft angle given the field of view in the scans, and defining the neck axis for each femur presented a significant challenge because of the abnormal morphology resulting from the cam deformities. The value of 40° was therefore chosen to automate the process as it appeared in all cases to orientate the neck axis approximately vertically. Sensitivity tests revealed that varying this angle affected cam severity measurements because the ellipses were captured on a different plane through the neck. However, even when varying the angle by 25%, these differences were generally less than the differences observed between individuals, so the cam-rad measure was still capable of detecting differences between cams of different severities. The cam-rad measurements were well correlated so the relative severity of the cams was consistent. The identified difference between cam position in males and females was also still apparent.

4.8.2.2 User variation in parametric and severity measures

The segmentation of bone surfaces from CT scans followed a set protocol and user variability would be unlikely to cause more than minor differences in final parametric models. Once bone surfaces have been segmented from CT scans, the method is mostly automatic. The femoral parameterisation and severity measurements assessing the cam are obtained fully automatically through scripts. The acetabular parameterisation requires manual intervention (including some expert adjustments) to select nodes on the acetabulum to obtain an optimum fit, necessary because subject-specific irregularities in acetabular rim shape are not well captured using standard shapes. The measured angles were calculated from nodes around the rim, which were the most straightforward to place, limiting the effect of this variation on acetabular severity measurements. Whilst the process would need further refinement and optimisation to be used as a clinical tool, particularly on the acetabular side which has not been tested on pincer patients, it is presently capable of capturing complex hip geometry in a finite number of simple geometric parameters. Variations of both surfaces with alternative parameters can be generated automatically and it is possible to vary each parameter separately.

4.8.2.3 Image and mesh resolution

The purpose of the sphere generated and resampled in the +CAD module of ScanIP was to understand how much difference would exist between the parametric surface and the

segmented surface assuming the segmented surface was in reality well described by the mathematical shapes used. That is, to establish baseline noise. When the femoral parameterisation procedure was applied to the sphere, the ellipses in each slice had centres close to $(0, 0)$ and two approximately equal radii, providing an initial check that the script was working as expected. When the segmented and parametric sphere were viewed in Abaqus, it was clear there was a very good fit between the surfaces. Nevertheless MATLAB recorded a fit error of 0.22 mm. Because the triangles making up the mesh on the parametric surface were half squares, their vertices were always positioned at corners of squares. Nodes on the segmented surface vertices may be in the centre of these squares, hence the nearest parametric node could be some distance away despite the surfaces matching up well.

4.8.2.4 Sensitivity of severity measures to parametric method

Due to the baseline noise (as the best possible fitting error was seen to be 0.22 mm), the measures describing cam severity are relative rather than absolute. The highest value of cam-rad, 100.4%, should be interpreted as indicating a particularly severe cam where there is very little head-neck offset, rather than suggesting the cam radius is literally greater than that of the head. Cam-rad is sensitive to the position of slices used for lofting, which is why the method for choosing number of slices was standardised as equal to the head radius and linearly spaced slices were chosen automatically. Whilst a more accurate value for cam-rad could be obtained from the full segmented surface, the described method allows all the severity measurements to be derived automatically using only the geometrical parameters describing the bone shape, and the precision was sufficient to demonstrate differences between two population groups.

4.8.3 Conclusions

The study on 20 patients and 18 control subjects in this chapter furthered the preliminary results of Chapter 3 in demonstrating that it is possible to represent segmented geometry of the acetabular cavity and proximal femur bone with a cam deformity, using a small number of parameterised curves and achieve a low overall fitting error. The 3D cam severity measurements obtained from the parameterised geometry provide a systematic method of assessing impingement risk, and impart more information on the shape and position of cams when compared with using only radiographic measurements, which may not give a good indication of the full extent and exact location of bony abnormalities. The potential severity, i.e. risk of impingement, on the femoral side can be assessed by

the cam size resulting from head-neck offset (captured by cam-rad) in a manner that is not dependent on a 2D view. Combining this with the position and extent of the cam (captured by cam-angle and cam-width), and with the acetabular severity measurements, could allow impingement to be predicted based on bone shape in different scenarios, although there are other factors that play a role in its severity, such as patient activity level and vulnerability of the labrum and articular cartilage to injury. The cam measures also allowed investigation of the differences in cams between males and females, which showed that cams in males are more likely to be superiorly located.

Variations of the parametric bone surfaces can be automatically generated and the cam measures can define the severity of deformity in the new model. In Chapter 6, parametric models are generated to investigate the effect of certain morphologies on soft tissue strains in impingement scenarios. First the development of modelling methodology is covered in Chapter 5.

Chapter 5

Development of Finite Element Modelling Methodology

5.1 Introduction

The purpose of this chapter is to describe the development of methodology to create parametric and segmentation-based finite element models of hips with impingement characteristics, using Abaqus. Some measurements of the hip that may be of clinical interest, such as tissue strains occurring during motions that result in impingement, can be difficult to derive without using computational models (Anderson et al., 2007). Finite element analysis uses numerical techniques to solve highly complex models (Section 2.6), and provides a suitable *in silico* method for investigating stresses and strains occurring in the hip joint.

The primary aim of developing finite element models in this work was to investigate the effects of morphological variations in the hip on soft tissue strains that relate to potential impingement damage mechanisms. In this context, the term ‘soft tissue’ is used to refer to femoral and acetabular cartilage layers and the acetabular labrum, in order to distinguish them from bone tissue in the hip joint. However, note that the full definition of ‘soft tissue’ also encompasses a range of other tissues in the body, such as muscle, fat, ligaments, nerves and blood vessels. In order to achieve the modelling aim, parametric models were used to investigate the effect of varying morphologies, captured by geometric parameters in models simulating an impingement scenario. To provide confidence in the results from parametric models, it was important to validate specimen-specific parametric models against segmentation-based equivalents. Models of the 20 patients investigated in

Chapter 4 featuring parametric femoral surfaces were validated against equivalent models with segmented femoral surfaces, and this is covered in Chapter 6. In order to ensure valid comparison between parametric and segmented models, the settings used in these different model cases were required to be consistent. This includes the contact settings, fixed model geometry, and boundary conditions to represent an impingement scenario. Investigations were therefore necessary to determine efficacious methodology to achieve this.

This chapter concerns methodology development, and consists of some theory, some discussion of software constraints, and a primarily top level description of the sensitivity studies that were conducted to make progressive methodology decisions in terms of determining optimal modelling settings. Because the work presented in this chapter was conducted to identify settings to successfully run models whilst minimising the occurrence of errors, the actual values of the model outputs were of relatively little importance. Therefore results presented in this chapter predominantly take the form of discussions of the successes and failures encountered in terms of selecting software options that allowed key variations of models to run successfully.

The first stage of development consisted of preliminary investigations which were required to determine various basic settings to use in the models, including options regarding contact and element definitions. For this, sensitivity tests were conducted on a spherical hip geometry model to assess model behaviour when different contact options available in Abaqus were selected (Section 5.2).

The next stage of development was to develop methods for producing soft tissues to include in models created using the parametric and segmented surfaces discussed in Chapters 3 and 4. The labrum and acetabular cartilage at the cartilage-labrum junction are the tissues generally damaged when impingement occurs, and FE simulations should not depend only on bone contact to assess hip impingement (Kapron et al., 2014; Kapron et al., 2015). In an ideal scenario, models with fully segmented specimen-specific tissues would be compared with specimen-specific parameterised equivalents. However, unlike bone, soft tissues were not visible in the clinical CT scans used in this work, hence it was not possible to obtain specimen-specific geometry for these tissues. Whilst it was not necessary for impingement models to capture all aspects of soft tissue geometry, such as the precise shape of the fossa, it was important to capture the basic shape of the acetabular cartilage and labrum, and of femoral cartilage, which covers the proximal head excluding the cam region. Methods were therefore required to produce artificial soft tissue geometries, and the development of these is described in Section 5.3.

Despite using the options found to be optimal in preliminary models, convergence difficulties were encountered due to overclosure errors between irregular articulating surfaces. Furthermore, it was not possible to automate the generation of acetabular soft tissue on complex bone geometries. This meant it was necessary to develop a simplified, spherical representation of the acetabulum, which was found to be more effective for rapid generation of parametric variations of the acetabular rim, and for limiting the occurrence of convergence issues in the models (Section 5.3.3.3).

The final developed models, which incorporated specimen-specific bone geometry, were ideally required to mimic the movements leading to impingement *in vivo*. An investigation of boundary conditions best suited to simulating impingement was therefore necessary, and this was conducted in tandem with testing of different geometry combinations, since model convergence difficulties resulted from a combination of geometry and boundary conditions. Repeated flexion and internal rotation can result in joint damage in hips with cam morphologies, as the cam displaces the labrum and compresses the cartilage (Section 2.3). Therefore boundary conditions simulating an impingement test, consisting of flexion followed by internal rotation of the femur, were sought. To accomplish this, the femur was rotated whilst the acetabulum was kept fixed in place, and Section 5.4 details three different approaches tested to constrain the femur within the acetabular cavity: translation control, force control and pinning the femoral head centre; the last of these was found to be most effective for obtaining results from segmented and parametric models using the same boundary conditions.

Finally, an overall discussion of the development and findings presented in this chapter, and their implications for the models in Chapter 6, is provided in Section 5.5.

5.2 Preliminary investigations for calibration of modelling settings

It is important to understand the effects of different options available when using FE modelling software. In this section, sensitivity tests were conducted on a spherical hip set up to assess model behaviour when different options available in Abaqus, regarding contact and geometrical non-linearities, were used.

5.2.1 Background

To analyse contact in FE models, interactions and constraints between surfaces must be defined (Section 2.8.4). For the models in this work, the interaction between the femoral and acetabular sides of the hip joint was of interest. However, modelling contact in FE analysis can be subject to convergence issues which prevent models from running.

When developing FE models using Abaqus, a sequence of analysis steps are defined. These steps provide a convenient way to capture changes in the displacement of nodes in the model during the course of the analysis (Abaqus 6.14 Documentation, 2014). Prior to analysis, the user can define modifications at each step to adjust model inputs including loading and boundary conditions, changes in interactions between parts in the model, and the addition or removal of parts. In each step, numerical algorithms are employed to solve the equilibrium equations describing the displacement of each node in the model in that step. In contact analysis, a number of constraints will change as the analysis progresses and bodies in the model come into contact, so nodal positions must be constantly updated. In order to reach a solution for complex problems, this means the problem must be solved in a series of increments.

Mathematical singularities can result when elements become highly deformed. In this case, Abaqus may apply small translations to nodes in order to try to resolve contact constraints while maintaining geometrical restrictions on elements. This can mean the software must run through a large number of increments in attempt to resolve the contact problem in a given step, but reaching a solution may require more increments than is practical. Given sufficient time and computational resources, the model may be able to solve, but in practice the analysis will be aborted because the singularity cannot be resolved in a realistic amount of time (that is, within a few days as opposed to several weeks on a standard working PC with around 16 GB of RAM). In this case, the model is said to be unable to converge. It is also possible that a given setup has no solution to converge to, in scenarios where contact surfaces are forced together.

Excessive distortion of elements resulting in these problems can occur due to large deformations. For example, when modelling impingement, the labrum may be displaced and consequently greatly deformed as the femur rotates and pushes against it. This can result in excessive distortion of elements in the labrum which prevents the model from converging.

A key example of element distortion occurring during the modelling of joint articulation is distortion due to severe overclosure of contacting surfaces. This is frequently encoun-

tered when contacting surfaces do not conform, since the lack of conformity means that some elements in cartilage layers become highly compressed as movement is simulated. Contact pressure between two surfaces at a point is defined in Abaqus as a function of the interpenetration of the surfaces, referred to as the “overclosure” (Figure 5.1). The function depends on the definition chosen by the user. When hard contact is used, the pressure is zero when there is no contact and increases when parts in the model are translated into contact and/or force is applied (Abaqus 6.14 Documentation, 2014). When the linear penalty contact constraint enforcement method is used (recommended for the finite-sliding, surface-to-surface contact formulation used in the models in this work), contact force is proportional to the penetration distance, so some degree of penetration will occur during the solution process. The severity of overclosure resulting from a given translation depends on the dimensions of the elements involved. For a small slave element, a small translation of elements from another body towards it may result in a greater percentage of that slave element being affected by overclosure, and consequently greater distortion of the element will occur to allow for this.

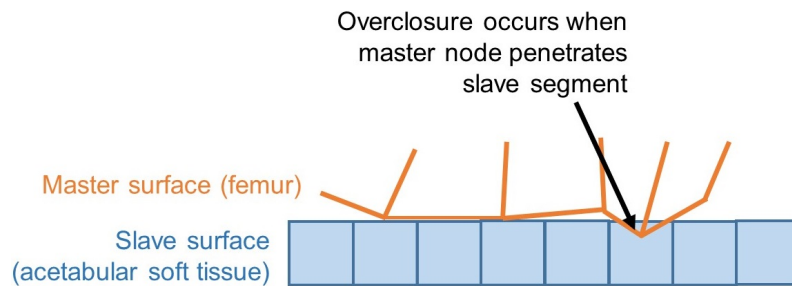


Figure 5.1: Overclosure occurs when the master surface penetrates the slave surface.

In order to minimise the occurrence of errors resulting from excessive element distortion, it was necessary to conduct preliminary investigations to establish the contact settings in Abaqus most conducive to obtaining results from simulations.

5.2.2 Preliminary model sensitivity tests

In order to establish the most effective options to use in Abaqus to simulate contact interactions in a hip impingement scenario, an initial model assembly representing a simplified right hip was created. This assembly featured spherical acetabular and femoral surfaces (Figure 5.2). Femoral and pelvic bones were modelled as rigid (Anderson et al., 2008; Chegini et al., 2009), and soft tissues were modelled as isotropic, linearly elastic materials, following the approach used by Chegini et al. (2009) and Liechti et al. (2015) in parametric hip models. Values for material properties used were also taken from the lit-

erature. Cartilage elements were assigned $E = 12$ MPa and $\nu = 0.4$ and the labrum was assigned $E = 20$ MPa and $\nu = 0.4$. Material properties are discussed in more detail in Section 5.5.3.

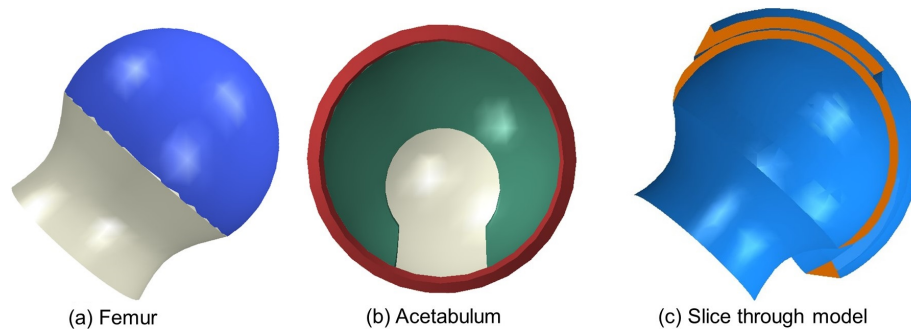


Figure 5.2:

- (a) Coronal view of preliminary model femur with femoral cartilage in blue.
- (b) Preliminary model acetabulum, view into cavity, with labrum in red and cartilage in green.
- (c) Cross section in coronal plane of the geometrical assembly used in preliminary models.

Frictionless, finite sliding surface-to-surface interactions with hard contact were defined between contacting surfaces, meaning the penetration of the slave surface into the master surface is minimised. In addition to defining interactions between articulating surfaces, tie constraints were defined to fix soft tissue parts, whose geometry was generated separately (Section 5.3), to the relevant bone parts. Tie constraints work by constraining the displacement of each slave node so that they each have the same motion as the point on the master surface to which it is closest (Abaqus 6.14 Documentation, 2014). The following interactions and constraints were defined in all models (in each case the first part mentioned is the master surface, based on the discussion in Section 2.8.4):

- Interaction: between femoral cartilage and acetabular soft tissue
- Interaction: between femur and acetabular soft tissue
- Constraint: Tie femur and femoral cartilage
- Constraint: Tie acetabular bone and acetabular soft tissue

Sensitivity tests were conducted on the basic set up (Figure 5.2) to assess model behaviour when different contact options available in Abaqus were used. The articular surfaces were initially positioned to be conforming, and further assemblies were generated in which the position of the femoral geometry was adjusted to alter its alignment with the acetabular side, so that less conforming contact could be tested. With the acetabulum fixed, the femur was translated to contact with the cartilage regions (Figure 5.3) and rotated to cause impingement against the labrum (Figure 5.4). These translation and rotation steps were

performed until the model aborted. The location of loading area was arbitrarily chosen since the models were spherical and their purpose was to test whether the methodology could produce models that converged. The effects of using different options were observed. Further details for each are given below. In particular the following tests were performed; in each case adjustments were made to the specified parameters to optimise for model convergence:

1. Mesh density, cartilage thickness, and options in contact interaction and constraint definitions.
2. Angle of femoral rotation performed in each analysis step.
3. Nonlinear geometry option.
4. Enhanced hourglass control option.
5. Unsymmetric matrix storage equation solver option.

1. In modelling situations where contact pressures and areas are of particular interest, cartilage clearance and thickness values may be crucial to the results (Li et al., 2013). These factors are of less importance in impingement simulations where the regions of interest are at the acetabular rim and cartilage-labrum junction, rather than central regions of the joint cavity. The mesh density and thickness in the acetabular cartilage was varied, and contact and constraint options in Abaqus that define the adjustment of nodes were also varied in order to test the effects of these factors on optimising for convergence and minimise the occurrence of overclosure issues discussed in Section 5.2.1.

2. In addition to translation boundary conditions to establish contact between the femur and acetabulum, rotation boundary conditions were applied to the femur to simulate impingement against the labrum. The entire desired rotation, specifically 35° of internal rotation from a flexion position, cannot be defined in a single analysis step because the model will not be able to converge. Using a large number of analysis steps however increases the runtime of a model. The number of analysis steps and hence degree of rotation in each step were tested to optimise for convergence whilst limiting model runtime.

3. Nonlinear static problems are those where the stiffness matrix $[k]$ and/or the force vector $[F]$ are functions of the nodal displacements $\{U\}$ (Section 2.8.4). This may occur as a result of nonlinearities in the material properties, the geometry, the combined effects of these, or contact conditions of the problem. The nonlinear geometry option in Abaqus (nlgeom) allows the solver to distinguish between undeformed and deformed configurations to account for nonlinear effects of large deformations or displacements, and should therefore be enabled to obtain reliable results when large deformations are expected to occur during analysis. This is the case in simulations of impingement, since large defor-

mations of acetabular soft tissue structures resulting from femoral rotation are predicted to arise. Models were tested with the nlgeom enabled and disabled.

4. One particular problem that can occur is a spurious deformation of elements known as hourglassing, where individual linear, reduced integration elements take on an hourglass like appearance as a result of bending with no strain energy generated (Figure 5.4a). Abaqus includes “hourglass stiffness” in elements to limit the propagation of this issue. The enhanced hourglass control element formulation can be used for solid elements. It has a higher computational cost (observed to increase estimated GFLOPS per iteration in a simple hip model from 4.41 to 4.43), but gives improved accuracy with coarser meshes compared with the default hourglass formulation (total stiffness). It performs better when modelling nonlinear material response at high strain levels (Abaqus 6.14 Documentation, 2014). Models were tested with the enhanced hourglass control option enabled and disabled.

5. When Abaqus generates a stiffness matrix, the software by default automatically selects a symmetric or unsymmetric matrix storage and solution scheme. However, normal contact constraints due to the surface-to-surface discretisation result in unsymmetric terms in both two- and three-dimensional cases. These terms have a strong effect on the convergence rate in regions where the master and slave surfaces are not parallel to each other. The unsymmetric matrix storage equation solver is therefore strongly recommended for finite-sliding surface-to-surface contact problems (Abaqus 6.14 Documentation, 2014) (Section 2.8.4). Models were tested with the unsymmetric matrix storage option enabled and disabled.

5.2.3 Findings of preliminary investigations

The basic set up demonstrated the approach to modelling could successfully result in contact between the femoral and acetabular regions of the model (Figure 5.3).

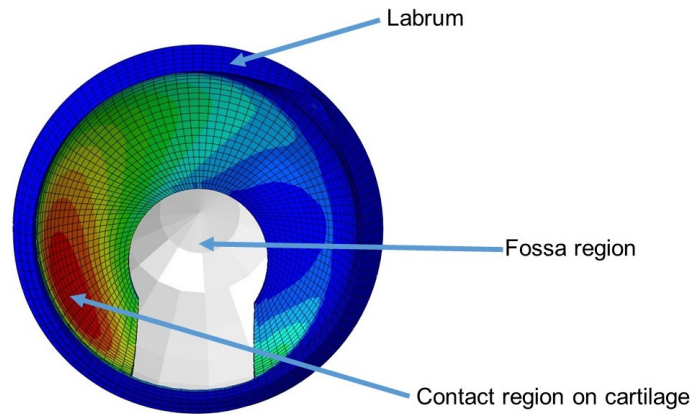


Figure 5.3: Example of a contact pattern on the acetabulum in a conforming model; in this case the femur was translated into the posterior region of the cartilage.

5.2.3.1 Balancing mesh refinement and cartilage thickness with contact convergence

Using larger elements in the cartilage parts (that is, coarser meshes) was seen to be effective for reducing the occurrence of overclosure errors since more translation of the femur into the acetabulum was possible before element distortion became such that the model aborted. However reducing mesh density is not a feasible method to use to achieve model convergence since lower mesh densities produce less accurate results. Conversely, finer meshes give more accuracy but overclosure related errors occur following smaller translations of the femoral surface into the acetabulum. This is because overclosure is measured relative to element size.

With poorly conforming surfaces, decreasing the thickness of the cartilage layers can decrease the number of regions exhibiting high levels of interpenetration when contact is established. However this increases the severity of overclosure problems as the elements are also necessarily smaller. Furthermore, when thin cartilage layers were tied to the underlying bone parts, their elements became prone to distortion so that Abaqus defined them as “zero or negative volume”, preventing the analysis from progressing unless these elements were removed. The “adjust slave surface initial position” setting for the tie constraints is used to align the nodes of the slave surface with those of the master surface and disabling this option reduced the severity of this problem as the initial shape of cartilage elements was no longer distorted as a result of tying them to bone parts.

With thicker layers of cartilage, contact between layers was established with relatively small translations, resulting in excessive overclosure occurring with boundary conditions that would have been sufficient for running a model with thinner cartilage layers. The “ad-

just only to remove overclosure” option for surface interactions is used to make strain-free nodal adjustments when initial overclosure (resulting from the placement of part instances in the assembly) is within a set tolerance. When there was little joint space, enabling this option could avoid errors resulting from element distortion that would otherwise prevent the analysis from beginning.

These issues are summarised in Table 5.1.

Table 5.1: Overclosure relationships to meshing and cartilage thickness.

Mesh density	Accuracy of solution	Chance of overclosure
Coarser	↓	↓
Finer	↑	↑

Cartilage thickness	Severity of overclosure	Chance of overclosure
Thinner	↑	↓
Thicker	↓	↑

5.2.3.2 Applying femoral rotations

When applying rotation boundary conditions to rotate the femur, it was found that defining more analysis steps with smaller rotations in each step, as opposed to larger rotations in fewer steps, allowed models to progress further, as the solver calculates increasing strain more gradually. Even so, excessive distortion of elements can occur and result in convergence problems. Rotations of 5° per step were found to be optimal for limiting convergence problems whilst avoiding excessively long run times. Another method of achieving this would be to impose a minimum number of rotation increments within a single step, but the method of defining multiple steps was chosen as this made the process of extracting results from specific rotation levels easier to automate.

5.2.3.3 Nonlinearities

When nlgeom was enabled, it was observed that models aborted earlier compared to when nlgeom was disabled. This makes intuitive sense because models with nlgeom enabled approach solving the contact problem more rigorously by always taking into account the current element area for calculating stresses. When compared in steps in which both models had converged, output stress and strain values did not exhibit any differences.

The observation that these models converge less readily highlights the need to avoid large overclosures in order to achieve convergence.

Using the enhanced hourglass control element formulation option was found to reduce the occurrence of the hourglass form of spurious element deformation that was otherwise observed particularly in the labrum (Figure 5.4b).

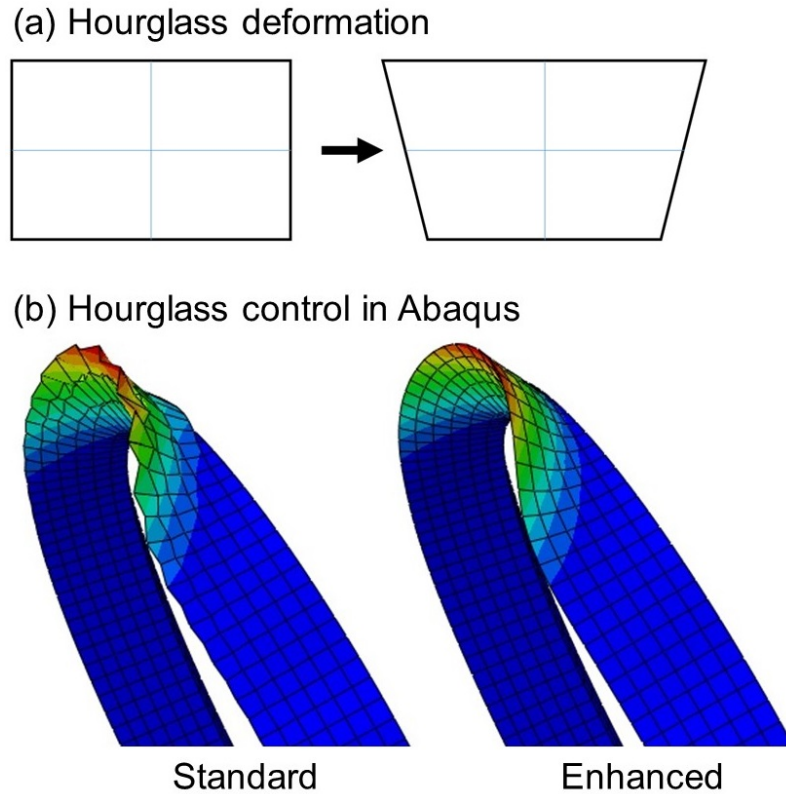


Figure 5.4:

(a) Hourglass deformation can occur in linear, reduced integration elements. The blue lines have not changed length so no strain energy is generated.

(b) An example of a deformed labrum mesh with standard (left) and enhanced (right) hourglass control. Enhanced hourglass control can prevent unrealistic distortion of elements.

When the unsymmetric matrix storage option was enabled, it was found that models could progress to greater levels of rotation and hence labrum deformation before aborting. When compared in steps in which both models had converged, output stress and strain values did not exhibit any differences.

5.2.4 Conclusion of preliminary investigations

The determination of optimal cartilage thickness and mesh density are discussed further in Section 5.3 when methods for their geometry are introduced. Based on the discussion in this section, the following practices were adopted for the FE models developed in this thesis:

- Enable “adjust only to remove overclosure” option in contact interaction definitions.
- Disable “adjust slave surface initial position” option in tie constraint definitions.
- Perform femoral rotations of 5° in individual analysis steps.
- Enable nlgeom option in all steps.
- Enable enhanced hourglass control for elements in acetabular cartilage and labrum.
- Enable unsymmetric matrix storage option in all steps.

5.3 Development of soft tissue representation

Models should not depend only on bone contact to assess hip impingement (Kapron et al., 2014; Kapron et al., 2015). However, unlike bone, soft tissues were not visible in the clinical CT scans used in this work (Figure 5.5a), hence it was not possible to obtain specimen-specific geometry for these tissues. Additionally, in many of the patient CT scans, pelvic and femoral bone appeared to be in contact in certain regions, likely due to the joint being in a compressed state during the scan, and the limitations of the scan resolution. This suggests that even if soft tissues could be delineated in the images, a mask segmented in ScanIP could be an inaccurate representation of the normal soft tissue in an uncompressed state.

To ensure the validity of the comparison between models with segmented and parametric bone surfaces in Chapter 6, it was important to produce soft tissue geometries which were as equivalent as possible for both model cases. Therefore it was necessary to develop standard methods to produce artificial soft tissue geometries for use in models incorporating the segmented and parametric bone surfaces.

In micro-CT scans (voxel size 0.082 mm³) of cadaveric hip specimens (Section 1.2) (Figures 5.5b and c), soft tissues in the hip were visible due to their higher resolution than clinical CT (patient radiation exposure must be minimised), and because the hip joints had been dissected from most of the surrounding tissue. It was therefore possible to use ScanIP to segment soft tissues from these scans into masks separate from the bone. How-

ever, it was unclear exactly where cartilage and labral tissues were bounded since all the soft tissue had a similar greyscale value, and residual non-cartilaginous soft tissue was also present on the specimens following their dissection. However, segmented cadaveric scans were used for visual checks when assessing the suitability of methodologies for producing artificial soft tissue geometries to use with bone surfaces from patient scans.

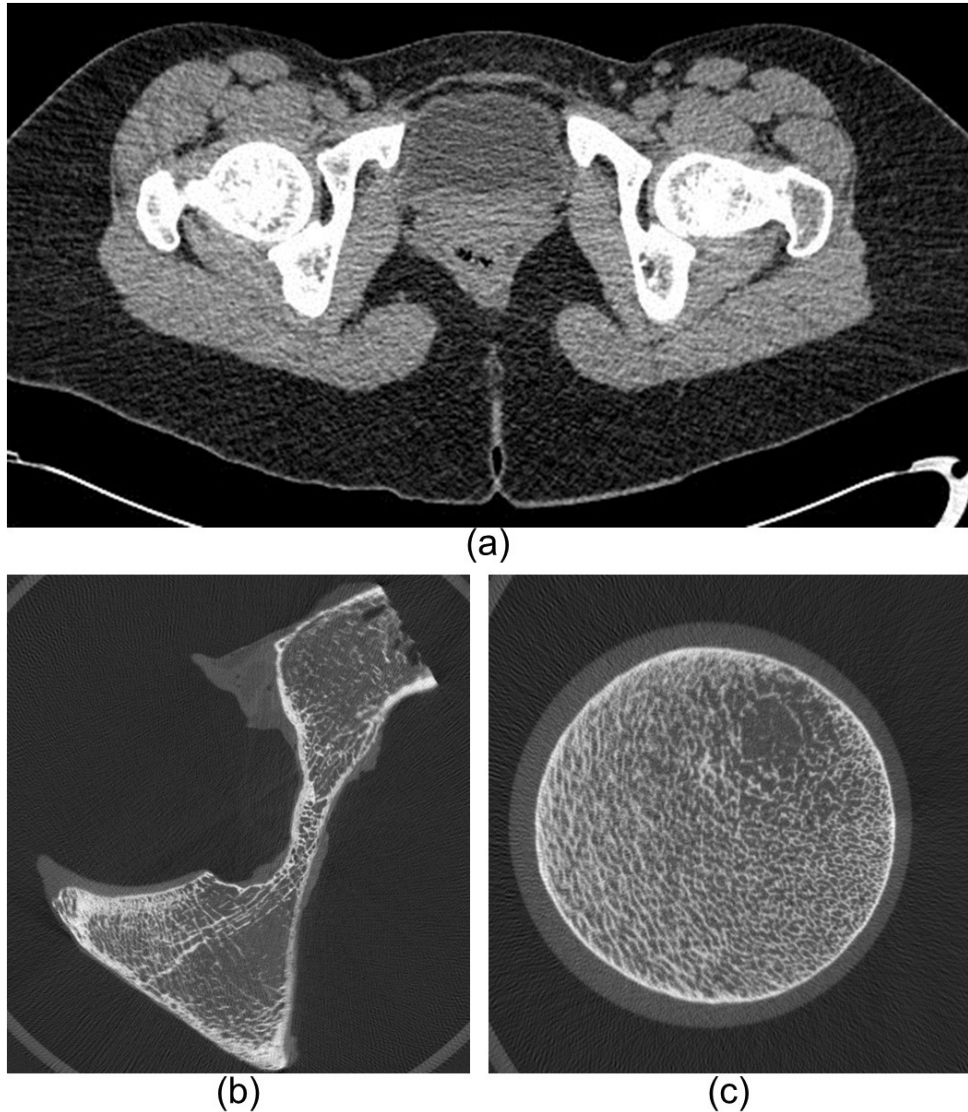


Figure 5.5: Examples of slices from CT scans:

(a) Axial slice from a clinical pelvic scan of a patient; bone is visible but detail of soft tissues in the joints are not.

(b) Slice from a high resolution scan of a cadaveric acetabulum; soft tissues are visible around the bone.

(c) Slice from a high resolution scan of a cadaveric femur, cartilage is visible surrounding the femoral head.

Based on the appearance of tissues observed in cadaveric scans and literature evidence (Chapter 2) (Chegini et al., 2009; Jorge et al., 2014; Liechti et al., 2015), the following

requirements were determined for artificial soft tissue geometries:

- Same process of generation on parameterised and segmented bone surfaces.
- Smooth articular surfaces without initial overlap.
- Femoral cartilage covering proximal region of femoral head, excluding cam region on the femoral neck.
- Acetabular cartilage covering the lunate surface of the acetabulum.
- Labrum with triangular cross section following the acetabular rim, extending its cover of the femur and directed towards the centre of the cavity rather than extending out.
- Transverse acetabular ligament included to bridge acetabular notch and extend the labrum to a full circle about the acetabular rim.
- Cartilage layers with thicknesses in the approximate range 1 – 2 mm.

In order to meet these requirements, methods of producing geometry in ScanIP and in Abaqus were considered. Generally part instances in Abaqus are defined in terms of their geometry, and later a mesh is generated associated with this geometry. In addition, parts can be included as “orphan” meshes, where the elements of the mesh are not associated with any underlying geometry. Orphan meshes provide more freedom in terms of the shape that can be represented, and can be manually generated within Abaqus or imported from other software, including ScanIP.

5.3.1 Initial generation in ScanIP

Initially, trial soft tissue masks were generated within ScanIP using dilations and Boolean operations on the bone surfaces (Figure 5.6). Femoral cartilage was generated by dilating the femoral bone mask in the relevant region of the head. For the generation of acetabular soft tissue, the +CAD Module for ScanIP was used to create a sphere, and the intersection of this sphere and the pelvic bone mask formed the acetabular cartilage mask. Adjusting the position and shape of this sphere, and dilating the mask resulting from its intersection with the pelvic bone mask, produced an approximation of labral tissue on the acetabular rim.

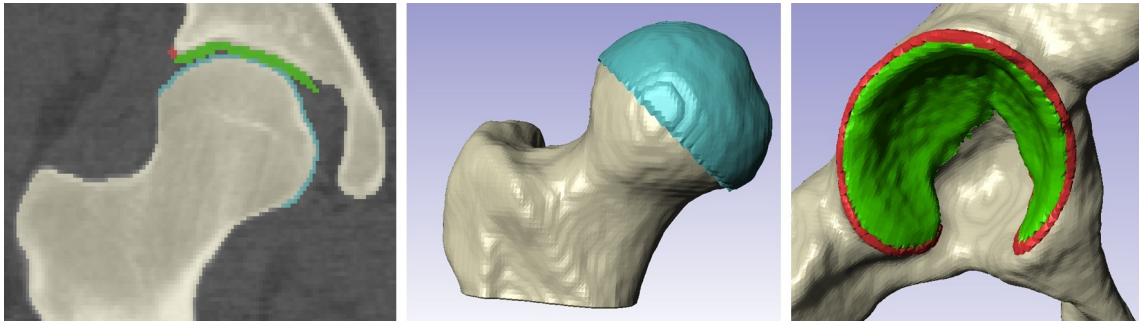


Figure 5.6: Example of trial soft tissue geometry creations in ScanIP; this method proved to be suboptimal.

Generating cartilage layers in ScanIP generally resulted in poorly conforming layers which overlapped. Even in regions without overlapping, the cartilage surfaces were not smooth since they followed the bone outline. Subtracting a spherical mask from the acetabular articular surface to smooth it was not practical as this process often resulted in gaps in the mask unless an unrealistically high cartilage thickness, filling most of the joint space, was used. Similarly, using a sphere as the base of femoral cartilage (rather than dilating the bone mask) resulted in a mask that was too thick in some areas and too thin with gaps in others. The labrum masks were also problematic; they did not have a triangular cross section or constant length due to acetabular rim irregularities, and omitted the transverse acetabular ligament due to lack of bone in that region. Furthermore, the irregular shape of soft tissue masks generated in ScanIP meant they proved difficult to mesh. These issues meant the decision was made to instead investigate methods within Abaqus to generate soft tissue geometries. For this purpose, it was necessary to export bone surfaces using the +NURBS Module for ScanIP.

5.3.2 Using ScanIP +NURBS

Linear tetrahedral elements are stiffer than hexahedral elements, and using tetrahedral elements for contact problems can result in locking, large and unrealistic stress concentrations, and poor estimations of contact areas (Maas et al., 2016). However, hexahedral meshes are more challenging to produce than tetrahedral meshes when working with complex geometries. In order to generate hexahedral meshes for cartilage layers by offsetting the bone mesh (Section 5.3.3.1), quadrilateral meshes were required on bone parts, modelled as rigid surfaces.

Because parametric surfaces representing bone structures are relatively simple, quadrilateral meshes could be readily generated on them within Abaqus following some par-

titioning. Segmented bone surfaces however are more geometrically complex, and their surfaces are usually exported from ScanIP in the triangulated STL format. When this is imported in Abaqus, the surface is defined as an orphan mesh of triangle elements. In order to instead generate quadrilateral meshes on the bone surfaces, the +NURBS module for ScanIP was used. The +NURBS Module for ScanIP allows segmented surfaces to be exported in Initial Graphics Exchange Specification (IGES) format. The surface geometry in this case is made up of patches described using Non-Uniform Rational Basis Splines (NURBS) instead of by smaller triangular faces. NURBS are parametrically defined curves widely used in computer graphics to allow arbitrary curved geometries to be represented (Schneider, 1996). Surfaces described in this way can be meshed with quadrilateral elements within Abaqus (Figure 5.7). In ScanIP, NURBS patches are largely defined automatically, with some options available to adjust the position of resulting patches. For femoral surfaces, the curvature detection method was used to obtain patches of roughly even size to produce more uniform meshes on the proximal head. For acetabular surfaces, the contour detection method was used instead as this produced patches that more closely followed the acetabular rim, making it easier to define the region where cartilage would be generated.

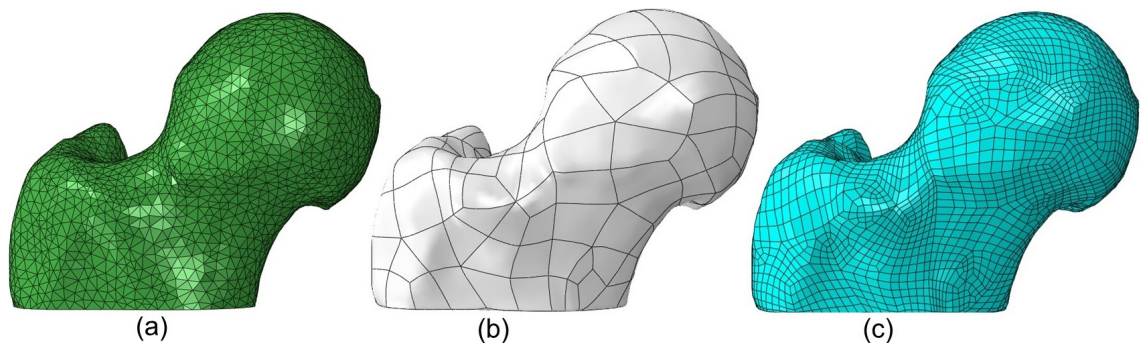


Figure 5.7: An example of a segmented femur in:

(a) STL format meshed with triangle elements, from ScanIP.

(b) IGES format described by NURBS patches, from ScanIP.

(c) IGES format meshed with quadrilateral elements, generated in Abaqus.

5.3.3 Producing soft tissue geometry within Abaqus

5.3.3.1 Cartilage generation using mesh offsetting

Femoral cartilage layers were produced as orphan meshes by offsetting the mesh on the femoral head. Generating offset meshes in Abaqus produces orphan elements by extending the 2D shape of element faces on a surface in the direction normal to that surface.

In this case, layers of hexahedral elements were generated by extending the shape of the quadrilateral elements on the femoral surface. These layers had 2 elements across their thickness of 1 mm. A partition was automatically placed on parametric femoral surfaces prior to meshing to ensure the offset was executed only in the desired location. This was chosen to be approximately 5 mm down from the proximal part of the femoral head, scaled based on femoral head radius. Specifically, femoral cartilage was added from the top of the femoral head to the position corresponding to $z = 5 \times \frac{HR}{22.95}$, where z is the femoral neck axis starting at 0 from the top of the head, and HR is the head radius (Figure 5.8). The value of 22.95 was used as it was the average head radius for the 20 cam patient hips. This method captured the proximal head in all cases whilst avoiding the neck region including the cam on the neck. The same method was used on segmented femoral surfaces, but because the meshes depended on the shape of the NURBS patches generated in ScanIP, it was necessary to import shapes generated from masks made in ScanIP capturing only the region where cartilage cover was required, so that NURBS patches aligned with the position where a cartilage mesh was required (Figure 5.9).

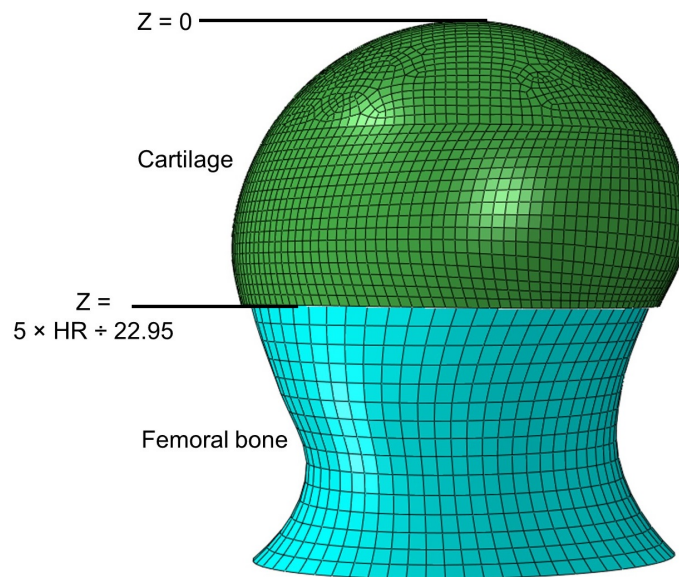


Figure 5.8: Position of femoral cartilage shown on an example of a parameterised femoral head.

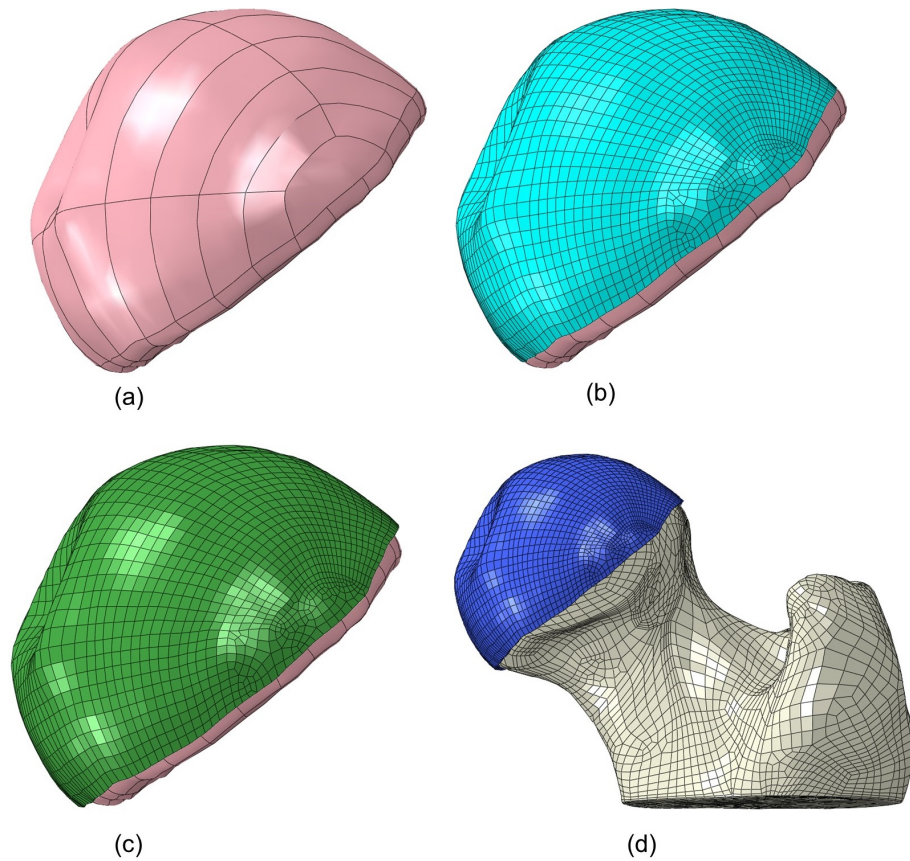


Figure 5.9: Generation of femoral cartilage:

- (a) NURBS surfaces on a mask where cartilage is required, from ScanIP.
- (b) Quadrilateral mesh generated on this surface, generated in Abaqus.
- (c) Offset to generate femoral cartilage as hexahedral mesh, generated in Abaqus.
- (d) Femoral cartilage on femur surface meshed with quadrilaterals, generated in Abaqus.

5.3.3.2 Manual generation of acetabular soft tissue

The rigid bone surfaces representing the acetabulum (segmented and spline-based parametric) were meshed using quadrilateral elements within Abaqus. In these cases, acetabular cartilage layers were generated as hexahedral orphan meshes by offsetting the bone mesh following the method to create femoral cartilage (Section 5.3.3.1). For the segmented cases, it was again necessary to generate NURBS masks incorporating only the acetabular region of interest and mesh these in order to generate an offset mesh in the required region. The irregularity of NURBS patches meant that specific regions had to be selected for the offset to produce cartilage in the desired areas (Figure 5.10).

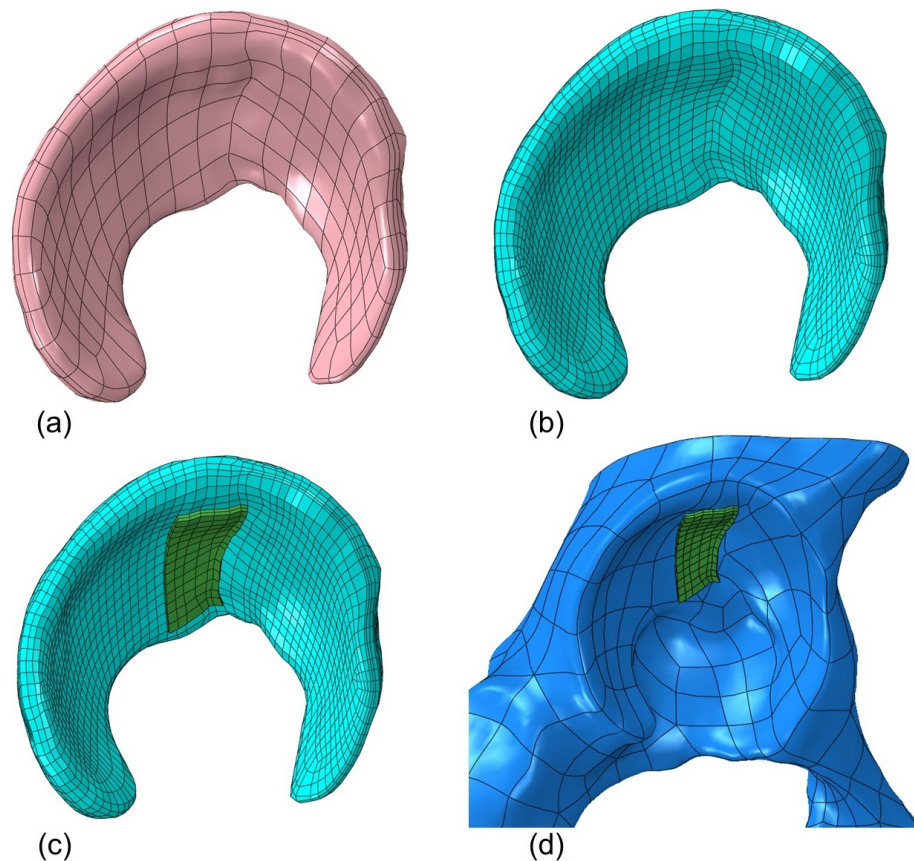


Figure 5.10: Generation of acetabular cartilage in a specific region:

(a) NURBS surfaces on a mask where cartilage is required, from ScanIP.

(b) Quadrilateral mesh generated on this surface, in Abaqus.

(c) Offset a specific region to generate cartilage as hexahedral mesh, in Abaqus.

(d) Acetabular cartilage on full bone surface in Abaqus; cartilage in only a specific region has been generated to emphasise that the shape of the mesh can be manually adjusted depending on where cartilage and/or labral elements are required.

To produce labrum geometry, initial tests involved sweeping a triangle sketch (representing the labral cross section) around a path defined by edges along the acetabular rim. However this generally resulted in labral geometry with a jagged appearance that intersected with the cartilage elements and could not itself be effectively meshed. Instead selecting cartilage rim elements to perform a further mesh offset also resulted in poor labral geometry with self intersections, because mesh offsets produce orphan elements extending in the direction normal to the surface being offset from. In order to avoid these issues, a new approach was taken in which a “bottom-up” orphan mesh was generated.

Bottom-up meshing in Abaqus is a manual, incremental meshing process that allows the building of a hexahedral mesh in any solid region. This technique allows the generation of hexahedral meshes ignoring some geometric features on parts because the constraint

tying the mesh to the geometry is relaxed. More importantly here, it can also be used for the generation of orphan elements. The bottom-up meshing approach was used to produce orphan elements to represent the labrum by extruding the shape of selected elements from the mesh around the rim of the cartilage. Using this approach meant that the vector used for the extrude could be varied around the rim to avoid self intersections, which was not possible using mesh offsets normal to the cartilage surface.

Labrum parts were generated in this way as bottom-up orphan meshes added to the segmented bone geometry and to the spline-based bone geometry. On segmented bone surfaces, the labrum was added by manually defining surfaces on elements around the rim of the cartilage mesh and using these surfaces as the source for an extruded bottom-up mesh. For spline-based parametric acetabular surfaces, to extend their size so that labrum could be generated in this same position, the surfaces were merged with scaled up copies of themselves ($\times 1.1$). Lofting was then performed between these sections, creating a rim onto which surfaces were defined as a base for extruding the labrum.

In both cases, the vector used for extruding was varied around the rim so that the labrum was directed towards the centre of the cavity whilst avoiding self intersections, with the length scaled to the head radius such that a head radius of 25 mm would result in a labrum length of 7 mm (Chegini et al., 2009; Garabekyan et al., 2016). To include the transverse acetabular ligament, an 8-node hexahedral element was created to link the inferior sides of the rim, and then split into multiple elements. The overall acetabular soft tissue consisted of a single part with several element sets that were assigned with cartilage or labrum material properties as appropriate (Figure 5.11). This process required selection of elements based on their label numbers which needed to be determined manually. Thus unlike most model generation aspects, the process for generating labrum geometry could not be automated using Python. Therefore at higher mesh densities, this method was less practicable.

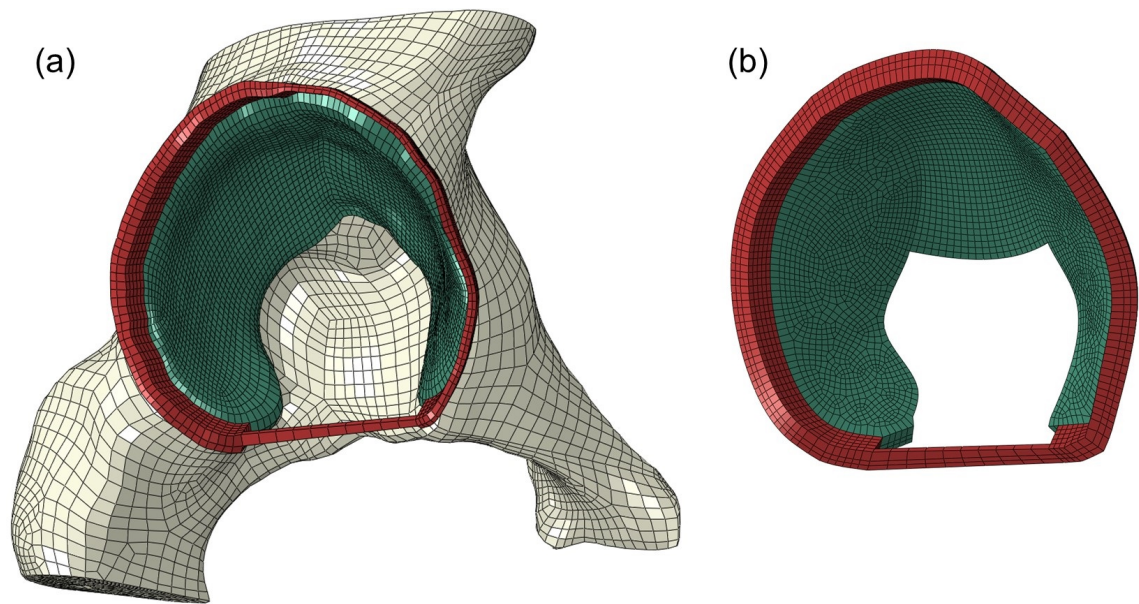


Figure 5.11: Manually generated acetabular soft tissue with labrum elements in red and acetabular cartilage elements in green:

(a) On a segmented acetabular bone surface.

(b) On a spline-based parametric acetabular bone surface.

5.3.3.3 Spherical acetabulum geometry

Despite using the options found to be optimal in preliminary models (Section 5.2), convergence difficulties were encountered due to overclosure errors between these more irregular articulating surfaces (Section 5.2.1). Furthermore, acetabular soft tissue generation using a bottom-up mesh approach could not be automated (Section 5.3.3.2). This meant it was necessary to develop a simplified geometry to represent the acetabulum (Figure 5.12).

Simplified geometry representing the acetabulum was created within Abaqus as a spherical cup shape with 33% of the surface area of a complete sphere. A spherical acetabular cartilage layer was included, with the acetabular fossa represented by removing a notch from the centre region. The labrum was generated by sweeping a triangular cross section (Chegini et al., 2009; Banerjee and Mclean, 2011) about the circular acetabular rim. This basic acetabular geometry was scaled according to the head radius of each femur to provide a mean cartilage thickness of approximately 1 mm across all models. Let HR denote the femoral head radius of a given model, then the acetabular cartilage thickness was assigned as $\frac{HR}{A}$, where $A = 22.95$ mm, based on the average head radius for the 20 hips. The labrum length was $\frac{7HR}{25}$ mm, based on the labrum height of 7 mm used by Chegini et al. (2009) for a head radius of 25 mm, since specific labrum heights could not be obtained from the patient scans. In all models, the acetabulum was rotated to simulate

a standardised anteversion angle of 20° and centre edge angle of 30° . These orientation angles were chosen on the basis of reported average values for CE and AV angles, including the subjects in this study (Tannast et al., 2007; Chegini et al., 2009; Ergen et al., 2014; Cooper et al., 2017), and provided an orientation allowing sufficient joint space to permit small translations.

The soft tissues on the simplified acetabulum were made from geometric parts. These were automatically meshed in Abaqus using hexahedral elements. For the cartilage this required some partitioning, whilst for the labrum a swept mesh approach was used. As these were preliminary models used to establish methodology, the mesh density was kept low for computational efficiency. For the models in Chapter 6, higher mesh densities were adopted following mesh convergence tests (Section 6.3.1.2).

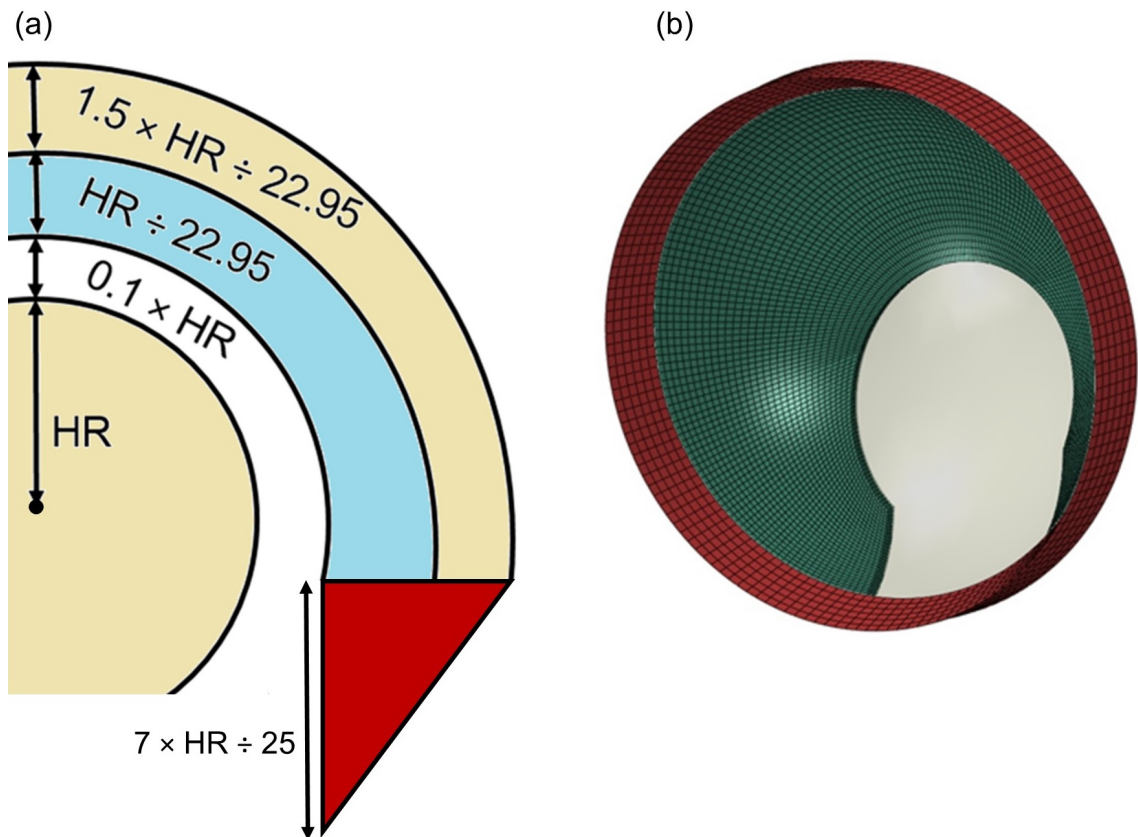


Figure 5.12: Simplified spherical acetabular geometry:

(a) Dimensions shown on a sketch (not to scale) of a cross section through the simplified hip geometry.

(b) Example of meshed spherical acetabular geometry.

5.4 Models to investigate boundary conditions and geometry

5.4.1 Methods

The remaining part of this chapter concerns specimen-specific models created in order to investigate boundary conditions for simulating impingement. The aim was to develop a methodology for simulating impingement in quasi-static models that could be used with both segmented and parametric femurs. In this way it would be possible to assess whether parametric surfaces can produce results similar to those found using segmented surfaces, which is covered in Chapter 6. The models here used segmented and parametric bone surfaces discussed in Chapters 3 and 4.

Precursory tests using the ellipse-based parametric femurs revealed that rotations of the femur sufficiently high to establish cam-labrum contact could result in the distal end of the femoral neck (marking the termination of the geometric model) slipping into the acetabular cavity (Figure 5.13a). Therefore parametric femurs were generated with a 5th ellipse added onto the distal end of the modelled geometry, extending the length from the top of the head (proximal to distal) from HR to $1.2 \times HR$ (where HR is the head radius). To achieve this, the femoral masks in ScanIP required some adjustment to remove the trochanter in order to fit an ellipse to the distal neck without vertices from the trochanter interfering with the ellipse fit (Figure 5.13b). The same mesh refinement was used in ScanIP to generate this mask and the rest of the surface was exactly the same as the original parametric models, hence the ellipse parameters matched the original data. The four model geometry combinations tested are summarised in Figure 5.14.

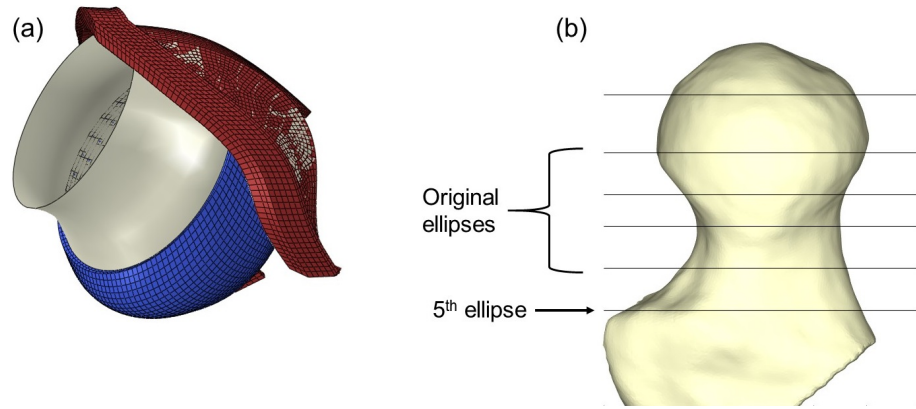


Figure 5.13:

(a) Femurs generated using 4 ellipses were sometimes prone to slipping, with the distal edge of the femoral neck moving into contact into the cavity.

(b) Removing some of the trochanter from a segmented femur allows a 5th ellipse to be fitted on the distal neck.

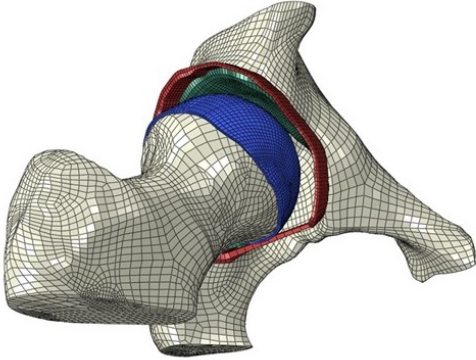
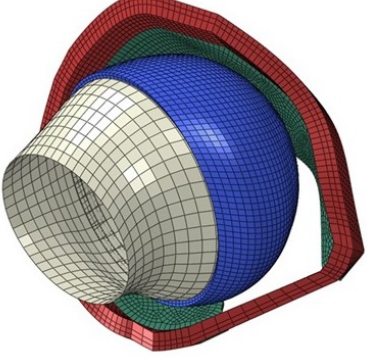
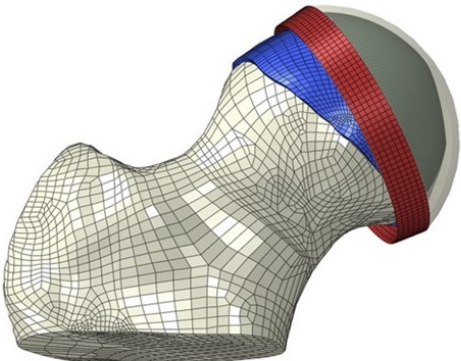
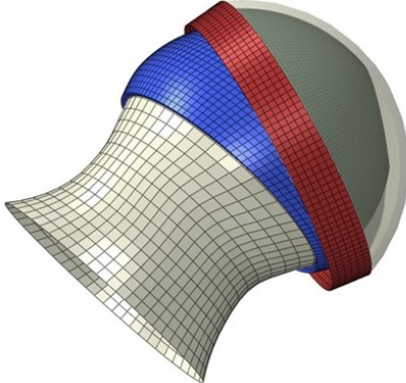
Model	Femur Geometry	Acetabulum Geometry
<p>S1</p> 	Segmentation	Segmentation
<p>P1</p> 	Ellipse based parametric	Spline based parametric
<p>S2</p> 	Segmentation	Spherical parametric
<p>P2</p> 	Ellipse based parametric	Spherical parametric

Figure 5.14: Meshed hip models created for testing boundary conditions:

S1: Fully segmented model.

P1: Equivalent parametric model.

S2: Segmented model using spherical acetabulum.

P2: Parametric model using spherical acetabulum.

In order to simulate impingement, boundary conditions were required to rotate the femur to mimic a clinical impingement test, resulting in abutment of the cam against the labrum and cartilage-labral junction. To achieve this in a manner emulating the *in vivo* scenario, where the femur is rotated into flexion and internal rotation, it was necessary to ensure the femoral head remained in place within the acetabular cavity as rotational movements were applied. To accomplish this, boundary conditions were applied to the reference points defined on the rigid body femoral and acetabular bone parts. In all cases, the acetabulum was fixed in place whilst the femur was positioned in the assembly into an initial position of flexion and internally rotated to impinge against the labrum. Three methods were tested to constrain the femur's position within the acetabular cavity during its rotation: translation control, force control and pinned (Table 5.2). In all cases the boundary conditions on the femur were applied to a reference point at the centre of the head, constraining all nodes on the surface to move with respect to the movement of that reference point.

In the translation controlled models, an initial translation was made to the femur to move it medially and superiorly to establish contact between the femoral and acetabular parts. The displacement boundary condition could be adjusted in each step in order to translate the femur with respect to acetabulum as it rotated. In the force controlled models, this translation boundary condition was replaced with a concentrated force load to hold the femur in place in the joint as it rotated. The force was initially taken as the reaction force produced following a translation step to establish contact, and could also be adjusted in subsequent steps. In pinned models, the femur reference point was pinned to prevent any translation occurring during the rotation steps.

Table 5.2: Impingement boundary conditions for each of three cases. Each boundary condition was applied only in the step indicated, unless propagation to subsequent steps is stated.

Step	Translation Control	Force Control	Pinned
Initial	BC1: Encastre acetabulum	BC1: Encastre acetabulum	BC1: Encastre acetabulum
Move	BC2: Translate femur to establish contact BC3: Prevent femur rotations	BC2: Translate femur to establish contact BC3: Prevent femur rotations Propagate BC3	n/a
Apply force	n/a	Load: Apply concentrated force	n/a
Rotation	BC4: Fix femur translation at current position BC5: Rotate femur about y axis	Propagate or modify Load BC4: Rotate femur about y axis	BC2: Femur reference point pinned BC3: Rotate femur about y axis
Subsequent rotations	Propagate or modify BC4 Propagate BC5	Propagate BC4	Propagate BC2 Propagate BC3

The material properties and surface interactions used in the models in this section were the same as those defined in preliminary models (Section 5.2.1). Models were generated from a selection of patients using different combinations of geometry and boundary conditions (Figure 5.14 and Table 5.2) in order to establish a methodology for comparing segmented and parametric models of several patients for the study in Chapter 6. The decision process was primarily based on which models were subject to overclosure errors, explained in Table 5.3. The following models were tested, assessed for whether convergence was possible:

- Translation control in P1 & S1
- Force control in P1 & S1
- Force control in P2 & S2
- Pinned in P2 & S2

5.4.2 Process automation using Python

Python scripts were developed to automate the process of generating models in Abaqus. For parametric models, the scripts generated specimen-specific parametric bone parts using input parameters as described in Section 3.4.2. Similarly, simplified acetabulum geometry was automatically generated, with scaling according to the femoral head radius. For segmentation-based models, the scripts imported the NURBS surfaces of the segmented bones created in ScanIP as IGES files into Abaqus.

All model set up stages were automated, including the definition of material properties, setting up of analysis steps, meshing, defining contact interactions, and setting the boundary conditions. Directions were automatically adjusted as appropriate to take into account the orientation of left and right hips. Generation of soft tissue geometry and defining of surfaces was automated on the parametric femoral surfaces and the simplified acetabulum. This was possible because points lying on these surfaces could be defined in terms of the input geometrical parameters. In other cases, soft tissues were manually generated (cartilage on the segmented femurs and acetabular soft tissues for both the spline-based and segmented acetabula) because the surfaces required manual selection for each hip. Coordinates of points on these surfaces for specific patients were then extracted from the Abaqus journal files so that the surfaces could later be selected automatically and the manual stages only needed to be performed once as long as no changes to the soft tissues were required. Finally, a function to define and submit jobs was also included in the scripts so that several models could be generated and run in succession using a single script with no

further user intervention.

5.4.3 Findings of boundary condition and geometry tests

Models S2 and P2 using the pinned boundary conditions were found to be the most successful and were chosen to take forward into subsequent studies (Chapter 6). The process for determining this is outlined in Table 5.3.

Table 5.3: Decision process for selecting boundary conditions and geometry.

Model and BCs	Issues and decision
P1 & S1 Translation control	<ul style="list-style-type: none"> • Manual generation of acetabular soft tissue is required. • Overclosure in P1 can be reduced with manual translation adjustment, artificially influencing contact region. • Overclosure in S1 can be reduced with manual translation adjustment, when coarse mesh is used. <p><i>Decision:</i> Reject translation control BC</p>
P1 & S1 Force control	<ul style="list-style-type: none"> • Manual generation of acetabular soft tissue is required. • High forces still lead to overclosure errors in S1. • Lower forces result in the femur displacing from cavity. <p><i>Decision:</i> Reject complex acetabular geometry</p>
P2 & S2 Force control	<ul style="list-style-type: none"> • Simpler geometry reduces overclosure errors. • Generation of acetabular soft tissue now automated. • Matching forces for P2 and S2 still results in the femur displacing from cavity. <p><i>Decision:</i> Reject force control BC</p>
P2 & S2 Pinned	<ul style="list-style-type: none"> • Simpler geometry reduces overclosure errors. • Generation of acetabular soft tissue now automated. • Pinned boundary condition allows impingement to be simulated using either segmented or parametric femurs. <p><i>Decision:</i> Accept pinned boundary condition with P2 & S2</p>

5.4.3.1 Translation control boundary conditions

Models with complex acetabular geometry (P1 and S1) were found to be prone to convergence problems resulting from contact between the complex articular surfaces. Because of the undulating geometry of the acetabular surfaces (opposed to conforming with the femoral surface), some regions were in good contact (i.e. contact without overclosure),

whilst other regions of the cartilage were compressed sufficiently to result in overclosure errors (Figure 5.15). Translation boundary conditions could be adjusted to reduce the occurrence of these errors by translating the femur away from regions of cartilage as they became compressed as rotation progressed. However, it was not possible to do this in a way that ensured the same boundary conditions were used for parametric and segmented models. In S1 models, this approach generally only worked when a coarse mesh was used. Furthermore, avoiding overclosure by simply translating the femur meant that impingement severity was artificially influenced, resulting from the chosen boundary conditions rather than solely from the geometry.

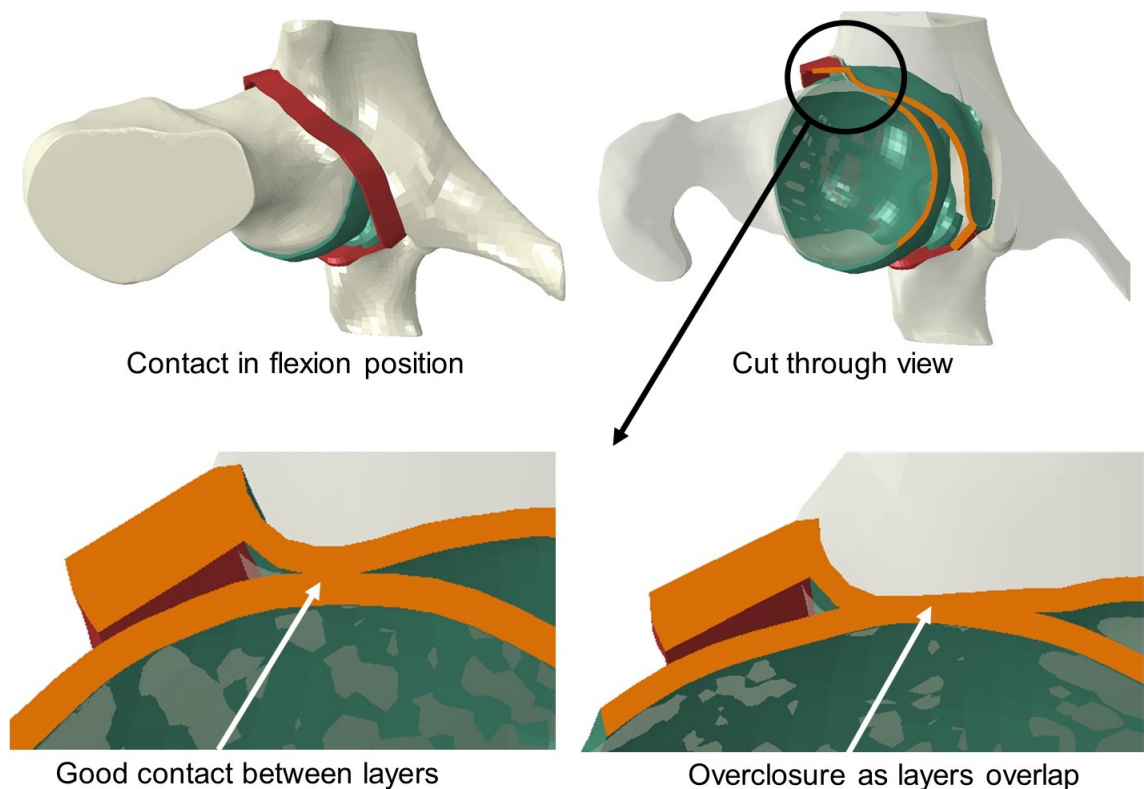


Figure 5.15: When translation control boundary conditions were used, in some regions the articulating layers were in contact, whilst in other regions, errors resulted from overclosure due to excessive cartilage compression. Editing boundary conditions to avoid these issues could essentially render the results meaningless by artificially influencing the region of contact and impingement severity.

5.4.3.2 Force control boundary conditions

In force controlled models, the translation boundary condition was replaced with a concentrated force load to hold the femur in place in the joint as it rotated. This method was used in attempt to avoid artificial influence to the results from selection of translations to achieve convergence. Initial contact must be established before a force can be success-

fully applied, and this was required to be achieved using the same initial translation on the segmented and parametric femurs. Because the segmented and parametric acetabula did not exactly match in shape, overclosure occurred in different acetabular regions between the segmented and parametric models. Thus, like when translation boundary conditions were used, it was necessary to adjust forces as rotation progressed to move the femur away from regions becoming highly compressed. In this way it was sometimes possible to set boundary conditions that allowed models individually to converge. However the force boundary conditions were required to match in segmented and parametric models, and achieving convergence this way was not possible, because the mismatch between the segmented and parametric acetabular geometries meant acetabular elements were positioned differently relative to the femur. Thus overclosure occurred in some cases in one model where it did not occur in the other. When forces were applied to reduce compression in one of the models, the other model aborted due to overclosure now occurring in a different region of this model. However, when a lower force was applied in attempt to mitigate this issue, the force was overcome by resistance from the labrum, so that the femur was translated inferiorly and laterally out of the acetabular cavity.

5.4.3.3 Simplified acetabular geometry

These convergence issues led to development of models P2 and S2, using the same subject-specific femoral surfaces but incorporating simplified, spherical acetabular geometry scaled to the head radius of each femur. Although the articular surfaces in these models were still not conforming, the simplified articular surface of the acetabular side decreased the occurrence of convergence issues due to overclosure. These models also had the significant advantage of rapid automated geometry generation for parametric study (Section 5.5). However, it was still not possible to use the same boundary conditions with segmented and parametric femurs in these models as the analysis aborted when high forces were used, and lower forces still resulted in the femur translating out of the cavity (Figure 5.16).

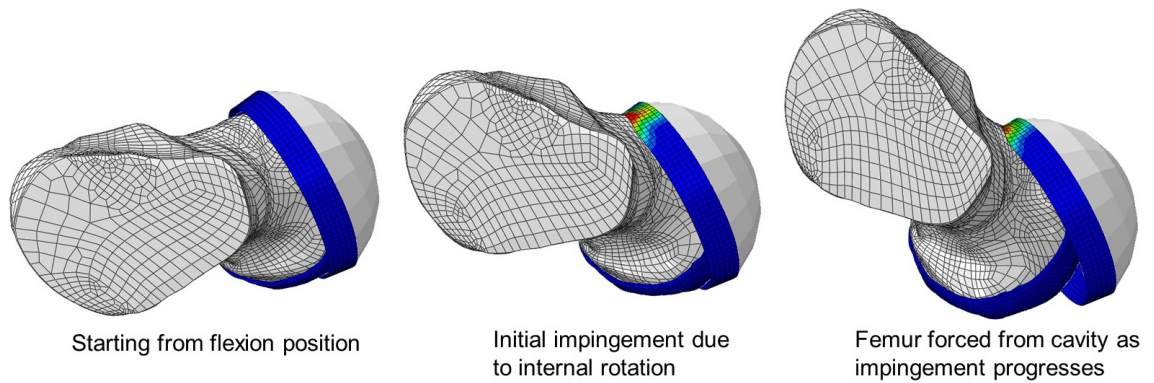


Figure 5.16: When force control boundary conditions were used, the femur was pushed from the cavity by the labrum, whilst greater forces led to the models aborting.

5.4.3.4 Pinned boundary conditions

Using the pinned boundary condition, there were no translations or forces applied to the femur that could be adjusted in each step, so the problem of artificially influencing the region of contact in attempt to achieve model convergence was avoided. Using models S1 and P1, this was not practical because the models rapidly aborted due to overclosure in the cartilage elements closest to femoral head as it rotated. The simplified acetabular geometry used in models S2 and P2 reduced the occurrence of overclosure errors because the smoother surfaces meant there were fewer bumpy regions where the cartilage would be excessively compressed. These models only aborted once a relatively high labral deformations were reached, occurring at anatomically unrealistic levels of internal rotation ($> 30^\circ$), so the range of movement was modelled as far as needed. Whilst cartilage in much of the cavity was not in contact with the femur, this method allowed deformation of the labrum and compression of the cartilage in the impingement region to be simulated without overclosure errors occurring in the other regions (Figure 5.17).

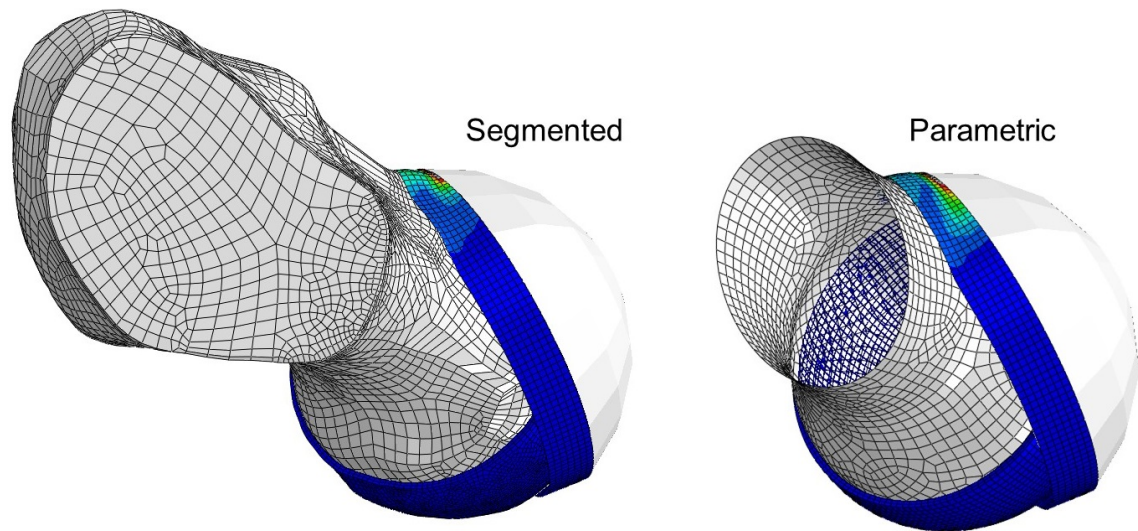


Figure 5.17: When pinned boundary conditions were used with models P2 and S2, models simulated impingement without encountering convergence issues.

5.4.3.5 Model run times

Using coarse meshes (that is, just one or two elements through the acetabular cartilage thickness), once optimal conditions to minimise overclosure in each case had been determined, run times for translation and force models were generally in the region of 0.5 to 3 hours. There was substantial variation depending on the level of rotation achieved in a given model. A considerable amount of the runtime of an analysis can be spent when the model attempts to solve the final step it reaches before aborting. This elevated runtime can be mitigated by limiting the number of increments permitted in each step, at the expense of accepting that the model will abort sooner than it may otherwise have done. Higher mesh models with pinned boundary conditions (up to six elements through the acetabular cartilage thickness) generally required around 7 to 12 hours to run. Using optimised pinned boundary conditions in the studies in Chapter 6, run times were reduced to between 1 and 3 hours using high performance computing facilities, and the determination of final mesh densities for these models is discussed in Section 6.3.1.2.

5.5 Discussion

Because the work in this chapter aimed to identify contact and boundary condition settings to successfully run models whilst minimising the occurrence of errors, the actual values of the model outputs were of relatively little importance. In Chapter 6, models are developed to assess whether trends identified in parametric models match those in segmented

models, and again the exact values of the model outputs will be of less importance than comparisons between them. Furthermore, since the motivation for developing parametric models was to isolate the effects of particular geometric parameters and thereby rapidly obtain predictions about the behaviour of many different hip geometries without requiring the development of multiple complex subject-specific models, it was desirable to keep models as simple as possible whilst maintaining the ability to generate meaningful results.

5.5.1 Geometry considerations

Models incorporating conforming cartilage layers were less prone to overclosure errors than more geometrically complex models because the extent of cartilage regions undergoing high compression due to their undulating geometry was minimised. However these models did not feature subject-specific detail that was included to varying degrees in the parametric and segmented surfaces. The most successful approach to limit the occurrence of errors was to focus on the femur geometry and simplify the acetabular geometry. Limitations due to geometrical simplifications are well documented in literature (Section 2.9.2), but the acetabular simplification allowed models with segmented and parametric femurs to run with the same boundary conditions, and this was required to assess whether the parametric femur model can provide a representation of segmented cam geometry sufficient to assess tissue deformation in the context of impingement. Furthermore, in the impingement loading scenario where the soft tissue strains occurred in the labrum and cartilage-labrum junction, the rest of the acetabular shape has minimal effect on outputs.

Parametric variation was impracticable to apply to the labrum parts generated as bottom-up meshes on surfaces in S1 and P1 because they required significant manual steps to generate. Element selections for defining surfaces were ascertained manually and a process of trial and error was necessary to find suitable vectors by which to extrude the surface mesh to generate hexahedral elements to represent the labrum whilst avoiding self-intersections. Outcomes were sensitive to the vectors used to generate the meshes and these vectors could not be applied consistently between hips due to differences in rim geometry meaning self-intersections in the labrum representations arose with different vectors. Furthermore, this method meant the shape of the labrum depended on the surface mesh, which itself depended either on NURBS patches generated on the segmented acetabular geometry, or on the splines used to generate the parametric surface, which were not factors that could be readily controlled. Conducting parametric studies with this labral geometry, especially at a high mesh density where more elements would require manual selection, would therefore be impractically time consuming. This difficulty of generating

soft tissue for parametric bone surfaces extends to other methods of parameterising the acetabulum, such as the method used by Hua et al. (2015) to generate parametric acetabula, which omitted the labrum. Hua et al's method produced sharp corners on the acetabular representation, meaning it would be challenging to automate hexahedral labral elements onto this rim.

The generation of soft tissue is even more challenging for segmentation-based models. In order to conform during articulation, acetabular and femoral surfaces must both be spherical, otherwise as soon as rotation occurs, the geometries no longer conform. Therefore when subject-specific geometry is used, offsetting the femur mesh and using a further offset as acetabular cartilage never results in rotational conformity. When conforming spherical cartilage layers were generated over non-spherical segmented bone surfaces, the resulting geometry could not be readily meshed using hexahedral elements. The alternative method of creating cartilage as offset orphan meshes allowed hexahedral elements to be used. The cartilage was terminated at roughly 5 mm from the top of the head down the femoral neck axis (for $HR = 22.95$ mm, scaled according to head radius) so that the cam was not covered. However all surfaces interactions were modelled as frictionless, and whilst this is appropriate for cartilage-on-cartilage contact, it may be less appropriate for bone on soft tissue. When impingement was simulated, contact occurred between the femoral bone and the labrum and a small region of the acetabular cartilage at the junction, as well as between cartilage layers. Some other studies have avoided this issue by covering the whole femoral head including cam region with cartilage Jorge et al. (2014). This is less anatomically realistic, and including a frictionless interaction between bone and soft tissue allows the effects of rigid bone displacing the cartilage-labrum junction to be observed.

The circular acetabular rim used in the simplified acetabular models allowed the labrum to be automatically generated and meshed with no manual intervention in such a way that it could be readily parametrically varied, which was not practical using the spline-based parametric geometry. The simplified spherical acetabulum could be controlled precisely and the labrum was generated about the rim using a triangle cross-section, with parameterised dimensions. This allowed for parametric study of the effects of labrum length and labrum/bone coverage ratio, which is covered in Chapter 6. The volume of soft tissue structures in the simplified acetabulum were scaled according to femoral head radius since cartilage thickness is related to bone size (Shepherd and Seedhom, 1999). In practice, the variation in cartilage thickness between models was in the region of 0.1 mm, and since the outputs of interest were extracted primarily from the cartilage-labrum junction, this variation was observed to have little effect on model outputs.

5.5.2 Boundary condition considerations

Using translation boundary conditions, it was sometimes possible to avoid overclosure errors by setting up boundary conditions to adjust the position of the femur part way through the rotation used to simulate impingement. Force control was tested as a potentially more realistic method of moving the femur within the cavity, but in practice it was also necessary in these cases to adjust forces during analysis to artificially prevent overclosure that would otherwise lead to convergence issues. Moreover, even when overclosure errors could be avoided, deformation of the labrum occurred in conjunction with unrealistic translation of the femur away from the cavity. Increasing the forces to avoid this issue also resulted in the models aborting.

The chosen boundary condition method of pinning the femur was simplest of the three tested methods, with only rotational motion permitted and no translation occurring. This is a simplification of the situation *in vivo*, since the femur does not really rotate around a fixed point, but the assumption was deemed reasonable since the congruency of *in vivo* articulating surfaces means there is usually very little detectable translation and most of the motion between the femoral head and acetabulum is rotational (Harding et al., 2003; Bowman et al., 2010). By using a boundary condition to pin the centre of the femur, overclosure in cartilage elements was avoided and these models only aborted when very high labrum deformation occurred as a result of testing unphysiologically high rotations.

In comparison, many other studies used loading based on force data from patients with instrumented hip replacements, published by Bergmann et al. (2001) (Table 2.1). This was considered inappropriate for this study since FAI patients are younger and have deformities that could result in altered gait and movement patterns. Furthermore, the focus here was on simulating an impingement test, and there was no specimen-specific force data available for this.

5.5.3 Material properties

Geometry drives most of the changes to contact pertinent in these impingement models (location of regions undergoing high strain and its severity). Nevertheless, the effects of simplified material models should be discussed.

Given other simplifications, it is unlikely that modelling bone as fully rigid, as opposed to elastic with a much higher modulus than cartilage (that is, around 17 GPa), would affect the results in terms of the trends they suggest (Chegini et al., 2009; Jorge et al., 2014). Ad-

ditionally, modelling bone as deformable would require solid bone geometry. This is very difficult to mesh with hexahedral elements, although a hexahedral mesh is less important for bone since it is not expected to exhibit much deformation or incompressibility.

The complex composition and structure of articular cartilage mean it has complex material behaviour (Section 2.8.3.1), so the limitations of the simplified material model approach taken here should be noted. Depending on the level of geometric representation, and assuming realistic boundary conditions, the location and area of contact in linear elastic models would likely be similar to those occurring *in vivo*, and the use of more complex constitutive equations to describe cartilage material behaviour would be unlikely to yield significant changes in contact areas; some validated specimen-specific studies have suggested that contact stress and area may be relatively insensitive to material nonlinearity and spatial inhomogeneity in cartilage constitutive models (Henak et al., 2014b). However, peak values of pressure and soft tissue strain may be less realistic when using linear elastic material properties. It may be necessary to consider material anisotropy to obtain more accurate estimates of outputs such as shear strains in the cartilage and circumferential strains in labrum that could potentially further elucidate mechanisms of damage to the soft tissues. The material model used here for cartilage did not take into account the following:

- Fluid located between the articular cartilage and subchondral bone plate.
- Time dependency of cartilage behaviour.
- Cartilage modulus directional dependency.
- Labrum modulus directional dependency.

These limitations mean numerical results from these models may not match well with experimental predictions, but it is initially more important that parametric models are able to distinguish between cases and provide reliable qualitative predictions of trends, rather than producing accurate quantitative data. More sophisticated material definitions incorporating directional dependency were subsequently investigated (Section 6.2).

5.5.4 Conclusions

The work in this chapter has assessed the challenges in using different geometries to represent femoral and acetabular surfaces, and in establishing effective boundary conditions to simulate impingement. It was important to establish a methodology that allowed the same boundary conditions to be used for models incorporating segmented femurs and those incorporating parametric femurs, in order to go on to conduct a comparison study

in Chapter 6. At the same time it was necessary to avoid or limit the occurrence of excessive compression and overclosure of articular surfaces, which lead to models aborting as a result of highly distorted elements preventing convergence. Settings to use in Abaqus to optimise hip impingement simulations for convergence were identified. Acetabular geometry was ultimately simplified in order to allow for automated parametric variation and to lessen convergence issues related to overclosure arising in irregular articular surfaces. Boundary conditions to simulate impingement were also simplified by pinning the femur to prevent translations as it rotated, both to aid model convergence and because no specimen-specific loading data was available.

Chapter 6

Finite Element Model Study

6.1 Introduction

In order to investigate the effects of bone morphology on tissue strains computationally, it is useful to be able to automatically generate many different geometries representative of the population variation. This can be achieved using a parametric approach to finite element models of the hip (Chegini et al., 2009; Hua et al., 2015). In previous chapters, a geometric parameterisation system was developed, capable of representing segmented femurs with cam deformity with root mean squared surface fitting errors in the region of 0.6 mm, allowing isolation of the size and position of cams.

Recently Hua et al. (2015) demonstrated that parameterised models are able to identify differences in contact mechanics between two different subjects with healthy hips across a loading cycle, providing confidence that such models can be used to systematically evaluate the effects of clinically relevant changes in morphology. However, some studies suggest that models with idealised or simplified geometry can lead to poor estimates of hip contact stresses (Anderson et al., 2010; Gu et al., 2011) (Section 2.9.2). It is therefore important that parametric models are compared with segmented patient-specific models in order to understand the effects of smoothing out local undulations in subject-specific articular geometries. As well as isolating the effects of individual changes in joint features, parametric models with simplified articular surfaces can alleviate computational convergence issues (Hellwig et al., 2016) reported to occur when using more complex geometry (Jorge et al., 2014) (Section 5.5.1).

It is also important that geometrical variations generated in parametric models are well

defined. Clinically used radiographic measurements such as the alpha angle are highly dependent on the two-dimensional radiographic view of the joint and do not capture the full three-dimensional geometry (Harris et al., 2014; Cooper et al., 2017); alpha angles can therefore be ambiguous and are not well suited to describing geometrical variation, as seen in Chapter 4.

Previous studies that developed natural hip models have reported stresses and contact pressures (Anderson et al., 2010; Gu et al., 2011; Jorge et al., 2014). Contact pressures have been widely used to assess the degree of cartilage compression (Ng et al., 2016a), but strains and changes in position of soft tissues, especially the labrum and cartilage-labrum junction, may be more pertinent for improving understanding of when impingement damage may occur. Abutment of the cam against the acetabular rim may result in damage due to compression and abrasion of cartilage, and translation of the labrum away from the joint (Banerjee and Mclean, 2011; Kuhns et al., 2015).

In Chapter 5, preliminary FE models were used to identify contact settings and boundary conditions that can be used to simulate FAI. This chapter uses this methodology to generate further parametric models, including patient-specific models of the 20 introduced in Chapter 4. Specifically, the aims of the study in this chapter were to:

1. Investigate the effects of extending the material property model to include transverse isotropy in parametric models.
2. Establish the effect of geometric simplification in finite element models of impingement by validating results from models using geometrically parameterised femurs against models using their segmented equivalent, built from 20 patients diagnosed with cam deformity.
3. Demonstrate the capability of the parameterisation system in distinguishing the effects of cam size and position, beyond what is possible using an alpha angle measurement.
4. Assess the effects of parametrically varying labrum size and labrum-bone ratio.

6.1.1 Study methodology

Quasi-static finite element models were developed and automated using Python scripts following the methodology introduced in Chapter 5. Bone surfaces were modelled as rigid and femoral cartilage was assigned with isotropic linearly elastic material properties ($E = 12 \text{ MPa}$, $\nu = 0.4$). As established in Section 5.2.1, contact between surfaces was modelled as frictionless with finite sliding and hard contact with the linear penalty contact

constraint enforcement method.

Simplified acetabular geometry (Section 5.3.3.3) was used in all models in this chapter, and acetabular cartilage and the labrum were modelled as linearly elastic materials and meshed with hexahedral elements within Abaqus. Section 6.2 describes investigations of including directional dependence in the material properties for the acetabular cartilage and labrum based on collagen fibril alignment.

The ellipse-based parameterisation system was then used to develop models of the 20 cam patients using specimen-specific parametric femurs. Results from these models were validated against equivalent models using segmented femoral geometry in order to ascertain whether parametric femurs are able to provide an approximation of the cartilage and labrum deformation found in models using segmented femurs (Section 6.3). The Advanced Research Computing 2 (ARC2) high performance computing facility was used to run models with higher density meshes (Section 6.3.1.2). Parallelisation options were used so that Abaqus could run jobs on multiple processing cores.

The parameterisation method also allowed the generation of new femoral geometries with the neck region described by ellipses. Models assessing parametric variations to cam morphology are described in Section 6.4.1.1, and the results of these models demonstrated the issues with using alpha angles to quantify cam severity. The simplified spherical acetabulum allowed the parametric study of clinically relevant morphology changes to the acetabular rim. Models assessing parametric variations to acetabular rim morphology are described in Section 6.4.1.2, and these models found more severe impingement occurred with greater bony coverage.

6.2 Material property sensitivity

To establish the effects of considering collagen fibril alignment by including material directional dependency, models were developed with different combinations of isotropic and transversely isotropic material properties assigned to the acetabular cartilage and labrum. These models simulated the basic impingement scenario of (25°) of internal rotation from an initial flexion position (90°) using an automatically generated parametric femur (cam-rad = 96.25%, cam-angle = 40° , cam-width = 38%). (Section 6.4.1.1 details the method for generating femurs with desired cam parameters, and these particular values were chosen as the averages of the cases developed for parametric study.)

As a base case, acetabular cartilage and the labrum were modelled as linearly elastic, with

cartilage layers assigned $E = 12$ MPa and $\nu = 0.4$, and the labrum assigned $E = 20$ MPa and $\nu = 0.4$ (following the methods used for models in Chapter 5). In three additional models, acetabular soft tissues were assigned transversely isotropic properties based on typical collagen fibril alignment. To generate a more complex acetabular cartilage model, cartilage was modelled as three distinct layers, with the overall dimensions matching those in the acetabular cartilage part used in the original simplified acetabular geometry definition (Section 5.3.3.3). Thus the total thickness was 1 mm, and the process was automated as before, with the script adapted to merge the three layers into a single part. The three sections of the resulting part were then assigned with different material properties. Two elements were used across the thickness of each acetabular cartilage layer, thus six elements in total were used across its thickness (Section 6.3.1.2).

In order to define directionally dependent material properties, it was necessary to define part-specific coordinate systems (Figure 6.1). A part-specific coordinate system was created on the acetabular cartilage such that one axis was perpendicular to the articular surface (normal axis) and the other two axes (transverse axes) were perpendicular to the normal axis. A cylindrical coordinate system was created on the labrum such that one axis followed the circumferential direction about the acetabular rim (circumferential axis) and the other two axes (radial axes) were normal to this axis in any given cross section of the labrum.

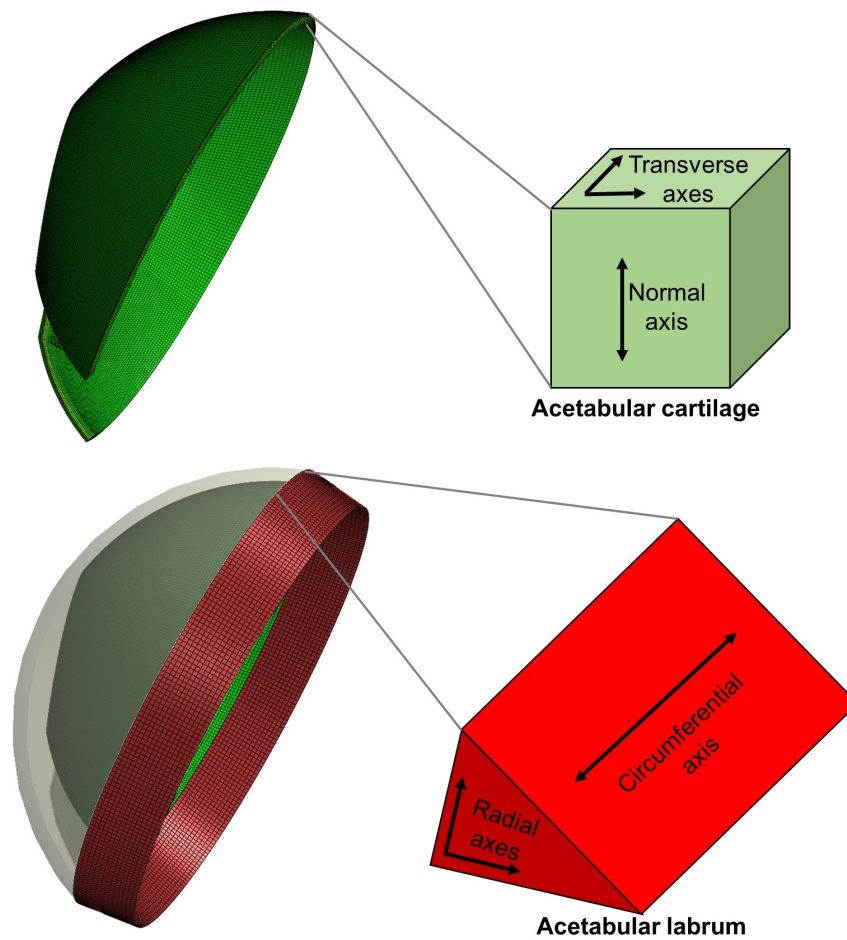


Figure 6.1: Axes defined on acetabular soft tissues.

Transversely isotropic material properties were defined by assigning values to the engineering constants in Abaqus; the Young's modulus, shear modulus and Poisson's ratio in each of the three directions. The shear moduli and Poisson's ratios were the same across all models, whilst the Young's moduli were varied. In all acetabular cartilage layers and in the labrum, Poisson's ratio, ν , was set as 0.4 and the shear modulus, G , was assigned so that $2G = (E_{\text{mean}})/(1 + \nu)$. The Young's moduli were varied based on collagen fibril alignment.

Collagen fibrils in cartilage are believed to be orientated parallel to the articular surface in outer layers, but perpendicular and anchored to the bone in inner layers (Chen et al., 2001; Fox et al., 2009; Osawa et al., 2014; Meng et al., 2017a) (Section 2.8.3). Thus in the acetabular cartilage, the transverse elastic modulus was assigned to be greater at the surface, reduced in the middle layer and lowest at the base layer forming the boundary between subchondral bone and cartilage ($E = 15, 12, 9$ MPa respectively). The axial modulus was assigned to be lowest at the articular surface, increased in middle layers and greatest at the base layer ($E = 9, 12, 15$ MPa respectively). At the osteochondral interface between cartilage and bone, there is a calcified layer of cartilage (Flachsmann

et al., 1995; Fox et al., 2009) above the subchondral bone. In mature tissue, delamination may occur along the tidemark between the articular cartilage and calcified cartilage above the subchondral bone (Tannast et al., 2007; Banerjee and Mclean, 2011; Bredella et al., 2013). The much higher modulus of the calcified region was taken to be incorporated into the rigid bone layer for the purposes of the models developed here.

Collagen fibrils in the labrum are believed to be predominantly aligned circumferentially (Petersen et al., 2003; Grant et al., 2012) (Section 2.8.3), so a greater modulus was assigned in the circumferential direction compared to the radial directions ($E = 20$ MPa and 12 MPa respectively).

In summary, the four model variations run in this section were:

- Isotropic acetabular cartilage and isotropic labrum.
- Isotropic acetabular cartilage and transversely isotropic labrum.
- Transversely isotropic acetabular cartilage and isotropic labrum.
- Transversely isotropic acetabular cartilage and transversely isotropic labrum.

6.2.1 Results and discussion

In all models the typical deformation pattern consisted of displacement of the labrum and compression of the cartilage-labrum junction (Figures 6.2 and 6.3). The location of peak strain moved as rotation progressed, beginning in the posterior-medial cartilage, moving to the tip of the labrum at the start of impingement, and increasing most in the anterior-superior cartilage-labral junction at the peak of impingement (Figure 6.4).

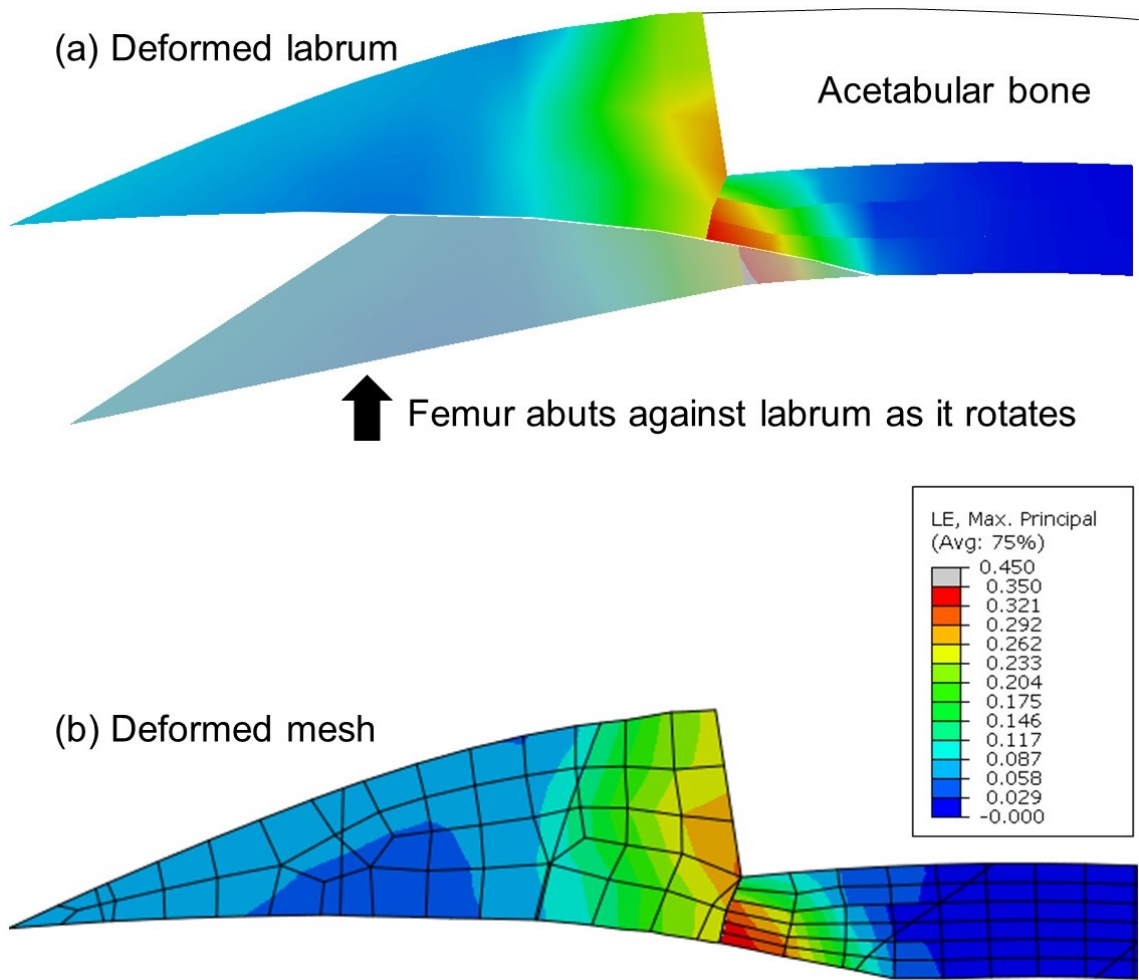


Figure 6.2:

(a) Example of a cross section of the deformed (bright colour) and undeformed (shaded) cartilage-labrum junction. Regions of high tensile strain are displayed in red.

(b) The same deformed cartilage labrum junction shown meshed.

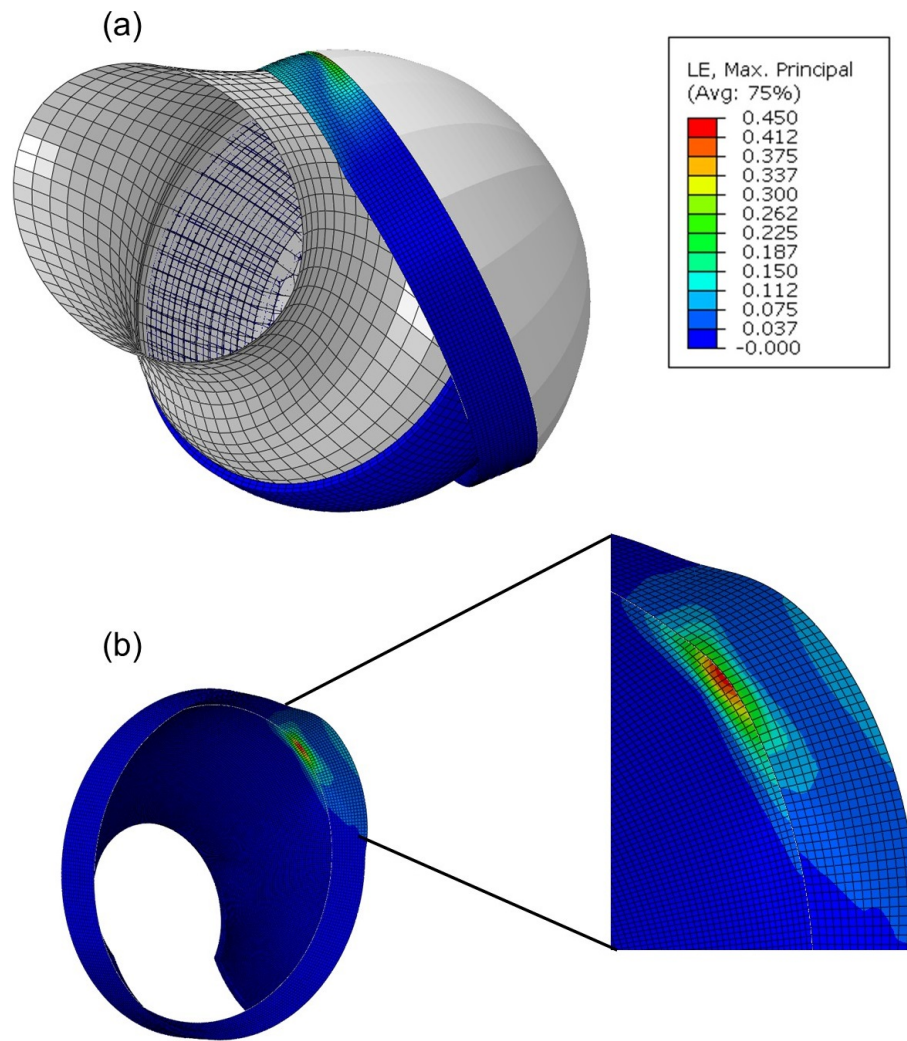
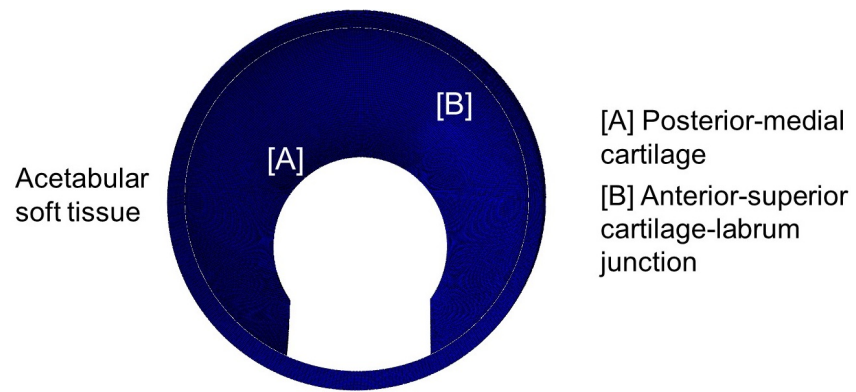


Figure 6.3: Specific example of high strains occurring in elements at the cartilage labrum junction:

(a) In the coronal view with the femur visible.

(b) In rotated view with the femur hidden to highlight the region of impingement contact on acetabular soft tissue.



Location of peak strain at given internal rotation

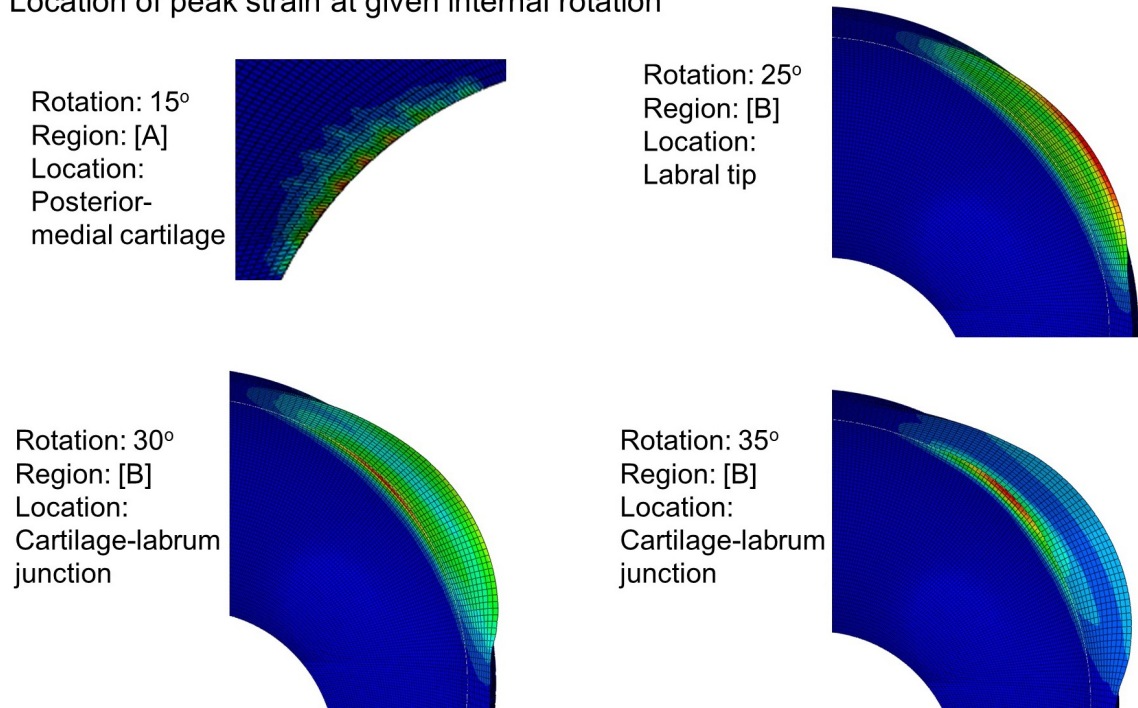


Figure 6.4: Location of peak strain moves from the cartilage to the labral tip and ultimately to the cartilage-labrum junction as impingement progresses.

Labral displacement was similar in the four different cases, whilst tensile strain decreased as transverse isotropy was included in the cartilage and labrum (Figure 6.5). Displacements and strains in the models at 90° of flexion and 25° of internal rotation are shown in Figure 6.5. The strain values are explicitly tabulated in Figure 6.6, which also shows the directions of the tensile strains occurring in the labrum and cartilage in each case. The model with transversely isotropic cartilage had lower peak maximum tensile strain (0.127) in the cartilage-labrum junction compared to the isotropic case (0.137). The model with the transversely isotropic labrum also had lower peak maximum tensile strain (0.126) in the cartilage-labrum junction compared to the isotropic case (0.137). When transverse isotropy was included in both the cartilage and the labrum, the peak maximum tensile strain in the cartilage-labrum junction was even lower (0.116).

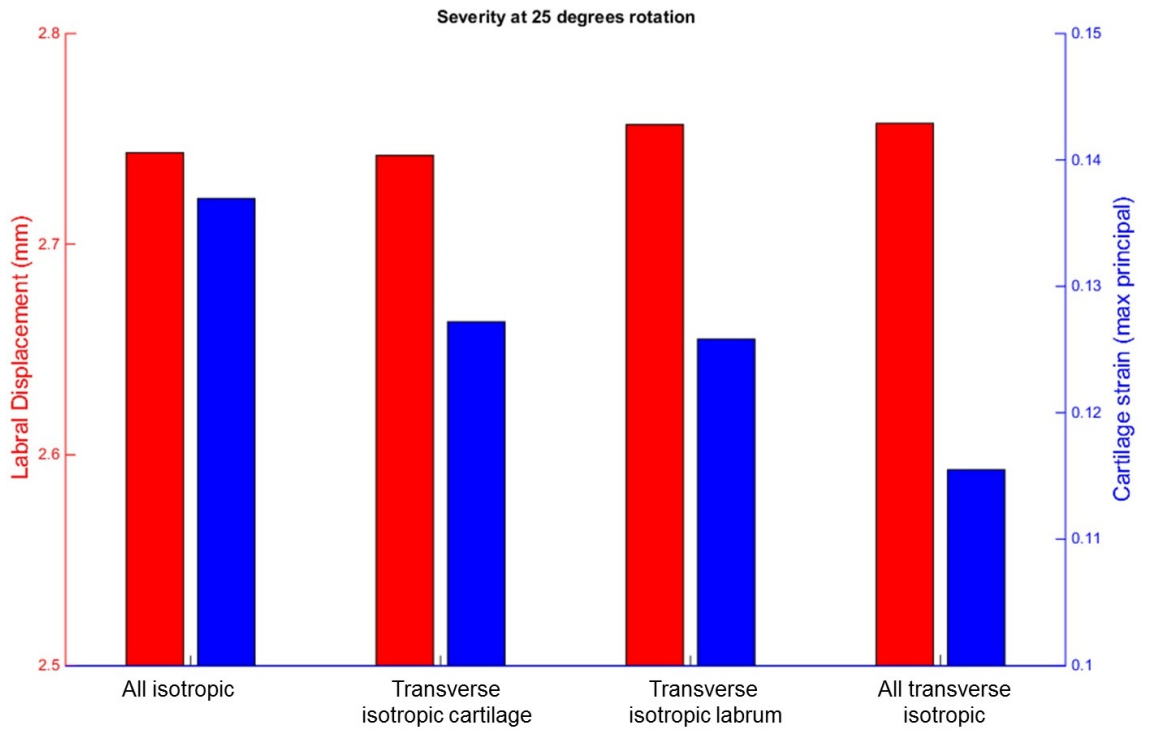


Figure 6.5: Labral displacement was similar in the four different cases, whilst tensile strain decreased as transverse isotropy was included in the cartilage and labrum.

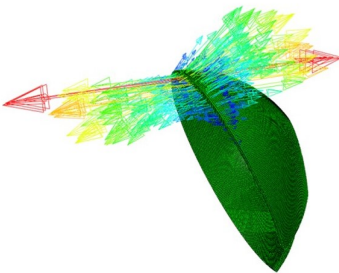
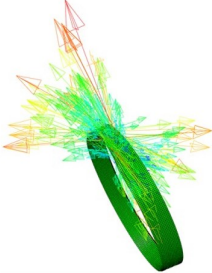
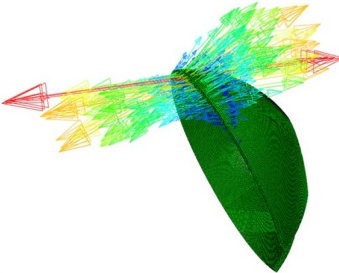

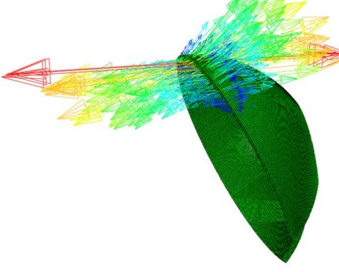

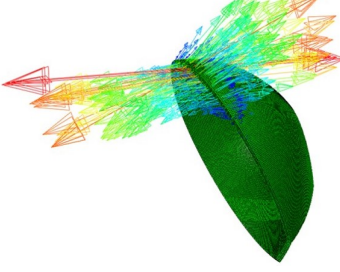
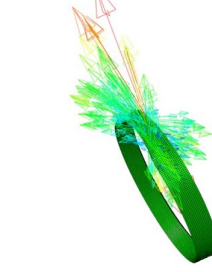
Model	1. Peak max. princ. strain in cartilage 2. Peak max. princ. strain in labrum 3. Peak radial strain in labrum 4. Peak circum. strain in labrum	Directions of maximum principal strains	
		Cartilage	Labrum
All isotropic	0.137 0.094 0.090 0.142		
Transverse isotropic cartilage	0.127 0.095 0.091 0.143		
Transverse isotropic labrum	0.126 0.143 0.138 0.114		
All transverse isotropic	0.116 0.142 0.137 0.113		

Figure 6.6: Strain values found in the labrum and cartilage-labrum junction at 25° of internal rotation for each of the four material property cases. The directions of the tensile strains are shown on the cartilage and labrum parts; red colours show the direction of the highest tensile strains, but note the difference in peak values for the different cases.

The decrease in strain in the transversely isotropic cartilage model occurred because the transverse stiffness of the cartilage was higher in the articular surface layer, meaning there was less cartilage compression in the region where the greatest tensile strains occurred. Representing the cartilage as three distinct layers with different Young's moduli led to a decrease in overall compression even though the average properties over the layers were the same as the properties used in the base model, highlighting the importance of including these different properties to observe effects resulting from different strains presenting

in distinct layers. The directions of the tensile strains remained largely the same as the cartilage was compressed.

Decreasing the stiffness of the labrum in the radial directions meant that radial strains in the labrum were increased and circumferential strain was decreased (Figure 6.6). The decrease in circumferential strain in the labrum decreased tensile strain in the cartilage since the cartilage was pulled less by local displacement of the labrum at the junction region. The higher tensile strains in the labrum were more concentrated in the direction perpendicular to the cartilage layer at the cartilage-labrum junction (Figure 6.6). Furthermore, in all transversely isotropic cases, the region of influence of the cam was larger due to the softer materials, so the tensile strains were decreased as the compression spread over a greater region. In cases with transverse isotropy in the labrum, the strain level was higher in the labrum than in the cartilage as radial strains increased in the region where the labrum attaches to the acetabular bone.

Since the inclusion of transverse isotropy in both the cartilage and the labrum were observed to have an effect on output strains, they were both carried forward to the rest of the models in this chapter.

6.3 Segmented vs parametric femoral geometry

6.3.1 Methods

In this part of the study, segmented and parametric femoral surfaces from the 20 patients investigated in Chapter 4 were developed into finite element models (Figure 6.7).

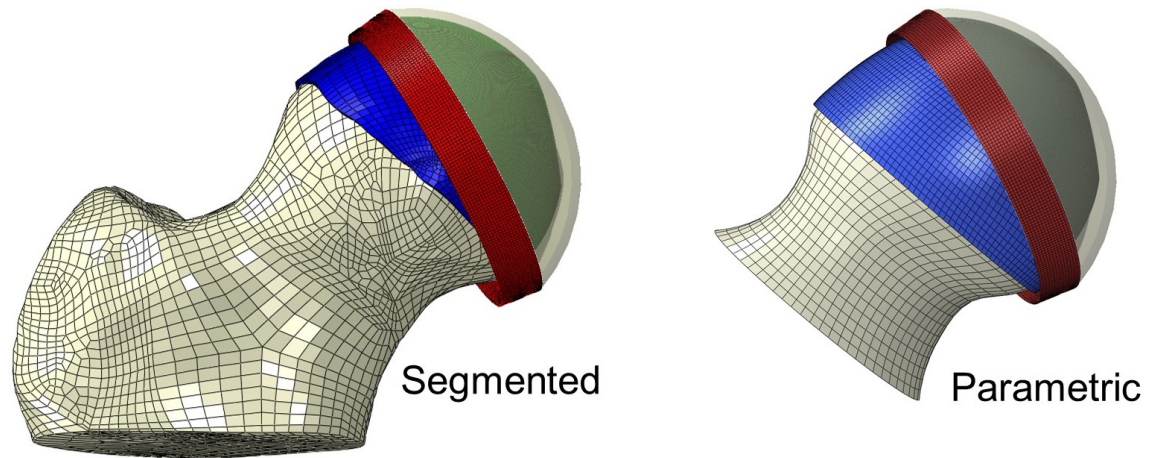


Figure 6.7: Examples of meshed models:

- (a) Incorporating a segmented femur.
- (b) Incorporating a parameterised femur.

These models again used the pinned boundary conditions applied to the femoral head, established as effective in Section 5.4. Starting from a flexion position (90°), boundary conditions were used to simulate internal rotation of the femurs up to a maximum of 35° . In all cases, the acetabulum was fixed in place whilst the femur was constrained in translation and rotated to impinge against the labrum.

By default femurs were rotated about their femoral head centre, but in practice this was only successful in 6 of the cases. In the other 14 cases, this rotation either caused severe overclosure of the femoral and acetabular surfaces, or did not result in the cam contacting the labrum. Such issues were observed to occur for both parametric and segmented models, since they resulted from the position of the cam relative to the acetabulum. In these cases the position for the centre of rotation was determined by trialling different positions along the femoral neck axis in order to optimise for model convergence whilst achieving impingement against the labrum. The same boundary conditions were used for the segmented and parametric models of each individual patient, but in this way were varied across patients to optimise for convergence without overclosure due to the irregular contact surfaces.

6.3.1.1 Outputs of interest

Peak displacements in the labrum and tensile strains (maximum principal logarithmic strain) at the cartilage-labrum junction were recorded throughout the simulations. Maximum displacements occurred at the labral tip and, taken in the context of labral length, this gave one indication in each case of the severity of impingement as the labrum was

deformed by the cam. Tensile strain occurring at the cartilage-labrum junction area was also of interest because this deformation may relate to the cause of cartilage surface fibre damage.

Although the results from each patient should not be directly compared due to the difference in boundary conditions used, agreement of the segmented and parametric models was also assessed by ranking the severity across the 20 patients.

Python scripts were developed to automatically extract from the Abaqus output (odb) files the maximum values of these outputs for each step of each model, facilitating the generation of multiple graphs automatically using MATLAB.

6.3.1.2 Mesh convergence

The mesh density adopted was determined after mesh convergence tests. Displacements seen in the models were converged at the mesh density of 3 elements across the thickness of the acetabular cartilage and labrum, but local strain was more sensitive to mesh resolution. To achieve convergence for all outputs of interest, 6 elements were used across the thickness of the acetabular cartilage and labrum (that is, 2 elements for each distinct cartilage layer), resulting in approximately 156,000 elements for the acetabular soft tissue. Only 2 elements were used across the thickness of the femoral cartilage because outputs from acetabular side were of interest and the femoral cartilage did not play a role in the contact of the bony cam and acetabular labrum junction. In practice, the similar trends between segmented and parametric models were also apparent at the lower mesh density. This can be seen for a particular patient for both displacement and strain in Figure 6.8, which shows the results using 1 and 2 elements through the thickness of each distinct acetabular cartilage layer respectively. The graphs for all patients at the lower mesh density are provided in Figure 6.9, and the final graphs for all patients are provided in Figure 6.10.

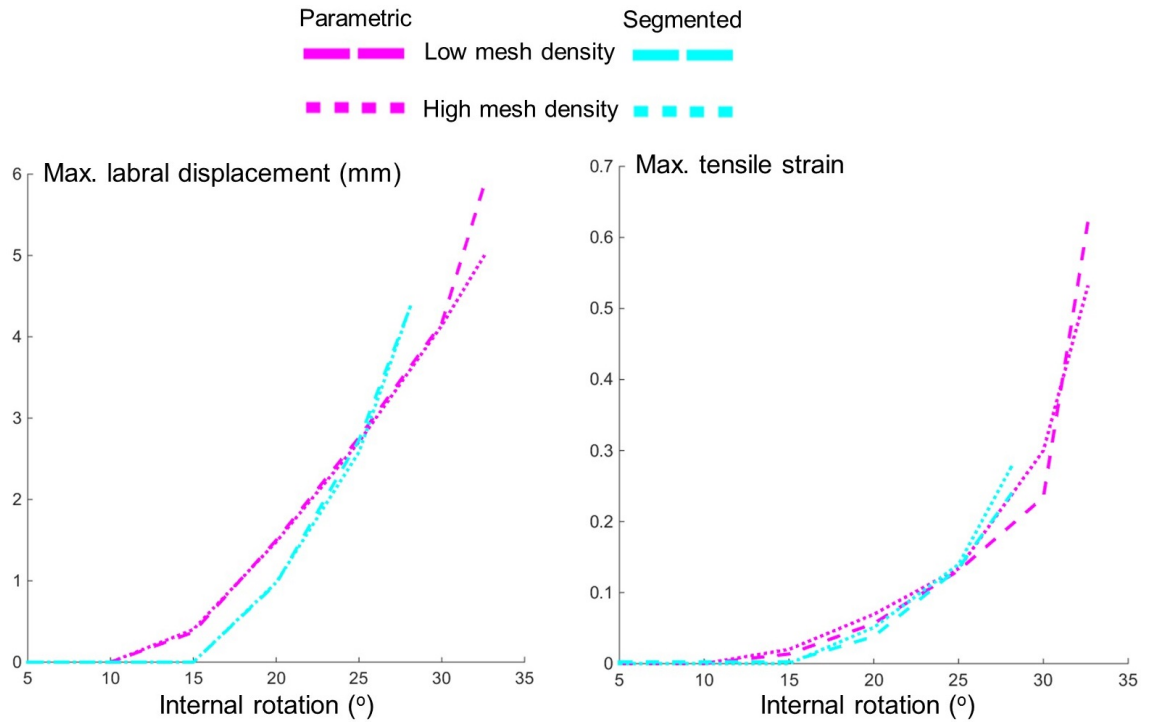


Figure 6.8: Graphs for a particular patient (Hip 28L) demonstrating similar results for displacements and strains for low (3 elements through acetabular cartilage) and high (6 elements through acetabular cartilage) mesh densities.

6.3.2 Results

The range of positions used for the centre of rotation was -2 mm to 4 mm (where positive is more proximal and 0 indicates the femoral head centre). The centre positions used for each model are tabulated in Appendix B (Table A5). The average centre position was 1.2 mm proximally above the femoral head centre, along the femoral neck axis. Even so, not all models converged at the full 35° of internal rotation.

Generally similar displacements and strains occurred in the segmented and equivalent parametric models; this could be seen at lower mesh densities as well as in the final models. Figures 6.9 and 6.10 consist of graphs displaying results from segmented and parametric models for each of the 20 cam patients. The x-axes show internal rotation in degrees. Displacements (blue, left y-axes) are in mm. Strains (red, right y-axes) are peak maximum principal logarithmic strains. Results from segmented models are displayed as solid lines, and the equivalent parametric model results in each case are displayed as dashed lines. The scales for axes on the graphs were chosen to aid clarity of comparison between segmented and parametric results by ensuring the strain and displacement lines were not overlaid.

Although the results from different patients should not be directly compared due to the difference in boundary conditions used, the severity ranking across the 20 patients was similar when assessed using the segmented and parametric results. For strain after 25° of internal rotation (converged for all patients), the ranking order was well matched, indicated by a Spearman's rank correlation coefficient of 0.9035.

In the high density mesh models, the range in root mean squared difference in results for the segmented and parametric models was 0.0039 – 0.1292 mm for peak labral displacement and 0.0002 – 0.0134 for peak strain. For context, displacements peaked at 5.4 mm, and strains peaked at 0.53. The scales were chosen for clarity of differences and mean that some of the peak displacements are not visible.

The lower levels of agreement between strains and displacements in the parametric and segmented models occurred when the local fitting errors between the parametric and segmented surfaces in the cam region were larger, particularly > 1 mm (Figure 6.12). This was a result of ellipses failing to adequately capture the shape of slices through the segmented surfaces (6.11).

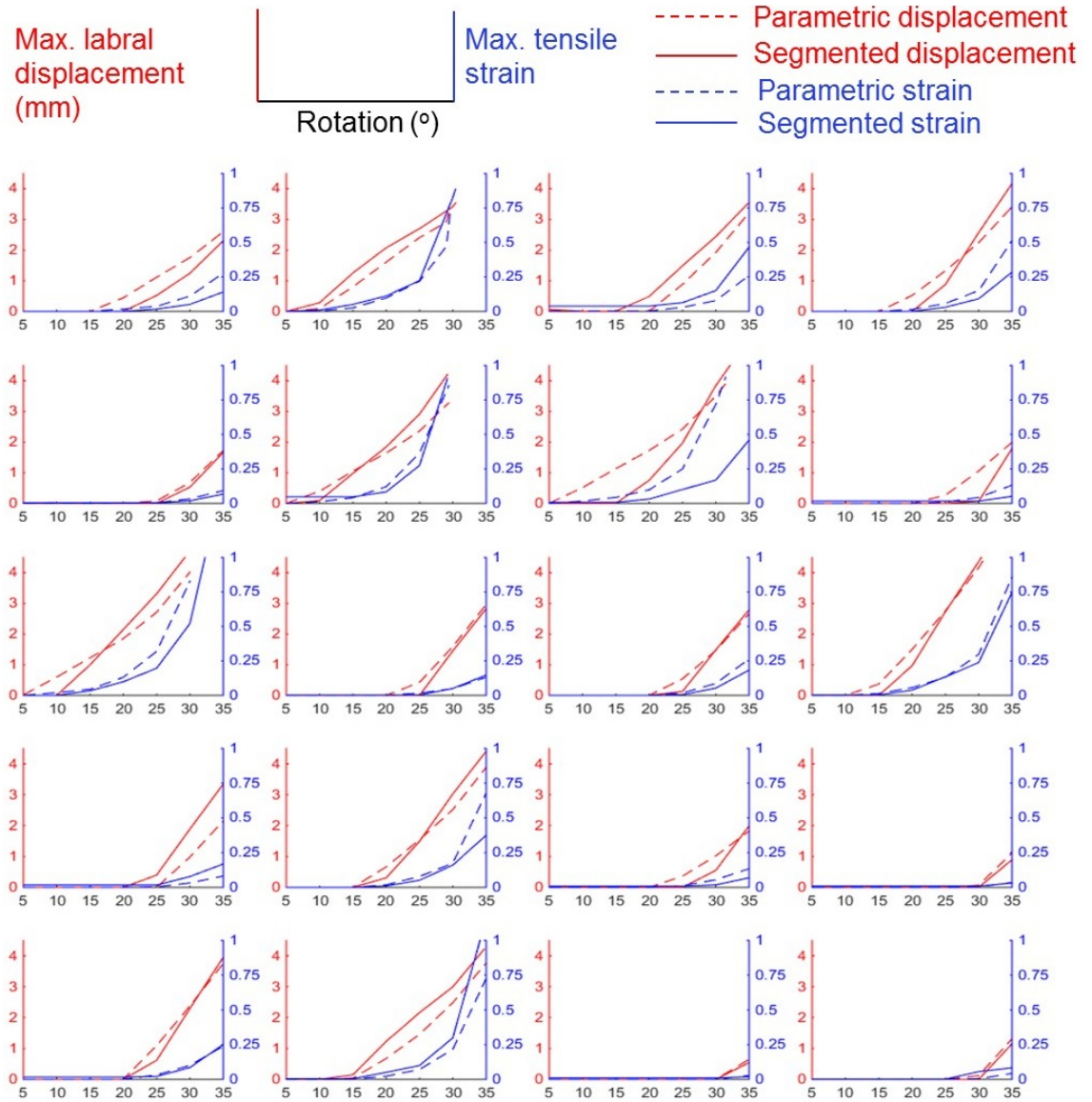


Figure 6.9: Graphs for each patient from low mesh density models comparing maximum labral displacement and acetabular soft tissue strain with increasing internal rotation, in segmented and parametric femur models.

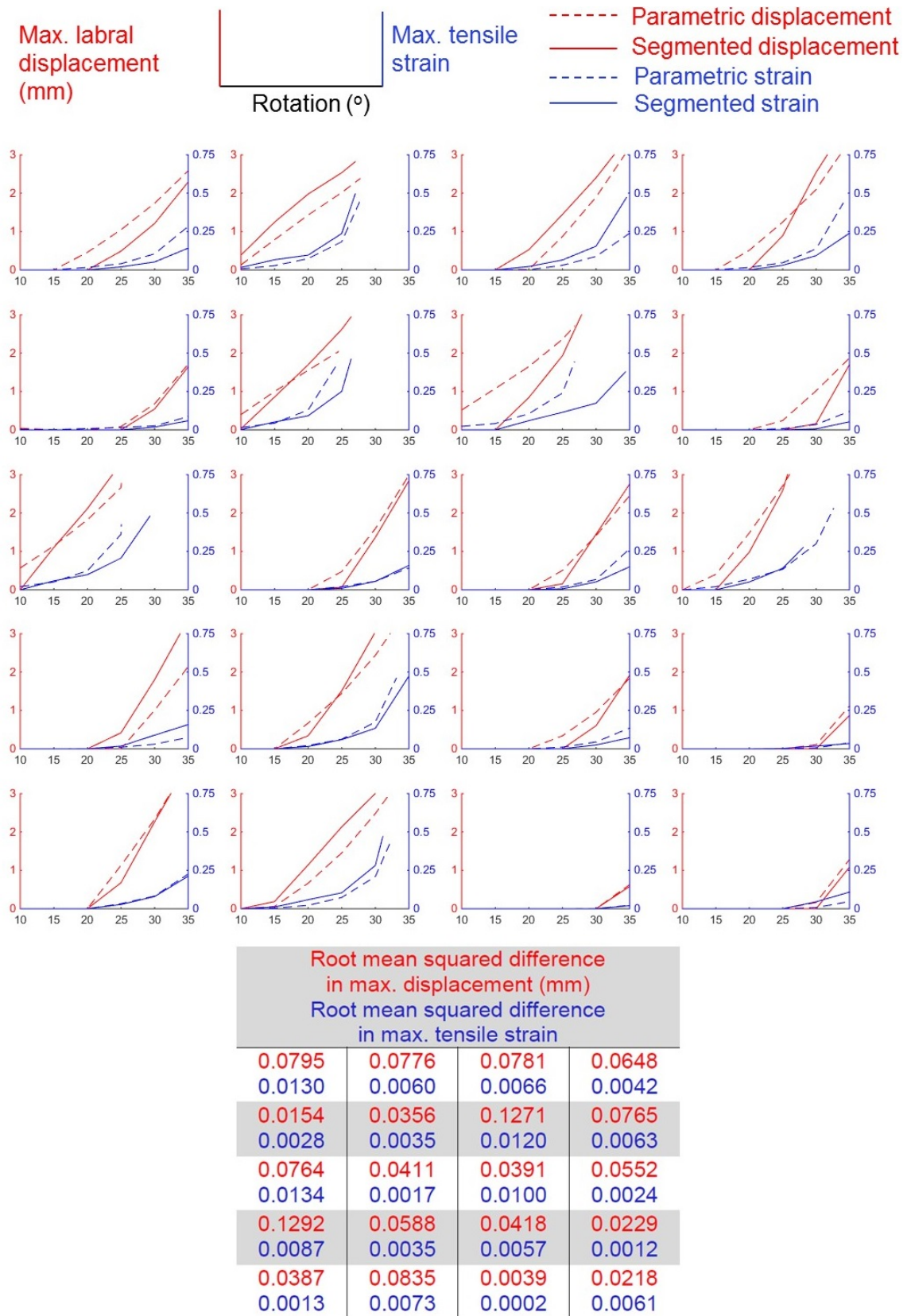


Figure 6.10: Graphs for each patient from high mesh density models comparing maximum labral displacement and cartilage-labrum junction strain with increasing internal rotation of the femur. Root mean squared differences between the segmented and parametric results for each output are tabulated beneath the graphs.

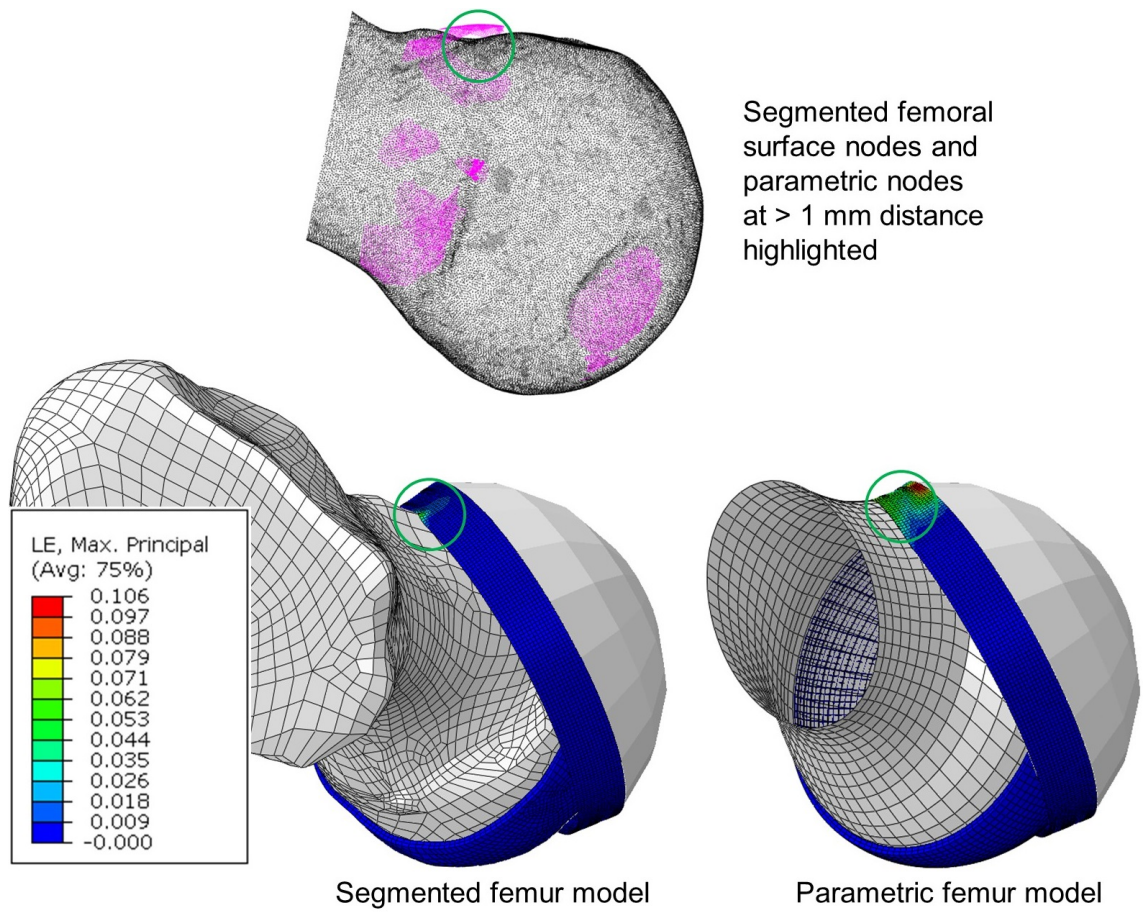


Figure 6.11: A model where the local fit between the segmented and parametric femoral surfaces in the cam region is poor, shown by highlighting (in pink) parametric nodes at a distance > 1 mm from the nearest segmented node. As a result, labral strain and displacement is higher in the parametric femur model, shown here at 20° of internal rotation.

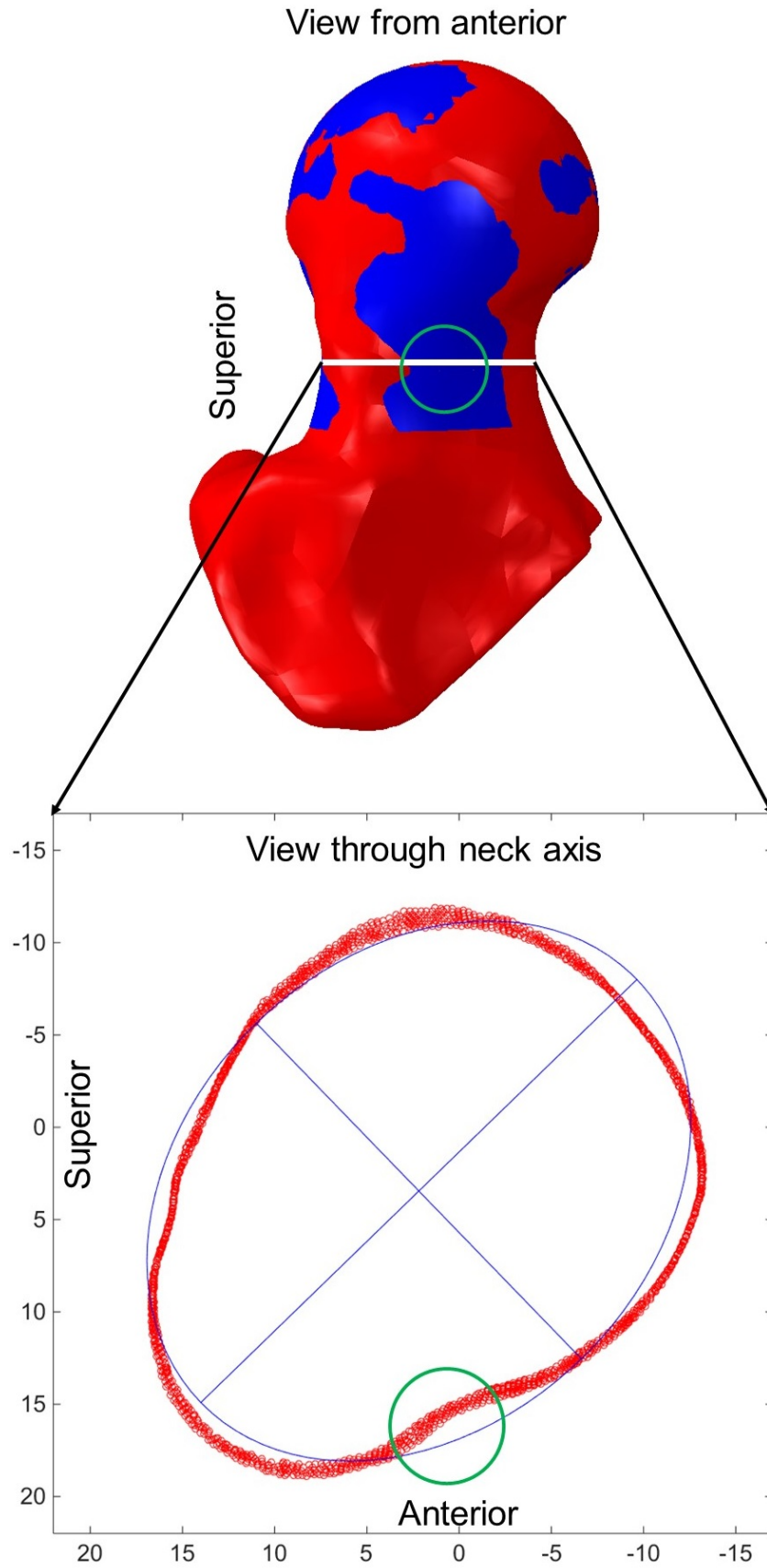


Figure 6.12: When there is a poor local fit in the cam region, differences between segmented femur (red) and parametric femur (blue) models can occur. The poor local fit is a result of the best fit ellipse (blue) failing to adequately capture the shape made by vertices in a 2 mm thick slice of the segmented femoral neck (red).

These results are discussed further in Section 6.5, but overall they provided an indication that the parameterised femoral geometry can be representative of real patients when applied in a basic impingement scenario with simplified acetabular geometry. Therefore the parametric approach was used in the next section to investigate potential effects of morphological changes.

6.4 Parametric study of morphology changes

6.4.1 Methods

6.4.1.1 Parametric cam morphology tests

In order to demonstrate the capability of the parameterisation system, it was used to generate further parametric femurs with cam morphology (Figure 6.13). A MATLAB script was developed to generate variations of femur morphology by defining the desired values of cam-rad and cam-angle (recall that cam-width results from these parameters as it is the percentage of the neck circumference whose distance from the head centre is greater than 90% of the distance defined by cam-rad). Consistent with the original definition in Chapter 4, cam-rad was defined based on the two central ellipses; that is, the 2nd and 3rd ellipses when counting starting from the most proximal. The script was used to generate geometry in which these ellipses were orientated such that the position where cam-rad was defined coincided with major ellipse radii.

Maintaining a constant head radius of 25 mm, parameters defining the neck region were adjusted to define four different models. Variations were defined based on the measures introduced in Section 4.2, with cam-rad used to describe the size of the cam and cam-angle used to describe its position in terms of anterior or posterior. Values were chosen to represent extreme cases in terms of cam size and superior location, and relatively low cases. Thus values at approximately the 35th and 95th percentiles for the cam-rad and cam-angle data from the 20 patients were used. The four models used two cam radii (low and high radii: cam-rad, cam-width = 92.5%, 46% and = 100%, 34%) and two cam positions (more anterior and more superior cam: cam-angle = 60° and 20°).

Alpha angles of these four parametric femurs were measured as the angle between the line passing through the femoral neck midpoint and the femoral head centre, and the line from the femoral head centre to the anterior point where the femoral head diverges from spherical. This was done in anterior-posterior (AP) and in cross-table lateral views

using ImageJ. These parametric models were run with boundary conditions to simulate flexion starting from 70° up to 90°, followed by internal rotation (up to 35° or until lack of convergence) to mimic a clinical impingement test. The centre of rotation was set as the centre of the femoral head.

Although these parametrically varied models had controlled geometry allowing the same boundary conditions to be used for all cases, in some instances high deformation of elements in the cartilage-labrum junction prevented models converging past a certain level of internal rotation. Therefore rotation levels where all models in the comparison converged were used to generate comparison graphs; this was 15° for the models where cam morphology was varied, since some models had very large cams which rapidly compressed the cartilage-labral junction region.

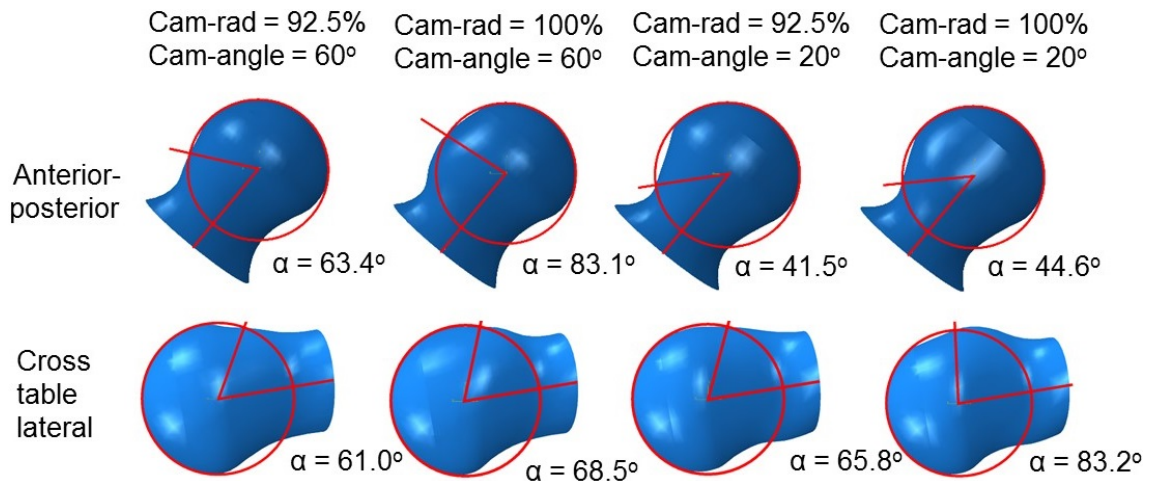


Figure 6.13: Overview of parametric models with variations to the femur.

6.4.1.2 Parametric acetabular morphology tests

In order to investigate the effect of changes in acetabular depth and labrum / bone ratio, five models were generated in which the labrum was parametrically varied (Figure 6.14). In these cases the femur was assigned a constant cam radius and position, as used in the models made to test material properties in Section 6.2 ($HR = 25$ mm, cam-rad = 96.25%, cam-angle = 40°, cam-width = 38%). The value of cam-rad and cam-angle were the respective averages of the two variations of these parameters used in the parametric femoral variation part of the study (Section 6.4.1.1).

The base model used the same acetabular geometry used in the previous models. Four additional cases were generated: increased labrum length (with unchanged and increased overall coverage) and decreased labrum length (with unchanged and decreased overall coverage). These variations to acetabular geometry were achieved by adjusting the Python

script that generated the geometry. Let LH denote the terminal position of the labrum. In order to adjust the labrum to bone ratio whilst maintaining the same overall level of acetabular coverage, LH was fixed whilst the percentage of a sphere used to represent acetabular bone was adjusted by $\pm 10\%$ from its base value of 33%. In order to adjust the labrum length, consequently also adjusting the acetabular coverage, the labrum length parameter was varied by $\pm 10\%$ from its base value of 7 mm (indicating a length of 7 mm for a HR of 25 mm), with the percentage of a sphere used to represent acetabular bone remaining fixed. LH was then recalculated based on the new labrum length value, hence changing the overall coverage because the terminal position of the labrum was changed.

As with the models with varied cam morphology, these models were run with boundary conditions to simulate flexion from 70° up to 90° , followed by up to 35° of internal rotation, with the centre of rotation being the centre of the femoral head. In these models, convergence was achieved for 25° of internal rotation so this value was used for comparison graphs.

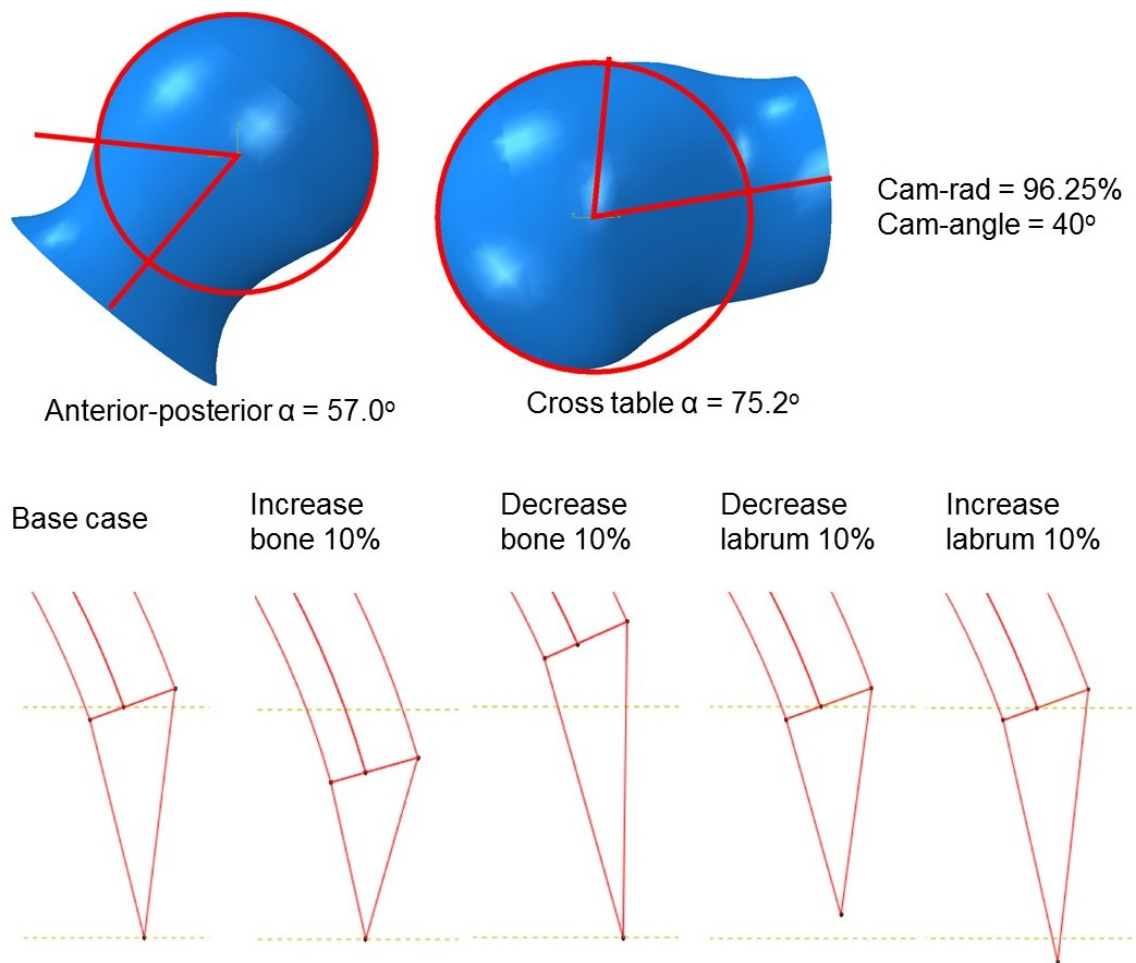


Figure 6.14: Overview of parametric variations made to labral and bony acetabular coverage.

6.4.2 Results

In the models where cam morphology was parametrically varied, there was no correlation between measured alpha angles and outputs of interest (Figure 6.15). In particular, AP alpha angles were higher ($\alpha = 63.4^\circ$, $\alpha = 83.1^\circ$) in the cases with no labral displacement occurring at 15° rotation than in the cases where labral displacement did occur at this point ($\alpha = 41.5^\circ$, $\alpha = 44.6^\circ$). The cross-table lateral alpha angle was largest ($\alpha = 83.2^\circ$) in the most severe impingement case (peak strain = 0.3793), but did not distinguish between the other models (α range = $61.0^\circ - 68.5^\circ$) where impingement severity varied as a result of cam size and position as defined on the neck ellipses (strain range = 0.0283 – 0.0341, displacement range = 0 – 1.52 mm).

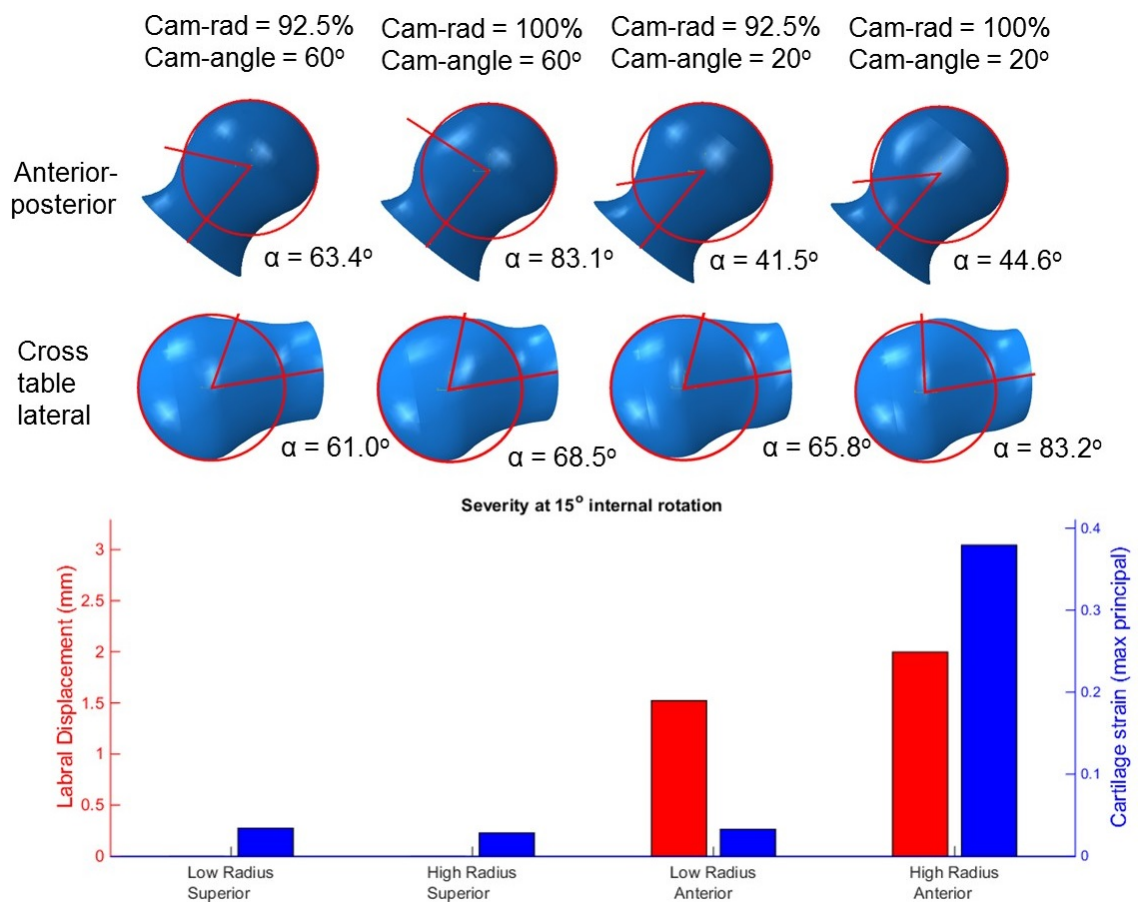


Figure 6.15: Alpha angles measured from anterior-posterior view and from cross table lateral view showed poor correlation to results from parametric models assessing labral displacement and cartilage strain due to cam impingement (results for 15° internal rotation at full flexion).

When variations were made to the acetabular rim, the increase to bone coverage had the greatest effect on impingement severity (Figure 6.16). A 10% increase in bone coverage

(with the labrum decreased in size to maintain the same overall coverage) increased strain in the cartilage labral-junction from 0.1155 to 0.4053. Increasing labral length by 10% (thus increasing overall coverage) increased labral displacement from 2.76 mm to 3.29 mm, but had relatively little effect on junction strain, which increased from 0.1155 to 0.1253.

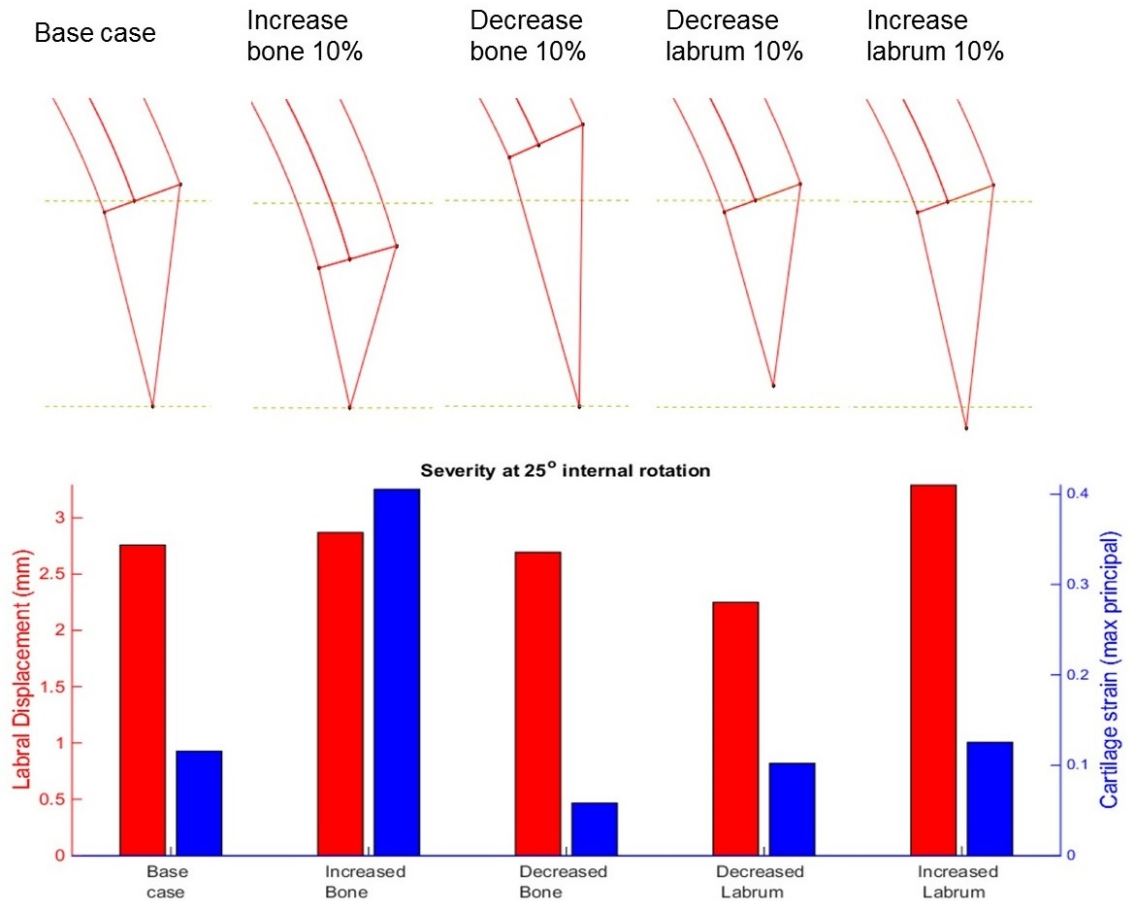


Figure 6.16: Variations in bone coverage and / or labral length, and the resultant labral displacement and cartilage strain resulting from impingement with a medium cam, showing strain is increased with greater bone coverage (results for 25° internal rotation at full flexion).

In both studies, no direct link was observed between increased labral tip translation and elevated strains in the cartilage-labral junction.

6.5 Discussion

The aims of the studies in this chapter were to validate the use of geometrically parameterised femoral surfaces against segmented equivalents, and to use parametric models to

assess key hip shape morphological variations in 3D. Subject-specific parametric models were compared with segmented models and trends in parametric models were found to be largely in agreement with segmented models. Additionally generated parametrically defined femurs demonstrated the issues with relying on 2D alpha angle measures as an indication of impingement severity potential. A simplified labrum geometry allowed rapid investigation of the effects of morphological variations and suggested bony overcoverage can increase severity of cam impingement by elevating strains in the cartilage-labrum junction.

6.5.1 Damage regions and mechanisms

Finite element models have previously identified elevated contact pressures and stresses in the anterosuperior cartilage and labrum in scenarios involving high flexion and internal rotation (Chegini et al., 2009; Jorge et al., 2014; Ng et al., 2016a), matching clinical reports of damage (Beck et al., 2005). This corroborates with findings of high strain in the cartilage-labral junction seen in the models developed in this study. Other studies comparing segmented and parameterised models suggested idealised geometry can underestimate contact stresses occurring in the hip (Anderson et al., 2010; Gu et al., 2011), but did not specifically investigate geometry related to impingement. In the impingement scenario modelled here, it was possible to identify the underlying cause of differences in model outputs by quantifying poor fitting between the smooth, parametric surfaces and more undulating, segmented surfaces in contact regions. The lack of model convergence observed at higher levels of internal rotation is not unusual when complex articular surfaces are used; Jorge et al. (2014) for example reported levels of 24° of internal rotation before stoppage due to lack of convergence.

High strains at the cartilage-labral junction resulting from direct compression of the cartilage by the cam, rather than the stretching of cartilage as a result of displacement of the labrum, were seen to be the driver of elevated tensile strains in cartilage in the cam models (Figure 6.17). This was particularly evident in the low radius, anterior cam model, where a fairly large labral displacement (1.52 mm) did not translate into a high strain at the junction (strain = 0.0341). In models with varied acetabular geometry, tensile strain was again more a function of deformation of the cartilage when it undergoes a compressive force normal to the bone, as opposed to stretching due to labral movement, with the worst case being when bone coverage was increased.

Contact between the labrum and femoral head or neck has been reported to limit motion during an impingement test (Kapron et al., 2015), which combined with the possibility

of pelvic motions, suggests that the use of bone-to-bone distance (Bedi et al., 2012) may not well suited for predicting impingement (Kapron et al., 2014). Since severity was seen here to be driven more by cartilage compression than labral displacement, bone-to-bone distance may actually be a better indicator of impingement severity than expected, at least for impingement occurring in this scenario. It should be noted however, that this affect may be exaggerated due to the simplified acetabular geometry. In reality, the femur may fit more precisely in the acetabular cavity, and labral movement could therefore be more closely linked to peak strain occurring at the cartilage-labrum junction.

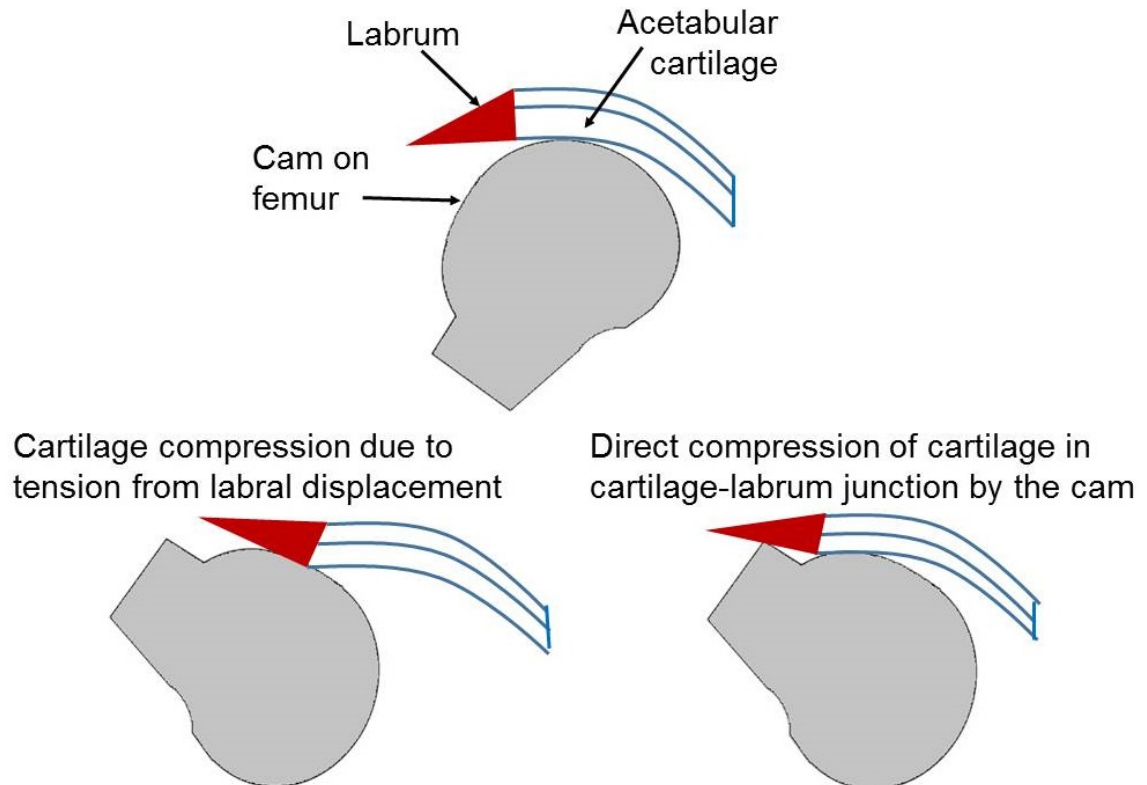


Figure 6.17: Schematic of mechanisms of elevated tensile strains in cartilage in the cam models. The mechanism depends on the geometry and movement of the femur. In the models in this chapter, high tensile strains at the cartilage-labral junction resulted more from direct compression of the cartilage by the cam, as opposed to stretching of cartilage as a result of displacement of the labrum.

6.5.2 Segmented vs parametric models

Similar displacements and strains occurred in the segmented and equivalent parametric models. This suggested that these outputs were relatively insensitive to the local undulations on the articular surface, which were present in the segmented models but smoothed out in the parametric representation. This was further evidenced by the good match in severity ranking order of the patients when assessed using parametric and segmented

models, although the actual rankings were not considered to be consequential due to the different boundary conditions used for each patient to ensure convergence.

The comparison between segmented and parametric models provided confidence in the results qualitatively, in that trends present in segmented models could be replicated in parametric models. There was no quantitative validation however, since there were other simplifications to the models in terms of boundary conditions and material properties, and a fairly large sample of 20 patients was modelled. Measurement of impingement risks by the outcome of the FE models should therefore not be understood as absolute risk.

Given the chosen boundary conditions, displacement of the labrum is a result of the position and peak size of the cam. When a poorer fit between the parametric and segmented surfaces at the cam region was present, impingement contact occurred at appreciably smaller rotation angles in one of the models, depending on whether the parametric surface over- or under-estimated the radius of the segmented cam. Earlier contact in the model with the larger radius resulted in more displacement of the acetabular soft tissue at lower angles of rotation. When higher labral displacement occurred in the segmented or parametric model, the tensile strain in the cartilage-labrum junction was usually also higher, since the cartilage was both more compressed by the cam and stretched more as a result of the labral displacement. However discrepancies in the local fit between surfaces at the cam region could be such that the labral tip displacement was higher, whilst the cartilage was compressed less and had lower tensile strain. This emphasises that although a low overall geometrical fitting error can be achieved, it does not guarantee that the parametric geometry is able to precisely capture the shape of all cams. The fit in localised regions may be poorer than the overall fit, which in the impingement scenario is of particular importance in the cam region (Figure 6.11). Poor local fit can arise because the parameterisation system relies on fitting ellipses to the neck region, and where the neck is less well described by an ellipse, this can lead to differences between the models.

6.5.3 Parametric tests

The models used to investigate cam morphology effects were generated with the same geometry except that the cam was varied in position and extent. These models were used to assess the reliability of alpha angle measurements as indicators of impingement severity (Figure 6.15). In the simulated movement (flexion followed by internal rotation), cams positioned more anteriorly resulted in more severe impingement in the models. However, the AP alpha angle on both the anterior cam models was lower than those on the superior cam models. The AP alpha angles gave the opposite prediction to the actual severity

indicated by the model outputs. This was because superior cams were more visible in the AP view and were better detected by AP alpha angles. In the anterior cam models, the AP alpha angle increased by only 3.3° when the cam radius was increased, but the severity in the model increased dramatically, indicated by an increase in tensile strain in the cartilage-labrum junction from 0.0327 to 0.3793. For superior cams, increasing the cam radius substantially increased the AP alpha angle, but the additional severity observed in the model was less than that seen between the anterior cam models. Thus using an AP alpha angle, it was not possible to predict the severity of impingement in the simulated impingement test scenario.

Alpha angles above 55° have been suggested as indicators of cam impingement (Pfirrmann et al., 2006; Tannast et al., 2007; deSa et al., 2014), so the alpha angles generated in this study were clinically relevant. The cross-table lateral alpha angle was largest in the most severe impingement case (83.2°), but did not however distinguish between the other models, with similar angles (all above 60° , with a range of 7.5°) recorded for the three models. The differences in severity predicted by the models were a result of both the extent and the position of the cams defined in 3D measurements.

In the acetabular coverage tests, greater bony coverage resulted in increased strain. The models therefore predicted that an increase in acetabular coverage due to excess bone (pincer morphology) is likely to increase impingement severity for a given level of rotation. Generally the displacement of the labral tip appeared to be driven by the position of the tip relative to the cam rather than overall labral length. The case with increased labrum length but the same overall coverage (so less bony coverage), exhibited less strain at the junction, because the bulk of the labrum was located further from the labral tip when impingement was initiated. It has been suggested that in hips with dysplasia (acetabular undercoverage), labral length may be increased in the weightbearing zone, potentially compensating the lack of bony coverage (Garabekyan et al., 2016). The results reported here suggest that the increase in coverage caused by this reaction may not increase impingement severity to the same extent as in cases where the overall coverage is elevated as a result of bony overcoverage.

6.5.4 Study limitations and challenges

Although the models in this study suggest direct compression of the cartilage by the cam as the main cause of impingement damage, it is important to consider limitations to the models, such as the simplified acetabular geometry, which could mean that the effect of labral displacement is underemphasised. Previous studies have suggested that models that

depend on bone contact to predict impingement in hips may be unrealistic (Kapron et al., 2014; Kapron et al., 2015), hence it is important to include soft tissues when developing models of impingement. Soft tissues were not visible in the patient CT scans and as such, femoral cartilage geometry was estimated by expanding the geometry of the bone, making the methodology consistent between parametric and segmented surfaces. Femoral cartilage was modelled as isotropic since the outputs of interest were on the acetabular side. The modelling simplifications were considered suitable because the models were able to differentiate between different geometries, and this was deemed more useful than generating only a small number of more complex models which may produce more accurate output values.

6.5.4.1 Geometric simplifications

Simplified acetabular geometry was chosen for all models in order to facilitate parametric study of labral changes, and to mitigate convergence issues related to overclosure errors that result from contact between irregular articular surfaces. It is important to appreciate that significant subject-specific differences also occur on the acetabular side, and these would likely result in altered tissue strains, since the fit of the femoral head into the acetabulum may vary between patients. Parametric study of geometrical changes to the femur here assumed the acetabular geometry remains unchanged. Whilst parametric study of changes to the labrum was also conducted, the labrum was defined on a circular acetabular rim, and not verified against subject-specific cases as the femurs were. This was because labral tissue could not be segmented from the clinical CT scans. In the study comparing segmented and parametric femoral surfaces, using specimen-specific values for the acetabular angles was not deemed appropriate because the simplification to spherical geometry meant that adjusting these angles would have a large effect on the possible range of movement of the femur, and it was important to ensure a certain degree of impingement occurred in all cases to allow the parametric and segmented models to be compared.

6.5.4.2 Boundary conditions

As discussed in Section 5.5.2, the boundary conditions used to simulate impingement in these models used displacement (rotation with fixed translation) rather than load control, both to aid model convergence and because no specimen-specific loading data was available. Loading data published by Bergmann et al. (2001) was deemed inappropriate for this study since FAI patients are younger than the hip replacement patients from that

study, and their deformities could result in altered gait and movement patterns.

The initial flexion step used in the other parametric models was omitted from the models in the part of the study comparing parametric and segmented femurs because it was challenging to run the segmented models without overclosure causing errors in the analysis. Femurs were generally rotated about their head centre; in some cases this caused severe overclosure of the femoral and acetabular surfaces, and so the point of rotation was translated to optimise for model convergence whilst achieving impingement against the labrum. The boundary conditions were always the same for the parametric and segmented models of each specimen, in order to ensure the parametric and segmented models were comparable. Differences between boundary conditions used for distinct patients however meant that models of different patients were not directly comparable. The use of parametric models (without the restriction of requiring boundary conditions to match a segmented case) mitigates this problem because the smoother surfaces are less prone to these errors. Parametric models varying the femur and acetabulum could therefore be developed and used to assess the effects of individual morphological variations. Even so, high deformation of elements in the cartilage-labrum junction prevents models converging past a certain level of rotation, so results from lower rotation levels were required to compare models exhibiting severe impingement.

6.5.4.3 Material properties

As mentioned in Section 5.5.3, cartilage is a complex composite material with chemical influence on its mechanical properties; it has been characterised as an elastic, viscoelastic or biphasic material (Fox et al., 2009), but these are all approximations to enable the mechanical behaviour to be represented (Henak et al., 2013). For simulating loads throughout the gait cycle, time-dependent properties may therefore be important, but evidence suggest that elasticity is an appropriate simplification for modelling the material behaviour of cartilage to predict short term contact stresses (Ateshian et al., 2007; Henak et al., 2013), and elasticity was therefore used to investigate the impingement scenario.

6.5.5 Conclusions

The study in this chapter has quantified the effect of taking a smooth parameterised approach to model geometry when investigating femoroacetabular impingement using finite element models, by comparison with a gold standard segmentation approach. The displacement discrepancy between model types was driven by local fitting error, which on

average can be controlled to be less than 1 mm. Poor local fit in the cam region can also result in differences in tensile strain in the cartilage-labrum junction, but trends between the segmented and parametric models were similar. Overall this provides an indication that models with parametric femoral geometry can yield similar results to those with segmentation-based geometry, when used to simulate a basic impingement scenario. Patient-specific models required full image segmentation, but there is potential to further develop the parametric methods to assess likely impingement severity based on measures of the neck and acetabulum when three-dimensional patient imaging is available.

Models automatically generated using the parametric approach were used to demonstrate the enhanced capability of a three-dimensional analysis over current clinical measures of planar alpha angles. It was shown that potential for tissue damage, as indicated through local strain, was not at all predicted by the alpha angle measures. For further parametric investigations, it is crucial to report details of how the full 3D geometry is defined, rather than relying on clinical measures which are highly dependent on view. In Chapter 4, it was observed that among the 20 patients included in this study, females were more likely to have cams located in an anterior position, which are less visible in AP radiographs. In the impingement scenarios tested here, anterior cams were found to cause greater levels of soft tissue strain and could therefore result in more severe impingement leading to articular damage. Although cams are more common in males and tend to be more diffuse in females, their position in females could make them more severe if movements involving high flexion and internal rotation are regularly performed. However this also depends on the acetabular geometry, which was standardised in these models, and movement conditions, which here was limited to internal rotation from a high flexion position.

Overall the work in this chapter has demonstrated that using parametric approach to investigate morphological changes in both the femur and acetabulum can yield information on how these changes affect tissue strains. Such information could be used to stratify the patient population since certain morphologies could be at greater risk of symptomatic impingement. The concluding chapter that follows gives an overall review of the work that has been presented in this thesis.

Chapter 7

Overall Discussion and Conclusions

7.1 Summary

The computational investigation of hip contact mechanics is promising because it assists in improving the understanding of the pathomechanisms of damage resulting from abnormalities in hip morphology. As a result there are now an increasing number of finite element studies of the natural hip joint. However, it can be unclear exactly how variations are made to the 3D geometry of models of the hip, particularly when 2D parameters such as alpha angles are referenced in 3D parametric models (Chegini et al., 2009). Furthermore, many studies using specimen-specific hip geometries have used relatively small sample sizes (Jorge et al., 2014). The work presented in this thesis makes a step forward in 3D geometric realism in parametric models, achieved through the development of a parameterisation system allowing the generation of specimen-specific parametric models. Specimen-specific parametric models generated from a database of 20 cam patients were used to define novel measures of potential impingement severity based on hip bone anatomy. Parametric models were assessed against their segmentation-based model equivalents in terms of geometric surface fitting errors and tissue strains resulting from FE simulations of basic impingement scenarios.

The primary morphological factors considered to be pertinent to impingement were the shape and position of the cam, and the acetabular rim geometry. The aim of this work was to quantify some of the effects of these factors in impingement scenarios. To this end, geometric parameterisation systems to describe the bony geometry of hips with cam deformities were developed in Chapter 3, and the most successful methodology for this was to use lofting procedures to generate surfaces from shapes fitted to cross sections

through segmented bone geometries. In Chapter 4 severity measurements were derived from the geometric parameters, and these revealed that the parameterisation system was sufficiently sensitive to identify differences in male and female patient groups. The development of geometric parameterisation systems to describe the bones forming the hip joint, and derivation of severity measurements to assess them, was then incorporated into finite element models. These were used to investigate the potential severity of impingement resulting from abnormal bone morphologies, by assessing soft tissue strains resulting from variations in hip morphology. Limitations with the software influenced the approach to developing FE models, as discussed in Chapter 5. Nevertheless it was still possible in Chapter 6 to automatically generate parametric models that were used to demonstrate how morphology can affect the severity of impingement, highlighting the importance of reporting the full three-dimensional geometry of models used to investigate these issues. In particular, models generated using the parametric approach showed that potential for tissue damage, indicated through local strain, was not predicted by alpha angles measured in 2D views, but resulted from cam extent and position as defined by ellipses describing the shape of the femoral neck region.

7.2 Key achievements and findings

Parameterisation:

1. An ellipse-based parameterisation approach for the femur, which considered the cam as part of the overall neck geometry, was more successful than a system in which the cam was captured separately. The ellipse-based parameterisation system produced femoral surfaces more closely matching the segmented bone, quantified using surface fitting errors.
2. The basic shape of the articular acetabular surface was successfully captured using 3D splines fitted to manually selected points on the segmented acetabulum, allowing an automated extraction of coverage and version angles on the acetabulum.
3. Measures of acetabular angles on 3D parametric surfaces were well correlated with measures on 2D reconstructed radiographs, and provided additional information on the angles at different positions on the articular surface.
4. Novel severity measurements were derived from the parametric femoral surfaces, indicating the size and position of the cam on the femur. Measures of cam severity were significantly different in a cam patient femurs compared with control femurs.
5. When applied to 20 cam hips, a significant difference was identified in cam position between males and females, with male cams generally positioned more superiorly.

6. 2D alpha angle measurements on the cam patients in two different views were only moderately correlated with each other, and both alpha angles were only moderately correlated with the parametric cam size severity measures. Furthermore, subjects with similar alpha angles were seen with different 3D severity measures, highlighting the limitations of assessing impingement in 2D.
7. Changes to individual parameters could be made to automatically generate surfaces with precisely defined morphological differences, making them suitable for use in parametric finite element modelling studies.

Finite element modelling:

1. A method was developed to produce simplified, spherical acetabular geometry in order to alleviate convergence issues when modelling contact and allow automation of hexahedrally meshed labrum and acetabular cartilage geometry.
2. Segmented bone surfaces were extracted from ScanIP as NURBS surfaces, allowing quadrilateral meshes to be generated on bone surfaces within Abaqus, and femoral cartilage to be represented using orphan hexahedral meshes produced using mesh offsetting.
3. Boundary conditions in which the acetabulum was fixed in place, whilst the femur was rotated with no translational movement, were established as effective for simulating impingement. This approach allowed consistent conditions to be used in models featuring subject-specific parameterised and segmented femurs.
4. The inclusion of transverse isotropic material properties in cartilage and the labrum were both observed to have an effect on output strains in sensitivity tests, and transverse isotropy was included in subsequent models.
5. Models were developed of 20 patients using parametric and segmentation-based femoral geometry. As simulated rotation progressed, similar increases in labral displacements and strains occurred in the segmented and equivalent parametric models. Discrepancies in the local fit between surfaces at the cam region could cause differences in model results.
6. Models generated using the parametric approach showed that potential for tissue damage, indicated through local strain, was not predicted by measured alpha angle, but resulted from cam extent and position as defined by ellipses representing cross sections of the femoral neck region.
7. When spherical acetabular geometry was parametrically varied, additional bone coverage caused a substantial increase in cartilage-labral junction strain, whilst increasing labrum coverage slightly increased labral displacement but had relatively little effect on junction strain.

7.3 Overall discussion

7.3.1 Femoral shape analysis

The final geometric parameterisation system developed to represent the femur was used to produce parametric surfaces by lofting through ellipses fitted to 2 mm thick slices of vertices on the segmented bone surface. Combined with a spherical cap fitted to the proximal head, four ellipses in the head-neck region were sufficient to generate surfaces representing the femoral head, and the middle two of these were used for deriving cam severity measurements. For finite element models, it was necessary to add a fifth ellipse to extend the modelled surface in order to avoid the surface slipping into the cavity following high levels of rotation. It was possible to adapt the ellipse-based parameterisation system to use thinner slices (limited by the density of the mesh describing the segmented surface) and loft through a large number of ellipses fitted to these slices. In this way it was possible to generate parametric surfaces closely matching the original segmented geometry inasmuch as each slice could be approximated by an ellipse. However this produced excessively undulating surfaces rather than smooth surfaces. Moreover, it was beneficial to loft through a smaller number of fitted ellipses because it was desirable to minimise the size of the parameter set so that anatomical differences could be readily described in terms of parameter variations. For the same reason, fitting a more complex curve than the ellipse, or directly fitting a complex 3D surface, would not provide any further benefit.

An alternative method that can be used to represent geometrical changes in joint geometry is statistical shape modelling (Harris et al., 2013; Väänänen et al., 2015). Developing statistical shape models typically includes using Procrustes analysis to remove the effects of orientation and size, after which principal component analysis can be used on a sample of geometries to provide the mean shape and modes that describe the variation in the sample. New shapes can be generated with a statistical model by varying values along the modes. However, several factors are usually captured by each mode, so these modes themselves cannot be considered as individual parameters that can be varied with well defined anatomical meanings. Hip models generated using these techniques could however be analysed with respect to their risk of impingement, and a regression could be derived between particular modes and impingement risk to highlight geometric risk factors. Differences between controls and cam patients may also be highlighted, in particular by assessing differences in landmark positions. One advantage of instead using the custom-made parameterisation system developed here is that each parameter precisely defines an aspect of the geometry and can be adjusted to result in specifically desired differences for

investigation in models. Although it may be challenging to visualise the physical meanings of parameters (for example, the interaction of ellipse angles and radii can be difficult to interpret in terms of anatomy), they were post-processed into severity measurements with clear individual meanings. This provided an automated method of assessing differences between cam and control populations as well as between groups within the patients. This approach was also advantageous because new models could be generated with pre-defined anatomy-based impingement risks using the relationships between the severity measurements and the geometric parameters. The relationship of these severity measures and differences in tissue strains derived from FE models was then assessed.

7.3.2 Cam severity measurements

In addition to verification using fitting errors against segmented surfaces, the ellipse-based parameterisation system was seen to be sufficiently sensitive to identify a difference between male and female cams in the sample of 20 patients. This information was not captured by 2D alpha angle measurements, which did not exhibit strong correlations when taken in different views or when compared with the 3D severity measures. The identified difference in cam position between sexes may relate to aetiological differences, as discussed in Section 2.5.3. Specifically, differences in activities and pelvic shapes could lead to bone stresses occurring in different regions. More superior cams were seen in males, and this could have implications for diagnosis. Anterior cams seen in females are less visible in AP radiographs, whilst more pistol-grip like deformities may exhibit less obviously on an impingement test involving flexion and internal rotation. Such movements occur during daily activities including walking (Bergmann et al., 2001), although range of motion may be different between males and females (Halim et al., 2015). When the impingement test movement was applied to parametric models, the anterior cams displayed higher impingement severity in terms of resulting tissue strains in this scenario. These aspects again highlight the need for 3D analysis of bone geometry, both when developing models and for clinical diagnosis.

In future work, it may be possible to define an additional method for measuring the cam extent. Cam-width is defined as the percentage of the neck circumference whose distance from the head centre is greater than 90% of the distance defined by cam-rad. Cam-width therefore indicates the extent to which the circumference of the neck is affected by the cam, but is difficult to compare between models since it depends on cam-rad. An additional measure could be used to provide the absolute width covered by the cam. It may also be beneficial to assess cam height by using cam-rad measures on further regions in

addition to on the original fitted ellipses.

The novel method of investigating cam impingement presented in this thesis uses parametric femoral representations, and the method is currently not intended as a clinical tool. One of the primary reasons for this is that it requires segmentation of bone from 3D images. There may be potential to further develop the parametric methods of assessing impingement severity based on measures of the neck and acetabulum without need for full bone segmentation. This would however still require three-dimensional imaging of patients to be available. One approach would be to segment only of the region of interest. Another would be to develop methods to automatically detect regions of bone in the neck with low offset from the head, which may be possible by directly using greyscale values from CT images. These methods would likely also require the assumption of anatomical alignment in the hip scans, but could ultimately have clinical applications in surgical planning.

7.3.3 Acetabular shape analysis

Parametrically representing the acetabulum was more challenging than the femur, since its geometry is more complex. The spline-based acetabular parameterisation required manual steps and ultimately was not used in FE models, in part due to convergence problems, but also because of the difficulty in automating soft tissue generation. When selecting nodes to define splines for the parametric acetabular bone, optimisation of the fit was possible by using a script to select alternative adjacent nodes. However the large number of possible combinations meant this approach was impractical. By focusing only on the anterior region this optimisation process could potentially be accelerated to find more closely matching acetabular surfaces. Furthermore, additional scripts could be developed to provide an alternative method to produce labrum geometry on more complex acetabular surfaces, although this is challenging and previous specimen-specific parametric acetabular representations have not included the labrum (Hua et al., 2015). This would likely require the use of an additional software other than those used in the studies presented here, for example a dedicated CAD software, an approach which has been previously used for generating soft tissue geometry (Jorge et al., 2014) and simplified parametric hips (Liechti et al., 2015). If such processes were developed, it would be beneficial to test them on patients with clinically diagnosed pincer impingement.

When investigating the effects of different cam geometries in the impingement scenario simulated, soft tissue strains primarily occurred in the labrum and cartilage-labrum junction, so the precise acetabular shape had relatively little effect on outputs. Therefore, since

it was found to be impractical to produce labral and cartilage geometry with hexahedral meshes on the spline-based parametric acetabular surfaces, the acetabular geometry was simplified to a spherical representation. A spherical approach has been reported in previous simplified models (Chegini et al., 2009; Liechti et al., 2015), and here it allowed rapid generation of different labrum morphologies which could be meshed with hexahedral elements. This set up permitted investigations of the effects that different morphologies may have on potential damage mechanisms. These tests revealed that bony coverage is more influential than labral coverage in terms of resulting impingement severity, with increased bone coverage resulting in elevated strains in the cartilage-labrum junction, indicative of higher impingement damage potential.

7.3.4 Parametric and segmentation-based FE models

Segmentation-based models utilising patient scans have shown high contact pressures in areas corresponding with clinical damage (Li et al., 2013; Jorge et al., 2014), but are time consuming to generate and analyse. Parameterised models, the focus of this work, are more generic models incorporating simplified geometric features described mathematically to capture key aspects of hip morphology, and these provide an alternative for analysing a large number of different morphologies (Chegini et al., 2009; Hua et al., 2015; Liechti et al., 2015). Parametrically defined models are ideally suited for the automatic generation of many different geometric variations, and permit isolation of the effects of individual parameters by varying each parameter separately, whilst identifying which aspects of joint morphology result in differences in model outputs is difficult using segmentation-based models. The challenge of a parametric approach however is to identify a set of parameters that is capable of producing distinct, subject-specific results, and the challenge was met in this work by fitting geometric shapes to segmented bone geometry of real patients. Having developed a methodology of producing parametric surfaces, it behooves the developer to test these against segmented geometry in modelling scenarios.

Although it has been reported that idealised models may not accurately assess stresses present in joints (Anderson et al., 2010; Gu et al., 2011), segmentation-based models are particularly prone to convergence issues due to their more complex articulating surfaces, and all published modelling studies feature some inherent limitations (Table 2.1). Geometric subject-specificity is beneficial for obtaining clinically relevant results (Harris et al., 2012), and whilst the models presented in this thesis were simplified and featured a spherical acetabulum, they also incorporated patient-specific cam geometries generated through the ellipse-based geometric parameterisation method. Concerns regarding the ef-

fects of simplified geometry on the femoral side were addressed through comparison with models incorporating segmented femoral surfaces. Attempts to develop fully segmented models were limited by errors resulting from overclosure of articulating surfaces, whereas the parametric models were better suited to achieving convergence whilst also incorporating a degree of subject-specific femoral geometry, and allowing rapid study of different hip joint geometries. Although quantitative differences were observed in the results predicted by the segmentation-based and parametric models, agreement in their predicted trends suggested that qualitative conclusions predicted using simpler models are likely to be reliable. In the future, more work in this area could lead to improved understanding of the effects of geometric aspects in FE models for biomechanical applications, both in the hip (Hua et al., 2015), and in other joints such as the knee (Meng et al., 2017b).

Parametric models of the 20 cam patients studied in this project were seen to produce results representative of segmented models, with similar increases in strain occurring for parametric and segmented models as impingement was simulated through femoral rotations (Section 6.3). This provided qualitative confidence in the result trends seen in the models, but model simplifications meant the results were not quantitatively validated so FE model outputs should not be understood as indicating absolute impingement risk. In particular, it would be erroneous to directly compare the patients using the results of these models. In order to ensure both the segmented and parametric models could converge, boundary conditions were optimised in each case and this meant the centre of rotation was not consistent between models of different patients. Nevertheless, it was possible to use the parameterisation system to generate models with different cam severity parameters, and these models were run with consistent boundary conditions, allowing a parametric study of clinically relevant morphological changes (Section 6.4). It was demonstrated that cams for which the measured alpha angle was very similar in certain views can actually have quite different characteristics in terms of 3D shape and position, and hence lead to different tissue strains with potentially different damage mechanisms and likelihoods for joint degradation.

7.3.5 Software constraints

Limitations were associated with Abaqus, the chosen finite element software used in this work. In particular, the generation of meshes on certain geometries was challenging, and models with more complex articulating surfaces were prone to convergence difficulties. FEBio was considered as a possible alternative, but FEBio has less user support and is generally only advantageous over Abaqus when trying to model biphasic cartilage prop-

erties, whereas for elastic models, FEBio is not thought to perform any better than Abaqus (Meng et al., 2013). Thus Abaqus was chosen because, as a commercial software, it has more support, and even more crucially, it has an in-built Python scripting interface, which was key to automating the generation of parametric models.

The lack of model convergence stemming from overclosure of articular surfaces meant that boundary conditions were simplified in order to achieve impingement simulation without errors preventing analysis progression. Contact analysis is complex and addressing these issues is very time-consuming. The focus of this project was primarily to obtain results from parametric models in order to assess the effectiveness of a parametric approach as an alternative for investigating potential impingement damage mechanisms when compared with segmentation-based models. Future work could aim to develop further models with more complex geometries and simulate a wider range of movements, potentially making use of alternative modelling software and patient-specific loading conditions. If compared with parametric models, this could provide further confidence in understanding the effects of geometric simplification.

The quantity of output data could be increased by generating additional variations of parametric models, giving a wider indication of the morphology most likely to result in impingement. Whilst the automation of model geometry significantly speeds up development time, models at high mesh density still required several hours to run (in the region of 10 hours on a PC and 3 hours when submitted to the University's high performance computing facilities). To generate a very large data set more quickly, one approach would be to develop machine learning techniques in order to attempt to predict model outputs (e.g. max tissue strain and its location on the cartilage-labrum junction) from input parameters (e.g. cam-rad, cam-angle), thus bypassing the need to run further models. This would however require a large initial training dataset of model inputs and outputs to be generated using FE software.

7.3.6 Model outputs to assess soft tissue damage

As well as simplifications to geometry, it is also necessary for models to feature simplifications of real material behaviour. In order to develop models with highly realistic material property definitions, experimental methods are necessary to derive model inputs. In order to plan such experiments, it is useful to know which aspects have the greatest affect on model outputs of interest. For this, hypotheses are required on damage mechanisms in order to determine which outputs are most likely to be relevant to FAI. Whether such outputs fundamentally change when more realistic features are added, such as more

complex material properties, should then be established. In this way increasingly realistic models could be used to investigate changes that occur as a result of clinically relevant differences in hip morphology. A parallel set up of FE models and experimental rigs could be used to provide validation for such complex models if their outcomes were to be interpreted in a clinical context.

The scope of this project was to focus primarily on geometry, and bone surfaces were modelled as rigid, and soft tissues were modelled as linearly elastic based on evidence and approaches used in the literature (Table 2.1). Investigations were conducted to understand whether it would be beneficial to increase the level of detail of material constitutive models in terms of anisotropy, and it was seen that strain patterns were affected by considering directionally dependent moduli based on reported collagen fibril alignments in the soft tissues. This has also recently been reported to be important when considering biphasic effects in cartilage (Meng et al., 2017a). Therefore transversely isotropic properties were used for acetabular soft tissues, which is where the outputs of interest were extracted.

Although many studies have reported elevated contact pressures in areas corresponding with clinical damage (Li et al., 2013; Jorge et al., 2014; Hua et al., 2015; Liechti et al., 2015), outputs with potentially more direct relevance specifically to impingement were sought for the models in this project. One way of considering severity of impingement is to define severity in terms of a restricted range of motion, but this is difficult to assess in models since convergence is affected by the deformation of elements. Models can however abort for various reasons and failure of analysis progression to continue is not necessarily indicative of restricted motion in an actual joint. Furthermore, the functional range of motion for a given patient in reality may depend on their individual pain tolerance. In order to compare models, strains at fixed levels of rotation were considered to be suitable indicators of impingement severity, with elevated strains suggestive of more severe impingement. This was quantified using two primary outputs of interest from the models:

- Maximum displacement of labrum, which has potential relevance to cleavage of the labrum from cartilage, and the tears occurring within labrum.
- Maximum tensile strain in cartilage (max principal logarithmic strain), which has potential relevance to fibre damage as cartilage is stretched and compressed by the shearing of the cam into the acetabular cavity. In the modelling scenario investigated, this was seen to occur at the cartilage-labral junction.

In future work, the nature of strains occurring in soft tissues could be analysed in more

detail. For example, the relative occurrence of shear stresses and strains in different scenarios could be assessed (Henak et al., 2014a), which may be more reliable if a non-frictionless contact definition was used between articulating surfaces. Furthermore, modelling an interaction between cartilage and bone, rather than using a tie constraint to fix them together, could allow the simulation of cartilage delamination from underlying bone, which may also influence labrum displacement (Kuhns et al., 2015). Further sensitivity tests could also be conducted on the effects of different material properties, for example by including deformable bone materials to assess any effects of impingement scenarios on subchondral bone (Ng et al., 2012; Ng et al., 2016b). The models developed in this project also did not include the capsule seal which surrounds the hip joint, which has been reported to affect the stability of hip replacements (Elkins et al., 2011). Inclusion of features such as the capsule seal and ligaments surrounding the hip in more complex models may reveal whether these also play a role in impingement. However, the benefit of any additional complexities added to models would need to be weighed against the additional computational cost in terms of development and analysis time.

7.4 Conclusion

In this thesis, a new three-dimensional parameterisation system to describe variations in cam femur geometry has been presented, providing novel quantitative measures of the size and position of cam deformities. This has also resulted in a flexible method for the automated generation of a range of hip geometries featuring cam deformities to be used in parametric finite element models.

Bibliography

- AAOS (2015). *American Academy of Orthopaedic Surgeons: Femoroacetabular Impingement*. <https://orthoinfo.aaos.org/en/diseases--conditions/femoroacetabular-impingement/>, accessed 2015.
- Abaqus 6.14 Documentation (2014). Dassault Systèmes.
- Allen, D., Beaulé, P., Ramadan, O., and Doucette, S. (2009). Prevalence of associated deformities and hip pain in patients with cam-type femoroacetabular impingement. *Journal of Bone & Joint Surgery, British Volume* 91.5, pp. 589–594. DOI: 10.1302/0301-620X.91B5.22028.
- Alonso-Rasgado, T., Jimenez-Cruz, D., Bailey, C. G., Mandal, P., and Board, T. (2012). Changes in the stress in the femoral head neck junction after osteochondroplasty for hip impingement: a finite element study. *Journal of Orthopaedic Research* 30.12, pp. 1999–2006.
- Anderson, A. E., Peters, C. L., Tuttle, B. D., and Weiss, J. A. (2005). Subject-specific finite element model of the pelvis: development, validation and sensitivity studies. *Journal of biomechanical engineering* 127.3, pp. 364–373. DOI: 10.1115/1.1894148.
- Anderson, A. E., Ellis, B. J., and Weiss, J. A. (2007). Verification, validation and sensitivity studies in computational biomechanics. *Computer methods in biomechanics and biomedical engineering* 10.3, pp. 171–184. DOI: 10.1080/10255840601160484.
- Anderson, A. E., Peters, C. L., Weiss, J. A., Ellis, B. J., and Maas, S. A. (2008). Validation of finite element predictions of cartilage contact pressure in the human hip joint. *Journal of biomechanical engineering* 130.5, p. 051008. DOI: 10.1115/1.2953472.
- Anderson, A. E., Ellis, B. J., Maas, S. A., and Weiss, J. A. (2010). Effects of idealized joint geometry on finite element predictions of cartilage contact stresses in the hip. *Journal of biomechanics* 43.7, pp. 1351–1357. DOI: 10.1016/j.jbiomech.2010.01.010..
- Anderson, L. A., Kapron, A. L., Aoki, S. K., and Peters, C. L. (2012). Coxa profunda: is the deep acetabulum overcovered? *Clinical Orthopaedics and Related Research*® 470.12, pp. 3375–3382. DOI: 10.1007/s11999-012-2509-y.

- Arbabi, E., Chegini, S., Boulic, R., Tannast, M., Ferguson, S. J., and Thalmann, D. (2010). Penetration depth method - novel real-time strategy for evaluating femoroacetabular impingement. *Journal of Orthopaedic Research* 28.7, pp. 880–886. DOI: 10.1002/jor.21076.
- Ateshian, G. A., Ellis, B. J., and Weiss, J. A. (2007). Equivalence between short-time biphasic and incompressible elastic material responses. *Journal of biomechanical engineering* 129.3, pp. 405–412. DOI: 10.1115/1.2720918.
- Bachtar, F., Chen, X., and Hisada, T. (2006). Finite element contact analysis of the hip joint. *Medical and Biological Engineering and Computing* 44.8, pp. 643–651. DOI: 10.1007/s11517-006-0074-9.
- Bah, M. T., Shi, J., Browne, M., Suchier, Y., Lefebvre, F., Young, P., King, L., Dunlop, D. G., and Heller, M. O. (2015). Exploring inter-subject anatomic variability using a population of patient-specific femurs and a statistical shape and intensity model. *Medical Engineering & Physics* 37.10, pp. 995–1007.
- Banerjee, P. and Mclean, C. R. (2011). Femoroacetabular impingement: a review of diagnosis and management. *Current reviews in musculoskeletal medicine* 4.1, pp. 23–32. DOI: 10.1007/s12178-011-9073-z.
- Beck, M., Kalhor, M., Leunig, M., and Ganz, R. (2005). Hip morphology influences the pattern of damage to the acetabular cartilage: femoroacetabular impingement as a cause of early osteoarthritis of the hip. *Journal of Bone & Joint Surgery, British Volume* 87.7, pp. 1012–1018. DOI: 10.1302/0301-620X.87B7.15203.
- Bedi, A., Dolan, M., Magennis, E., Lipman, J., Buly, R., and Kelly, B. T. (2012). Computer-assisted modeling of osseous impingement and resection in femoroacetabular impingement. *Arthroscopy: The Journal of Arthroscopic & Related Surgery* 28.2, pp. 204–210. DOI: 10.1016/j.arthro.2011.11.005.
- Bergmann, G., Deuretzbacher, G., Heller, M., Graichen, F., Rohlmann, A., Strauss, J., and Duda, G. (2001). Hip contact forces and gait patterns from routine activities. *Journal of biomechanics* 34.7, pp. 859–871. DOI: 10.1016/S0021-9290(01)00040-9.
- Bergmann, G., Graichen, F., Rohlmann, A., Bender, A., Heinlein, B., Duda, G., Heller, M., and Morlock, M. (2010). Realistic loads for testing hip implants. *Bio-medical materials and engineering* 20.2, pp. 65–75. DOI: 10.3233/BME-2010-061.
- Blausen (2015). *Blausen Medical: Scientific and Medical Animations*. <https://blausen.com/>, accessed 2015.
- Botser, I. and Safran, M. R. (2013). MR Imaging of the Hip: Pathologies and Morphologies of the Hip Joint, What the Surgeon Wants to Know. *Magnetic resonance imaging clinics of North America* 21.1, pp. 169–182. DOI: 10.1016/j.mric.2012.08.008.

- Bouma, H., Hogervorst, T., Audenaert, E., and Kampen, P. van (2015). Combining femoral and acetabular parameters in femoroacetabular impingement: the omega surface. *Medical & biological engineering & computing* 53.11, pp. 1239–1246. DOI: 10.1007/s11517-015-1392-6.
- Bowman, K. F., Fox, J., and Sekiya, J. K. (2010). A clinically relevant review of hip biomechanics. *Arthroscopy: The Journal of Arthroscopic & Related Surgery* 26.8, pp. 1118–1129. DOI: 10.1016/j.arthro.2010.01.027.
- Bredella, M. A., Ulbrich, E. J., Stoller, D. W., and Anderson, S. E. (2013). Femoroacetabular impingement. *Magnetic Resonance Imaging Clinics of North America* 21.1, pp. 45–64. DOI: 10.1016/j.mric.2012.08.012.
- Byrd, J. T. and Jones, K. S. (2011). Arthroscopic management of femoroacetabular impingement in athletes. *The American Journal of Sports Medicine* 39.1 suppl, 7S–13S. DOI: 10.1177/0363546511404144.
- Cereatti, A., Margheritini, F., Donati, M., and Cappozzo, A. (2010). Is the human acetabulofemoral joint spherical? *Journal of Bone & Joint Surgery, British Volume* 92.2, pp. 311–314. DOI: 10.1302/0301-620X.92B2.22625.
- Cerveri, P., Manzotti, A., and Baroni, G. (2014). Patient-specific acetabular shape modelling: comparison among sphere, ellipsoid and conchoid parameterisations. *Computer methods in biomechanics and biomedical engineering* 5, pp. 560–567. DOI: 10.1080/10255842.2012.702765.
- Chegini, S., Beck, M., and Ferguson, S. J. (2009). The effects of impingement and dysplasia on stress distributions in the hip joint during sitting and walking: a finite element analysis. *Journal of Orthopaedic Research* 27.2, pp. 195–201. DOI: 10.1002/jor.20747.
- Chen, A., Bae, W., Schinagl, R., and Sah, R. (2001). Depth-and strain-dependent mechanical and electromechanical properties of full-thickness bovine articular cartilage in confined compression. *Journal of biomechanics* 34.1, pp. 1–12. DOI: 10.1016/S0021-9290(00)00170-6.
- Cilingir, A., Ucar, V., and Ucar, C (2011). Comparison of finite element models of natural hip joint - Abstracts of the Fifth International Participated National Biomechanics Congress. *Journal of Biomechanics* 44, p. 5. DOI: 10.1016/j.jbiomech.2011.02.031.
- Cobb, J., Logishetty, K., Davda, K., and Iranpour, F. (2010). Cams and pincer impingement are distinct, not mixed: the acetabular pathomorphology of femoroacetabular impingement. *Clinical Orthopaedics and Related Research*® 468.8, pp. 2143–2151. DOI: 10.1007/s11999-010-1347-z.

- Cooper, R. J., Mengoni, M., Groves, D., Williams, S., Bankes, M. J. K., Robinson, P., and Jones, A. C. (2017). Three-dimensional assessment of impingement risk in geometrically parameterised patient hips compared with standard clinical measures. *International Journal for Numerical Methods in Biomedical Engineering*, e2867. DOI: 10.1002/cnm.2867.
- Cowin, S. C. and Doty, S. B. (2007). *Tissue Mechanics*. New York: Springer.
- Dalstra, M., Huiskes, R., and Van Erning, L (1995). Development and validation of a three-dimensional finite element model of the pelvic bone. *Journal of biomechanical engineering* 117.3, pp. 272–278.
- Dandachli, W., Islam, S. U., Liu, M., Richards, R., Hall-Craggs, M, and Witt, J (2009). Three-dimensional CT analysis to determine acetabular retroversion and the implications for the management of femoro-acetabular impingement. *Journal of Bone & Joint Surgery, British Volume* 91.8, pp. 1031–1036. DOI: 10.1302/0301-620X.91B8.22389.
- deSa, D, Urquhart, N., Philippon, M., Ye, J.-E., Simunovic, N., and Ayeni, O. R. (2014). Alpha angle correction in femoroacetabular impingement. *Knee Surgery, Sports Traumatology, Arthroscopy* 22.4, pp. 812–821. DOI: 10.1007/s00167-013-2678-6.
- Elkins, J. M., Stroud, N. J., Rudert, M. J., Tochigi, Y., Pedersen, D. R., Ellis, B. J., Callaghan, J. J., Weiss, J. A., and Brown, T. D. (2011). The capsule's contribution to total hip construct stability—a finite element analysis. *Journal of Orthopaedic Research* 29.11, pp. 1642–1648.
- Ergen, F. B., Vudalı, S., Şanverdi, E., Dolgun, A., and Aydınğöz, Ü. (2014). CT assessment of asymptomatic hip joints for the background of femoroacetabular impingement morphology. *Diagnostic and Interventional Radiology* 20, pp. 271–276. DOI: 10.5152/dir.2013.13374.
- Fagan, M. J. (1992). *Finite Element Analysis Theory and Practice*. New Jersey: Prentice Hall.
- Ferguson, S., Bryant, J., Ganz, R, and Ito, K (2000). The influence of the acetabular labrum on hip joint cartilage consolidation: a poroelastic finite element model. *Journal of biomechanics* 33.8, pp. 953–960. DOI: 10.1016/S0021-9290(00)00042-7.
- Flachsmann, E., Broom, N., and Oloyede, A (1995). A biomechanical investigation of unconstrained shear failure of the osteochondral region under impact loading. *Clinical biomechanics* 10.3, pp. 156–165. DOI: 10.1016/0268-0033(95)93706-Y.
- Fox, A. J. S., Bedi, A., and Rodeo, S. A. (2009). The basic science of articular cartilage: structure, composition, and function. *Sports Health: A Multidisciplinary Approach* 1.6, pp. 461–468.

- Gander, W., Golub, G. H., and Strebel, R. (1994). Least-squares fitting of circles and ellipses. *BIT Numerical Mathematics* 34.4, pp. 558–578. DOI: 10.1007/BF01934268.
- Ganz, R., Parvizi, J., Beck, M., Leunig, M., Nötzli, H., and Siebenrock, K. A. (2003). Femoroacetabular impingement: a cause for osteoarthritis of the hip. *Clinical orthopaedics and related research* 417, pp. 112–120. DOI: 10.1097/01.blo.0000096804.78689.c2.
- Garabekyan, T., Ashwell, Z., Chadayammuri, V., Jesse, M. K., Pascual-Garrido, C., Petersen, B., and Mei-Dan, O. (2016). Lateral Acetabular Coverage Predicts the Size of the Hip Labrum. *The American journal of sports medicine*, p. 0363546516634058. DOI: 10.1177/0363546516634058.
- Grant, A. D., Sala, D. A., and Davidovitch, R. I. (2012). The labrum: structure, function, and injury with femoroacetabular impingement. *Journal of children's orthopaedics* 6.5, pp. 357–372. DOI: 10.1007/s11832-012-0431-1.
- Grassi, L., Väänänen, S. P., Ristinmaa, M., Jurvelin, J. S., and Isaksson, H. (2016). Prediction of femoral strength using 3D finite element models reconstructed from DXA images: validation against experiments. *Biomechanics and Modeling in Mechanobiology*, pp. 1–12. DOI: 10.1007/s10237-016-0866-2.
- Gu, D.-Y., Hu, F., Wei, J.-H., Dai, K.-R., and Chen, Y.-Z. (2011). “Contributions of non-spherical hip joint cartilage surface to hip joint contact stress”. *Engineering in Medicine and Biology Society, EMBC, 2011 Annual International Conference of the IEEE*. IEEE, pp. 8166–8169.
- Gu, D., Chen, Y., Dai, K., Zhang, S., and Yuan, J. (2008). The shape of the acetabular cartilage surface: A geometric morphometric study using three-dimensional scanning. *Medical engineering & physics* 30.8, pp. 1024–1031. DOI: 10.1016/j.medengphy.2007.12.013.
- Halim, A., Badrinath, R., and Carter, C. (2015). The importance of sex of patient in the management of femoroacetabular impingement. *American journal of orthopaedics* 44.4, pp. 172–175.
- Harding, L., Barbe, M., Shepard, K., Marks, A., Ajai, R., Lardiere, J., and Sweringa, H. (2003). Posterior-anterior glide of the femoral head in the acetabulum: a cadaver study. *Journal of Orthopaedic & Sports Physical Therapy* 33.3, pp. 118–125. DOI: 10.2519/jospt.2003.33.3.118.
- Harris, M. D., Anderson, A. E., Henak, C. R., Ellis, B. J., Peters, C. L., and Weiss, J. A. (2012). Finite element prediction of cartilage contact stresses in normal human hips. *Journal of Orthopaedic Research* 30.7, pp. 1133–1139. DOI: 10.1002/jor.22040.

- Harris, M. D., Datar, M., Whitaker, R. T., Jurrus, E. R., Peters, C. L., and Anderson, A. E. (2013). Statistical shape modeling of cam femoroacetabular impingement. *Journal of Orthopaedic Research* 31.10, pp. 1620–1626. DOI: 10.1002/jor.22389.
- Harris, M. D., Kapron, A. L., Peters, C. L., and Anderson, A. E. (2014). Correlations between the alpha angle and femoral head asphericity: Implications and recommendations for the diagnosis of cam femoroacetabular impingement. *European journal of radiology* 83.5, pp. 788–796. DOI: 10.1016/j.ejrad.2014.02.005.
- Harris-Hayes, M. and Royer, N. K. (2011). Relationship of acetabular dysplasia and femoroacetabular impingement to hip osteoarthritis: a focused review. *PM&R* 3.11, pp. 1055–1067. DOI: 10.1016/j.pmrj.2011.08.533.
- Hellwig, F., Tong, J., and Hussell, J. (2016). Hip joint degeneration due to cam impingement: a finite element analysis. *Computer methods in biomechanics and biomedical engineering* 19.1, pp. 41–48. DOI: 10.1080/10255842.2014.983490.
- Henak, C. R., Ellis, B. J., Harris, M. D., Anderson, A. E., Peters, C. L., and Weiss, J. A. (2011). Role of the acetabular labrum in load support across the hip joint. *Journal of biomechanics* 44.12, pp. 2201–2206. DOI: 10.1016/j.jbiomech.2011.06.011.
- Henak, C. R., Anderson, A. E., and Weiss, J. A. (2013). Subject-specific analysis of joint contact mechanics: Application to the study of osteoarthritis and surgical planning. *Journal of biomechanical engineering* 135.2, p. 021003. DOI: 10.1115/1.4023386.
- Henak, C. R., Ateshian, G. A., and Weiss, J. A. (2014a). Finite Element Prediction of Transchondral Stress and Strain in the Human Hip. *Journal of biomechanical engineering* 7. DOI: 10.1115/1.4026101.
- Henak, C. R., Kapron, A. L., Anderson, A. E., Ellis, B. J., Maas, S. A., and Weiss, J. A. (2014b). Specimen-specific predictions of contact stress under physiological loading in the human hip: validation and sensitivity studies. *Biomechanics and modeling in mechanobiology* 2, pp. 387–400. DOI: 10.1007/s10237-013-0504-1.
- Henninger, H. B., Reese, S. P., Anderson, A. E., and Weiss, J. A. (2010). Validation of computational models in biomechanics. *Proceedings of the Institution of Mechanical Engineers, Part H: Journal of Engineering in Medicine* 224.7, pp. 801–812. DOI: 10.1243/09544119JEIM649.
- Hogervorst, T., Eilander, W., Flikkers, J. T., and Meulenbelt, I. (2012). Hip ontogenesis: how evolution, genes, and load history shape hip morphotype and cartilotype. *Clinical Orthopaedics and Related Research*® 470.12, pp. 3284–3296. DOI: 10.1007/s11999-012-2511-4.

- Hua, X., Li, J., Wilcox, R. K., Fisher, J., and Jones, A. C. (2015). Geometric parameterisation of pelvic bone and cartilage in contact analysis of the natural hip: An initial study. *Proceedings of the Institution of Mechanical Engineers, Part H: Journal of Engineering in Medicine* 8, pp. 570–80. DOI: 10.1177/0954411915592656.
- Ito, K, Minka, M., Leunig, M, Werlen, S, and Ganz, R (2001). Femoroacetabular impingement and the cam-effect a MRI-based quantitative anatomical study of the femoral head-neck offset. *Journal of Bone & Joint Surgery, British Volume* 83.2, pp. 171–176. DOI: 10.1302/0301-620X.83B2.11092.
- Jaberi, F. M. and Parvizi, J. (2007). Hip pain in young adults: femoroacetabular impingement. *The Journal of arthroplasty* 22.7, pp. 37–42. DOI: 10.1016/j.arth.2007.05.039.
- Jones, A. C. and Wilcox, R. K. (2008). Finite element analysis of the spine: towards a framework of verification, validation and sensitivity analysis. *Medical engineering & physics* 30.10, pp. 1287–1304. DOI: 10.1016/j.medengphy.2008.09.006.
- Jorge, J., Simões, F., Pires, E., Rego, P., Tavares, D., Lopes, D., and Gaspar, A (2014). Finite element simulations of a hip joint with femoroacetabular impingement. *Computer methods in biomechanics and biomedical engineering* 5, pp. 1275–1285. DOI: 10.1080/10255842.2012.744398.
- Kapron, A. L., Aoki, S. K., Peters, C. L., and Anderson, A. E. (2014). Subject-specific Patterns of Femur-labrum Contact are Complex and Vary in Asymptomatic Hips and Hips With Femoroacetabular Impingement. *Clinical Orthopaedics and Related Research*® 472.12, pp. 3912–3922. DOI: 10.1007/s11999-014-3919-9.
- Kapron, A. L., Aoki, S. K., Peters, C. L., and Anderson, A. E. (2015). In-vivo hip arthrokinematics during supine clinical exams: Application to the Study of Femoroacetabular Impingement. *Journal of biomechanics* 48.11, pp. 2879–86. DOI: 10.1016/j.jbiomech.2015.04.022.
- Kempson, G., Freeman, M., and Swanson, S. (1968). Tensile properties of articular cartilage. 220.
- Kenyon, P. J., Perry, D., Barrett, M., Carroll, F. A., and Thomas, G. (2014). The use of hip radiographs in primary care: the inter-observer agreement of reporting native hip pathology. *Hip International* 24.3, pp. 290–4. DOI: 10.5301/hipint.5000120.
- Khanna, V., Caragianis, A., DiPrimio, G., Rakhra, K., and Beaulé, P. E. (2014). Incidence of Hip Pain in a Prospective Cohort of Asymptomatic Volunteers Is the Cam Deformity a Risk Factor for Hip Pain? *The American journal of sports medicine* 42.4, pp. 793–797. DOI: 10.1177/0363546513518417.
- Khennane, A. (2013). *Introduction to Finite Element Analysis Using MATLAB and Abaqus*. Florida: CRC Press.

- Kuhns, B. D., Weber, A. E., Levy, D. M., and Wuerz, T. H. (2015). The Natural History of Femoroacetabular Impingement. *Frontiers in surgery* 2. DOI: 10.3389/fsurg.2015.00058.
- Laborie, L., Lehmann, T., Engesæter, I., Sera, F., Engesæter, L., and Rosendahl, K (2014). The alpha angle in cam-type femoroacetabular impingement new reference intervals based on 2038 healthy young adults. *Bone & Joint Journal* 96.4, pp. 449–454. DOI: 10.1302/0301-620X.96B4.32194.
- Laborie, L. B., Lehmann, T. G., Engesæter, I. Ø., Eastwood, D. M., Engesæter, L. B., and Rosendahl, K. (2011). Prevalence of radiographic findings thought to be associated with femoroacetabular impingement in a population-based cohort of 2081 healthy young adults. *Radiology* 260.2, pp. 494–502. DOI: 10.1148/radiol.111102354.
- Lee, S.-S., Duong, C.-T., Park, S.-H., Cho, Y., Park, S., and Park, S. (2013). Frictional response of normal and osteoarthritic articular cartilage in human femoral head. *Proceedings of the Institution of Mechanical Engineers, Part H: Journal of Engineering in Medicine* 227.2, pp. 129–137. DOI: 10.1177/0954411912462815.
- Lepage-Saucier, M., Thiéry, C., Larbi, A., Lecouvet, F. E., Berg, B. C. V., and Omoumi, P. (2014). Femoroacetabular impingement: normal values of the quantitative morphometric parameters in asymptomatic hips. *European radiology* 24.7, pp. 1707–1714. DOI: 10.1007/s00330-014-3171-4.
- Li, J., Stewart, T. D., Jin, Z., Wilcox, R. K., and Fisher, J. (2013). The influence of size, clearance, cartilage properties, thickness and hemiarthroplasty on the contact mechanics of the hip joint with biphasic layers. *Journal of biomechanics* 46.10, pp. 1641–1647. DOI: 10.1016/j.jbiomech.2013.04.009.
- Liechti, E. F., Ferguson, S. J., and Tannast, M. (2015). Protrusio acetabuli: joint loading with severe pincer impingement and its theoretical implications for surgical therapy. *Journal of orthopaedic research* 33.1, pp. 106–113.
- Liu, Q., Wang, W., Thoreson, A. R., Zhao, C., Zhu, W., and Dou, P. (2016). Finite element prediction of contact pressures in cam-type femoroacetabular impingement with varied alpha angles. *Computer Methods in Biomechanics and Biomedical Engineering*, pp. 1–8. DOI: 10.1080/10255842.2016.1224861.
- Maas, S. A., Ellis, B. J., Rawlins, D. S., and Weiss, J. A. (2016). Finite element simulation of articular contact mechanics with quadratic tetrahedral elements. *Journal of biomechanics* 49.5, pp. 659–667. DOI: 10.1016/j.jbiomech.2016.01.024.
- Masjedi, M., Nightingale, C., Azimi, D., and Cobb, J. (2013a). The three-dimensional relationship between acetabular rim morphology and the severity of femoral cam lesions. *Bone & Joint Journal* 95.3, pp. 314–319. DOI: 10.1302/0301-620X.95B3.30901.

- Masjedi, M., Harris, S. J., Davda, K., and Cobb, J. P. (2013b). Mathematical representation of the normal proximal human femur: Application in planning of cam hip surgery. *Proceedings of the Institution of Mechanical Engineers, Part H: Journal of Engineering in Medicine* 227.4, pp. 421–427. DOI: 10.1177/0954411912466353.
- Mast, N. H., Impellizzeri, F., Keller, S., and Leunig, M. (2011). Reliability and agreement of measures used in radiographic evaluation of the adult hip. *Clinical Orthopaedics and Related Research*® 469.1, pp. 188–199. DOI: 10.1007/s11999-010-1447-9.
- Meng, Q., Jin, Z., Fisher, J., and Wilcox, R. (2013). Comparison between FEBio and Abaqus for biphasic contact problems. *Proceedings of the Institution of Mechanical Engineers, Part H: Journal of Engineering in Medicine* 227.9, pp. 1009–1019. DOI: 10.1177/0954411913483537.
- Meng, Q., An, S., Damion, R. A., Jin, Z., Wilcox, R., Fisher, J., and Jones, A. (2017a). The effect of collagen fibril orientation on the biphasic mechanics of articular cartilage. *Journal of the mechanical behavior of biomedical materials* 65, pp. 439–453. DOI: 10.1016/j.jmbbm.2016.09.001.
- Meng, Q., Fisher, J., and Wilcox, R. (2017b). The effects of geometric uncertainties on computational modelling of knee biomechanics. *Royal Society Open Science* 4.8, p. 170670. DOI: 10.1098/rsos.170670.
- Meyer, D. C., Beck, M., Ellis, T., Ganz, R., and Leunig, M. (2006). Comparison of six radiographic projections to assess femoral head/neck asphericity. *Clinical orthopaedics and related research* 445, pp. 181–185. DOI: 10.1097/01.blo.0000201168.72388.24.
- Mow, V., Kuei, S., Lai, W., and Armstrong, C. (1980). Biphasic creep and stress relaxation of articular cartilage in compression: theory and experiments. *Journal of biomechanical engineering* 102.1, pp. 73–84. DOI: 10.1115/1.3138202.
- Murgier, J, Reina, N, Cavaignac, E, Espié, A, Bayle-Iniguez, X, and Chiron, P (2014). The frequency of sequelae of slipped upper femoral epiphysis in cam-type femoroacetabular impingement. *Bone & Joint Journal* 96.6, pp. 724–729. DOI: 10.1302/0301-620X.96B6.33000.
- Nepple, J. J., Lehmann, C. L., Ross, J. R., Schoenecker, P. L., and Clohisy, J. C. (2013). Coxa profunda is not a useful radiographic parameter for diagnosing pincer-type femoroacetabular impingement. *The Journal of Bone & Joint Surgery* 95.5, pp. 417–423. DOI: 10.2106/JBJS.K.01664.
- Ng, K. G., Rouhi, G., Lamontagne, M., and Beaulé, P. E. (2012). Finite element analysis examining the effects of cam FAI on hip joint mechanical loading using subject-specific geometries during standing and maximum squat. *HSS Journal*® 8.3, pp. 206–212. DOI: 10.1007/s11420-012-9292-x.

- Ng, K. G., Lamontagne, M., Labrosse, M. R., and Beaulé, P. E. (2016a). Hip Joint Stresses Due to Cam-Type Femoroacetabular Impingement: A Systematic Review of Finite Element Simulations. *PLoS one* 11.1. DOI: 10.1371/journal.pone.0147813.
- Ng, K. G., Mantovani, G., Lamontagne, M., Labrosse, M. R., and Beaulé, P. E. (2016b). Increased Hip Stresses Resulting From a Cam Deformity and Decreased Femoral Neck-Shaft Angle During Level Walking. *Clinical Orthopaedics and Related Research*®, pp. 1–11. DOI: 10.1007/s11999-016-5038-2.
- Nötzli, H., Wyss, T., Stoecklin, C., Schmid, M., Treiber, K., and Hodler, J (2002). The contour of the femoral head-neck junction as a predictor for the risk of anterior impingement. *Journal of Bone & Joint Surgery, British Volume* 84.4, pp. 556–560. DOI: 10.1302/0301-620X.84B4.12014.
- Okano, K and Yamaguchi, K (2013). Femoral head deformity and severity of acetabular dysplasia on the hip. *The Bone and Joint Journal* 95.B, pp. 1192–1196. DOI: 10.1302/0301-620X.95B9.31503.
- Omoumi, P., Thiery, C., Michoux, N., Malghem, J., Lecouvet, F. E., and Vande Berg, B. C. (2014). Anatomic features associated with femoroacetabular impingement are equally common in hips of old and young asymptomatic individuals without CT signs of osteoarthritis. *American Journal of Roentgenology* 202.5, pp. 1078–1086. DOI: 10.2214/AJR.12.10083.
- Osawa, T., Moriyama, S., and Tanaka, M. (2014). Finite element analysis of hip joint cartilage reproduced from real bone surface geometry based on 3D-CT image. *Journal of Biomechanical Science and Engineering* 9.2, pp. 13–00164. DOI: 10.1299/jbse.13-00164.
- Petersen, W., Petersen, F., and Tillmann, B. (2003). Structure and vascularization of the acetabular labrum with regard to the pathogenesis and healing of labral lesions. *Archives of orthopaedic and trauma surgery* 123.6, pp. 283–288. DOI: 10.1007/s00402-003-0527-7.
- Pfarrmann, C. W., Mengiardi, B., Dora, C., Kalberer, F., Zanetti, M., and Hodler, J. (2006). Cam and Pincer Femoroacetabular Impingement: Characteristic MR Arthrographic Findings in 50 Patients. *Radiology* 240.3, pp. 778–785. DOI: 10.1148/radiol.2403050767.
- Rakhra, K. S., Sheikh, A. M., Allen, D., and Beaulé, P. E. (2009). Comparison of MRI alpha angle measurement planes in femoroacetabular impingement. *Clinical orthopaedics and related research* 467.3, pp. 660–665. DOI: 10.1007/s11999-008-0627-3.
- Ranawat, A. S., Schulz, B., Baumbach, S. F., Meftah, M., Ganz, R., and Leunig, M. (2011). Radiographic predictors of hip pain in femoroacetabular impingement. *HSS journal* 7.2, pp. 115–119. DOI: 10.1007/s11420-010-9192-x.

- Reichenbach, S., Leunig, M., Werlen, S., Nüesch, E., Pfirrmann, C. W., Bonel, H., Odermatt, A., Hofstetter, W., Ganz, R., and Jüni, P. (2011). Association between cam-type deformities and magnetic resonance imaging–detected structural hip damage: A cross-sectional study in young men. *Arthritis & Rheumatism* 63.12, pp. 4023–4030. DOI: 10.1002/art.30589.
- Reynolds, D, Lucas, J, and Klaue, K (1999). Retroversion of the acetabulum A cause of hip pain. *Journal of Bone & Joint Surgery, British Volume* 81.2, pp. 281–288.
- Roels, P, Agricola, R, Oei, E., Weinans, H, Campoli, G, and Zadpoor, A. (2014). Mechanical factors explain development of cam-type deformity. *Osteoarthritis and Cartilage* 22.12, pp. 2074–2082. DOI: 10.1016/j.joca.2014.09.011.
- Rothenfluh, E., Zingg, P., Dora, C., Snedeker, J. G., and Favre, P. (2012). Influence of resection geometry on fracture risk in the treatment of femoroacetabular impingement: a finite element study. *The American journal of sports medicine* 40.9, pp. 2002–2008.
- Russell, M., Shivanna, K., Grosland, N., and Pedersen, D. (2006). Cartilage contact pressure elevations in dysplastic hips: a chronic overload model. *Journal of orthopaedic surgery and research* 1.6. DOI: 10.1186/1749-799X-1-6.
- Schneider, P. J. (1996). *NURB Curves: A Guide for the Uninitiated*. http://www.mactech.com/articles/develop/issue_25/schneider.html, accessed 2015.
- Shepherd, D. and Seedhom, B. (1997). A technique for measuring the compressive modulus of articular cartilage under physiological loading rates with preliminary results. *Proceedings of the Institution of Mechanical Engineers, Part H: Journal of Engineering in Medicine* 211.2, pp. 155–165.
- Shepherd, D. and Seedhom, B. (1999). Thickness of human articular cartilage in joints of the lower limb. *Annals of the rheumatic diseases* 58.1, pp. 27–34.
- Siebenrock, K. A. and Schwab, J. M. (2013). The cam-type deformity—what is it: SCFE, osteophyte, or a new disease? *Journal of Pediatric Orthopaedics* 33, S121–S125.
- Stops, A., Wilcox, R., and Jin, Z. (2012). Computational modelling of the natural hip: a review of finite element and multibody simulations. *Computer methods in biomechanics and biomedical engineering* 15.9, pp. 963–979. DOI: 10.1080/10255842.2011.567983.
- Sutter, R., Dietrich, T. J., Zingg, P. O., and Pfirrmann, C. W. (2012). How useful is the alpha angle for discriminating between symptomatic patients with cam-type femoroacetabular impingement and asymptomatic volunteers? *Radiology* 264.2, pp. 514–521. DOI: 10.1148/radiol.12112479.
- Tannast, M., Siebenrock, K. A., and Anderson, S. E. (2007). Femoroacetabular impingement: radiographic diagnosis—what the radiologist should know. *American Journal of Roentgenology* 188.6, pp. 1540–1552. DOI: 10.2214/AJR.06.0921.

- Tibor, L. and Leunig, M (2012). The pathoanatomy and arthroscopic management of femoroacetabular impingement. *Bone and Joint Research* 1.10, pp. 245–257.
- Väänänen, S. P., Grassi, L., Flivik, G., Jurvelin, J. S., and Isaksson, H. (2015). Generation of 3D shape, density, cortical thickness and finite element mesh of proximal femur from a DXA image. *Medical image analysis* 24.1, pp. 125–134. DOI: 10.1016/j.media.2015.06.001.
- Wang, Y., Wei, H.-W., Yu, T.-C., and Cheng, C.-K. (2007). Parametric analysis of the stress distribution on the articular cartilage and subchondral bone. *Bio-medical materials and engineering* 17.4, pp. 241–247.
- Wei, H.-W., Sun, S.-S., Jao, S.-H. E., Yeh, C.-R., and Cheng, C.-K. (2005). The influence of mechanical properties of subchondral plate, femoral head and neck on dynamic stress distribution of the articular cartilage. *Medical engineering & physics* 27.4, pp. 295–304. DOI: 10.1016/j.medengphy.2004.12.008.
- Weinberg, D. S., Gebhart, J. J., Liu, R. W., and Salata, M. J. (2016). Radiographic Signs of Femoroacetabular Impingement Are Associated With Decreased Pelvic Incidence. *Arthroscopy: The Journal of Arthroscopic & Related Surgery*. DOI: 10.1016/j.arthro.2015.11.047.
- Wenger, D. R. (2013). Is there a role for acetabular dysplasia correction in an asymptomatic patient? *Journal of Pediatric Orthopaedics* 33, S8–S12. DOI: 10.1097/BPO.0b013e3182771764.
- Wriggers, P. (2008). *Nonlinear Finite Element Methods*. Berlin: Springer.
- Yanke, A. B., Khair, M. M., Stanley, R., Walton, D., Lee, S., Bush-Joseph, C. A., Orias, A. A. E., Inoue, N., and Nho, S. J. (2015). Sex differences in patients with CAM deformities with femoroacetabular impingement: 3-dimensional computed tomographic quantification. *Arthroscopy: The Journal of Arthroscopic & Related Surgery* 31.12, pp. 2301–2306. DOI: 10.1016/j.arthro.2015.06.007.
- Yoshida, H, Faust, A, Wilckens, J, Kitagawa, M, Fetto, J, and Chao, E. Y.-S. (2006). Three-dimensional dynamic hip contact area and pressure distribution during activities of daily living. *Journal of biomechanics* 39.11, pp. 1996–2004. DOI: 10.1016/j.jbiomech.2005.06.026.

Appendix A: Publications

Journals

1. **Cooper RJ**, Mengoni M, Groves D, Williams S, Bankes MJK, Robinson P, Jones AC. (2017). Three-dimensional assessment of impingement risk in geometrically parameterised hips compared with clinical measures. *International Journal for Numerical Methods in Biomedical Engineering*. e2867.
DOI: 10.1002/cnm.2867
2. **Cooper RJ**, Williams S, Mengoni M, Jones AC. Patient-specific parameterised cam geometry in finite element models of femoroacetabular impingement of the hip. Under Review.

Conferences

1. **Cooper RJ**, Williams S, Mengoni M, Jones AC. Three-Dimensional Assessment of Cam Impingement Severity with Parameterised Finite Element Models. Podium. International Society for Technology in Arthroplasty. Seoul, South Korea. September 2017.
2. **Cooper RJ**, Mengoni M, Williams S, Jones AC. Parametric and Segmented Femoral Surfaces in Finite Element Models of Cam Impingement. Podium. International Conference on Computational and Mathematical Biomedical Engineering. Pittsburgh, USA. April 2017.
3. **Cooper RJ**, Mengoni M, Groves D, Williams S, Bankes MJK, Robinson P, Jones AC. Assessing Cam Impingement in Three-dimensions using Geometric Parameterisation. Poster No. 2327. Orthopaedic Research Society. San Diego, USA. March 2017.
4. **Cooper RJ**, Mengoni M, Groves D, Williams S, Bankes MJK, Robinson P, Jones AC. Three-dimensional Assessment of Impingement Risk in Geometrically Parameterised Patient Hips. Podium. European Society of Biomechanics. Lyon, France. July 2016.

Appendix B: Tabulated raw data for parameterisation study

Table A1: Femoral severity measurements obtained from parameterised surfaces representing the 20 cam femurs and 18 control femurs.

Hip	Sex	Cam-Rad	Cam-Angle	Cam-Width	20 rot	Control Hip	Sex	Cam-Rad	Cam-Angle	Cam-Width	20 rot
01R	F	92.64	4.37	29.5		C01R	F	89.66	35.72	64.0	
06R	F	93.67	17.14	46.0		C13L	F	91.10	8.93	50.5	
11R	F	99.11	29.10	64.0		C07R	F	85.22	30.25	40.0	
16R	F	99.62	18.29	49.0		C08L	F	90.68	13.32	67.5	
18R	F	94.84	4.00	28.0		C15R	F	87.81	2.85	100.0	
28L	F	89.04	6.00	50.5		C14R	F	90.34	14.97	36.0	
33L	F	90.91	10.86	32.0		C22R	F	91.09	15.19	92.5	
51L	F	86.19	30.93	31.5		C10L	F	85.15	13.95	89.5	
75L	F	95.29	9.91	67.0		C05R	F	89.08	10.31	41.5	
81L	F	86.07	34.70	49.5	✓	C11L	F	90.91	7.80	35.5	
02R	M	100.42	50.19	63.5	✓	C06L	M	93.19	28.51	29.5	
07R	M	95.87	34.34	64.5		C16R	M	93.93	13.61	70.5	
09R	M	97.00	24.86	34.0		C17L	M	89.63	26.64	40.5	
17L	M	97.51	48.83	49.5		C18L	M	91.20	22.84	51.5	
22R	M	89.74	35.80	55.5		C09L	M	88.96	21.54	60.0	
27R	M	91.11	65.50	50.0		C20R	M	79.20	5.05	58.0	
34L	M	100.17	60.71	57.5		C23L	M	88.83	50.81	48.5	
38L	M	95.16	21.17	58.5		C24R	M	91.32	33.19	39.0	✓
53L	M	89.30	22.01	30.5	✓						
79L	M	93.49	41.83	31.5							

Table A2: Cross table lateral alpha angle measurements performed by each user for the 20 cam patients, plus the CT alpha angle measurements performed by PR.

Hip	PR	RJC	MM	Average	Std Dev	CT alpha
01R	65.8	69.4	49.2	61.5	8.8	78.5
06R	56.2	58.9	75.0	63.4	8.3	74.8
11R	67.4	62.3	76.7	68.8	6.0	73.3
16R	58.3	54.7	72.5	61.8	7.7	53.6
18R	71.1	52.1	55.5	59.6	8.3	73.2
28L	48.1	57.0	58.0	54.4	4.4	50.1
33L	68.5	70.7	65.6	68.3	2.1	52.4
51L	62.7	54.8	68.2	61.9	5.5	54.3
75L	69.8	53.9	67.6	63.8	7.0	63.4
81L	47.3	56.8	62.1	55.4	6.1	47.1
02R	79.4	77.3	69.2	75.3	4.4	86.7
07R	64.2	67.4	75.5	69.0	4.8	75.4
09R	58.9	61.2	68.6	62.9	4.1	57.8
17L	65.2	55.7	65.3	62.1	4.5	57.2
22R	57.0	57.6	61.3	58.6	1.9	47.4
27R	69.7	64.8	58.0	64.2	4.8	61.4
34L	60.0	65.1	68.2	64.4	3.4	59.4
38L	79.9	53.5	66.9	66.8	10.8	55.0
53L	60.1	56.5	58.0	58.2	1.5	54.7
79L	60.7	47.9	65.7	58.1	7.5	42.8

Table A3: CE angle measurements performed by each user for the 20 cam patients, plus the CE angle measurements on each spline for the parameterised acetabular surfaces.

Hip	PR	RJC	ACJ	MM	Average	Std Dev	3D CE angles					Max CE
01R	35.1	30.7	34.5	35.8	34.0	2.0	28.5	28.3	27.3	25.1	13.2	28.5
06R	26.2	21.3	20.0	19.2	21.7	2.7	18.3	17.5	14.1	11.0	5.0	18.3
11R	31.1	32.0	29.2	29.1	30.3	1.2	21.7	25.0	26.2	26.4	21.7	26.4
16R	43.3	43.8	40.5	42.4	42.5	1.3	44.9	37.8	37.4	35.0	16.1	44.9
18R	28.0	34.9	28.4	30.4	30.4	2.8	24.7	27.0	25.3	14.1	7.5	19.7
28L	35.0	36.8	34.2	35.3	35.3	0.9	36.7	33.5	32.0	29.8	12.1	36.7
33L	30.0	30.6	31.8	26.8	29.8	1.9	24.7	25.3	20.9	10.3	6.7	25.3
51L	27.6	28.5	28.2	27.1	27.9	0.5	19.9	21.8	23.2	22.5	6.6	23.2
75L	30.7	36.0	37.5	34.1	34.6	2.5	21.1	31.8	35.7	30.9	9.3	35.7
81L	26.6	30.8	28.3	28.1	28.4	1.5	25.3	23.6	24.2	21.3	4.7	25.3
02R	35.2	35.0	32.1	32.7	33.7	1.4	31.0	31.1	27.6	22.2	8.4	31.1
07R	28.8	35.6	29.5	29.5	30.8	2.8	24.6	26.5	27.7	24.3	22.0	27.7
09R	25.1	31.6	24.1	23.9	26.2	3.1	20.1	21.7	22.7	17.6	7.1	22.7
17L	36.1	39.3	38.8	33.5	36.9	2.3	30.9	32.9	33.9	32.5	28.4	33.9
22R	29.9	28.9	24.6	27.9	27.8	2.0	17.8	23.7	22.9	24.7	18.1	24.7
27R	33.3	38.0	35.5	33.3	35.0	1.9	29.3	31.0	34.1	31.1	23.2	34.1
34L	25.8	23.4	26.1	19.4	23.7	2.7	15.6	18.2	22.2	23.9	24.6	24.6
38L	29.8	28.9	32.1	30.5	30.3	1.2	24.6	29.1	29.7	26.1	8.9	29.7
53L	30.7	26.1	27.2	22.3	26.6	3.0	26.1	24.6	24.5	25.8	6.7	26.1
79L	32.6	33.7	34.1	29.5	32.5	1.8	20.8	21.2	27.9	31.0	28.4	31.0

Table A4: AV angle measurements performed by each user for the 20 cam patients, plus the AV angle measurements on each spline for the parameterised acetabular surfaces.

Hip	PR	RJC	ACJ	MM	Average	Std Dev	3D AV angles					Mean AV
01R	20.7	15.1	23.5	15.0	18.6	3.7	24.2	23.4	18.7	18.8	20.5	21.1
06R	17.4	20.9	20.7	22.5	20.4	1.8	18.8	18.1	20.7	19.7	25.9	20.6
11R	9.5	16.7	10.4	7.1	10.9	3.6	4.1	6.9	9.4	10.9	6.5	7.5
16R	18.2	22.0	22.2	23.4	21.4	2.0	8.8	14.2	12.4	14.7	13.7	12.7
18R	21.1	20.9	19.4	21.1	20.6	0.7	18.8	17.6	20.8	14.1	11.3	16.5
28L	20.3	23.5	21.7	20.9	21.6	1.2	9.7	13.4	15.6	12.7	9.5	12.2
33L	22.3	24.1	23.1	26.3	24.0	1.5	12.1	14.5	7.3	12.1	14.1	12.0
51L	16.0	11.4	13.2	14.4	13.7	1.7	10.7	15.3	17.4	15.5	12.5	14.3
75L	14.5	14.2	12.8	16.3	14.5	1.2	3.6	6.3	2.7	6.2	3.0	4.4
81L	19.1	19.9	21.3	21.2	20.3	0.9	7.0	14.8	19.1	15.8	16.3	14.6
02R	20.8	19.0	22.9	16.2	19.7	2.5	17.8	24.7	18.1	14.3	20.9	19.2
07R	11.6	11.3	13.0	19.1	13.7	3.2	5.5	7.3	4.7	5.1	3.0	5.1
09R	18.3	19.5	18.9	14.7	17.8	1.9	17.1	20.1	17.6	16.6	13.5	17.0
17L	13.7	19.3	16.8	15.4	16.3	2.0	1.0	14.4	16.9	7.7	7.2	9.4
22R	12.9	16.0	16.8	11.5	14.3	2.2	0.6	6.3	9.1	9.0	5.1	6.0
27R	12.7	15.0	15.8	13.5	14.3	1.2	3.7	8.5	9.7	6.7	5.1	6.7
34L	14.2	15.1	13.1	13.1	13.9	0.8	4.6	4.7	4.0	5.7	5.4	4.9
38L	14.4	20.7	19.8	19.1	18.5	2.5	6.3	13.7	9.2	10.7	7.1	9.4
53L	18.4	23.4	23.5	18.2	20.9	2.6	14.5	18.8	16.8	10.7	7.7	13.7
79L	11.6	13.3	13.6	14.5	13.3	1.0	6.4	5.4	4.2	1.1	0.1	3.4

Table A5: Strain in the acetabular soft tissue after 25 degrees of internal rotation, and the position of the centre of rotation used for the 20 patient-specific models (segmented and parametric).

Hip	Rot cent	Par E	Seg E
01R	1	4.055E-02	1.972E-02
06R	1	3.053E-02	6.514E-02
11R	0	4.405E-01	2.508E-01
16R	-2	2.400E-01	1.144E-01
18R	0	3.612E-01	2.066E-01
28L	0	1.338E-01	1.397E-01
33L	1.5	1.023E-02	1.777E-02
51L	3	1.693E-15	2.238E-03
75L	1.5	7.351E-02	1.039E-01
81L	4	3.275E-15	2.812E-08
02R	0	1.839E-01	2.374E-01
07R	0	4.670E-02	3.034E-02
09R	1	1.594E-02	4.663E-15
17L	1	7.946E-03	3.386E-15
22R	4	2.026E-02	9.796E-03
27R	3	1.822E-02	6.142E-03
34L	0	6.245E-02	6.000E-02
38L	1	1.089E-02	5.440E-15
53L	2	3.279E-02	2.780E-02
79L	2	2.244E-10	1.266E-14